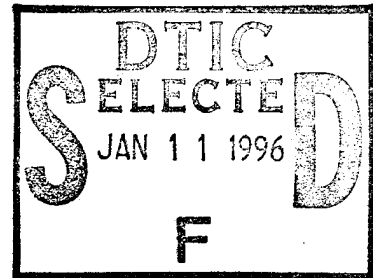


**Final Technical Report**

**The Near-Electrode Regions  
in Arcjet Thrusters**

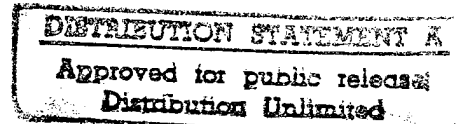


**Prepared by:**

**Mark A. Cappelli  
Principal Investigator  
Stanford University  
Stanford, CA 94305-3032**

**Prepared for:**

**Air Force Office of Scientific Research**



**Grant No. F49620-92-J-0449**

**October 1995**

**19960103 210**

**HIGH TEMPERATURE GASDYNAMICS LABORATORY  
Mechanical Engineering Department  
Stanford University**

**L  
G  
T  
H**

# REPORT DOCUMENTATION PAGE

Form Approved  
OMB No. 0704-0188

Public reporting burden for this collection of information is estimated to average 1 hour per response, including the time for reviewing instructions, searching existing data sources, gathering and maintaining the data needed, and completing and reviewing the collection of information. Send comments regarding this burden estimate or any other aspect of this collection of information, including suggestions for reducing this burden, to Washington Headquarters Services, Directorate for Information Operations and Reports, 1215 Jefferson Davis Highway, Suite 1204, Arlington, VA 22202-4302, and to the Office of Management and Budget, Paperwork Reduction Project (0704-0188), Washington, DC 20503.

1. AGENCY USE ONLY (Leave blank)	2. REPORT DATE October 31, 1995	3. REPORT TYPE AND DATES COVERED Final Technical Report 8/92-7/95
4. TITLE AND SUBTITLE Fundamental Studies of the Electrode Regions in Arcjet Thrusters <span style="margin-left: 150px;">(W)</span>	5. FUNDING NUMBERS PE - 61102F PR - 2308 SA - AS G - F49620-92-J-0449	
6. AUTHOR(S)  Mark A. Cappelli	7. PERFORMING ORGANIZATION NAME(S) AND ADDRESS(ES) Stanford University Stanford, CA 94305-3032	
8. PERFORMING ORGANIZATION REPORT NUMBER  AFOSR-TP- 95-0795		9. SPONSORING / MONITORING AGENCY NAME(S) AND ADDRESS(ES) AFOSR/NA 110 Duncan Avenue, Suite B115 Bolling AFB, DC 20332-0001
10. SPONSORING MONITORING AGENCY REPORT NUMBER		11. SUPPLEMENTARY NOTES
12a. DISTRIBUTION / AVAILABILITY STATEMENT  Approved for public release; distribution is unlimited	12b. DISTRIBUTION CODE	
13. ABSTRACT (Maximum 200 words)  A study of the electrode regions and arc-electrode interaction in arcjet thrusters is presented. The investigation was performed by optical diagnostics including imaging, emission and laser-induced fluorescence.		
14. SUBJECT TERMS  Arcjet, Thruster, Electric Propulsion, Electrode	15. NUMBER OF PAGES 162	
16. PRICE CODE		17. SECURITY CLASSIFICATION OF REPORT Unclassified
18. SECURITY CLASSIFICATION OF THIS PAGE Unclassified	19. SECURITY CLASSIFICATION OF ABSTRACT Unclassified	20. LIMITATION OF ABSTRACT UL

AFOSR Final Report

**Fundamental Studies of the Near-Electrode Regions of Arcjet Thrusters**

Grant No. F49620-92-J-0449

P.I.: Mark A. Cappelli

Department of Mechanical Engineering  
Stanford University  
Stanford, California

September 30, 1995

Availability Codes	
DTIC	<input checked="" type="checkbox"/>
AD	<input type="checkbox"/>
AS	<input type="checkbox"/>
NTIS	<input type="checkbox"/>
By	
Distribution/	
Availability Codes	
Dist	Avail. and/or Special
A-1	

## I. Summary of Progress

In the first year of this study the near-cathode plasma region was investigated through an axial emission diagnostic. A collisional-radiative model was developed to predict the radiant emission along the axis of the arcjet. This numerical work was supplemented with measurements of the axial emission spectrum, leading to the determination of electron number densities in the arcjet constrictor as a function of both radial position and specific power. These measurements were performed on both a low power (1 kW) and medium power (5 kW) hydrogen arcjet thruster.

During the second year of this contract, we focused on two areas: 1) a study of the arc and its interaction with the electrodes, and 2) the measurement of plasma properties at the arcjet exit plane for the validation of arcjet models. The former research area was concerned with the physics of the arc, including an understanding of the arc stability, arc current density distribution and both anode and cathode attachment mechanisms. The latter area involved two optical diagnostics, emission and Raman spectroscopy, used to measure exit-plane plasma properties.

In the final year of the contract three new studies were initiated: namely, optical imaging of the electrodes for temperature and arc attachment measurements, laser-induced fluorescence measurements of atomic hydrogen velocity within the arcjet nozzle, and stagnation pressure measurements in the arcjet plume. This final report summarizes these three studies; summaries of the previous studies can be found in the previous annual reports.

The arc-electrode interaction was studied experimentally through our electrode imaging work. In this study the cathode was imaged on a CCD camera which provided a means of directly measuring in-situ cathode temperature profiles. This in turn permitted a measurement of the cathode spot size and the arc current density distribution at the cathode surface. The anode temperatures were estimated from the imaged emission from the interior of the anode surface. Laser induced fluorescence was performed on the atomic hydrogen Balmer-alpha transition in the plasma in the interior of the arcjet nozzle. Axial velocities were measured from the Doppler shift of the linecenter relative to a stationary plasma source. In the plasma plume, stagnation pressure profiles were taken using a water-cooled Pitot probe, and these profiles were converted into Mach number profiles assuming a constant static pressure.

These studies are discussed in this report and the results have been presented in recent publications. Copies of these publications are given in Appendix I.

## II. Imaging of the Arcjet Electrode Regions

Arc-electrode interaction is the main determinate of arcjet performance and lifetime. The position of the arc and the geometry of the arc attachment at both the cathode and anode govern the electrode material temperature profiles and power transfer efficiency to the propellant. The electrode temperature profiles control thruster lifetime due to material loss and deformation. The energy transfer from the arc to the propellant determines the performance potential of the arcjet. Therefore, knowledge of the physical nature of the arcjet electrode region is quite important for prediction of arcjet lifetime and performance.

Measurement of electrode temperatures and arc attachment is difficult due to the harsh chemical environment in these regions. Previous studies have been conducted where various in-situ

measurements were obtained for arc attachment and cathode temperatures. Segmented anodes were used to measure arc anode-attachment for different types of arcjet geometries.<sup>1-4</sup> In these studies information was obtained showing that the arc anode-attachment can either be diffuse when the attachment is downstream of the nozzle throat in a low pressure region, or the arc attachment can be a constricted-spot attachment when the attachment is upstream of the nozzle throat in the high pressure region. However, questions remain as to the disruption of the arc caused by anode segmentation. Imaging of the electrode region of an exposed cathode plasma device similar to an arcjet has been performed on-axis and normal to the flow direction.<sup>5</sup> This study was at higher powers and with larger electrode geometries than normally used with state-of-the-art arcjets. Axial emission measurements have also been presented for both low and medium power arcjets.<sup>6,7</sup> From these measurements various parameters were calculated including cathode temperature and electron number densities at the center of the arcjet (cathode tip, center of anode throat).

The purpose of this investigation is to develop a non-intrusive in-situ measurement technique for on-axis spectral imaging of the electrode region of a conventional arcjet. A large field of view and high spatial resolution were desired. This technique allows measurement of both cathode and anode temperatures, cathode spot size, and may provide anode attachment geometry determination. The electrode imaging study is described in paper AIAA-95-1957 (Appendix I).

A high-resolution (12  $\mu\text{m}$  per pixel - 384 x 578 pixel area) CCD camera coupled with a tele-microscope was used for these measurements. Optical access to the arcjet was attained through a 3" window downstream of the arcjet exit plane in our low-power arcjet vacuum facility. The end-on view of the arcjet provided optical access to both the cathode tip and the diverging side of the anode/nozzle. The arcjet observed was a typical NASA Lewis 1 kW modular arcjet design. The arcjet nozzle had a throat diameter of 0.635 mm and an exit diameter of 9.5 mm (225 area ratio). The cathode tip was conical in shape with a 30 degree half angle. A CCD camera and a tele-microscope were the major components of this system. The tele-microscope had a focal range of 36" to 96" with magnification of 17x (at 36") and 7x (at 96"). The advantage of this device for this application was its large field width, 10 mm (at 36") and 23 mm (at 96"). With other lenses and attachments the magnification could be increased. The camera has 14 bit A/D conversion, and exposure time range of 5 ms to 23 hours, a readout rate with 100 kHz capability, and a shutter time of 5-6 ms. For viewing of the continuous radiation from the cathode tip, an RG-665 color glass filter was used to eliminate the majority of the radiation from the hydrogen plasma. The  $H_{\alpha}$  hydrogen line of the plasma was also viewed separately by using interference filters corresponding to the line center wavelength, 656.3 nm  $\pm$  5 nm.

Electrode images were obtained during arc operation by acquiring the emitted continuum radiation. From these images, the cathode radial temperature distribution and the cathode spot size could be measured. The cathode temperature was calculated from comparison of the cathode tip local radiation, for various arcjet operation levels, with calibrated data obtained from a tungsten arc lamp. Given the temperature distribution, other properties can be determined such as the current density distribution along the cathode, the cathode spot size, and electric field in front of the cathode.

The temperatures were obtained from calibration of a graybody source at known temperature. The CCD signal was converted to graybody intensity using the calibration. This graybody intensity was then converted to a blackbody intensity using an emissivity of 0.4. The temperature was then calculated from the blackbody intensity using the equation which relates these two values, the Planck distribution. Due to the lack of information on tungsten emissivity at temperatures higher than 2600 K, a constant of 0.4 was used. This assumption will introduce

slight errors in the temperature calculation. If accurate emissivity data were available it would be possible to iterate on the temperature to get more precise values.

Figure 1 illustrates a typical temperature profile obtained from an image of the cathode at a specific power of 101.2 MJ/kg. The profile is a cross-section through the center of the nozzle. The origin is the local center, determined by choosing the location of the peak temperature, and does not necessarily correspond to the exact geometric center of the cathode tip. The errors in temperature have been calculated to be approximately  $\pm 80$  K near the cathode and  $\pm 200$  K in the anode regions, beyond radius of approx. 0.3 mm.

Figure 2 shows the calculation of current density for the temperature profile shown in Fig. 1. Two current densities are shown in this figure, the current density for a purely thermionic emitting cathode and the current density for a field-enhanced thermionically emitting cathode. Previous researchers<sup>8</sup> have suggested that the cathodes in these types of devices emit electrons based on the principle of field-enhanced thermionic emission. The work function assumed for pure tungsten was based on previous experiments which showed that the thorium in the cathode migrates out of the cathode tip and after short operation times the cathode tip is left with virtually no thorium.<sup>8</sup> This cathode had been run extensively, therefore, it was expected that the cathode tip was pure tungsten. Based on the temperature distributions it is possible to calculate the current density at each radial location where there is a temperature value. The integral of current density times the differential area gives the total enclosed current. The electric field is then varied until the total enclosed current matches the measured current of the arcjet.

The results indicate that the measured peak temperatures are in the range from 4000-4200 K. These values are above the melting point of tungsten which could be due to the fact that the cathode tip is expected to be molten and the molten pool could be at a superheated temperature. The electric fields calculated are on the order of  $3.0 \times 10^8$  V/m. The error on these values was calculated to be  $\pm 1.0 \times 10^8$  V/m. These electric fields are on the same order of magnitude as values previously reported.<sup>7-9</sup> These fields can be shown to be order-of-magnitude-correct by looking at what cathode fall voltage arises with these field magnitudes. As an example, for the data presented in Fig. 2, the electron number density in front of the cathode is expected to be approximately  $4.0 \times 10^{23}$  m<sup>-3</sup>.<sup>6</sup> If a plasma temperature of 10,000 K is assumed, the Debye length is approximately 1.0  $\mu$ m. Assuming the plasma sheath thickness in front of the cathode is on the order of the Debye length, the cathode fall voltage would be on the order of 4 Volts. This agrees well with what is expected for high pressure discharges.<sup>10</sup>

It should be noted that these field magnitudes should be considered as upper limits to what might actually exist. Fields in excess of  $10^7$  V/m start to distort the potential barrier at the electrode to the extent that electron tunneling through the barrier becomes significant. This tunneling phenomenon, commonly referred to as field emission, becomes important when the thickness of the barrier approaches the wavelength of the free electrons in the tungsten electrode. In essence, the mechanism for current transfer from cathodes in these arcjets may be more complicated than previously thought.

### III. LIF Measurements of Atomic H Velocity in the Arcjet Nozzle

As arcjet thrusters have advanced from laboratory devices to in-flight operational thrusters for satellite north-south station-keeping, there has been an increase in interest in improving arcjet efficiency and operating range. These improvements will be obtained primarily through advanced analytical modeling of arcjets; however, the validation of the models can only be

performed by comparison with experimental measurements of operating parameters and plasma properties. During the past several years a number of optical diagnostics have been developed to investigate properties in the plasma plume of the arcjet. Primary among these diagnostics is laser-induced fluorescence (LIF), which has proven very useful due to its abundant signal level, very good spatial resolution and specie-specific nature. Plasma properties in the plume of an arcjet thruster operating on a variety of different propellants have been measured using LIF. Liebeskind et. al. measured atomic hydrogen translational temperature and velocity at the exit plane of a 1 kW hydrogen arcjet thruster,<sup>11</sup> and investigated slip velocity by the fluorescence of helium in a helium-seeded hydrogen arcjet.<sup>12</sup> Ruyten and Keefer measured velocity in an argon plume of a 0.3 kW arcjet,<sup>13</sup> and Ruyten et. al. performed LIF on atomic hydrogen and nitrogen to measure velocity in a 1 kW arcjet plume using simulated ammonia as the propellant.<sup>13</sup> Recently, Pobst et al. measured ground state atomic hydrogen density, temperature and velocity profiles at the exit plane of a 1 kW hydrogen arcjet using pulsed two-photon LIF.<sup>15</sup>

Although LIF has been successfully applied to arcjet thrusters as a plasma plume diagnostic, it has not previously been used to investigate plasma properties within the nozzle due to geometric constraints and reduced signal-to-background noise ratios. Optical studies of the plasma in the interior of the arcjet were previously performed only in emission; a summary of such work is presented in Ref. 16. An analysis based on collisional-radiative modeling suggested the feasibility of applying laser-induced fluorescence to the plasma in the interior of a low power hydrogen arcjet.<sup>17</sup> This study is the first use of laser-induced fluorescence for spatially resolved plasma velocity measurements within an arcjet nozzle. The arcjet was operated on a propellant of pure hydrogen. Fluorescence was performed on the Balmer- $\alpha$  transition and axial velocities were measured from the Doppler shift of the spectral linecenter. The arcjet operating conditions have been chosen to facilitate a comparison between these measurements and arcjet modeling results of Butler et. al.<sup>18,19</sup>

The fluorescence excitation was provided by a continuous wave ring dye laser pumped by an argon-ion laser. Dye laser output up to 200 mW was obtained with a pump laser power of 4 W. Scanning the ring dye laser was performed with a tunable, piezoelectrically driven intracavity etalon. The laser beam was directed axially into the plasma in order to probe the interior of the arcjet nozzle and to use the nozzle as a beam dump. Consequently, the axial velocity component was measured from the Doppler shift of the line. The fluorescence was collected at an angle of 16 degrees from the arcjet axis, and detected with a photomultiplier tube. The spatial resolution was approximately 0.6 mm in the axial direction and 30 mm in the transverse directions, as determined by the laser beam waist and the collection optics. The spectral resolution was  $4 \times 10^{-4}$  nm. By translating the arcjet axially and radially, fluorescence was obtained along the arcjet centerline as well as radially at a few axial positions. A fraction of the excitation laser beam from the dye laser was split off and sent to a photodiode detector and a wavemeter to monitor the laser intensity and wavelength. Since the fluorescence signal was considerably smaller than the background emission, phase-sensitive detection was performed by mechanically chopping the excitation beam and detecting the signal with a digital lock-in amplifier. Noise at the chopping frequency, due mainly to scattered laser light in the arcjet, was the primary limitation in obtaining a significant signal in regions of weak fluorescence. Velocity measurements were obtained along the axis of the nozzle from the exit plane to within 1.5 mm of the throat, at which point the LIF signal became lost in the background of scattered laser light. The recorded fluorescence signal was normalized by the photodiode output to account for variations in the laser power during the scan. The wavelength was determined from the output of the wavemeter. The Doppler shift of the linecenter was accurately determined by fitting the measured lineshape with a Gaussian profile.

Measurements of axial velocities along the nozzle centerline and along three diameters are given in Figs. 3 and 4 respectively. The axial position is defined as zero at the exit plane and negative into the nozzle. Hence, the nozzle throat is located at -12.1 mm. The centerline velocity is seen to drop monotonically from a peak of approximately 17.5 km/s at 1.3 mm downstream of the throat to around 12 km/s at the exit plane. Since no other measurements of velocity have been made within the arcjet nozzle, the results can only be compared to the arcjet model of Butler et al.<sup>18</sup> The results of two versions of this model are shown in Fig. 3. One version includes mass diffusion terms in the species momentum equation, while the other does not include such terms. There is remarkably good agreement between the measurements and the former model, clearly indicating the importance of including diffusional processes to correctly model the transport of heavy species in the plasma. This is not surprising considering the large radial gradients in plasma properties within the nozzle.<sup>19</sup>

Fig. 4 displays radial profiles of the axial velocity measured at three axial positions within the nozzle (2.54, 5.08, and 6.35 mm from the exit plane). The LIF signal intensity dropped off quickly with radial position, indicating a rapid radial decrease in the  $n=2$  excited state number density of atomic hydrogen. This loss in signal restricted the measurement domain to within approximately 2 mm of the nozzle centerline. The dashed lines in the figure are the model results at the same axial locations as the measurements. The measurements and the model show remarkably good agreement; however, the measured velocities are somewhat greater than those of the model away from the arcjet centerline. Although the centerline velocity decreases axially, the velocities away from the centerline increase with axially position. Since most of the mass convection occurs in this outer region, the total kinetic energy of the flow is clearly increasing downstream, as is expected in a supersonic diverging nozzle.

This LIF work is summarized in paper AIAA-95-2381 in Appendix I. At present, experiments are underway to perform a more comprehensive study to map the velocity flowfield at various arcjet specific energies for both hydrogen and simulated hydrazine propellants.

#### IV. Stagnation Pressure Measurements in the Arcjet Plume

Due to their high specific impulse and moderate thrust levels, arcjet thrusters are playing an increasing role in satellite propulsion. Existing and planned applications include arcjet thrusters for station-keeping and on-orbit maneuvering. Low power hydrazine arcjets are now in use on the TelStar IV class of communications satellites and the first space test of a high power arcjet will be launched in 1996 under the Air Force ESEX program. Arcjet technology is steadily improving as our understanding of the physics governing their operation increases. Efforts that combine both experimental and theoretical studies are necessary in order to build reliable models of arcjet performance that can be then used as design tools for next generation thrusters. These next generation thrusters will extend the envelope of low power arcjet operation to higher specific impulse. This study is motivated by the need to measure arcjet flow properties that can be used to verify the predictions of performance models. In this study, we discuss the results of Pitot pressure measurements in the plume of a low power arcjet thruster. These results are presented in Appendix I in paper AIAA-95-2818.

There have been only a few reported studies that have used Pitot probes to understand the behavior of electrothermal thruster plumes. A study performed by the McDonnell Corporation in the 1960's examined the impact pressure on a Pitot probe in the plume of several 30 kW class hydrogen arcjets.<sup>20</sup> A more recent study by Penko, et al., examined the plume of a nitrogen

resistojet with a Pitot probe for verification of direct simulation Monte Carlo (DSMC) and Navier Stokes continuum models.<sup>21</sup> To our knowledge, no such measurements have been published on low power hydrogen arcjets. Therefore, pressure measurements with several Pitot probe geometries were performed for both cold and arc heated flows in the plume of a low power arcjet. The results were compared to arcjet models available in the current literature. These include DSMC calculations<sup>22</sup> for un-ignited (no arc) hydrogen flow, and a magnetohydrodynamic (MHD) continuum model<sup>19</sup> for ignited flow in an arcjet of the same geometry. These results also complement the many non-intrusive spectroscopic studies that have been performed on this low power hydrogen arcjet plume that have provided measurements of velocity,<sup>11</sup> translational temperature,<sup>11,23</sup> rotational temperature,<sup>22</sup> and hydrogen number density.<sup>22</sup>

Pitot pressure measurements were performed for both cold and arc heated flows with several probe geometries. Resulting measurements were compared to numerical models available in the literature. These models included a direct simulation Monte-Carlo model (DSMC) of cold flow and a magnetohydrodynamic (MHD) model of arc heated flow. Cold flow Pitot pressures exhibited complex behavior not completely described by the model. Since differing probe geometries resulted in variations of certain flow features, some of the observed phenomena may be due probe-flow interactions or rarefied gas effects.

The Pitot pressure measurements of arc heated flow agreed well with the results calculated from the MHD model. Figure 5 compares the Pitot pressure cross-section for an arcjet power of 1.4 kW to the calculated Pitot pressures from MHD model simulations.<sup>19</sup> The Pitot pressure was calculated using three different ratios of specific heats; the first (1.40) to simulate no vibrational excitation, the second (1.33) to simulate full vibrational excitation, and the third (1.25) to simulate vibrational over-excitation by a factor of two. If effects due to rarefied flow are neglected, there is very good agreement between the experimental data and the model. The peak Pitot pressure is bracketed by the Pitot pressures calculated from the model results. There may be evidence of vibrational over-excitation in the wings.

If the model stagnation pressures are used to calculate a shock strength, the local Mach number may be determined from the measured Pitot pressures. Figure 6 shows the resulting Mach numbers using the Pitot pressures and assuming fully excited vibrational state ( $k = 1.33$ ) compared to the Mach numbers from the MHD code. The agreement is good and shows that the results are self consistent. The root finder was not able to converge on a Mach number beyond a radius of approximately 3.25 mm. In this region, analysis of the data showed that the MHD model stagnation pressures were slightly less than the measured Pitot pressures.

Figure 7 shows the plume Pitot pressure field for a power of 1.5 kW. The plume pressures appears symmetric and there is no evidence of a shock in the first 25 mm downstream of the exit plane. Assuming that the plume core flow is isentropic, the Pitot pressure along the center line can be used to determine plume temperatures. The procedure is to use a constant stagnation pressure, equal to the maximum calculated at the exit plane by the MHD model, and the measured Pitot pressure. Assuming full vibrational excitation ( $k = 1.33$ ), these quantities allow us to determine the local Mach number. Using reliable axial velocity data for the same arcjet (at a slightly lower power of 1.43 kW) from Liebeskind et al.,<sup>11</sup> a temperature can be extracted from the calculated Mach number. The resulting temperatures are plotted in Fig. 8 along with laser-induced fluorescence (LIF) based temperatures also measured by Liebeskind, et al.<sup>11</sup> As seen in this figure, the LIF temperatures are higher than those determined from the Pitot pressure measurements. However, it has recently been discovered that Stark broadening of the laser-probed transition was not taken into account in the study of Ref. 11. Correcting for Stark broadening, which will be significant only at the higher apparent temperatures, would lower the LIF temperatures at the exit plane to values that would be in close agreement with the

temperatures inferred from the measured Pitot pressure.<sup>23</sup> Further downstream from the exit plane, the agreement between the two temperatures is certainly apparent. At a distance 18 mm downstream of the exit plane, Liebeskind et al. found evidence of a shock. No evidence of a shock was found in the plume Pitot pressure field. It is not certain whether this is due to the perturbation of the probe in the plume flow or to the slightly higher power level used in these measurements.

### Acknowledgments

This work was supported by the Air Force Office of Scientific Research under grant No. F49620-92-J-0449 with M. Birkan as monitor. Special acknowledgment is also given to NASA Lewis Research Center for supplying the arcjet thruster, power supply and other equipment.

### References

1. Curran, F.M., *et al.*, "Performance Characterization of a Segmented Anode Arcjet Thruster," AIAA 90-2582, (also NASA TM 103227), July 1990.
2. Sankovic, J.M. and Berns, D.H., "Performance of a Low-Power Subsonic-Arc-Attachment Arcjet Thruster," AIAA 93-1898, June 1993.
3. Berns, D.H. and Sankovic, J.M., "Investigation of a Subsonic-Arc-Attachment Thruster Using Segmented Anodes," AIAA 93-1899, June 1993.
4. Berns, D.H., Heberlein, J., Zelesnik, D. and Sankovic, J.M., "Internal Nozzle Parameters of a Subsonic-Anode-Attachment Medium-Power Hydrogen Arcjet," AIAA 94-3248, June 1994.
5. Zhou, X., Berns, D.H. and Heberlein, J., "Investigation of Arc-Cathode Interaction," AIAA 94-3129, June 1994.
6. Storm, P.V. and Cappelli, M.A., "Axial Emission Diagnostics of a Low Power Hydrogen Arcjet Thruster," IEPC-93-219, September 1993.
7. Storm, P.V. and Cappelli, M.A., "Axial Emission Measurements on a Medium-Power Hydrogen Arcjet Thruster," AIAA 94-2743, June 1994.
8. F.M. Curran, T.W. Haag and J.F. Raquet; "Arcjet Cathode Phenomenon"; NASA Technical Memorandum 102099, 1989.
9. W.L. Bade and J.M. Yos; "Theoretical and Experimental Investigation of Arc Plasma-Generation Technology"; Part II, Vol. 1, ASD-TDR-62-729, AVCO Corp., 1962.
10. W. Finkelnburg and H. Maecker; "Electric Arcs and Thermal Plasma"; Translation from Handbuch der Physik, Bd. 22, Gasentladungen II, 1956.
11. J.G. Liebeskind, R.K. Hanson and M.A. Cappelli; "Laser-Induced Fluorescence Diagnostic for Temperature and Velocity Measurements in a Hydrogen Arcjet Plume"; *J. Applied Optics* 32, no. 30, 6117 (1993).
12. J.G. Liebeskind, R.K. Hanson and M.A. Cappelli; "LIF Measurements of Species Velocities in an Arcjet Plume"; IEPC-93-131; 23rd AIAA/AIDAA/DGLR/JSASS International Electric Propulsion Conference, September 1993.
13. W.M. Ruyten and D. Keefer; "Characterization of Electric Thruster Plumes using Multiplexed Laser Induced Fluorescence Measurements"; AIAA-92-2965; 28th Joint Propulsion Conference, July 1992.
14. W.M. Ruyten, D. Burtner and D. Keefer; "Laser-Induced Fluorescence Measurements on the Plume of a 1 kW Arcjet Operated on Simulated Ammonia"; IEPC-93-127; 23rd AIAA/AIDAA/DGLR/JSASS International Electric Propulsion Conference, September 1993.

15. J.A. Pobst, I.J. Wysong and R.A. Spores; "Laser Induced Fluorescence of Ground State Hydrogen Atoms at Nozzle Exit of an Arcjet Thruster"; AIAA-95-1973; 26th AIAA Plasmadynamics and Lasers Conference, June 1995.
16. M.A. Cappelli and P.V. Storm; "Interior Plasma Diagnostics of Arcjet Thrusters"; AIAA-94-2654; 25th AIAA Plasmadynamics and Lasers Conference, June 1994.
17. P.V. Storm and M.A. Cappelli; "Laser-Induced Fluorescence Measurements Within an Arcjet Thruster Nozzle"; AIAA-95-2381; 31st AIAA/ASME/SAE/ASEE Joint Propulsion Conference, July 1995.
18. G.W. Butler, A.E. Kull and D.Q. King; "Single Fluid Simulations of Low Power Hydrogen Arcjets"; AIAA-94-2870; 30th AIAA/ASME/SAE/ASEE Joint Propulsion Conference, June 1994.
19. G.W. Butler, I.D. Boyd and M.A. Cappelli; "Nonequilibrium Flow Phenomena in Low-Power Hydrogen Arcjets"; AIAA-95-2819; 31st AIAA/ASME/SAE/ASEE Joint Propulsion Conference, July 1995.
20. W.M. Van Camp et al.; "Study of Arc-Jet Propulsion Devices: Final Report"; NASA CR-54691, Mar. 1966.
21. P.F. Penko et al.; "Pressure Measurements in a Low Density Nozzle Plume for Code Verification"; AIAA-91-2110, 27th AIAA/ASME/SAE/ASEE Joint Propulsion Conference, June 1991.
22. I.D. Boyd, D.R. Beattie and M.A. Cappelli; "Numerical and Experimental Investigations of Low Density Supersonic Jets of Hydrogen"; *Journal of Fluid Mechanics*, vol. 280, pp. 41-67, 1995.
23. P.V. Storm and M.A. Cappelli; "High Spectral Resolution Study of a Low Power Hydrogen Arcjet Plume"; AIAA-95-1960; 26th AIAA Plasmadynamics and Lasers Conference, June 1995.

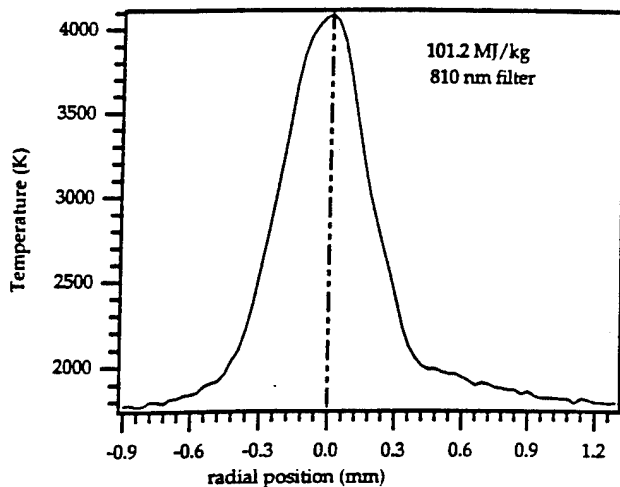


Figure 1. Radial temperature distribution of cathode.

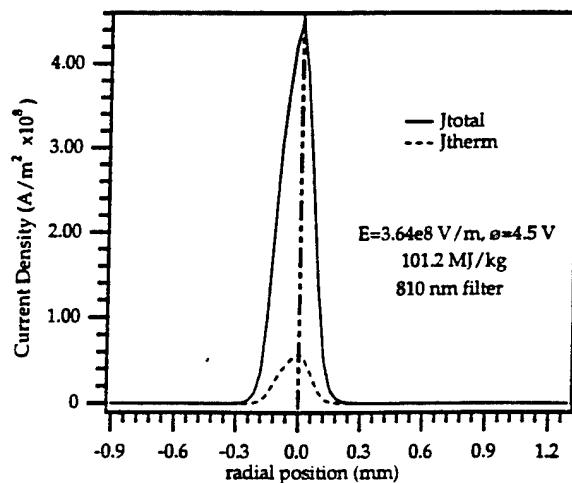


Figure 2. Current density profile on cathode obtained from temperature profile of Fig. 1.

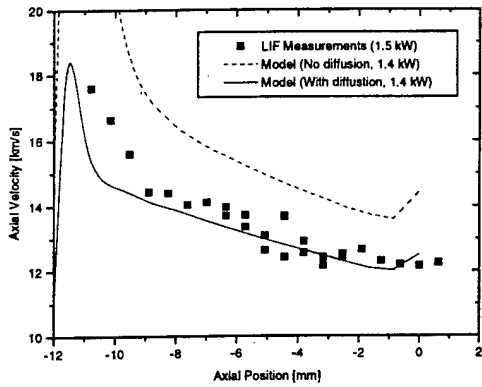


Figure 3. Axial velocity along the arcjet interior centerline.

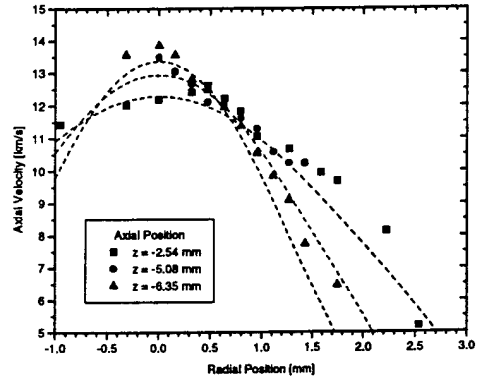


Figure 4. Radial profiles of axial velocity at three axial locations within the arcjet.

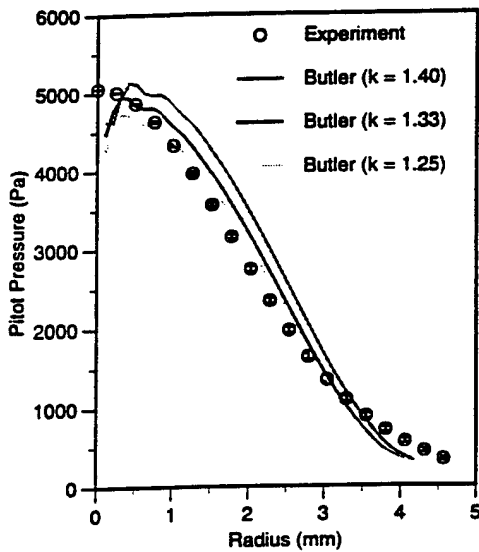


Figure 5. Comparison of Pitot pressures measured and calculated from the MHD model results of Butler et al.

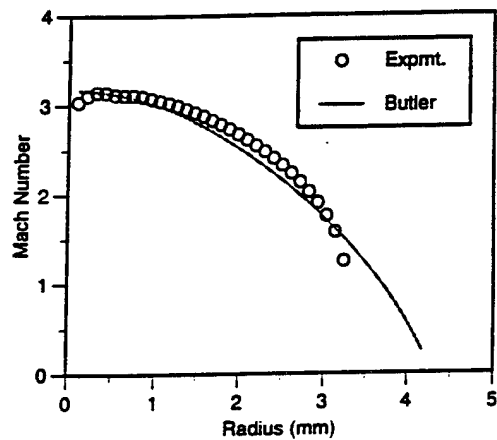


Figure 6. Comparison of calculated and predicted Mach number at the arcjet exit plane.

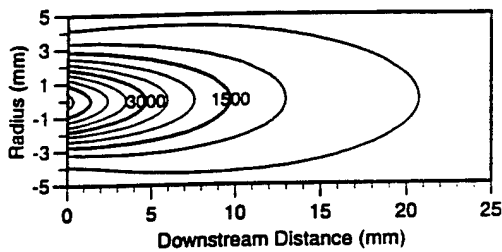


Figure 7. Plume Pitot pressure field (in Pascals)..

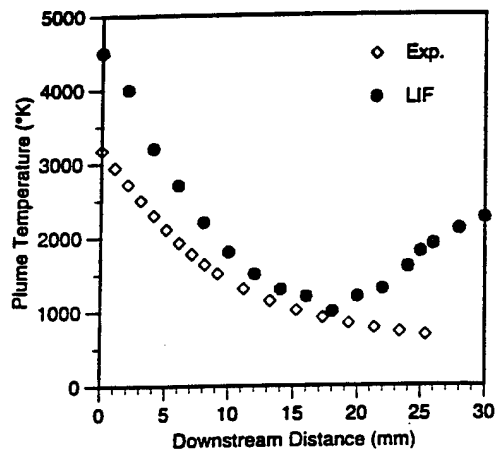


Figure 8. A comparison of translational temperatures determined from pressure measurements and LIF measurements.

Appendix I

# IEPC



**IEPC-93-219**

## **Axial Emission Diagnostics Of A Low Power Hydrogen Arcjet Thruster**

**P. V. Storm and M. A. Cappelli**

**High Temperature Gasdynamics Laboratory  
Department of Mechanical Engineering  
Stanford University  
Stanford, California**

**AIAA • AIDAA • DGLR • JSASS**

**23rd International Electric Propulsion Conference**

**Westin Hotel**

**Seattle, WA**

**September 13 - 16 1993**

# AXIAL EMISSION DIAGNOSTICS OF A LOW POWER HYDROGEN ARCJET THRUSTER

P. Victor Storm\* and Mark A. Cappelli\*\*

*High Temperature Gasdynamics Laboratory  
Department of Mechanical Engineering  
Stanford University  
Stanford, California, USA*

## Abstract

*A numerical and experimental investigation of the axial emission of a 1 kW class radiatively-cooled hydrogen arcjet thruster is presented. The numerical study consists of an integration of the 1-D radiative transfer equation along the arcjet centerline to predict the axial emission spectral intensity. A collisional-radiative model using plasma property inputs from a one-fluid MHD model is used to determine the atomic hydrogen line emission. The complete visible spectrum is predicted and compared to experimental measurements. The calculated spectrum indicates the possibility of measuring the cathode temperature and the arc electron number density. Axial emission measurements were performed and the results indicate a cathode temperature of approximately 3300 K at a power of 1.51 kW. The near-cathode electron number density was measured and found to increase linearly with arcjet power.*

## Introduction

During the last several years there has been an evolution of arcjet technology from laboratory devices to flight qualified thrusters.<sup>1</sup> As arcjet propulsion systems near deployment, interest in improving performance has intensified. To prove competitive with chemical propulsion systems, the arcjet must deliver 1000 s of specific impulse at 35 to 50 percent efficiency.<sup>2</sup> However, efficiencies approaching 50 percent at high specific impulse have not yet been achieved. The future design of more efficient and reliable thrusters capable of optimum performance requires a better understanding of the physical processes governing arcjet operation through a combination of experimental diagnostics and analytical modeling.

Several studies have been conducted to investigate arcjet performance under different operation conditions, electrical configurations and geometries. However, understanding the physical processes governing the arcjet operation requires a

detailed knowledge of the plasma properties everywhere in the flow field. A great deal of research has been conducted to measure the flow properties in the plume of the arcjet thruster using electrical and optical techniques.<sup>3-10</sup> Much less is known about the properties within the nozzle of the arcjet, yet it is here where the plasma behavior controls the arcjet performance. Most of the investigations into the plasma properties within the nozzle have been numerical,<sup>11-13</sup> while only a limited amount of experimental data has been taken in this region of the arcjet.<sup>14</sup> While numerical models of the arcjet are extremely useful, their accuracy can be judged only by comparison with a large body of experimental data. Therefore, a need clearly exists for further experimental investigations into the plasma properties within the arcjet nozzle.

This paper presents the first results in a new experimental program at Stanford University to investigate the physics of the arcjet in the near-cathode region. In this study, plasma properties within the arc are investigated by the axial emission of atomic hydrogen. An attempt is also made to directly measure the cathode temperature by radiative emission. This research consists of both a

\* Research Assistant, Student Member AIAA

\*\* Assistant Professor, Member AIAA

numerical prediction and the experimental measurement of the axial emission spectrum.

### Modeling of the Axial Emission

The emission spectrum of a hydrogen arcjet consists of atomic and molecular hydrogen line emission, continuum plasma emission from the free electrons, thermal emission from surfaces, and line emission from tungsten and thorium vaporized from the cathode. In this study, the emission spectrum emanating from the arcjet along its centerline is investigated. Here, the kinetic temperature is sufficiently high to fully dissociate the hydrogen, and hence no contribution to the spectrum from molecular hydrogen is expected. Furthermore, the only surface which can radiate directly along the axis of the arcjet is the cathode surface; therefore, the plasma emission would be superimposed on a background of graybody emission from the cathode. Finally, to simplify the calculation of the emission spectrum, the metal vapor concentration is assumed low enough that its emission can be neglected relative to that of the atomic hydrogen and free electrons.

The axial emission spectrum was calculated by integrating the one-dimensional radiative transfer equation along the centerline of the arcjet, beginning from the tip of the cathode. In steady-state, the one-dimensional radiative transfer equation is<sup>15</sup>

$$\frac{dI_\lambda(\lambda)}{dz} = \varepsilon_\lambda(\lambda) - k_\lambda(\lambda)I_\lambda(\lambda) \quad (1)$$

where the directional spectral intensity,  $I_\lambda$ , is the radiant power per unit area, per unit solid angle, per unit wavelength interval,<sup>16</sup> and  $\varepsilon_\lambda$  and  $k_\lambda$  are the plasma spectral volume emission and absorption coefficients, respectively, which include contributions from both the atomic hydrogen and the free electrons. The atomic hydrogen contribution involves line radiation from transitions between upper state  $j$  and lower state  $i$ , for which<sup>15</sup>

$$\begin{aligned} \varepsilon_\lambda^{ji}(\lambda) &= \frac{hc^2}{4\pi\lambda^3} n_j A_{ji} \Phi_\lambda^{ji}(\lambda) \\ k_\lambda^{ji}(\lambda) &= \frac{h}{\lambda} (n_i B_{ij} - n_j B_{ji}) \Phi_\lambda^{ji}(\lambda) \end{aligned} \quad (2)$$

where  $A_{ji}$ ,  $B_{ij}$  and  $B_{ji}$  are the Einstein coefficients and  $\Phi_\lambda^{ji}$  is the spectral lineshape function, subject to the normalization condition

$$\int_\lambda \Phi_\lambda^{ji}(\lambda) d\lambda = 1 \quad (3)$$

For an equilibrium plasma, the number densities  $n_i$  and  $n_j$  are determined from a Boltzmann distribution of the atomic state populations. However, as the plasma in the arcjet may not be in equilibrium, the number densities of the ground and excited states are calculated by solving the conservation equation for each state. Since the generation of excited states is by inelastic collisional and radiative processes, the process of calculating the state number densities requires a collisional-radiative model<sup>17</sup> and is described in detail in the following section.

The spectral lineshape function  $\Phi_\lambda^{ji}$  is determined by the broadening mechanisms.<sup>18</sup> The dominant broadening mechanism under the plasma conditions in the arc column is Stark broadening. In general, the Stark lineshape depends on the electron number density, temperature and, to a large extent, the particular electronic transition.<sup>18</sup> However, to simplify the calculations, it is often approximated by a Lorentzian function, to which it fits particularly well in the wings. In this study, the atomic emission lineshape was taken to be a Lorentzian function whose HWHM is identically equal to the  $\Delta\alpha_{1/2}$  Stark broadening parameter.<sup>19</sup> Since this parameter is obtained through the convolution of both Stark and Doppler broadening, the present calculation includes Doppler broadening in the determination of the line width, but does not correctly account for Doppler broadening in the lineshape. However, as the results indicate, the Stark broadening overwhelms the Doppler broadening for conditions in the arc and therefore this simplification is justified.

The contribution to the plasma spectral emission and absorption coefficients from the free electrons include continuum radiation from free-bound electron-ion interactions, and bremsstrahlung radiation from free-free electron-ion and electron-atom interactions.<sup>20</sup> The total volume emission coefficient for these three processes is given by<sup>21</sup>

$$\varepsilon_\lambda^e = \varepsilon_\lambda^{fb,ei} + \varepsilon_\lambda^{ff,ei} + \varepsilon_\lambda^{ff,ea} \quad (4)$$

where

$$\begin{aligned} \varepsilon_\lambda^{fb,ei} &= C_1 \frac{n_e^2}{\lambda^2 \sqrt{T_e}} \frac{g_1^+}{Q^+} \xi^{fb}(\lambda, T_e) \\ &\times [1 - \exp(-hc/\lambda k T_e)] \end{aligned} \quad (5a)$$

$$\varepsilon_{\lambda}^{ff,ei} = C_1 \frac{n_e^2}{\lambda^2 \sqrt{T_e}} \xi^{ff}(\lambda, T_e) \times \exp(-hc/\lambda k T_e) \quad (5b)$$

and

$$\varepsilon_{\lambda}^{ff,ea} = C_2 \frac{n_e n_a}{\lambda^2} T_e^{3/2} \left[ (1 + hc/\lambda k T_e)^2 + 1 \right] \times Q^{el}(T_e) \exp(-hc/\lambda k T_e) \quad (5c)$$

In these expressions,  $g_1^+$  and  $Q^+$  are the ion ground state degeneracy and partition function, respectively,  $\xi^{fb}$  and  $\xi^{ff}$  are the Biberman factors,<sup>22</sup> and  $Q^{el}$  is the elastic collision cross section. The constants are

$$C_1 = 1.63 \times 10^{-43} \text{ W m}^4 \text{ K}^{1/2} / \text{sr}$$

and

$$C_2 = 1.026 \times 10^{-34} \text{ W m}^2 \text{ K}^{-3/2} / \text{sr}$$

The corresponding spectral absorption coefficients for these processes are determined from the principle of detailed balance.<sup>23</sup>

Having obtained the sum of the spectral volume emission and absorption coefficients at every wavelength, the 1-D radiative transfer equation was numerically integrated along the centerline of the arcjet using a Crank-Nicolson implicit integration scheme<sup>24</sup> for stability and accuracy with reasonable step sizes. The graybody emission intensity from the cathode was used as the initial condition. The Doppler shift was taken in to account as the radiant intensity was being emitted and absorbed by the plasma with an axially varying velocity.

### The Collisional-Radiative Model

As previously indicated the number densities are calculated by solving an n-level collisional-radiative model.<sup>17</sup> This model consist of the steady-state continuity equation for the n-1 excited states,

$$\nabla \cdot n_m \underline{u}_m = \left[ \frac{dn_m}{dt} \right]_{CR} \quad (6)$$

for  $m=2..n$ , where  $\underline{u}_m$  is the velocity of excited state m. The production term is the net generation of excited state species by inelastic collisional and radiative processes.<sup>25</sup> In the stationary-state approximation, only the ground atomic state and ion have non-zero convection terms. Hence, the convective flux term for each excited state is zero, and we have

$$\left[ \frac{dn_m}{dt} \right]_{CR} = 0 \quad (7)$$

These processes include electron collisional excitation, de-excitation, ionization, three-body recombination, radiative recombination, and spontaneous emission. For the purpose of excited state number density calculations, photoionization and stimulated emission and absorption are neglected. An exception to this, however, is the treatment of resonance radiation since the ground state may be sufficiently populated for significant reabsorption to occur. This is taken into account by correcting the Einstein 'A' coefficient by an adjustable Holstein radiation escape factor.<sup>26</sup> The n-1 excited state continuity equations are then written in full as

$$0 = n_e \sum_{j \neq m} n_j K_{jm} - n_e n_m \sum_{j \neq m} K_{mj} - n_e n_m K_{mc} + n_e^3 \beta_{cm}^{(3)} + n_e^2 \beta_{cm}^{(r)} + \sum_{j > m} n_j \gamma_{jm} A_{jm} - n_m \sum_{j < m} \gamma_{mj} A_{mj} \quad (8)$$

where  $K_{mj}$  and  $K_{mc}$  are the electron collisional excitation and ionization rate coefficients,  $\beta_{cm}^{(3)}$  and  $\beta_{cm}^{(r)}$  are the electron collisional three-body and radiative recombination rate coefficients, and  $\gamma_{jm}$  is the Holstein escape factor for radiation between states j and m. The escape factors are unity except for those corresponding to transitions terminating on the ground state,  $\gamma_{j1}$ , which accounts for resonance radiation trapping. The present model uses the semi-empirical approximations for  $K_{mj}$ ,  $K_{mc}$ , and  $\beta_{cm}^{(r)}$  from Johnson,<sup>27</sup> while  $\beta_{cm}^{(3)}$  is determined from  $K_{mc}$  by detailed balance.<sup>23</sup> The spontaneous emission coefficients,  $A_{mj}$ , are obtained from the literature.<sup>28</sup> The collisional excitation rate coefficients are very close approximations to the Seaton rate coefficients.<sup>29</sup>

The preceding set of equations, combined with the equation of state,

$$p = \sum_m n_m kT + n_e kT + n_i kT_e \quad (9)$$

are solved for the atomic state populations,  $n_m$ , given the pressure, kinetic temperatures, and electron number density. These properties were obtained from a one-fluid MHD numerical model of the arcjet developed at Olin-Rocket Research Company.<sup>30</sup> The MHD model, incorporating finite rate ionization and dissociation, was run to simulate

operating conditions of 1.5 kW arcjet power and a hydrogen mass flow rate of 13 mg/s. As a single fluid model, a unique kinetic temperature was used for both the electrons and heavy particles. The model outputs, shown in Figure 1, provided the numerical inputs to the collisional-radiative model. The axial velocity is also shown as it was required as an input in the calculation of the spectral Doppler shift.

For the present calculations, the collisional-radiative model includes the lowest nine hydrogen atomic states and the continuum state. Neither the grouping of states nor the reduction of the ionization energy was performed. However, as a test of the model's accuracy, the excited state number densities were determined using an improved collisional-radiative model incorporating the reduction of the ionization limit due to Debye shielding. In this model, the number of levels used in the calculation was determined by assuming that, as a result of Debye shielding, a "bound" electron at one Debye length from the nucleus is essentially free. Hence, only the levels within a Debye length of the nucleus were considered bound levels, and the continuum state was consequently reduced in energy to the level beyond the last bound state. Using the plasma properties at several different axial positions, differences of only a few percent were observed in the lower excited state number densities between the present nine level model and the improved collisional-radiative model.

Finally, since the ground state number density is calculated from the equation of state, no provision is made for photoionization from the ground state. However, this process may be important in the ionizing region of the arcjet, and therefore the model is presently being improved to incorporate ground state photoionization.

## Modeling Results

Before examining the axial emission spectrum predicted by the model, it was first necessary to determine the effect of resonance radiation trapping and to test the validity of the stationary-state approximation. Figure 2 shows the number densities of the ground state and the first three excited states of atomic hydrogen calculated from the model as a function of axial position along the arcjet centerline. The abscissa origin is located at the arcjet throat. Negative axial position corresponds to the converging near-cathode region, while the expanding nozzle flow is in the positive

axial position. The exit plane is located at approximately 12.1 mm. The left plot shows the results with all radiative transitions optically thin, while the right plot shows the results with fully trapped resonance transitions. The only significant difference in the number densities appears in the expansion region of the nozzle for the  $n=2$  excited state. In the recombining nozzle region, the trapping of the resonance radiation results in a barrier to transitions to the ground state and hence a buildup in the  $n=2$  excited state number density. The other excited states are not affected significantly because they are able to radiate to lower states. As would be expected, the radiation trapping has no effect in the near-cathode region of the flow where the plasma is ionizing.

To test the validity of the stationary-state approximation, the convective flux terms in Eq. 6 were included but simplified to axial gradients only based on a 1-D approximation. With this simplification and no species diffusion velocity, the continuity equation for the excited states is

$$n_m \frac{du_z}{dz} + u_z \frac{dn_m}{dz} \approx \left[ \frac{dn_m}{dt} \right]_{CR} \quad (10)$$

The second term was found to be considerably smaller than the first term and was therefore omitted from the equations for simplicity. With the simplified convective fluxes included, the number densities were determined as a function of axial position and no change from Figure 2 was found anywhere in the flow. This provided the validation of the stationary-state approximation.

After having determined the axial distribution of the excited state number densities, the axial emission spectrum was calculated by integration of the equation of radiative transfer. Figure 3 shows the Balmer alpha emission lineshape at three axial positions between the nozzle throat and the exit plane. The initial condition on the intensity was that of graybody radiation from the cathode at a temperature of 3700 K and an emissivity of 0.4. The left plot shows the integrated intensity with all radiative transitions optically thin, while the right plot shows the results with fully trapped resonance transitions. The evolution of the spectral lineshapes are identical throughout the inner part of the nozzle, but differ considerably at the exit plane ( $z=12.1$  mm) due to the effect of resonance radiation trapping on the  $n=2$  number density in the expansion flow. The increased  $n=2$  population associated with the trapped resonance radiation

resulted in significant reabsorption of the  $H_{\alpha}$  line center radiation (right plot). Relative to the broad emission background lineshape, this reabsorption feature is both narrower, due to the lower electron number density in the expansion region, and shifted off-center, due to the lower axial velocity. The shift, however, is small and almost imperceptible. In the case of optically thin radiation, the lower  $n=2$  number density results in further emission in the expansion region rather than reabsorption (left plot); however, this "cold" emission feature is similarly narrowed and shifted. Figure 4 shows the Balmer alpha lineshape at the exit plane for different values of the resonance radiation escape factor from no trapping to fully trapped. A comparison of these lineshapes with the experimental  $H_{\alpha}$  spectrum indicates that the resonance radiation is nearly fully trapped, with the best fit escape factor of  $\gamma_{j1} = 0.1$ . All of the following calculations use this value unless otherwise noted.

Integration of the radiant intensity beyond the exit plane was also performed to determine the effect of the plume on the emission spectrum. In a worst case scenario, plume properties were taken to be the properties at the exit plane centerline. A remarkable difference was discovered between the optically thin case and the trapped resonance radiation case. In the former, the plume contributed to the emission intensity near the line center. In the latter, the line center reabsorption was complete by the exit plane and little change in the spectrum was seen through the plume. However, as it is generally believed that the MHD code does not accurately predict the exit plane temperature,<sup>31</sup> and since the plume temperature actually drops in the axial direction, the contribution to the emission spectrum from the plume is considered negligible.

The most remarkable feature of Figures 3 and 4 can be found not in the line center intensities, but in the wings of the lineshapes. It appears that the line wings are independent of both the resonance radiation escape factor and the axial position in the expansion region. This is to be expected since the broad emission lineshape originates from the ionizing near-cathode region of the flow. To determine its precise region of origin, Figure 5 shows a plot of intensity versus axial position for three off-center wavelengths and the line center wavelength ( $\lambda = 656.3$  nm) for comparison. The line center wavelength displays wide fluctuations in intensity due to both emission and reabsorption.

By contrast, the intensities of the three off-center wavelengths increase quickly due to emission in the near-cathode region, and then reach steady values approximately 0.5 mm past the arcjet constrictor. The lineshape wings are therefore entirely determined by the plasma properties within 1 mm of the cathode. In this arc region the electron number density is considerable and the lineshapes are overwhelmingly Stark broadened.<sup>18</sup> The usefulness of this observation as a diagnostic tool lies in the fact that a lineshape fit to only the wings of the axial emission spectrum will permit the determination of the electron number density in the arc, or near-cathode, region of the arcjet. This measurement, however, will be a line-of-sight average over the arc region, but will be weighted strongly towards the cathode where the number density of emitters is the greatest.

Since one of the objectives of this research is to determine the cathode temperature, it is instructive to investigate the dependence of the axial emission on cathode temperature. Figure 6 shows the calculated Balmer alpha emission spectrum for different values of the cathode temperature. The emissivity was fixed at 0.4 and the resonance radiation escape factor was taken to be 0.1. Not surprisingly, the line center reabsorption from the expansion flow region is independent of the cathode temperature, whereas the line wings, determined from properties in the near-cathode region, are sensitive to the cathode temperature. Fortunately, however, through background subtraction, the FWHM of the broad, near-cathode emission is quite insensitive to the cathode temperature. Therefore, the measurement of electron number density in the near-cathode region is not affected by the cathode temperature.

The entire computed visible spectrum of the axial emission at the arcjet exit plane is shown in Figure 7. The contributions to the spectrum from the cathode emission and from continuum radiation by the free electrons are indicated. The effect of the free electron radiation is to increase the broadband intensity above that of the cathode emission, and thereby essentially obstructing the view of the cathode. Fortunately, however, the continuum radiation is a small fraction of the cathode emission at long wavelengths. Therefore, a spectral window exists at wavelengths longer than 500 nm, but outside of interference of  $H_{\alpha}$ , for viewing the cathode and obtaining the cathode temperature.

The four lowest hydrogen Balmer lines are clearly visible in the spectrum. These lines are broadened substantially by the high electron number density in the arc region. The integrated line intensities have been calculated and are shown as a function of the transition upper state energy in the simulated Boltzmann plot of Figure 8. To determine whether the non-linearity is a result of non-equilibrium in the ionizing arc region or an effect of the radiation transfer on the spectral lines, the Boltzmann plot is compared to that of an optically-thin, uniform plasma with properties typical of the near-cathode region. Two cases, an LTE plasma and an ionizing plasma, both at  $T=35,000$  K and  $p = 2 \times 10^5$  Pa, were considered. The excited state number densities were determined using the collisional-radiative model and the integrated line intensities were then calculated using

$$I^{ji} = \int I_{\lambda}^{ji}(\lambda) d\lambda = \frac{hc}{4\pi\lambda^{ji}} n_j A_{ji} l \quad (11)$$

where the effective length,  $l$ , was taken to be 1 mm. Since the Boltzmann plot of the predicted emission spectrum displays a trend which is unlike those of the LTE and ionizing plasmas, it is believed that the radiation transfer has an effect on the line intensities in such a manner as to render the Boltzmann plot of the axial emission ineffective in determining the arc temperature. This is not surprising, however, since most of the line intensity comes from near line center, and the line center intensity varies considerably in the expansion region of the arcjet, as demonstrated in Figure 5.

## Experiment

Experiments were undertaken to measure the axial emission spectrum. The experimental setup is shown in Figure 9. The vacuum facility consisted of a 1.09 m x 0.56 m diameter stainless steel chamber maintained at a background pressure of 0.4 Torr by two mechanical pumps and 1250 cfm blowers. The arcjet used was a 1 kW class radiatively-cooled laboratory type thruster designed and built by NASA Lewis Research Center. The tungsten nozzle consisted of a 0.64 mm diameter constrictor and a 20 degree half-angle diverging section to an exit plane area ratio of 225. The 2% thoriated tungsten cathode was set approximately 0.45 mm from the nozzle constrictor. Details of this arcjet have been given previously.<sup>3,6</sup>

A 400 mm focal length lens was used to collect light axially from the arcjet throat and bring it to a focus on a 20  $\mu$ m diameter spatial filter. The image at the spatial filter was then focused, using a 150 mm focal length lens, onto the entrance slit of a Jarrell-Ash 0.5 m monochromator which contained a 1200 g/mm grating with a blaze angle of 500 nm. A Hamamatsu 1P21 photomultiplier tube was used as the photodetector. Phase-sensitive detection by a Stanford Research Systems SR850 digital lock-in amplifier was used for background noise rejection. The reference signal was provided by a mechanical beam chopper placed immediately before the spatial filter near the beam waist. The digitized output of the lock-in amplifier was transferred to a 486 PC for analysis. To minimize the light collection volume from the arcjet nozzle and plume, a 25 mm diameter aperture stop was placed in front of the collection lens, providing a collection optics  $f/\#$  of 28. The spatial resolution at the arcjet constrictor was calculated to be approximately 40  $\mu$ m. Intensity calibration was performed using an 18 A tungsten filament lamp whose temperature was determined by a Minolta Cyclops 152 optical pyrometer.

The experiments were run under the operating conditions of 13.1 mg/s of hydrogen propellant and arcjet power between 0.92 kW and 1.51 kW. Emission over the entire visible spectrum was collected on the arcjet centerline at four different values of  $P/\dot{m}$ . The Balmer lines were used to determine the arc centerline electron number density, while the background emission was used to estimate the cathode temperature. Furthermore, spectra of the Balmer alpha and beta lines were taken at different radial positions at one value of  $P/\dot{m}$  to determine the radial distribution of the electron number density within the arc.

## Experimental Results

Figure 10 shows the complete visible spectrum of the experimental axial emission at a power of 1.51 kW and a hydrogen flow rate of 13.1 mg/s, as well as the calculated spectrum for the same operating conditions and a cathode temperature of 3300 K. There are a number of conspicuous differences between the measured and calculated spectra. First, the background emission is considerably greater in the measured spectrum. The broad underlying emission feature beginning around 420 nm and reaching a peak at approximately 580 nm has no counterpart in the

calculated spectrum, and it is believed to be molecular hydrogen emission from the arcjet plume. Although the dissociation fraction is high, the collection volume is considerably larger in the plume than within the arcjet, so that significant molecular hydrogen emission may be collected in the optical train. At present, experiments are being undertaken at a higher collection optics  $f/\#$  to reduce this spectral feature.

The second significant difference between the measured and calculated spectra is that both the widths and intensities of the atomic hydrogen Balmer alpha and beta lines are greater in the former spectrum. Since it has been found that the widths are determined uniquely by the electron number density it can be concluded that the electron number density in the arc is higher than the MHD model predictions by estimated factor of 2 to 5. However, an increase in electron number density can only be accomplished by an increase in pressure since the plasma is fully ionized in the arc. The larger arc pressure would result in more emitters which is also consistent with the required increase in line intensity. A number of improvements are presently being made to the MHD model, including the addition of ambipolar diffusion and improved recombination rate determination.<sup>32</sup> It is believed that both of these improvements will increase the centerline number densities within the arc region.

As a result of the molecular hydrogen emission, the cathode temperature could not be determined by emission in the 500-650 nm range. However, the calculated spectrum shown in Figure 10, corresponding to a cathode temperature of 3300 K, fits very well to the measured spectrum at short wavelengths where the molecular hydrogen emission is not evident. Hence, in this manner the cathode temperature is estimated to be approximately 3300 K.

The visible emission spectra for a mass flow rate of 13.1 mg/s and four different arcjet powers are shown in Figure 11. All four spectra display the same features described in the 1.51 kW ( $P/\dot{m} = 115.3$  MJ/kg) case, but with decreasing intensity at lower power. The electron number densities in the arc were determined from a Lorentzian fit to the line wings of  $H_{\alpha}$  and  $H_{\beta}$  as described above, and are plotted as a function of arcjet specific power in Figure 12. The arc centerline electron number density increases with increasing specific power, and are larger than the MHD model predictions ( $n_e$

$\approx 2 \times 10^{23} \text{ m}^{-3}$  at  $P/\dot{m} = 115.3$  MJ/kg) by a factor of 2 to 5. This is consistent with the discrepancies in the line widths evident in Figure 10.

A Boltzmann plot of the integrated line intensities of the measured spectrum at  $P/\dot{m} = 115.3$  MJ/kg is shown, along with that of the calculated spectrum, in Figure 13. As previously discussed, a Boltzmann plot of the axial emission spectrum can not be used as a means of determining the arc temperature. However, it does provide an indication of the agreement between the measured and computed spectra. As evident in Figure 10, the line intensities of the three lowest Balmer lines are greater in the measured spectrum than in the predicted emission spectrum. This is reflected quantitatively in the Boltzmann plot. However, of greater significance is the agreement in the trends of the two Boltzmann plots, which indicates that, like the calculated line intensities, the experimentally measured intensities are affected by the radiation transfer through the nozzle expansion region.

Emission spectra of  $H_{\alpha}$  and  $H_{\beta}$  at an arcjet power of 1.51 kW and hydrogen flow rate of 13.1 mg/s were also taken as a function of radial position, and those for  $H_{\alpha}$  are shown in Figure 14. The spectra near the arcjet centerline show clearly the expansion region reabsorption at line center. It was from these measured spectra that a best fit resonance radiation escape factor of 0.1 was chosen for the collisional-radiative model. The off-centerline spectra show a decreasing broad "arc" emission width and intensity corresponding to a radial drop in both the arc electron number density and temperature away from the arcjet centerline. As the arc region emission decreases in intensity, the plasma within the nozzle flow region becomes the dominant source of emission. Since this line emission originates in a colder expanding plasma, the spectral lineshape is more narrow and less intense.

The electron number density in the arc region was determined from the line wings Lorentzian fit as previously described. Figure 15 shows the electron number density as a function of radial position calculated from both  $H_{\alpha}$  and  $H_{\beta}$  at a specific power of 115.3 MJ/kg. As in Figure 12, the electron number densities calculated from  $H_{\beta}$  are lower than those calculated from  $H_{\alpha}$  by a factor of approximately two. The reason for this discrepancy is not clear; however, in both cases the results indicate that the electron number density

slowly decreases linearly, but is nearly uniform, over a large part of the arcjet constrictor cross section.

## Conclusions and Summary

In this study, the axial emission of a 1 kW class hydrogen arcjet thruster was investigated. The radiative transfer equation was integrated from the cathode to the arcjet exit plane and beyond to predict the centerline axial emission spectrum. The atomic hydrogen line emission was calculated by a collisional-radiative model using input properties from a MHD arcjet code. The calculations predict the complete visible spectrum including contributions from atomic hydrogen line emission, continuum emission from the free electrons, and cathode graybody radiation, while radiation from molecular hydrogen and metal vapor is not included. Results from the modeling indicate that a spectral window exists for direct measurement of the cathode temperature by thermal emission. Furthermore, the modeling indicates that the lineshape wings of the atomic transitions depend only on the electron number density in the near-cathode region of the arcjet. Hence, the collisional-radiative model predicts an optical diagnostic technique to directly measure the electron number density in the arc without modification to the arcjet anode. Lastly, the modeling results indicate that the radiation transfer through the arcjet has an effect on the integrated line intensities, thereby rendering a Boltzmann plot incapable of providing a measure of the arc temperature in the near-cathode region.

Experiments were also performed to verify the modeling predictions. Some discrepancies were found between the measured and the calculated spectra; however, remarkable agreement was achieved considering the limitations of the model and the inherent difficulties of the measurements. The experiments indicate that molecular hydrogen may be a significant component of the emission spectrum. Due to the broadband molecular hydrogen emission, the cathode temperature could not be determined accurately as predicted. Nevertheless, an estimate of 3300 K at a power level of 1.51 kW and a mass flow rate of 13.1 mg/s was made by fitting the model predictions to the measured spectrum at short wavelengths. The electron number density in the arc was measured by the technique described above, and was found to be on the order of  $10^{24} \text{ m}^{-3}$ , which is higher than the

MHD model predictions by a factor of 2 to 5. The electron number density was found to be nearly spatially uniform over much of the constrictor cross section, and to increase linearly with  $P/m$ . Finally, a Boltzmann plot of the measured atomic line emission was found to have the same trend as that of the calculated spectrum.

At present, improvements are underway in both the modeling and the experimentation. The MHD model is being improved by the inclusion of ambipolar diffusion and more accurate recombination rates.<sup>32</sup> The collisional-radiative model is being modified to account for photo-ionization and the reduction of the ionization limit. New experiments are being undertaken at a much higher collection optics  $f/\#$  to possibly reduce the molecular hydrogen contribution to the emission spectrum. Additional emphasis is being placed on improving estimates of the cathode temperature.

## Acknowledgments

This work was supported by the Air Force Office of Scientific Research under grant No. F49620-92-J-0449 with M. Birkan as monitor. Partial support was provided by Olin-Rocket Research Company. Special acknowledgments are also given to G.W. Butler of Olin-Rocket Research Company for providing the arcjet plasma properties for use in the emission calculations, and to NASA Lewis Research Center for supplying the arcjet thruster.

## References

1. S. Yano and S.K. Knowles; "Simulated Flight Qualification of an Engineering Model Arcjet System"; 1989 JANNAF Conference, May 1989.
2. C. Vaughan and J. Cassady; "An Updated Assessment of Electric Propulsion Technology for Near-Earth Space Missions"; AIAA-92-3202; 28th AIAA/SAE/ASME/ASEE Joint Propulsion Conference, July 1992.
3. M.A. Cappelli, R.K. Hanson, J.G. Liebeskind, and D.H. Manzella; "Optical Diagnostics of a Low Power Hydrogen Arcjet Thruster"; IEPC-91-091; 22nd AIDAA/AIAA/DGLR/JSASS International Electric Propulsion Conference, October 1991.
4. D.H. Manzella, F.M. Curran, R.M. Myers, and D.M. Zube; "Preliminary Plume Characteristics of an Arcjet Thruster"; AIAA-90-2645; 21st AIAA/DGLR/JSASS International Electric Propulsion Conference, July 1990.
5. W.A. Hoskins, A.E. Kull, and G.W. Butler; "Measurement of Population and Temperature Profiles in an Arcjet Plume"; AIAA-92-3240; 28th

- AIAA/SAE/ASME/ASEE Joint Propulsion Conference, July 1992.
6. J.G. Liebeskind, R.K. Hanson, and M.A. Cappelli; "Flow Diagnostics of an Arcjet using Laser-Induced Fluorescence"; AIAA-92-3243; 28th AIAA/SAE/ASME/ASEE Joint Propulsion Conference, July 1992.
  7. D.H. Manzella and M.A. Cappelli; "Vacuum Ultraviolet Absorption in a Hydrogen Arcjet"; AIAA-92-3564; 28th AIAA/SAE/ASME/ASEE Joint Propulsion Conference, July 1992.
  8. L.M. Carney; "An Experimental Investigation of Arcjet Exhaust Using Langmuir Probes"; NASA TM 102346, 1988.
  9. J.M. Sankovic; "Investigations of the Arcjet Plume Near Field Using Electrostatic Probes"; NASA TM 103638, 1990.
  10. S.W. Jansen et al.; "Arcjet Plume Characterization, Part II: Optical Diagnostics Analysis"; AIAA-90-2643; 21st AIAA/DGLR/JSASS International Electric Propulsion Conference, July 1990.
  11. G.W. Butler, B.A. Kashiwa, and D.Q. King; "Numerical Modeling of Arcjet Performance"; AIAA-90-1474; 21st AIAA Fluid Dynamics, Plasma Dynamics and Lasers Conference, June 1990.
  12. M.A. Cappelli; "Modeling the Near-Electrode Region of Arcjets I: Coupling of the Flow Field to the Non-equilibrium Boundary Layer"; AIAA-92-3109; 28th AIAA/SAE/ASME/ASEE Joint Propulsion Conference, July 1992.
  13. R. Rhodes and D. Keefer; "Modeling Arcjet Space Thrusters"; AIAA-91-1994; 27th AIAA/SAE/ASME/ASEE Joint Propulsion Conference, June 1991.
  14. D.M. Zube and R.M. Myers; "Nonequilibrium in a Low Power Arcjet Nozzle"; AIAA-91-2113; 27th AIAA/SAE/ASME/ASEE Joint Propulsion Conference, June 1991.
  15. H.R. Griem; "Plasma Spectroscopy"; McGraw-Hill, Inc., New York, 1964.
  16. Here we write the directional spectral intensity on a per unit wavelength basis. However, as the experiments were calibrated on a per unit frequency basis and a direct comparison was desired, the calculated intensities were converted and plotted on a per unit frequency basis.
  17. B. van der Sijde, J.J.A.M. van der Mullen, and D.C. Schram; "Collisional Radiative Models in Plasmas"; *Beitr. Plasmaphys.*, **24**, pp. 447-473, 1984.
  18. W.L. Wiese; "Line Broadening"; *Plasma Diagnostic Techniques*, R.H. Huddlestone and S.C. Leonard, eds., Academic Press, New York, 1965.
  19. C.R. Vidal, J. Cooper and E.W. Smith; "Hydrogen Stark Broadening Tables"; *The Astrophysical Journal Supplement Series*, No. 214, **25**, pp. 37-136, 1973.
  20. L.M. Biberman and G.E. Norman; "Continuous Spectra of Atomic Gases and Plasma"; *Soviet Physics Uspekhi*, **10**, pp. 52-90, 1967.
  21. A.T.M. Wilbers, G.M.W. Kroesen, C.J. Timmermans and D.C. Schram; "Quant. Continuum Emission of an Arc Plasma"; *J. Quant. Spectrosc. Radiat. Transfer*, **45**, pp. 1-10, 1991.
  22. The Biberman factors for hydrogen are unity by definition.
  23. W.G. Vincenti and C.H. Kruger, Jr.; "Introduction to Physical Gas Dynamics"; Robert E. Krieger Co., New York, 1965.
  24. C.F. Gerald; "Applied Numerical Analysis", 4th ed.; Addison-Wesley Pub. Co., 1989.
  25. M. Mitchner and C.H. Kruger, Jr.; "Partially Ionized Gases"; John Wiley & Sons, New York, 1973.
  26. T. Holstein; "Imprisonment of Resonance Radiation in Gases II"; *Phys. Rev.*, **83**, p. 1159, 1951.
  27. L.C. Johnson; "Approximations for Collisional and Radiative Transitions Rates in Atomic Hydrogen"; *Astrophys. J.*, **174**, pp. 227-236, 1972.
  28. W.L. Wiese, M.W. Smith and B.M. Glennon; "Atomic Transition Probabilities: Hydrogen through Neon"; NSRDS-NBS4 Vol 1, May 1966.
  29. M.J. Seaton; "The Impact Parameter Method for Electron Excitation of Optically Allowed Atomic Transitions"; *Proc. Phys. Soc.*, **79**, p. 1105, 1962.
  30. G.W. Butler and D.Q. King; "Single and Two Fluid Simulations of Arcjet Performance"; AIAA-92-3104, 28th AIAA/SAE/ASME/ASEE Joint Propulsion Conference, July 1992.
  31. M. A. Cappelli, J.G. Liebeskind, R.K. Hanson, G.W. Butler, and D.Q. King; "A Comparison of Arcjet Plume Properties to Model Predictions"; AIAA-93-0820; 31st Aerospace Sciences Meeting and Exhibit, January 1993.
  32. M. A. Cappelli, J.G. Liebeskind, R.K. Hanson, G.W. Butler, and D.Q. King; "A Comparison of Hydrogen Arcjet Plume Properties to Single and Two-Fluid Model Predictions"; IEPC-93-220; 23rd AIAA/AIDAA/DGLR/JSASS International Electric Propulsion Conference, September 1993.

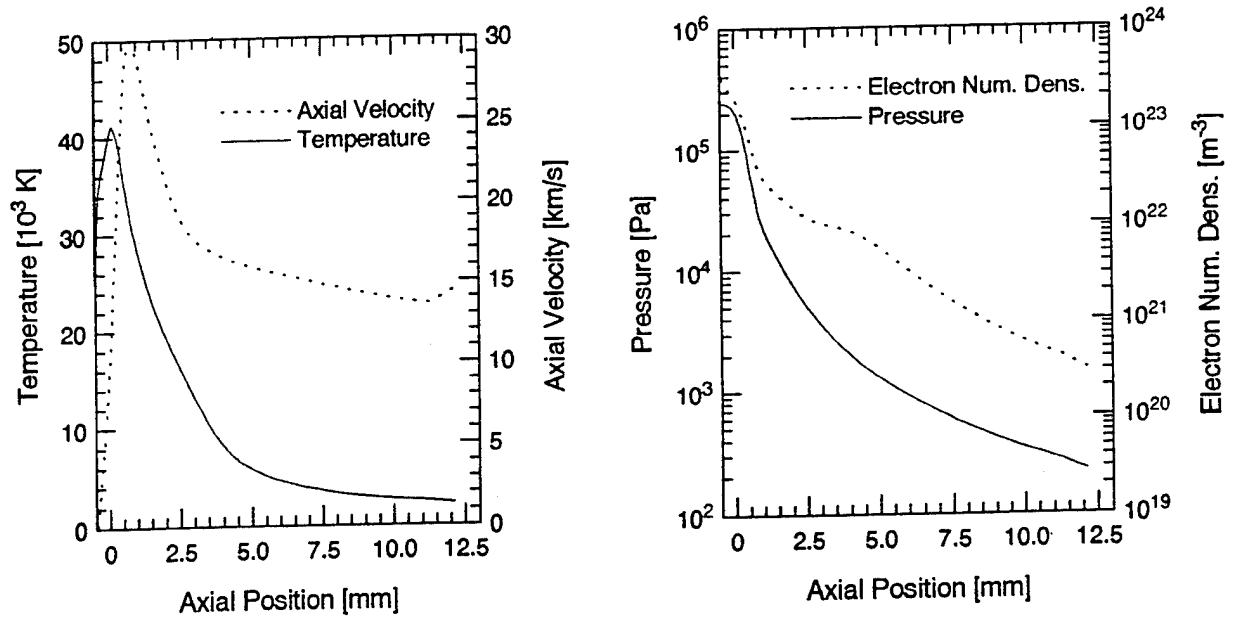


Figure 1. Axial properties  $T$ ,  $u_z$ ,  $p$  and  $n_e$  on the arcjet centerline from a one-fluid MHD code (Olin-Rocket Research Company)

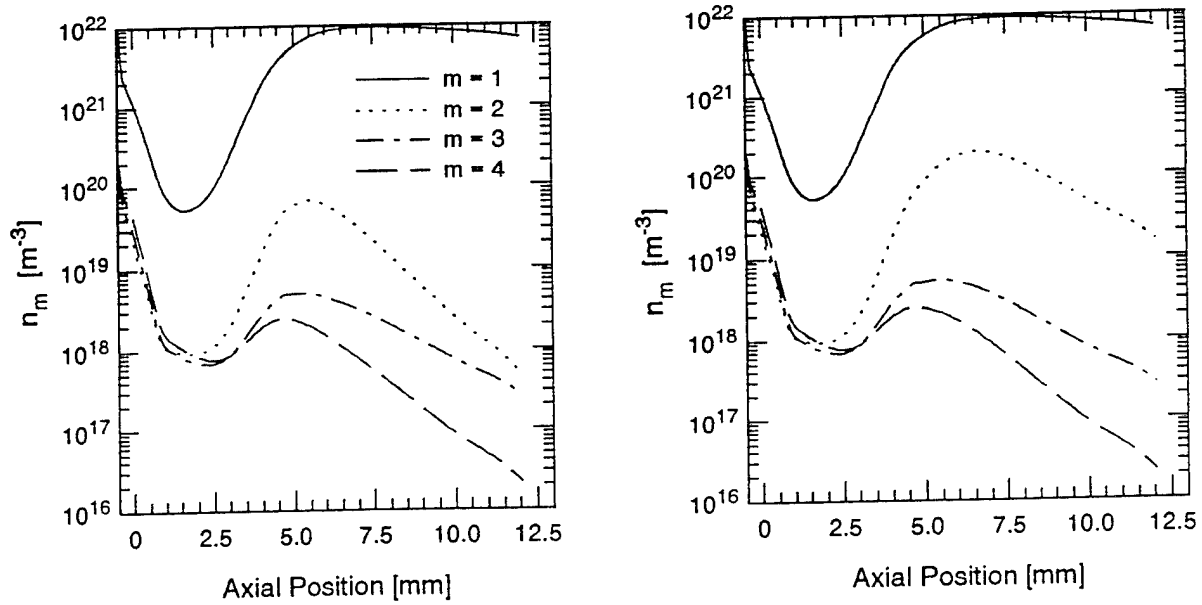


Figure 2. Calculated axial variation of the number densities of the lowest four atomic hydrogen states with optically thin radiation (left) and fully trapped resonance radiation (right).

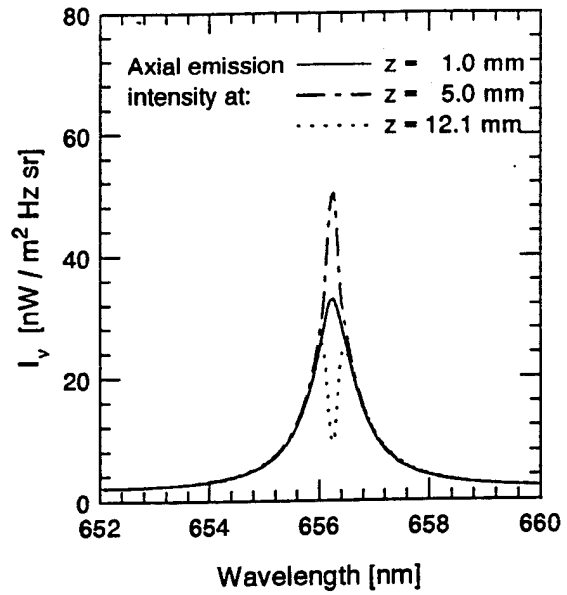
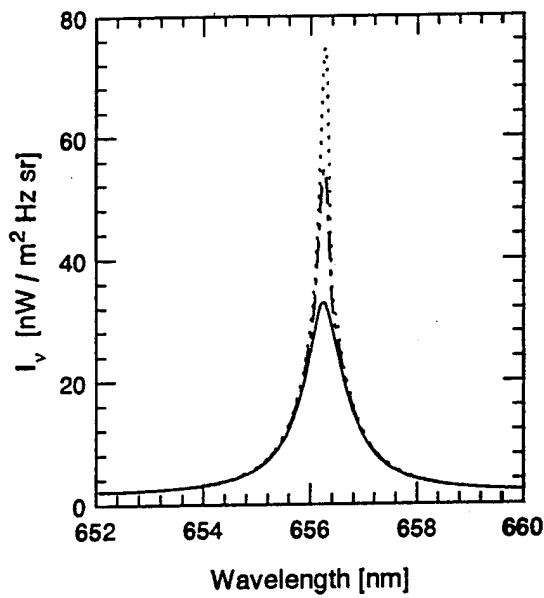


Figure 3. Calculated  $H_{\alpha}$  axial emission lineshape at various axial positions for a cathode temperature of 3700 K and emissivity of 0.4 with optically thin radiation (left) and fully trapped resonance radiation (right).

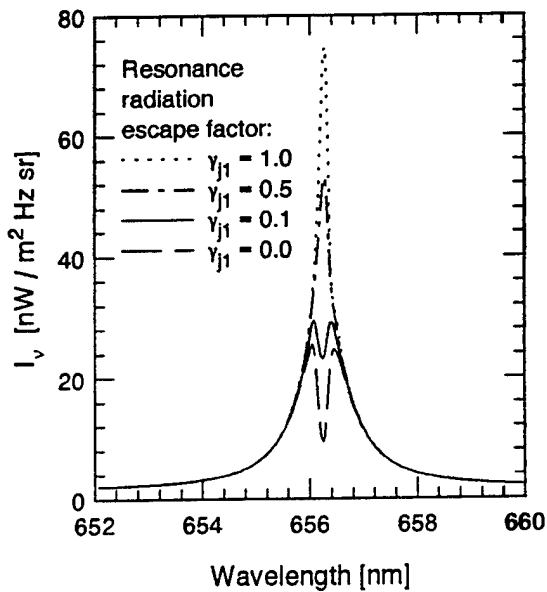


Figure 4. Calculated  $H_{\alpha}$  axial emission lineshape at the exit plane centerline for different values of the resonance radiation escape factor.

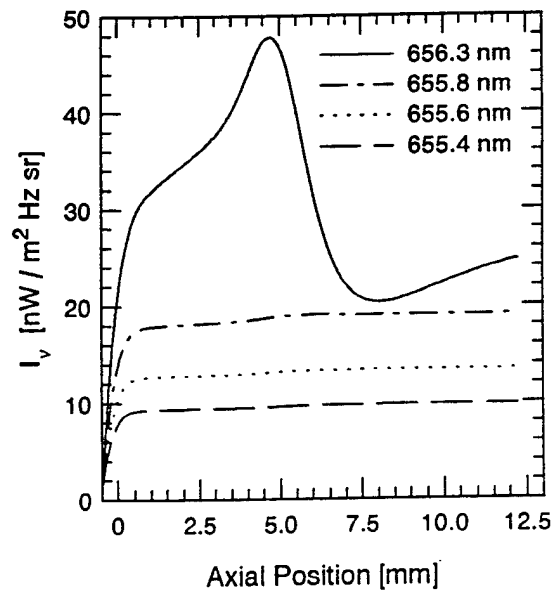


Figure 5. Calculated axial variation of the spectral intensity at the line center of  $H_{\alpha}$  and three off-center wavelengths.

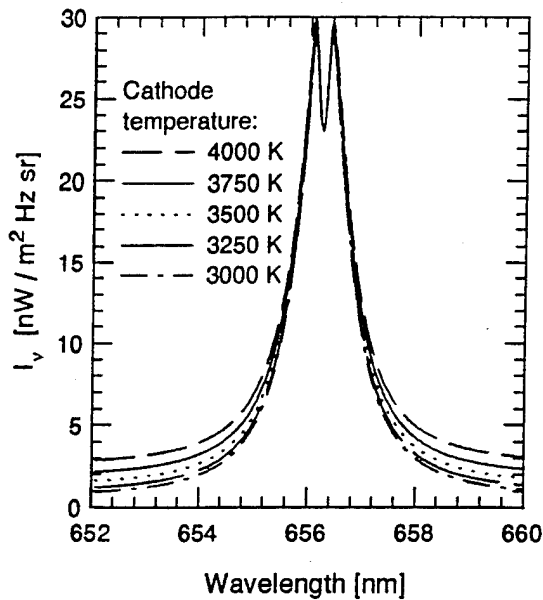


Figure 6. Calculated  $H_{\alpha}$  axial emission lineshape at the exit plane centerline for different values of the cathode temperature.

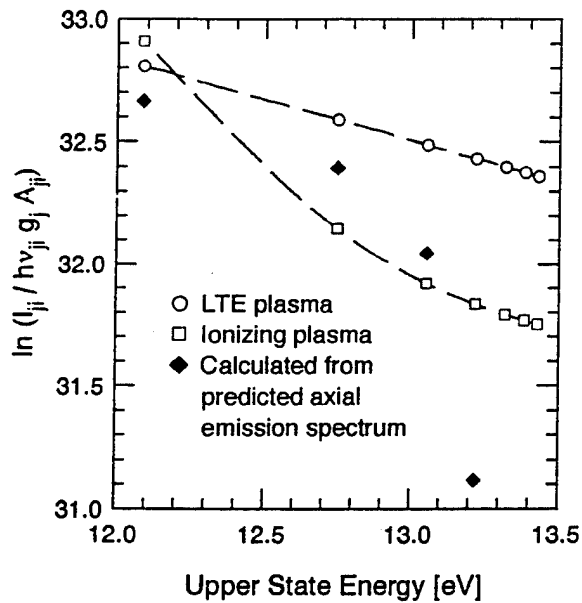


Figure 8. Boltzmann plot of the calculated axial emission spectrum. Also shown are Boltzmann plots of an LTE and ionizing plasma at typical conditions in the near-cathode region.

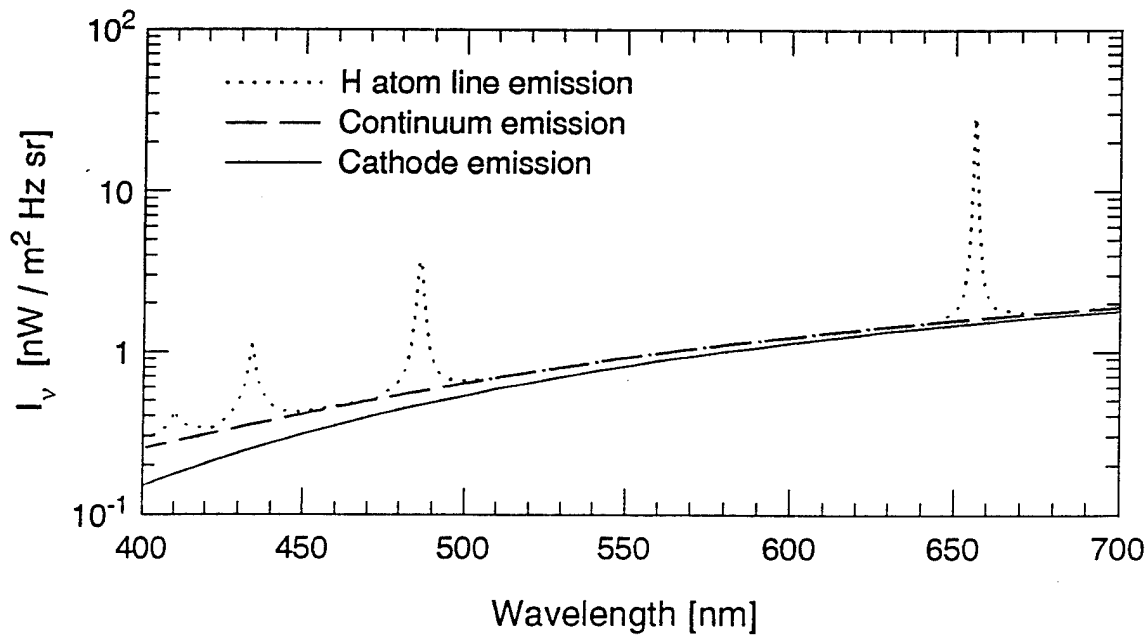


Figure 7. Calculated arcjet axial emission spectrum at the exit plane centerline under the operating conditions of 1.5 kW and 13 mg/s of hydrogen. The spectrum includes surface emission from the cathode at 3700 K, continuum electron emission, and atomic hydrogen line emission.

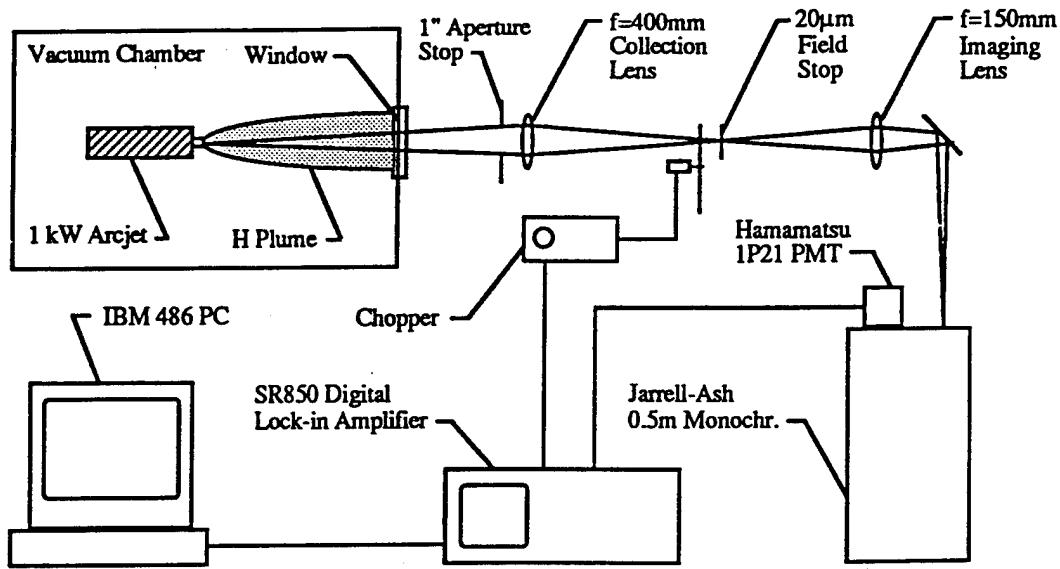


Figure 9. Schematic diagram of the axial emission experimental setup.

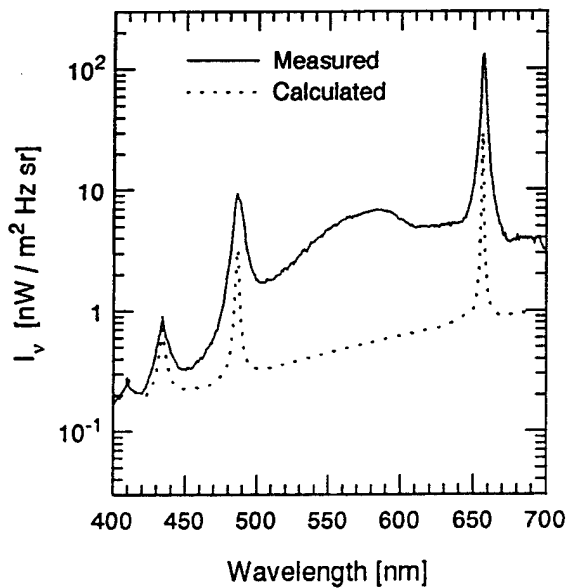


Figure 10. A comparison between the measured and calculated axial emission spectra for a mass flow rate of 13.1 mg/s and an arcjet power of 1.51 kW. The calculated spectrum has a cathode temperature of 3300 K.

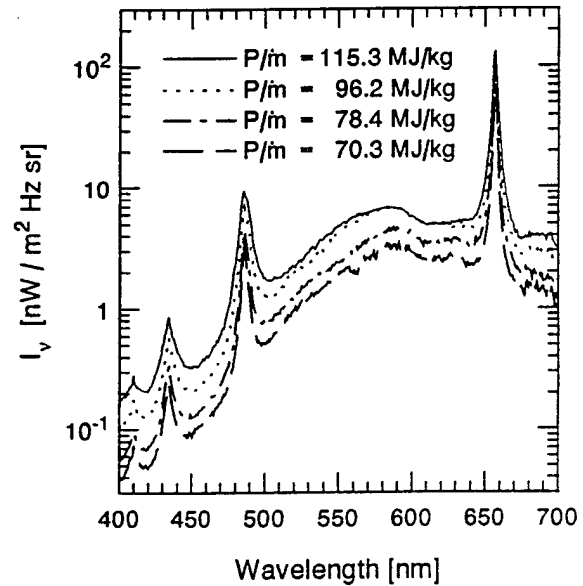


Figure 11. Measured axial emission spectra for four different arcjet powers and a mass flow rate of 13.1 mg/s.

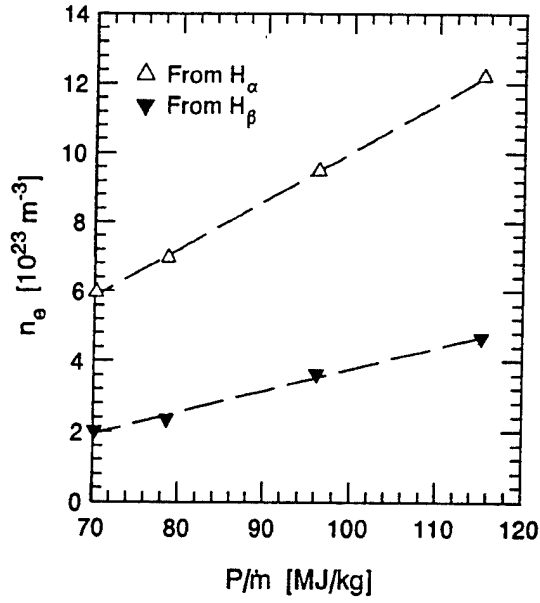


Figure 12. Measured centerline electron number density in the arc region as a function of arcjet specific power.

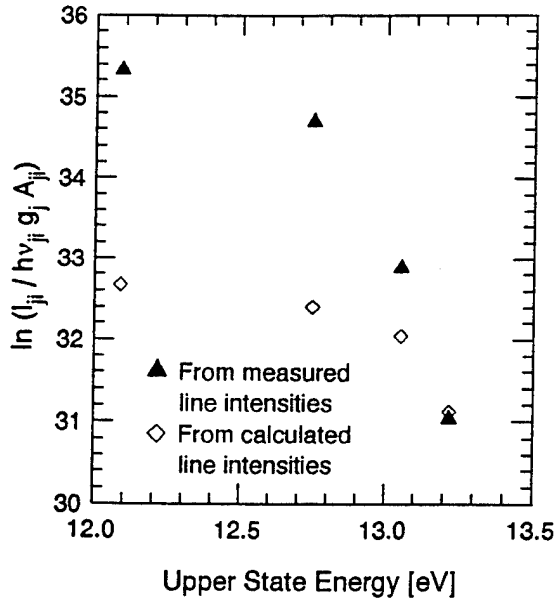


Figure 13. Boltzmann plot of the measured and calculated spectra at a specific power of 115.3 MJ/kg.

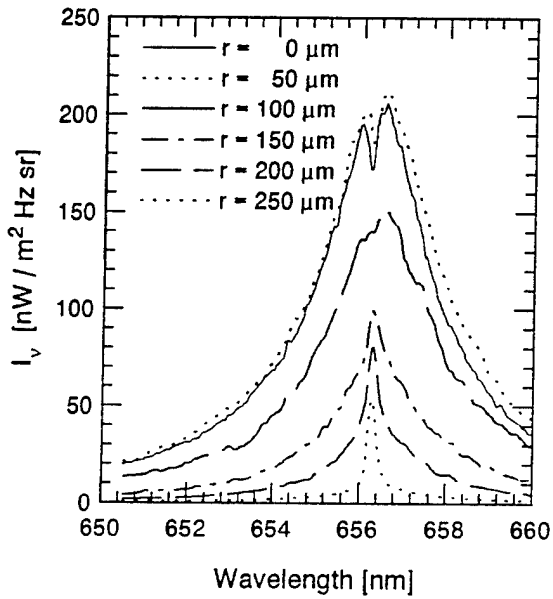


Figure 14. Measured axial emission spectra of  $H_\alpha$  at different radial positions for a specific power of 115.3 MJ/kg.

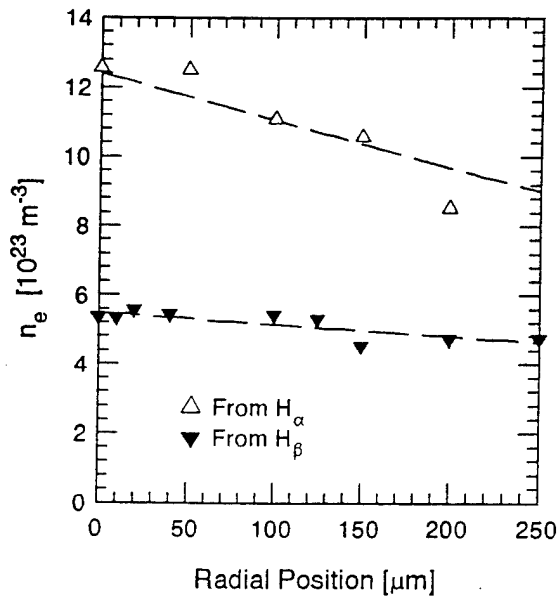


Figure 15. Measured electron number density in the arc region as a function of axial position for a specific power of 115.3 MJ/kg.



**AIAA 94-2654**

**Interior Plasma Diagnostics  
of Arcjet Thrusters**

M. A. Cappelli and P.V. Storm  
Stanford University  
Stanford, CA

**25th AIAA Plasmadynamics and Lasers  
Conference**

**June 20-23, 1994 / Colorado Springs, CO**

# Interior Plasma Diagnostics of Arcjet Thrusters

M.A. Cappelli\*\* and P.V. Storm\*  
*High Temperature Gasdynamics Laboratory*  
*Stanford University*  
*Stanford, CA 94305-3032*

## Abstract

In this paper, we review past and recent experimental studies designed to measure internal flow properties of arcjet thrusters. These measurements can be generally classified as either intrusive, (requiring design changes to prototype thrusters), or non-intrusive (optical), and include measurements of cathode temperature, as well as static pressure, temperature and plasma density, throughout the interior region extending to the exit plane. Comparisons are made to available model predictions. Supporting evidence exists that indicates that the nozzle plasma flow is removed from local thermodynamic equilibrium.

## I. Introduction

Arcjet propulsion systems have recently been deployed for stationkeeping applications. To enable other applications such as repositioning or orbit transfer, the arcjet must deliver 1000 s of specific impulse at 35 to 50 percent efficiency.<sup>1</sup> However, efficiencies approaching 50 percent at high specific impulse have not yet been achieved. The future design of more efficient and reliable thrusters requires a better understanding of the physical processes governing arcjet operation through a combination of experimental diagnostics and analytical modeling. Many studies have been conducted to investigate arcjet performance under different operating conditions, electrical configurations and geometries.<sup>2</sup> Understanding the physical processes governing the arcjet operation requires a detailed knowledge of the plasma properties everywhere in the flow field. A great deal of research has been conducted to measure the flow properties in the plume of arcjet thrusters using electrical and optical

techniques.<sup>2-4</sup> Much of this work was driven by the need to understand the effect that the partially ionized and chemically reacting plume may have on other spacecraft surfaces and satellite communication. As far back as the early sixties,<sup>5</sup> mass flux probes, impact probes, and enthalpy probes were implemented as exit plane and plume diagnostics to better understand the performance of these devices. More recently, advanced optical diagnostics<sup>6-9</sup> have been developed and implemented to measure the exit plane flow properties and to understand the nonequilibrium nature of arcjet flows. Although much has been learned from these exit plane studies, it is evident that little is known about the plasma properties within the core and nozzle of the arcjet, yet it is here where the plasma behavior controls the arcjet performance.

In this paper, we will review past measurements made by other researchers and our own recent measurements of flow properties in the nozzle interior and constrictor (near-cathode) region of arcjet thrusters. These measurements can be generally classified as intrusive or non-intrusive, depending on whether significant changes were made to the device in question in order

---

\* Research Assistant, Student Member AIAA  
\*\* Assistant Professor, Member, AIAA

to carry out the diagnostic. The measurements reviewed here include static pressure measurements in both low power, 1 kW class (simulated hydrazine decomposition products as propellant)<sup>10</sup> and high power, 30 kW class (nitrogen propellant) arcjets,<sup>11</sup> current distribution and floating potential using a segmented anode configuration in 1 kW class arcjets,<sup>12</sup> optical (spectroscopic) emission based measurements of electron number density and characteristic temperatures for vibrational, electronic and rotational excitation in the expansion nozzle of 1 kW class thrusters (simulated hydrazine decomposition products as propellant),<sup>13</sup> optical emission based measurements of electron number densities and electronic excitation temperatures in the constrictor region of a 1-3 kW arcjet operating with helium as the propellant,<sup>14</sup> and electron number densities in the near-cathode region, as well as cathode temperature of a 1 kW and 5 kW hydrogen arcjet thruster.<sup>15,16</sup> Despite the variations in propellant and differences in operating conditions, there are many common features in flow behavior associated with the various thrusters studied, some of which will be discussed below.

## II. Static Pressure Measurements

Static pressure measurements are useful in interpreting internal flow behavior in arcjets. In many cases, they can provide insight into the losses associated with non-ideal or viscous effects. In general, static pressure measurements reflect changes in the flowfield characteristics, which are expected to influence arcjet thruster performance and stability.<sup>17</sup>

Harris et. al.<sup>11</sup> presented a detailed study of the static pressure variation in a nominally 30 kW water-cooled arcjet thruster operating with nitrogen as a propellant. In that study, the arcjet was instrumented with sixteen

equally spaced pressure taps located in positions ranging from the arcjet plenum, through an extended constrictor, nearly to the exit plane of the nozzle. Such measurements can be classified as intrusive, in that it is not clear how the presence of such features may perturb or alter the internal flow characteristics, nonetheless, it is useful to examine here some of the conclusions drawn from that study.

An arcjet flow such as that investigated by Harris et. al. is expected to be far removed from ideal isentropic conditions and will suffer from imperfect gas effects. Despite this, it is interesting to note that the ratio of axial static pressure to stagnation pressure (taken to be the pressure measured by the upstream tap in the plenum) was independent of mass flow rate or arcjet power, as expected from a quasi-1D analysis if the entire nozzle flow is choked. Their measurements further indicated that the sonic point in all arc powers and flow rates studied was located beyond the end of the constrictor, indicating that viscous boundary layer growth is significant within the constrictor. Up to the sonic point, ideal quasi-1D analysis would suggest that the static pressure would increase with the square-root of temperature (for a constant mass flow rate) reflecting the drop in density with temperature and the choked condition at the sonic point. If the radial pressure gradients are small, then assuming that the plasma is significantly ionized in the arc core, the electron number density is expected to decrease with the square-root of the temperature. As is discussed below, recent measurements do not reflect this trend, strongly indicating a departure from ideal conditions.

Similar measurements have been performed by Talley et. al.<sup>10</sup> in a NASA Lewis 1 kW laboratory arcjet thruster operating on mixtures of hydrogen and nitrogen to simulate hydrazine decomposition products. This study contributes to the

growing body of data on these types of arcjets, which have been engineered and space qualified<sup>18</sup> by Olin Aerospace Company. In their facility, five pressure taps were machined into the anode housing, providing a static pressure measurement approximately 1.5 mm upstream of the throat, at the throat, and three measurements distributed along the expansion nozzle. Unlike the 30 kW arcjet of Harris et. al., there is no significant constrictor channel in these low power devices, and so it is more likely that the sonic point will coincide with the location of the throat. This is supported by the critical pressure ratio of 0.52 measured in the throat for the arc-ignited low power thruster,<sup>10</sup> unlike the 0.66-0.9 values measured in the constrictor region of the arc ignited high power thrusters.<sup>11</sup> Talley et. al. report, however, that their cold flow static pressure measured at the throat is significantly greater than the critical pressure ratio, indicating to us that the sonic point under cold flow conditions has moved downstream of the throat. They attribute this behavior to the strong swirl component of velocity in the cold flow case which they suggest is dampened out following arc ignition.

The throat static pressure measurements of Talley et. al. combined with an estimate of the temperature in the arc core of 20000 - 40000 K (not atypical for a constricted arc at high pressures), allows an estimate of the electron number densities in the core of the arc near the arcjet throat. Using the measured converging section static pressure measurements of Ref. 10 ranging from 20 - 50 psia for mass flow rates varying from 35 - 65 mg/s and specific powers of 10 - 30 MJ/kg, and taking  $p_{\text{throat}}/p_{\text{stag}} \sim 0.52$ , we arrive at throat electron number densities ranging from  $6 \times 10^{22}$  -  $3 \times 10^{23} \text{ m}^{-3}$ . Recently, Zube and Myers<sup>13</sup> measured electron number densities in the upstream region of the expansion nozzle of a nearly identical arcjet thruster (also operating on simulated hydrazine decomposition products) over a comparable

range of specific power, albeit at much higher mass flow rates (100 mg/s). Despite these different operating conditions, a comparison of these values to the measurements of Zube and Myers reported at a distance of 3 mm downstream of the throat ( $\sim 10^{21} \text{ m}^{-3}$ ) indicates that significant axial gradients in electron number density exist in the near vicinity of the cathode and throat. We speculate that such straining effects on the plasma just past the throat contribute to the stability of a diffuse arc attachment at the anode in this region of the nozzle.

The strong axial variations in electron number density in low power arcjet thrusters has been captured by recent single-fluid MHD models of arcjet thrusters developed by Butler and King at Olin Aerospace Company.<sup>19</sup> In Figure 1, we graph the model simulations for a nominally 1 kW class arcjet thruster operating with hydrogen as a propellant (mass flow rate of 13.1 mg/s and specific power of 115 MJ/kg). Although the results of Ref. 10 and Ref. 11 are for an entirely different propellant and for slightly different current, we include them on the graph for illustrative purposes. We see that in the hydrogen arcjet thruster, the axial variation in electron number density and pressure is in qualitative agreement with the observations in essentially the same thruster operating on simulated hydrazine decomposition products.

### III. Electrical Measurements

Until the recent electrical studies of Curran and Manzella,<sup>12</sup> we could only speculate as to the mode and distribution of current attachment along the anode surface in these low power (1kW) arcjets. In that study, an arcjet of identical geometry to those baselined for use in communications satellites was instrumented with a segmented anode. Although inherently an intrusive diagnostic, this segmented anode design allowed them to estimate the current distribution and floating

(plasma) potential as well as the anode fall voltage. In addition, they were able to perturb the attachment (i.e., electrically isolate various segments) to force current to a particular region along the anode.

The anode described in Ref. 12 was divided into 5 segments. The first consisted of the converging section up to the end of the constrictor/throat. The second, third and fourth sections were centered approximately 1 mm, 2.5 mm, and 4 mm downstream of the throat respectively. The last segment consisted of the remaining section of the nozzle. Each segment was separated from the others by thin boron-nitride spacers.

The most interesting finding is that under normal operation (all segments connected together and connected to the power supply) the current was nearly equally distributed to all but the first segment (which collected little or no current under steady operation). This finding indicates that the current density decreases significantly along the axial direction, consistent with the measured drop in electron number density<sup>13</sup>. The first segment, when electrically isolated, barely influenced the current attachment at the remaining four segments. This is an important result, in that it indicates that little or no current is collected by this region of the anode. Although the floating potential of this segment was not measured while all others were connected, it was found to be approximately 35V when the current was forced to the fifth segment.<sup>12</sup> Using 35V as an estimate of the voltage between the cathode and the end of the constrictor (which is approximately 0.75 - 1 mm from the cathode tip, depending on the gap spacing), we can estimate the extent of arc constriction (arc diameter). To do this, we need the electrical conductivity, which, if the arc core is fully ionized, is given by the well known Spitzer-Harm expression<sup>20</sup> (in MKS units):

$$\sigma_{SH} = 1.53 \times 10^{-2} \frac{T_e^{3/2}}{\ln \Lambda}$$

Here,  $\ln \Lambda$  is the Coulomb logarithm which depends (weakly) on both the electron number density and temperature<sup>20</sup>. If we assume an arc temperature of 30000 K, an electron number density of  $10^{23} \text{ m}^{-3}$  and that the arc core is highly ionized, we can estimate the electrical conductivity to be approximately  $16000 \text{ } \Omega^{-1} \text{ m}^{-1}$ . Using a current of 11A, we arrive at an arc diameter of approximately 200  $\mu\text{m}$ . This should be compared to the constrictor diameter of approximately 700  $\mu\text{m}$ , and indicates that the arc is constricted to about 10% of the throat area. This estimate is within a factor of two of what has been measured based on Stark broadened axial line emission from a 1 kW arcjet operating on hydrogen.<sup>15</sup>

Another interesting result from the Curran and Manzella study is that when the last segment is isolated from the power supply (and its current is shifted to the next upstream segment), the voltage on the last segment can be used to estimate the anode fall voltage which may exist at the next upstream segment. It is found that when isolated, the voltage of the fifth segment (relative to the cathode) was roughly equal to the voltage on all the remaining connected segments. This suggests that the anode fall voltage in the distant nozzle may be negligible. This result is not surprising if one considers that the field near the anode consists of both a resistive component balanced by an ambipolar component that is associated with gradients in plasma density:

$$E \approx \frac{J}{\sigma} - \frac{kT}{e} \frac{\nabla n_e}{n_e}$$

We see that at low current densities, the plasma potential can in fact be greater than the anode potential (giving rise to a negative fall).

It is the difference between a negative anode fall (observed at low temperatures or low current densities) or a positive anode fall which often distinguishes between the so called "low intensity" or "high intensity" arc at an anode. In the case at hand, it appears that the current densities are sufficiently low near the end of the nozzle that the anode fall is small. An interesting experiment described in the study of Curran and Manzella involved forcing the current to attach to the first (furthest upstream) segment by isolating the remaining four. The floating potential of the remaining four relative to that between the cathode and the first segment affords an estimate of the anode fall voltage at the first segment. Under these conditions, a high current density ensues and we would therefore expect the anode fall to increase significantly. Indeed this was the case,<sup>12</sup> with the anode fall voltage increasing to approximately 40V.

#### IV. Optical Emission Measurements

Much has been learned about the internal flow characteristics of these low power arcjet thrusters by studying the intrinsic plasma emission. The first and most thorough investigation of the nozzle flow by optical emission spectroscopy was performed by Zube and Myers.<sup>13</sup> In that study, a set of holes were drilled into the anode (nozzle) at three axial positions approximately 3, 6 and 9 mm from the throat of a nozzle with a maximum area ratio of 225:1 and at various radial positions approximately 9 mm from the throat of a similar nozzle and 9 and 12 mm from the throat of a nozzle of equal half angle (30°) but extended to an area ratio of 400:1. The research presented in Ref. 13 was motivated by the need to better understand the nonequilibrium processes in the nozzle of an arcjet thruster operating on mixtures of hydrogen and nitrogen to simulate hydrazine decomposition products. These nonequilibrium processes include vibrational,

rotational, and electronic excitation, as well as finite-rate recombination.

In that study, the electron number density was measured from the line-of-sight integrated spectral (primarily Stark broadened) linewidth associated with the  $H_{\beta}$  transition in atomic hydrogen. Their measured axial variation in electron number density are compared to single-fluid calculations for the same arcjet (albeit at slightly different operating conditions and for hydrogen as a propellant) in Figure 1. The differences between model predictions and measurements are within a factor of two to ten, and might be accounted for by the slight differences in operating conditions.

An interesting result of the Zube and Myers study is that extending the nozzle clearly perturbs the upstream current and plasma properties. They found that the electron number densities 9 mm from the throat of an arcjet with a 12 mm long nozzle was significantly less (by some 40% or so) than that at the same location in an extended nozzle (15 mm) of equal expansion angle. This result clearly reveals the influence that nozzle geometry may have on arc behavior. More importantly, it reveals that a significant fraction of the current extends down into the low density region of the flow, consistent with the electrical measurements and findings of Curran and Manzella.<sup>12</sup>

Their measured excitation, vibrational, and rotational temperatures (from the Balmer transition series of atomic hydrogen and the  $C^3\Pi_u - B^3\Pi_g$  electronic transition of molecular nitrogen) are displayed in Figure 2. Also displayed in the figure is the translational temperature computed by Butler<sup>15</sup> for a similar low power arcjet operating on hydrogen. Like the electron number density, the temperatures drops significantly, most noticeably for the atomic excitation temperature, which they argue to be close to

the free electron temperature because of rapid thermalization between the free and bound electrons in the high lying electronic levels from which the transitions originate.<sup>13</sup> The electron-proton and proton-atomic hydrogen translational energy relaxation times are estimated to be less than the residence times within the expansion nozzle, which is comparable to the hydrogen-molecular nitrogen relaxation time, and so Zube and Myers argue that the atomic excitation temperature should also reflect the translational temperature. This conclusion is seen to be supported by the model calculations for the comparable power hydrogen arcjet only very near the throat. It is apparent that translational energy exchange is less efficient downstream where the electron number densities drop significantly. It is also apparent from Figure 2 that the rotational and vibrational temperatures are less than the atomic excitation and translational temperatures. At first, one may conclude the presence of a substantial departure from local thermodynamic equilibrium for these internal energy modes, as suggested by Zube and Myers.<sup>13</sup> However, we remind the reader that these measurements are based on line-of sight averages of emission, and so the signal from any emitting species reflects the local properties in the region where the density of the emitting species is greatest. Because of the high centerline temperatures, it is likely that molecular emission originates from the cooler boundary region within the nozzle and so indicates a lower rotational and vibrational temperature.

The measurements of Zube and Myers were limited to positions 3 mm from the throat of the arcjet. Machining holes closer to the constrictor would be more difficult and precarious in such a small device. Recently, Ishi and Kuriki modified the constrictor region of a low power (1-3 kW) DC arcjet operating on helium as a propellant to accommodate optical access.<sup>14</sup> In that study, they positioned

optical viewports at four locations within the constrictor, which was 8 mm in length for their design. Their results clearly revealed an internal (constrictor) flow that was far removed from ionizational equilibrium, with the plasma significantly overdense with respect to Saha equilibrium. The departure from Saha equilibrium was found to be more pronounced as you move further downstream of the entrance to the constrictor. Although no direct measurements of the departure from ionizational equilibrium have been made in the constrictor or nozzle region of a low power, NASA Lewis arcjet, it is expected that a similar result would ensue. We would expect that the plasma is near ionization equilibrium in the throat or constrictor, and that the departure from Saha equilibrium would be more pronounced as one moves further into the diverging region of the nozzle, since electron-atom collisions become less frequent as densities fall.

Recent experimental measurements of the electron number density were made in the near-cathode region of NASA 1 kW and 5 kW arcjets by Storm and Cappelli.<sup>15,16</sup> No modifications to the prototype arcjets were made and so these measurements are considered to be non-intrusive. Using hydrogen as propellant, the centerline axial emission spectrum was measured and the near-cathode axial line-of-sight electron number density was obtained from the Stark broadening of the wings of the  $H_{\alpha}$  line. Radiative transfer effects on the spectral line are localized to near line-center, whereas the linewings are determined by the properties within approximately 1 mm of the cathode tip.<sup>15</sup> The thoriated tungsten cathode temperature was also measured by the broadband emission away from the Balmer lines, correctly accounting for molecular hydrogen and continuum emission, as necessary.

A typical axial emission spectrum in the visible region is shown in Figure 3. The

broadband background is a combination of thermal radiation from the cathode and continuum emission from the plasma electrons. Molecular hydrogen emission was negligible because of the use of very fast optics.<sup>16</sup> Using axial variations of  $n_e$  and  $T_e$  computed from the single-fluid arcjet model of Butler and King<sup>17</sup> (similar to those shown in Figures 1 and 2) for a 5 kW hydrogen arcjet, the continuum emission in the axial direction was calculated and is shown for comparison (dashed line) in Figure 3. The background is extremely well approximated by the cathode and continuum emission assuming a cathode temperature of 3730 K. In this manner the cathode temperature was estimated at different specific power levels and the results, shown in Figure 4, indicate that the temperature is very near or above the melting point of pure tungsten (3690 K) and increases with specific power. These results are consistent with well-documented cathode erosion measurements which infer the presence of a molten pool of tungsten at the cathode tip.<sup>21</sup> The increase in temperature with specific power predicts an increase in arc current density at the arc attachment, consistent with the measured increase in conductivity, or electron number density, as discussed below.

For comparison, Zhou et. al. measured the temperatures of thoriated tungsten cathodes in a stationary argon discharge using both single and two-color pyrometry.<sup>22</sup> They recorded tip temperatures between 3500 K and 3800 K depending on the cathode diameter and increasing with arc current, and hence, power. Although these experiments were performed at much higher currents, the current densities are comparable to those in the hydrogen arcjets, and the temperatures are in good agreement with the axial emission measurements.

Storm and Cappelli measured the near-cathode electron number density by the Stark broadening of the linewings of the  $H_\alpha$  line. The analysis is limited to the far wings of the

line because the line core is expected to experience significant distortion due to self-absorption. Sample  $H_\alpha$  emission spectra from the 5 kW arcjet are shown in Figure 5. The line is broadened considerably due to the large electron density upstream of the constrictor, and the central dip is due to reabsorption by the relatively cool plasma in the downstream expansion region and plume.<sup>15</sup> Based on the relative Doppler shift between the emitting plasma near the constrictor and the absorbing plasma in the plume, one would expect the central dip to be red-shifted by a small fraction of the width of the linewings, if, in accordance with linear Stark theory, the hydrogen lines are unshifted and symmetric. However, the exact opposite is observed in Figure 5. The large blue-shift in the central dip can be accounted for by the asymmetry in the Stark broadening of  $H_\alpha$ , which results in an apparent red-shift of the line at large electron number densities.<sup>23</sup> For  $n_e = 2 \times 10^{23} \text{ m}^{-3}$ , typical of the electron number density near the cathode (see Figure 1), the asymmetric Stark red-shift of  $H_\alpha$  linewings is approximately 0.12 nm, which is large compared to a Doppler blue-shift of approximately 0.03 nm. Unfortunately, due to the relatively small size of the Doppler shift and the uncertainty in determining the precise spectral line center, the axial velocity in the constrictor region could not be determined.<sup>16</sup>

The width of the linewings, however, could be determined relatively well, and from the Stark FWHM the electron number density in the near-cathode region was found.<sup>16</sup> Most previous measurements involving Stark broadening of the Balmer lines of hydrogen (incl. Ref. 15) have made use of the Stark broadening tables compiled by Vidal, Cooper and Smith<sup>24</sup> in the early seventies which assumed perturbations to the atomic energy levels by electron collisions while the ions remained static. Recent Monte-Carlo simulations by Oza, Greene and Kelleher taking into account dynamic ions have shown

that the VCS tables underpredict the linewidths of  $H_{\alpha}$  by a factor of approximately two at electron densities typical of the near-cathode centerline, and as much as a factor of 30 at lower densities.<sup>25</sup> Use of the VCS tables would then result in greatly overestimated electron number densities from  $H_{\alpha}$ , which was noted in Ref. 15. The present electron density measurements were made using the recent Monte-Carlo simulations, whose FWHMs are compared to those of the VCS tables in Figure 6. However, as these simulations were only performed up to  $n_e = 10^{23} \text{ m}^{-3}$ , electron densities larger than this were obtained by extrapolation. The measured near-cathode electron number densities for the 1 kW and 5 kW arcjets are shown as a function of specific power in Figure 7. The 1 kW results differ from those of Ref. 15 due to the improved Stark broadening calculations and line wing fits. The relatively large uncertainties in these measurements are due primarily to the uncertainty in determining precisely which parts of the spectra of Figure 5 constitute the line wings. In other words, the uncertainty reflects the very nature of these measurements being axial line-of-sight averages within approximately 1 mm of the cathode tip. Nevertheless, despite the significant uncertainties the increase in electron density, and therefore, plasma conductivity, with arcjet power is apparent. This is consistent with the measured increase in cathode temperature with power. Furthermore, the results for the 1 kW arcjet display reasonably good agreement to peak near-cathode electron number densities predicted by the MHD arcjet model simulations by Butler and King.<sup>16</sup> The measured densities are somewhat lower than the calculated peak densities due to the fact that they are line-of-sight averages over a small region.

## V. Summary

In this paper, we have reviewed past and recent measurements of flow properties in the

nozzle interior and constrictor (near-cathode) region of arcjet thrusters. Many of the measurements reveal flow behavior that is consistent with recent arcjet simulations. These measurements include static pressure, anode current distribution, plasma density and temperature, and cathode temperature. Advances have been made in the use of non-intrusive optical diagnostics to measure arcjet flow properties in the near-cathode and anode throat region, where the arc is greatly constricted and strongly contributes to heat transfer and device performance.

Static pressure measurements in low power (1kW class) arcjets indicate that the sonic point is very near the constrictor, in contrast to similar measurements in higher power (30kW) arcjets, where higher aspect ratio constrictors give rise to boundary layer growth that moves the sonic point downstream of the constrictor exit. Electron number densities based on static pressure measurements compare favorably to those computed on the basis of resistive MHD simulations. Optical measurements indicate that electron number densities drop precipitously downstream of the throat suggesting a concomitant decrease in the current densities and a substantial straining effect on the plasma. It is suspected that the drop in current density strongly favors diffuse attachment along the anode.

Electrical measurements using a segmented anode configuration support the notion that the anode arc attachment is diffuse as opposed to constricted. In low power arcjets, the current appears to be distributed across the anode in a way that is consistent with the observed decrease in plasma density (and hence plasma conductivity). Measurements of floating potential permit an estimate of the electric field strength in the throat. From this, we have estimated the extent of arc constriction and have found that the arc cross sectional area is approximately a

tenth of the constrictor area, consistent with recent estimates based on Stark broadened axial line emission. It is also apparent from floating potential measurements that the anode fall voltage varies dramatically along the anode, being near zero in the region of attachment near the exit plane and close to 40 V at the attachment near the throat.

A range of spectroscopic studies (both side-on through holes in the anode) and end on (by collecting light axially) support the conjecture that the nozzle flow is removed from thermal equilibrium. The departure from thermal equilibrium is evidenced by elevated electronic excitation temperature and is less severe as you move upstream towards the throat. This is expected, since the higher pressures and plasma densities in that region give rise to a plasma that is near Saha equilibrium. The expansion process creates an overdense plasma and subsequently overpopulates excited electronic levels.

Near-cathode electron number densities are found to be only weakly dependent on specific power. This trend is captured by the MHD simulations. An increase in static pressure is therefore expected to reflect an increase in throat temperatures, a result that has yet to be verified by experimental observations. For the first time, direct and non-intrusive measurements of cathode temperature have been made in 1 and 5 kW hydrogen arcjet thrusters. These measurements indicate that cathode temperatures apparently exceed the melting point of tungsten at modest specific powers (200 MJ/kg) and are apparently below the melting point at lower specific powers.

Despite the progress that has been made in diagnostics of the internal flow, many issues related to performance efficiency and lifetime are still unresolved. Although existing models do well at predicting the exit plane plasma conditions, they seem to still

overpredict thrust efficiency. It is the combined effort of modeling and experimental measurements of internal flow properties which will lead to a better understanding of plasma flow behavior and hence models with better predictive capabilities. These models in turn will benefit future design.

### Acknowledgments

This work was supported in part by the Air Force Office for Scientific Research, Olin Aerospace Company (formerly Rocket Research Company) and by NASA through the NASA Lewis Research Center. Part of the data presented was obtained while the authors were Visiting Scientists at the NASA Lewis Research Center. The many stimulating discussions with scientists at Lewis are gratefully acknowledged.

### References

1. C. Vaughan, and J. Cassady; "An Updated Assessment of Electric Propulsion Technology for Near-Earth Space Missions."; AIAA-92-3202; 28th Joint Propulsion Conference, Nashville, July 1992.
2. D.H. Manzella, F.M. Curran, R.M. Myers, and D.M. Zube; "Preliminary Plume Characteristics of an Arcjet Thruster"; AIAA-90-2645; 21st International Electric Propulsion Conference, Orlando, July, 1990.
3. W.A. Hoskins, A.E. Kull, and G.W. Butler; "Measurement of Population and Temperature Profiles in an Arcjet Plume"; AIAA-92-3240; 28th Joint Propulsion Conference, Nashville, July 1992.
4. L.M. Zana. "Langmuir Probe Surveys of an Arcjet Exhaust," AIAA- 87-1950, July 1987.

5. W.M. Van Camp, D.W. Esker, R.J. Checkley, W.G. Duke, J.C. Kroutil, S.E. Merrifield, R.A. Williamson, "Study of Arcjet Propulsion Devices," NASA CR-54691, 1966.
6. M.A. Cappelli, R.K. Hanson, J.G. Liebeskind, and D.H. Manzella; "Optical Diagnostics of a Low Power Hydrogen Arcjet"; IEPC-91-091; 22nd International Electric Propulsion Conference, October 1991.
7. J.G. Liebeskind, R.K. Hanson, and M.A. Cappelli; "Flow Diagnostics of an Arcjet Using Laser-Induced Fluorescence"; AIAA-92-3243 28th Joint Propulsion Conference, Nashville, July 1992.
8. J.G. Liebeskind, R.K. Hanson, and M.A. Cappelli, "LIF Measurements of Species Velocities in an Arcjet Plume," IEPC-93-131, Proceedings of the 23rd International Electric Propulsion Conference, Seattle, WA, September 13-16, 1993.
9. M.W. Crofton, R.P. Welle, S. Jansen, and R.B. Cohen, "Temperature, Velocity and Density Studies in the 1 kW Ammonia Arcjet Plume by LIF," AIAA-92-3242, 28th Joint Propulsion Conference, July, 1992.
10. K. Talley, W. Elrod, and F.M. Curran, "Static Pressure Measurements of the NASA Lewis 1.2 kW Arcjet" AIAA 92-3111, 28th Joint propulsion Conference, Nashville, July, 1992.
11. W.J. Harris, E.A. O'Hair, L.L. Hatfield, M. Kristiansen, and M.D. Grimes, "Static Pressure Measurements in a 30kWe Class Arcjet," AIAA 91-2457, 27th Joint Propulsion Conference, Sacramento, CA, June 24-27, 1991.
12. F.M. Curran and D.H. Manzella, "The Effect of Electrode Configuration on Arcjet Performance," NASA Technical Memorandum 102346, 1989.
13. D.M. Zube and R.M. Myers, "Nonequilibrium in a Low Power Arcjet Nozzle," AIAA 91-2113, 27th Joint Propulsion Conference, Sacramento, CA, June 24-27, 1991.
14. M. Ishi and k. Kuriki, "Optical and Analytical Studies of Arc Column in DC Arcjet," AIAA 87-1086, 19th International Electric Propulsion Conference, May 11-13, Colorado, 1987.
15. P.V. Storm and M.A. Cappelli; "Axial Emission Diagnostics of a Low Power Hydrogen Arcjet Thruster"; IEPC-93-219; 23rd International Electric Propulsion Conference, September 1993.
16. P.V. Storm and M.A. Cappelli, "Axial Emission Measurements on a Medium Power Hydrogen Arcjet Thruster", AIAA-94-2743, 30th Joint propulsion Conference, Indianapolis, IN, June, 1994.
17. G.W. Butler and D.Q. King, "Single and Two-fluid Simulations of Arcjet Performance", AIAA 92-3104, 28th Joint Propulsion Conference, July, 1992.
18. W.W. Smith, R.D. Smith, K. Davies, and D. Lichtin, "Low Power Hydrazine Arcjet System Flight Qualification," IEPC-91-148, 22nd International Electric Propulsion Conference, Viareggio, Italy, 1991.
19. D.Q. King and G.W. Butler, "Modeling and Measurements of N<sub>2</sub> Arcjet Performance," AIAA 90-2616, 21st International Electric Propulsion Conference, Orlando, July, 1990.

20. M. Mitchner and C.H. Kruger, Jr. *Partially Ionized Gases*, John Wiley and Sons, New York, 1974.
21. F. M. Curran, T.W. Haag and J.F. Raquet, "Arcjet Cathode Phenomenon," NASA Technical Memorandum 102099, 1989.
22. X. Zhou, D. Berns, and J. Heberlein; "Arc Electrode Interaction Study"; Final Report for NASA Grant NAG3-1332, 1994.
23. W. L. Wiese, D. E. Kelleher, and D. R. Paquette; "Detailed Study of the Stark Broadening of Balmer Lines in a High-Density Plasma"; *Phys. Rev. A* **6**, 1132 (1972).
24. C. R. Vidal, J. Cooper, and E. W. Smith; "Hydrogen Stark Broadening Tables"; *The Astrophysical Journal Supplement Series No. 214*, **25**, 37 (1973).
25. D. E. Kelleher, W. L. Wiese, V. Helbig, R. L. Greene, and D. H. Oza; "Advances in Plasma Broadening of Atomic Hydrogen"; *Physica Scripta* **T47**, 75 (1993).

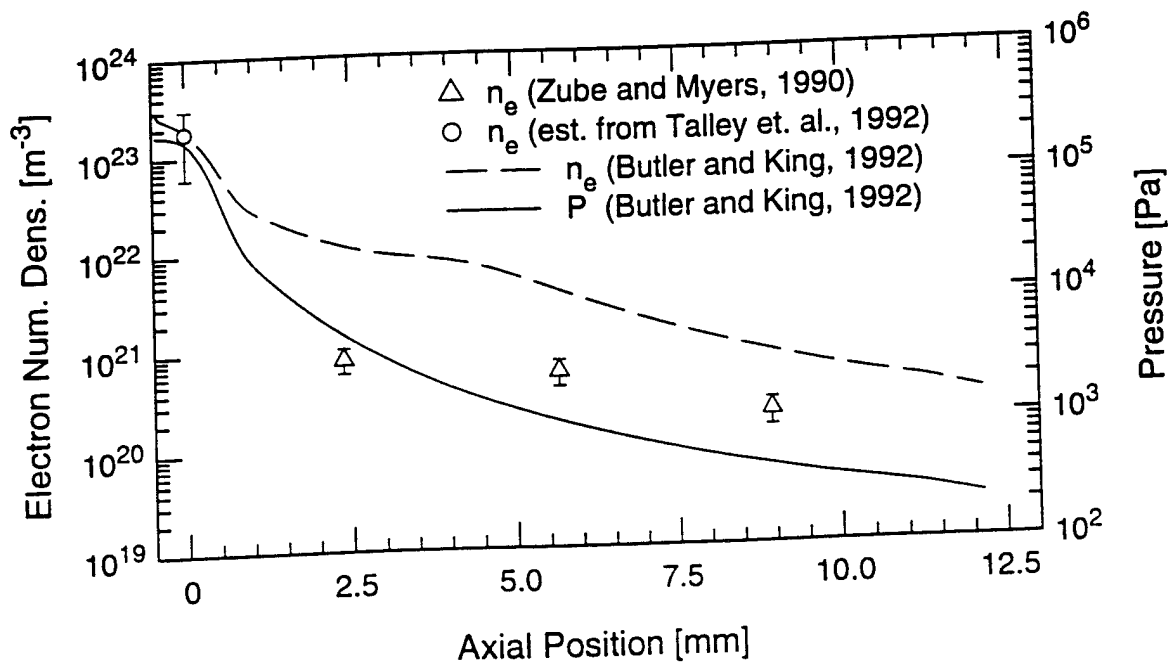


Figure 1. Axial variation in electron number density in a 1 kW class arcjet. The solid and dashed lines are the calculations of G.W. Butler (see Ref. 15) with hydrogen as a propellant. The data points are from Ref. 13 (triangles) and as estimated in the text (circle).

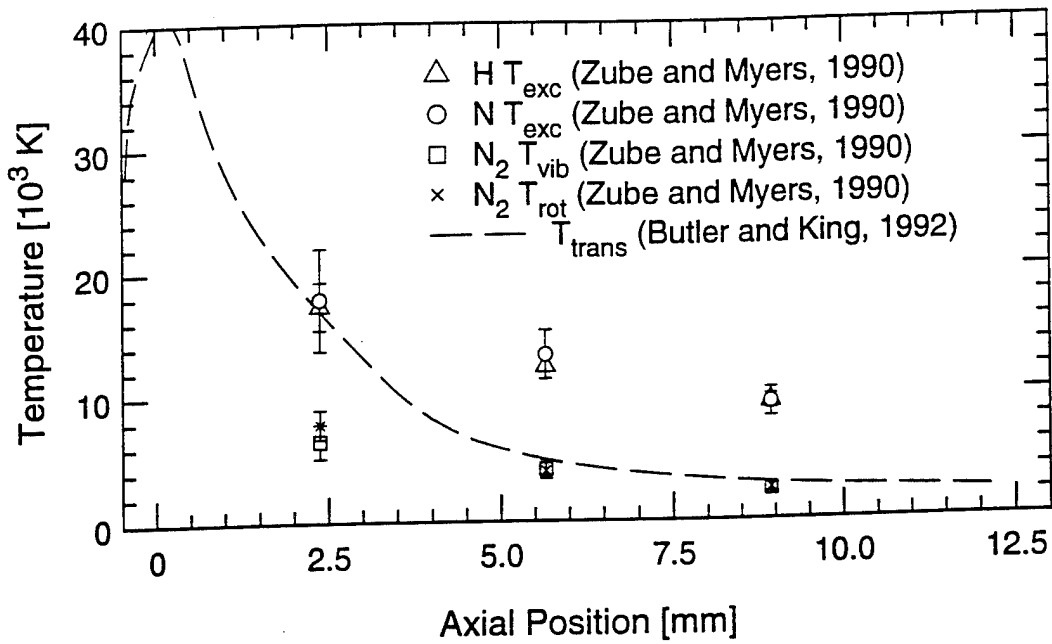


Figure 2 Comparison of axial variation in temperatures in the expanding nozzle of a low power arcjet thruster.

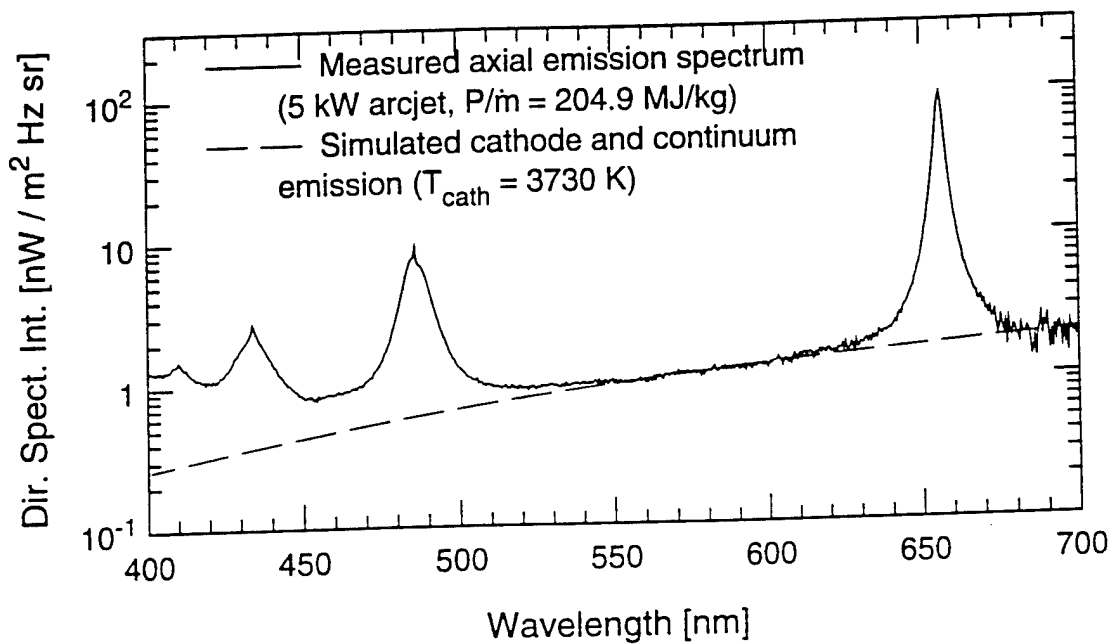


Figure 3 Axial emission spectrum of a 5 kW hydrogen arcjet (solid) and the calculated cathode/continuum emission (dashed) corresponding to a cathode temperature of 3730K.

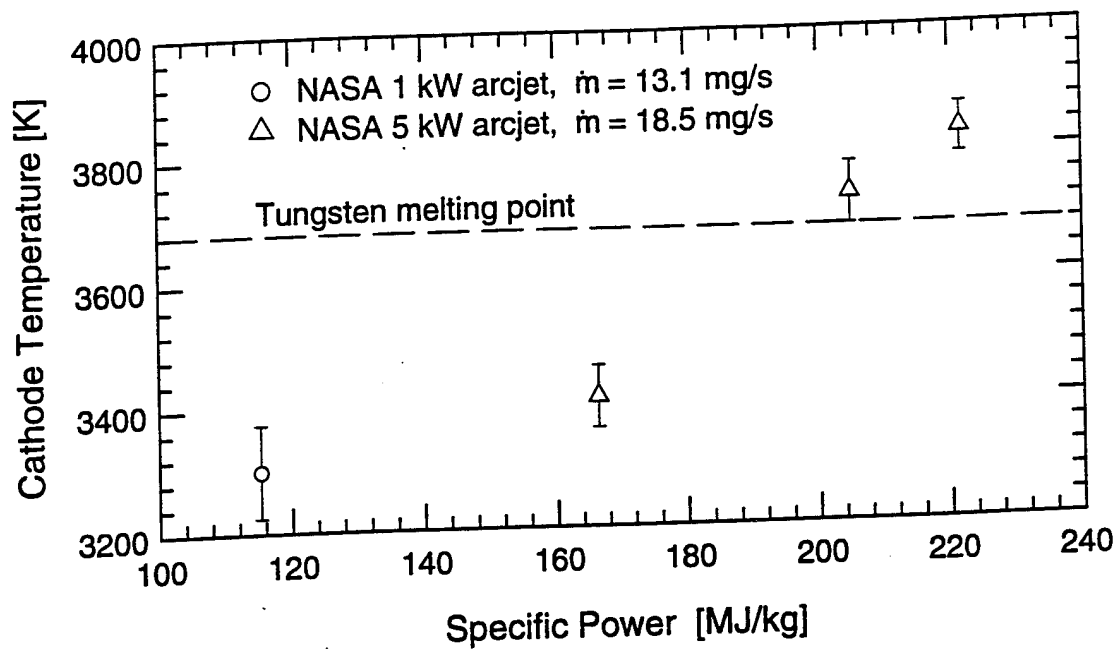


Figure 4 Measured cathode temperature in 1 kW (circles) and 5 kW (triangles) arcjets operating on hydrogen propellant.

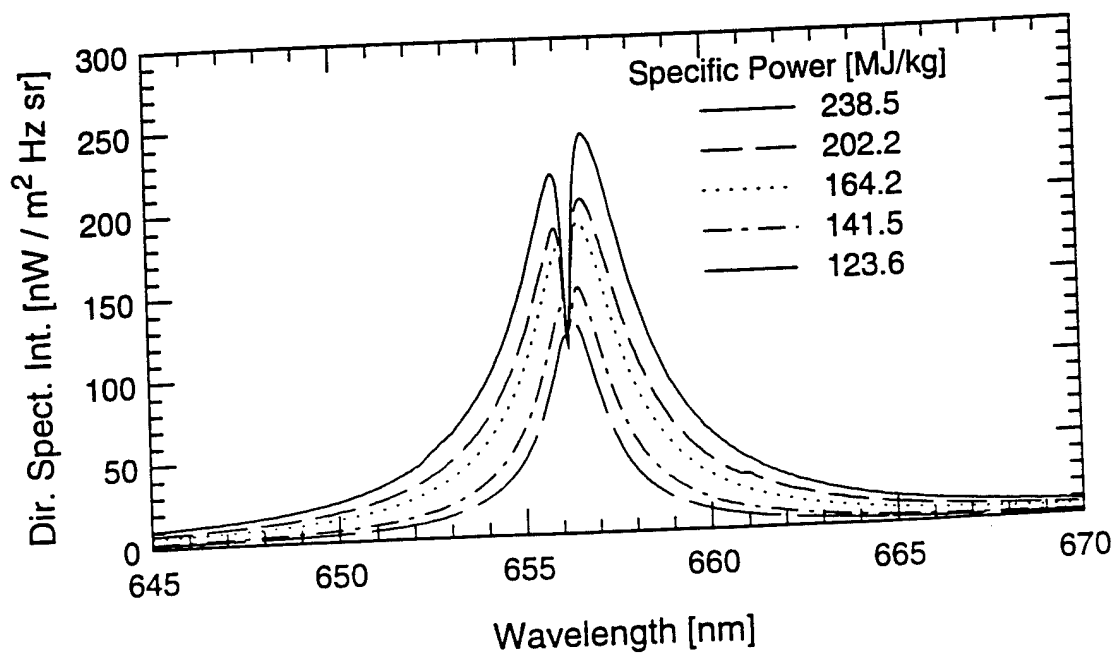


Figure 5 Axial emission spectra of the  $H_{\alpha}$  line at various specific powers for the 5 kW hydrogen arcjet showing the blue-shifted reabsorption dip near line-center.

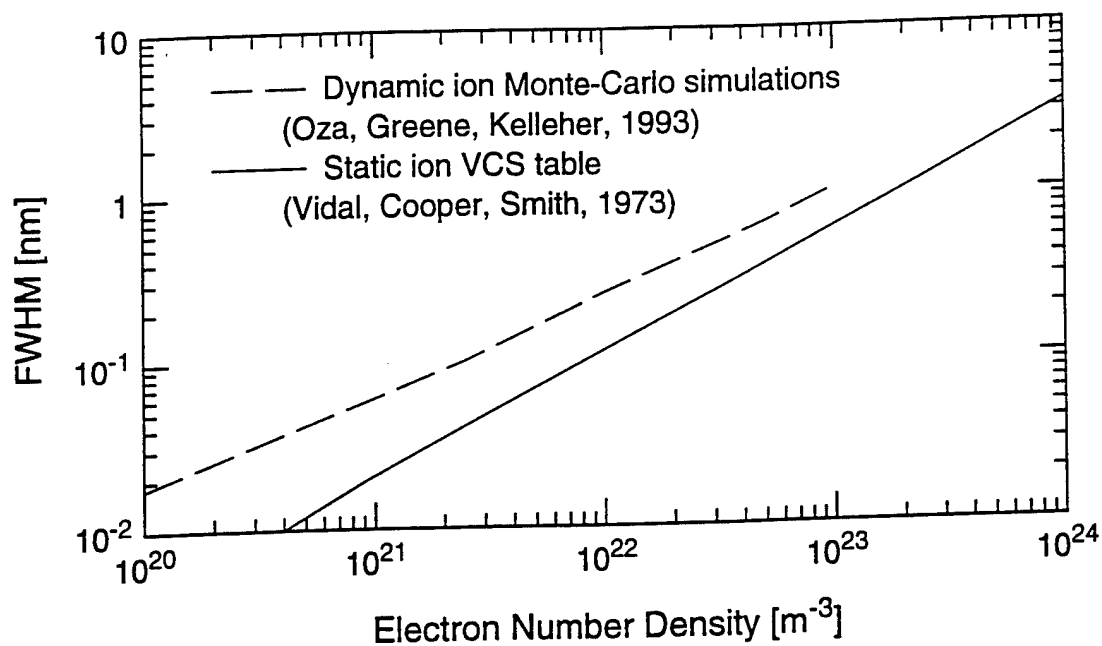


Figure 6 Stark broadened FWHM for  $H_{\alpha}$  showing the discrepancy between the computations by Vidal, Cooper and Smith and the recent Monte-Carlo simulations.

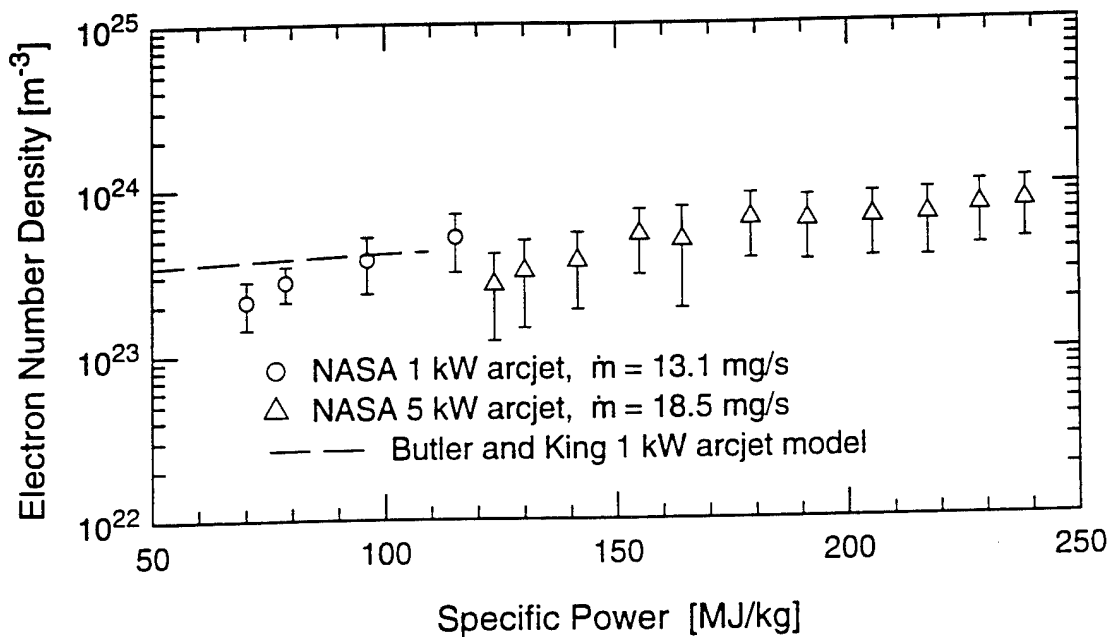


Figure 7 Measured near-cathode electron number densities in the 1 kW (circles) and 5 kW (triangles) arcjets, compared to the MHD 1 kW arcjet model of Butler and King (Ref.17) (dashed).



**AIAA 94-2743**

**Axial Emission Measurements On A Medium  
Power Hydrogen Arcjet Thruster**

P. V. Storm and M. A. Cappelli

High Temperature Gasdynamics Laboratory  
Department of Mechanical Engineering  
Stanford University  
Stanford, California

**30th AIAA/ASME/SAE/ASEE Joint  
Propulsion Conference**  
**June 27-29, 1994 / Indianapolis, IN**

For permission to copy or republish, contact the American Institute for Aeronautics and Astronautics  
370 L'Enfant Promenade, S.W., Washington, D.C. 20024

# AXIAL EMISSION MEASUREMENTS ON A MEDIUM POWER HYDROGEN ARCJET THRUSTER

P. Victor Storm\* and Mark A. Cappelli†

*High Temperature Gasdynamics Laboratory  
Department of Mechanical Engineering  
Stanford University  
Stanford, California, USA*

## Abstract

*A numerical and experimental investigation of the axial emission of a 5 kW class radiatively-cooled hydrogen arcjet thruster is presented. The complete visible spectrum is modeled, taking into account graybody thermal emission from the cathode and plasma radiation from hydrogen atoms and free electrons. The cathode temperature and the arc electron number density are obtained from the measured emission spectrum. The cathode temperature is found to be in the neighbourhood of the melting point of tungsten and increases with arcjet power at a constant mass flow rate, suggesting an increase in the current density at the arc attachment point. The measured near-cathode electron number density is also found to increase with power, supporting the idea of an increasing arc current density with arcjet power. The measured and modeled arc electron densities are, however, in discrepancy by a factor of approximately three.*

## I. Introduction

With the recent successful deployment of an arcjet thruster on the Telstar IV satellite, interest in improving arcjet performance for future satellite and spacecraft propulsion applications has increased. Arcjets operating on hydrazine propellant are presently capable of delivering up to 500 s of specific impulse at 30 to 35 percent efficiency,<sup>1</sup> making such thrusters suitable for north-south station keeping. Considerable benefits in satellite weight reduction and the possibility of LEO to GEO orbit transfer applications may be realized with the development of hydrogen arcjet thrusters having a specific impulse greater than 1000 s and efficiencies approaching 50 percent, while maintaining, or preferably improving, thrust levels. Achieving these improvements in arcjet performance requires a better understanding of the physical processes governing arcjet operation and the energy loss mechanisms. Such understanding is best obtained through a combination of experimental diagnostics and analytical modeling.

To date much effort has been made to model the arcjet,<sup>2-13</sup> with remarkable success in many cases considering the complex physics of the plasma equations. However, while numerical models of the arcjet are extremely useful, their accuracy can be judged only by comparison with a large body of experimental data. Substantial experimental work has been conducted to measure properties in the arcjet plume using electrical, optical and mass sampling techniques, and several comparisons have been made to the model predictions.<sup>14-18</sup> Considerably fewer experimental investigations have been undertaken to measure plasma properties within the nozzle of the arcjet,<sup>19</sup> yet it is here where the plasma behavior controls the arcjet performance to a large extent. The handful of investigations which have been undertaken in this regard were performed on several different arcjet geometries and powers using five different propellants. These measurements include emission<sup>20-21</sup> and static pressure<sup>22-23</sup> through holes in the side of the anode, and voltage-current characteristics to different segments of a segmented anode.<sup>24</sup> A summary of these investigations is given in Ref. 19. With such sparse and varied data available at present, a need exists for further experimental investigations into the plasma properties within the arcjet nozzle.

\* Research Assistant, Student Member AIAA

† Assistant Professor, Member AIAA

An experimental program was begun at Stanford University to investigate plasma properties within the arcjet nozzle and particularly in the near-electrode regions. The objective of this program is to obtain measurements of plasma properties, including temperatures, densities and velocities, within the arcjet nozzle, as well as an examination of the arc behaviour and arc attachment mechanism. This paper presents a continuation of previous work in which the electron number density was measured in the near-cathode region of the arcjet by analysis of the axial emission spectrum.<sup>25</sup> This work was performed on a 1 kW class radiation-cooled arcjet operating on hydrogen propellant. A discrepancy in the electron number density as measured from the Stark broadening of the H $\alpha$  and H $\beta$  lines was previously found. As well, emission from molecular hydrogen obscured the cathode, thereby hindering an accurate cathode temperature measurement by thermal radiative emission. In the present work, improvements were made to both the experiment and the analysis which facilitated considerably more accurate measurements of cathode temperature and arc electron number density. To reduce the collection volume of light and thereby the molecular hydrogen emission, the collection optics  $f/\#$  was increased by a factor of six to approximately 165. This provided a spectral window for viewing the cathode, obscured only by a small amount of continuum emission from the plasma electrons. The atomic hydrogen lineshape analysis was improved by the use of recent Monte-Carlo Stark broadening calculations incorporating perturbations to the electric field by the ion motion.<sup>26</sup> The results presented here include new measurements performed on a 5 kW arcjet, as well as a partial re-analysis of the previous 1 kW arcjet spectra.

## II. Modeling of the Axial Emission

A thorough description of the modeling of the axial emission spectrum is given in Ref. 25; therefore, only a brief summary will be presented here. The spectrum was calculated by integrating the one-dimensional radiative transfer equation along the centerline of the arcjet, beginning from the tip of the cathode. In steady-state, the one-dimensional radiative transfer equation is<sup>27</sup>

$$\frac{dI_{\lambda}(\lambda)}{dz} = \epsilon_{\lambda}(\lambda) - k_{\lambda}(\lambda)I_{\lambda}(\lambda) \quad (1)$$

where  $I_{\lambda}$  is the directional spectral intensity, and  $\epsilon_{\lambda}$  and  $k_{\lambda}$  are the plasma spectral volume emission and absorption coefficients respectively, which in this modeling work include contributions from atomic hydrogen and free electrons only. In general, the emission spectrum of a hydrogen arcjet consists of atomic and molecular hydrogen line emission, continuum plasma emission from the free electrons, thermal emission from surfaces, and line emission from tungsten and thorium vaporized from the cathode. However, we neglect emission from tungsten, thorium and molecular hydrogen assuming that such emission is small compared to that of atomic hydrogen, free electrons and the cathode surface.

The graybody emission intensity from the cathode was used as the initial condition to Eq. 1. The cathode emissivity was taken to be 0.4, and the cathode temperature was a parameter which was determined by fitting the calculated spectrum to the measured spectrum. The contributions to the axial emission from the free electrons and atomic hydrogen were incorporated into the spectral volume emission and absorption coefficients,  $\epsilon_{\lambda}$  and  $k_{\lambda}$ . The Doppler shift was taken into account as the radiant intensity was being emitted and absorbed by the plasma with an axially varying velocity.

Continuum radiation results from free electron processes which include free-bound electron-ion interactions and free-free electron-ion and electron-atom bremsstrahlung interactions.<sup>28</sup> The spectral emission coefficients for these processes were obtained in the literature,<sup>29</sup> while the corresponding spectral absorption coefficients were determined from the principle of detailed balance.<sup>30</sup>

The atomic hydrogen contribution involves line radiation from transitions between upper state  $j$  and lower state  $i$ , for which<sup>27</sup>

$$\begin{aligned} \epsilon_{\lambda}^{ji}(\lambda) &= \frac{hc^2}{4\pi\lambda^3} n_j A_{ji} \Phi_{\lambda}^{ji}(\lambda) \\ k_{\lambda}^{ji}(\lambda) &= \frac{h}{\lambda} (n_i B_{ij} - n_j B_{ji}) \Phi_{\lambda}^{ji}(\lambda) \end{aligned} \quad (2)$$

where  $A_{ji}$ ,  $B_{ij}$  and  $B_{ji}$  are the Einstein coefficients and  $\Phi_{\lambda}^{ji}$  is the normalized spectral lineshape function. Since the plasma within the arcjet is not in equilibrium, the number densities of the atomic states are found by solving a set of coupled rate equations in a collisional-radiative model.<sup>31</sup> These

equations consist of the steady-state continuity equation for the excited states,

$$\nabla \cdot n_m \underline{u}_m = \left[ \frac{dn_m}{dt} \right]_{C-R} \quad (3)$$

and the conservation of atoms equation

$$n_H = \sum_m n_m \quad (4)$$

where  $n_H$  is the total number density of hydrogen atoms in all atomic states. The stationary-state approximation is made for the excited states, and the production term on the right side of Eq. 3 is written in terms of the various collisional and radiative processes to give:

$$\begin{aligned} 0 = & n_e \sum_{j \neq m} n_j K_{jm} - n_e n_m \sum_{j \neq m} K_{mj} \\ & - n_e n_m K_{mc} + n_e^3 \beta_{cm}^{(3)} + n_e^2 \beta_{cm}^{(r)} \\ & + \sum_{j > m} n_j \gamma_{jm} A_{jm} - n_m \sum_{j < m} \gamma_{mj} A_{mj} \end{aligned} \quad (5)$$

for  $m=2,3,\dots$ , where  $K_{mj}$  and  $K_{mc}$  are the electron collisional excitation and ionization rate coefficients,  $\beta_{cm}^{(3)}$  and  $\beta_{cm}^{(r)}$  are the electron collisional three-body and radiative recombination rate coefficients, and  $\gamma_{jm}$  is a radiation escape factor.<sup>32</sup> The plasma is assumed to be optically thick to resonance radiation but optically thin to all other radiation. Semi-empirical rate coefficients are taken from the literature<sup>33</sup> or determined from the principle of detailed balance. The set of equations (Eqs. 4 and 5) are solved for the atomic state populations given the kinetic temperatures and the total atomic hydrogen and electron number densities. These properties, shown as a function of axial position in Figure 1, were obtained from a one-fluid MHD arcjet model developed by Butler and King<sup>2,3</sup> at Olin Aerospace Company applied to the NASA 5 kW arcjet. As a single fluid model, a unique kinetic temperature was used for both the electrons and heavy particles.

Finally, the spectral lineshape function  $\Phi_\lambda^{ji}$  is determined by the Stark broadening mechanism.<sup>34</sup> Although the Stark lineshape is neither Lorentzian nor Gaussian, a Lorentzian lineshape is assumed in Eq. 2 for simplicity. This approximation is very inaccurate for certain Balmer series lines of hydrogen, but is acceptably well suited for  $H_\alpha$ . Doppler and other line broadening mechanisms

were neglected in the modeling of the emission spectrum since the plasma properties within the arcjet are such that Stark broadening dominates. Figure 2 shows the Stark and Doppler broadened FWHMs of the  $H_\alpha$  line along the path of integration. The Stark broadening clearly dominates the Doppler broadening mechanism along the arcjet axis in the near-cathode region, the region of particular interest here. Other broadening mechanisms are significantly smaller still. By comparison, the lifetime broadening of  $H_\alpha$  is approximately  $1.3 \times 10^{-4}$  nm and pressure broadening of  $H_\alpha$  has a maximum value of about  $2 \times 10^{-3}$  nm near the cathode. For the other Balmer lines, the dominance of the Stark broadening mechanism is more marked.

### III. Experiment

Experiments were performed at NASA Lewis Research Center (LeRC) to measure the axial emission spectrum of a 5 kW arcjet in a manner similar to those previously performed on a 1 kW arcjet.<sup>25</sup> The experimental setup is shown in Figure 4. The vacuum chamber facility consisted of a 1.22 m diameter  $\times$  2.34 m long stainless steel chamber maintained at a background pressure of 0.25 torr by both mechanical and diffusion pumps. The arcjet employed was a NASA LeRC 5 kW class radiatively-cooled laboratory type thruster shown in Figure 5. The tungsten nozzle of this arcjet consisted of a 0.81 mm diameter constrictor and a 20 degree half-angle diverging section to an exit plane area ratio of 225. The 2% thoriated tungsten cathode was set approximately 0.9 mm from the nozzle constrictor.

A 500 mm focal length achromat lens was used to collect light axially from the arcjet throat and bring it to a focus on a 20  $\mu$ m diameter spatial filter. The image at the spatial filter was then focused, using an 80 mm focal length achromat lens, onto the entrance slit of a Jobin Yvon HR640 0.64 m Czerny-Turner monochromator containing a 2400 g/mm grating. Control of the monochromator was automated using a Spectralink controller and Prism 3.0 software. A Hamamatsu R928 photomultiplier tube was used as the photodetector. Phase-sensitive detection was performed for background noise rejection using a Stanford Research Systems SR850 digital lock-in amplifier. The reference signal was provided by a mechanical beam chopper placed near the intermediate focus at the spatial filter. The digitized output of the lock-in

amplifier was transferred to a personal computer for spectral analysis. To minimize the light collection volume from the arcjet plume and, hence, the molecular hydrogen emission, a 12.7 mm diameter aperture stop was placed in front of the collection lens, providing a collection optics  $f/\#$  of approximately 165. The resulting spatial resolution at the arcjet constrictor was at best 65  $\mu\text{m}$ . Intensity calibration was performed using an 18 A tungsten filament lamp placed at the location of the arcjet. The temperature of the lamp was determined using an Ircan Modline two color pyrometer.

The experiments were run under the operating conditions of 18.45 mg/s of hydrogen propellant and arcjet power between 2.3 kW and 4.4 kW. The current-voltage characteristics are shown in Figure 3. The propellant flow rate was maintained using a Unit Instruments UFC-2050A flow controller and the arcjet power was controlled by a NASA LeRC Model 5.2 PPU. Axial emission over the complete visible spectrum was collected on the arcjet centerline at three different power levels to obtain estimates of the cathode temperature during arcjet operation. As well, numerous scans of the Balmer alpha line were taken at several power levels and radial positions to determine the specific power and radial dependence of the electron number density within the arc.

#### IV. Spectrum Analysis

The previous study demonstrated the potential of determining near-cathode electron number densities from the linewings of the atomic hydrogen Balmer lines.<sup>25</sup> This is accomplished by fitting a Lorentzian line to the linewings only, since the line center is strongly affected by radiative transfer in the nozzle expansion region and in the plasma plume. The FWHM of the best fit Lorentzian is a direct measure of the electron number density in the arc by the Stark broadening mechanism.<sup>34</sup> The conditions within the arc, as determined by the best available arcjet models, indicate that Stark broadening is the only significant broadening mechanism in the near-cathode region. The results of the previous study indicated a larger electron number density calculated from the  $H_{\alpha}$  line than the  $H_{\beta}$  line and, in general, larger for both lines than the arcjet model predictions. These discrepancies initiated a further investigation into the lineshape analysis.

#### Stark broadening of $H_{\alpha}$

The discrepancy between the  $H_{\alpha}$  and  $H_{\beta}$  lines was found to be attributed to an error in the Vidal, Cooper, Smith (VCS) Stark broadening tables<sup>35</sup> for the  $H_{\alpha}$  line recently reported in the literature.<sup>36</sup> Monte-Carlo simulations with dynamical ion perturbations<sup>26</sup> have resulted in Stark broadening FWHMs for  $H_{\alpha}$  significantly larger than those given in the VCS tables in the range of electron number densities from  $10^{20}$  to  $10^{23} \text{ m}^{-3}$ . This discrepancy is shown clearly in Figure 6. Such an error was not found in the  $H_{\beta}$  line. By extrapolating the Stark widths to electron densities between  $10^{23}$  and  $10^{24} \text{ m}^{-3}$ , the densities predicted in the previous study using the  $H_{\alpha}$  line are reduced by a factor of two to three, resulting in very good agreement with those determined from the  $H_{\beta}$  line. These more accurate dynamical ion Stark broadening calculations are used in the analysis of the present data.

#### Lorentzian fit to linewings of $H_{\alpha}$

The discrepancy between the modeled and the measured electron number density was reduced after a more detailed analysis of the  $H_{\alpha}$  lineshape. The best fit Lorentzian was found to be very sensitive to the amount of the linewings to which the fit is performed. Figure 7 shows a typical measured  $H_{\alpha}$  lineshape with two different best fit Lorentzian lineshapes; the difference between the two best fits is the extent of the linewings in the fit, as indicated by the percentage of the peak intensity to which the fit is applied. It appears that both Lorentzian curves fit the wings extremely well; however, they differ in FWHM by nearly forty percent, corresponding to a discrepancy in  $n_e$  by approximately seventy percent. This uncertainty constitutes the limiting factor in accurately determining the arc electron number density from the linewings. On the one hand, to ensure that the fit is performed only to the part of the line originating near the cathode, it would be desirable to fit only the very far wings. This will reduce the systematic error associated with the radiation transfer near line center. On the other hand, since the noise is larger in the wings of the line, performing a linefit to only the far wings results in a very large statistical error in the determination of the linewidth. Consequently, the measured near-cathode electron number density has considerable uncertainty, often by a factor of two or more.

### Stark red shift of $H_{\alpha}$

The effect of a large electron number density is not only to broaden the  $H_{\alpha}$  line, but also to give rise to a Stark red shift. This symmetric Stark shift has been documented in the literature<sup>37</sup> for electron densities up to  $10^{23} \text{ m}^{-3}$  and is shown in Figure 8. By linearly extrapolating these measured shifts to typical electron densities near the cathode, say  $4 \times 10^{23} \text{ m}^{-3}$ , we find a red shift of approximately 0.25 nm, which is on the order of, but larger than, the expected Doppler blue shift. Because these two shifts are similar in magnitude and the axial velocity in the arc is not known, a measurement of this shift could not be used as an alternative method to obtain the near-cathode electron number density. Conversely, the large uncertainty in the measured arc electron number density, coupled with the uncertainty in determining the precise shift of the linewidths, precluded the measurement of axial velocity in the constricted arc.

One consequence of the Stark red shift at large electron number densities is that the reabsorption dip near the line center of the measured  $H_{\alpha}$  lines, shown in Figure 9, appears blue shifted relative to the line wings. This is contrary to what would be expected if only the Doppler shift is considered.

### Spectral Background

The region of the emission spectrum away from the Balmer series lines constitutes background graybody emission from the cathode surface and continuum radiation from the plasma electrons. This region of the spectrum was therefore used to measure the cathode temperature by fitting the modeled spectrum to the measured spectrum. The cathode temperature was a parameter of the model which could be adjusted until a good fit is obtained. Although the continuum radiation is accounted for in the modeling, it is generally a small fraction of the thermal radiation from the cathode for wavelengths greater than 500 nm.<sup>25</sup> Therefore, the precision of the cathode temperature measurements is primarily limited by the uncertainty in the emissivity of tungsten near and above its melting point.

## V. Results

### Emission spectrum modeling

The complete measured axial emission spectrum in the visible region is shown (solid) in

Figure 10 for an arcjet specific power of 220 MJ/kg. The calculated spectrum using the axial properties of Figure 1 is also shown (dashed). The baseline or background emission, corresponding to a cathode temperature of 3830 K, is seen to agree well with the measured spectrum above 550 nm. However, the simulated spectrum considerably underpredicts the width and intensities of the four lowest Balmer lines.

To understand this discrepancy, an investigation was performed to determine which property has the greatest effect on these line intensities and it was found that only an increase in the electron number density could significantly increase these line intensities. For the purpose of comparison, the axial emission was modeled using the same plasma temperature, axial velocity and atomic hydrogen number density given in Figure 1, but with the electron number density increased everywhere by a factor of three. This simulation, shown dotted in Figure 10, agrees remarkably well with the measured spectrum for all of the Balmer lines except perhaps  $H_{\delta}$ . (However, at the short wavelengths the measured spectrum may be inaccurate due to the difficulty in calibrating the intensity.) Since such a large increase in electron density increases the continuum radiation considerably, the cathode temperature had to be lowered by approximately ten percent to fit the measured background emission. Nevertheless, these results indicate that the MHD arcjet model is underpredicting the near-cathode electron number density by a factor of approximately three.

### Electron number density

Typical measured  $H_{\alpha}$  lines are shown at various specific power levels in Figure 9. These lines show clearly the previously mentioned absorption dip near line center and the Stark red shift of the linewidths. The measured electron number density in the near-cathode region is shown as a function of specific power in Figure 11 for both the 5 kW and 1 kW arcjets. Although the uncertainties are large, the densities show an increasing trend with specific power. In the 5 kW arcjet, the measured arc electron densities increase from about  $2.5 \times 10^{23}$  to  $8 \times 10^{23} \text{ m}^{-3}$  over a specific power range from 125 to 238 MJ/kg. The results for the 1 kW arcjet also show a similar increase. These trends are consistent with the fact that the arc current increases with increasing arcjet power. At a fixed mass flow rate, it is then expected that the plasma conductivity, and hence electron number density, in

the arc would increase with current density, and therefore power.

The 1 kW and 5 kW arcjet results can not be compared directly since both the arcjet geometry and the mass flow rates are different. However, the 1 kW results can be compared to peak near-cathode electron densities computed by the arcjet model of Butler and King,<sup>2,3</sup> shown as a dashed line in Figure 11. The agreement is quite good keeping in mind the uncertainties in the measurements, the approximations and numerical difficulties in modeling the arcjet, and the fact that the model results are peak electron densities while the measurements are line-of-sight averages over a small region near the cathode.

The arc electron number density was also measured as a function of radial position at a specific power of 238 MJ/kg. The results are shown in Figure 12, along with the radial distribution of electron density in the constrictor (dashes) and at the cathode tip (dots) as determined by the MHD arcjet model. The measured densities are larger than the model predictions near the line center by a factor of perhaps two to four, which is in quantitative agreement with the previous conclusion that the model predicts arc electron densities too low by a factor of about three. The discrepancy between the measured and modeled electron densities become very large away from the arcjet centerline. The measured densities are probably artificially high here because of the finite spatial resolution of the collection optics and the transient instabilities in the location of the arc.

#### Cathode temperature

The cathode temperature was measured from the spectral background in the manner described above. Using the axial properties from the MHD arcjet model, a cathode temperature of 3830 K gives the best fit to the measured spectrum of Figure 10. However, using the corrected electron number densities, the cathode temperature must be reduced by about ten percent due to the increased continuum radiation component of the background. Because of this uncertainty, it is preferable to have a means of measuring the cathode temperature which is independent of the MHD arcjet model.

This is achieved by assuming that the effect of the continuum radiation on the background spectrum can be reasonably well approximated by a uniform arc of some unknown length. The electron

number density in the arc is taken to be the value measured from the  $H_{\alpha}$  line wings, while the temperature and atomic density are assumed to be values typical of the arc. For the results presented here these values are 50,000 K and  $6 \times 10^{21} \text{ m}^{-3}$  respectively. The resulting spectrum is calculated using these plasma properties and the cathode thermal radiative properties. By fixing the cathode spectral emissivity at 0.4, the calculated background is fit to the measured spectrum, with the parameters of the fit being the cathode temperature and the thickness of the arc. The resulting cathode temperature measurements are shown in Figure 13. In all cases, an arc length of 0.29 mm was found to give the best fit. The error bars shown in Figure 13 are due only to the uncertainty in fitting the calculated spectrum to the measured spectrum, and not due to systematic errors in the measurement technique.

The measured cathode temperatures show an increasing trend with specific power. This may be explained by an increase in the current density at the arc attachment with increasing arcjet power, consistent with the measured increase in plasma conductivity, or electron number density, as discussed above. However, the cathode temperatures are found to be somewhat below the melting point of pure tungsten, which is inconsistent with documented cathode erosion measurements inferring the presence of a molten pool of tungsten at the cathode tip.<sup>38</sup> This discrepancy may be accounted for in the uncertainty in the spectral emissivity of molten tungsten at normal incidence. If the emissivity is below 0.4 then the temperatures will be larger than those shown here.

Having obtained a measurement of the cathode temperature, the electric field at the cathode tip and the cathode fall voltage can be estimated. Inspection of the cathode tip revealed a small crater of 0.75 mm diameter. At 220 MJ/kg the arcjet current was 36.0 A, and assuming that current was uniformly distributed over the crater, the resulting current density is approximately  $8 \times 10^7 \text{ A/m}^2$ . The Shottky-enhanced thermionic emission current density,  $j_{th}$ , is given by<sup>39</sup>

$$j_{th} = AT_c^2 \exp \left[ \frac{-e}{kT_c} \left( \phi_w - \left( \frac{eE}{4\pi\epsilon_0} \right)^{1/2} \right) \right] \quad (6)$$

where  $E$  is the electric field,  $T_c$  is the cathode temperature, and  $\phi_w$  is the work function. The

constant A is given by

$$A = 2 \left( \frac{2\pi m_e k^2}{h^3} \right) \quad (7)$$

Assuming a work function of 4.5 V for tungsten,<sup>40</sup> and a measured cathode temperature of roughly 3700 K, an electric field of  $5 \times 10^8$  V/m is required to produce the specified current density. Little experimental data exists on field strengths near cathodes in high pressure arcs; however, calculated values in the  $10^8$  V/m range have been reported.<sup>41</sup> The sheath thickness is approximately  $10^{-8}$  m, which implies a cathode fall voltage on the order of 5 volts. This agrees well with typical high pressure discharges.<sup>42</sup>

It is clear that field enhancement of the thermionic emission must be considered, since neglecting the electric field would necessitate a cathode temperature of 4400 K to sustain the required current density. However, such a high cathode temperature is inconsistent with the measured emission spectrum. With a cathode temperature of 4400 K, the calculated emission spectrum can be lowered to the measured background only by reducing the emissivity to 0.1; however, the agreement between the two spectra is very poor. It is therefore unlikely that the cathode temperature is this high; consequently, the electric field must play a significant role in the thermionic emission process at the cathode.

## VI. Summary and Conclusions

In this study the axial emission of a 5 kW class hydrogen arcjet was investigated, both numerically and experimentally. The emission spectrum was simulated numerically by integrating the equation of radiative transfer from the cathode tip to the arcjet exit plane. The atomic hydrogen excited state number densities were determined using a collisional-radiative model and the axial property inputs of kinetic temperature, axial velocity, total hydrogen density and electron density were obtained from a one-fluid MHD arcjet model of Butler and King.<sup>2,3</sup> The experiments were performed on a NASA LeRC designed radiation-cooled 5 kW arcjet thruster. The measured and simulated axial emission spectra are in excellent agreement when the electron number density is increased in the arc by a factor of three from the model predictions. This indicates that the present model is underpredicting the arc electron density.

Since the arc is fully ionized, an increase in the modeled electron density would require an increase in pressure. For a fixed mass flow rate this can only be achieved by increasing the arcjet power, resulting in a decrease in efficiency. However, this is desirable since the present model overpredicts the arcjet efficiency.<sup>16,17</sup>

The near-cathode electron number density was measured from the Stark broadening of the linewings of the  $H_\alpha$  line. There is considerable statistical error in this measurement technique which results in uncertainties in number density by a factor of two or more. Nevertheless, the measurements indicate that the arc electron density increases with specific power at a constant mass flow rate, which suggests that the arc current density increases with arcjet power rather than, or perhaps in addition to, an increase in the arc cross-sectional area. The radial distribution of the measured electron number density in the near-cathode region was compared to the arcjet model of Butler and King.<sup>2,3</sup> Near the arcjet centerline, the measured densities were greater than those of the model by a factor of two to four, which is consistent with the previously mentioned discrepancy. Away from the centerline the measurements are less reliable because of the limited spatial resolution and the instability of the arc.

The cathode tip temperature was measured at three different power levels and found to be in the neighbourhood of, but somewhat below, the melting point of pure tungsten, and increases with arcjet power. The latter result can be realized by an increase in current density at the arc attachment, which is in agreement with the measured increase in plasma conductivity, or electron number density, near the cathode. The former result is inconsistent with observations that the cathode tip is in a molten state during arcjet operation.<sup>38</sup> However, this discrepancy may be attributed to the uncertainty in the spectral emissivity of molten tungsten. Assuming a cathode temperature at the melting point, a calculation of the Shottky-enhanced thermionic emission from the cathode gives a cathode fall voltage in agreement with those of high pressure discharges. The accuracy of the cathode temperature measurements would be significantly improved with a better understanding of the spectral emissivity of molten tungsten.

## Acknowledgments

This work was supported in part by the Air Force Office of Scientific Research under grant No. F49620-92-J-0449 with M. Birkan as monitor. Partial support was provided by Olin Aerospace Company. M. Cappelli would like to acknowledge the Ohio Aerospace Institute for the Faculty Summer Fellowship which permitted this study, and to the Low Thrust Propulsion Branch at NASA Lewis Research Center for providing the opportunity to perform the experiments. Special acknowledgments are also given to D.C. Byers, F.M. Curran and D.H. Manzella at NASA Lewis for many stimulating discussions, and to G.W. Butler, D.Q. King and A.E. Kull of Olin Aerospace Company for their modeling of the arcjet.

## References

1. W.W. Smith, R.D. Smith, K. Davies and D. Lichtin; "Low Power Hydrazine Arcjet Flight Qualification"; IEPC-91-148; 22nd AIDAA/AIAA/DGLR/JSASS International Electric Propulsion Conference, October 1991.
2. G.W. Butler and D.Q. King; "Single and Two Fluid Simulations of Arcjet Performance"; AIAA-92-3104, 28th AIAA/SAE/ASME/ASEE Joint Propulsion Conference, July 1992.
3. G.W. Butler, A.E. Kull and D.Q. King; "Numerical Simulations of Hydrogen Arcjet Performance"; IEPC-93-249; 23rd AIAA/AIDAA/DGLR/JSASS International Electric Propulsion Conference, September 1993.
4. M.A. Cappelli; "Modeling the Near-Electrode Region of Arcjets I: Coupling of the Flow Field to the Non-equilibrium Boundary Layer"; AIAA-92-3109; 28th AIAA/SAE/ASME/ASEE Joint Propulsion Conference, July 1992.
5. E. Meeks and M.A. Cappelli; "Modeling the Near-Electrode Regions of Arcjets II: Inclusion of the Plasma Sheath with Full Coupling to Thermal and Velocity Boundary Layers"; AIAA-93-2103; 29th AIAA/SAE/ASME/ASEE Joint Propulsion Conference, June 1993.
6. G.W. Butler, B.A. Kashiwa, and D.Q. King; "Numerical Modeling of Arcjet Performance"; AIAA-90-1474; 21st AIAA Fluid Dynamics, Plasma Dynamics and Lasers Conference, June 1990.
7. S. Miller and M. Martinez-Sanchez; "Multifluid Nonequilibrium Simulations of Electrothermal Arcjets"; AIAA-93-2101; 29th AIAA/SAE/ASME/ASEE Joint Propulsion Conference, June 1993.
8. S. Miller and M. Martinez-Sanchez; "Non-equilibrium Numerical Simulations of Radiation-Cooled Arcjet Thrusters"; IEPC-93-218; 23rd AIAA/AIDAA/DGLR/JSASS International Electric Propulsion Conference, September 1993.
9. R. Rhodes and D. Keefer; "Non-Equilibrium Modeling of Hydrogen Arcjet Thrusters"; IEPC-93-217; 23rd AIAA/AIDAA/DGLR/JSASS International Electric Propulsion Conference, September 1993.
10. H. Okamoto, M. Nishida, K. Tanaka and A. Beylich; "Numerical Simulations of the Performance of a Radiation-cooled 1 kW Arcjet Thruster"; IEPC-93-181; 23rd AIAA/AIDAA/DGLR/JSASS International Electric Propulsion Conference, September 1993.
11. M. Andrenucci, L. d'Agostino and A. Ciucci; "Development of a Numerical Model of the Nozzle Flow in Low Power Arcjet Thrusters"; IEPC-93-182; 23rd AIAA/AIDAA/DGLR/JSASS International Electric Propulsion Conference, September 1993.
12. D. Zelesnik, M. Micci and L. Long; "DSMC Simulations of Low-Reynolds-Number Nozzle Flows"; AIAA-93-2490; 29th AIAA/SAE/ASME/ASEE Joint Propulsion Conference, June 1993.
13. R. Rhodes and D. Keefer; "Modeling Arcjet Space Thrusters"; AIAA-91-1994; 27th AIAA/SAE/ASME/ASEE Joint Propulsion Conference, June 1991.
14. M.A. Cappelli, J.G. Liebeskind, R.K. Hanson, G.W. Butler, and D.Q. King; "A Comparison of Arcjet Plume Properties to Model Predictions"; AIAA-93-0820; 31st Aerospace Sciences Meeting and Exhibit, January 1993.
15. M.A. Cappelli, J.G. Liebeskind, R.K. Hanson, G.W. Butler, and D.Q. King; "A Comparison of Hydrogen Arcjet Plume Properties to Single and Two-Fluid Model Predictions"; IEPC-93-220; 23rd AIAA/AIDAA/DGLR/JSASS International Electric Propulsion Conference, September 1993.
16. T. Moeller, D. Keefer and R. Rhodes; "Comparison of Experimental and Numerical Results for Radiation Cooled and Water Cooled Hydrogen Arcjets"; IEPC-93-214; 23rd AIAA/AIDAA/DGLR/JSASS International Electric Propulsion Conference, September 1993.
17. I. Boyd, D.R. Beattie and M.A. Cappelli; "Chamber Effects on Plume Expansion for a Low-Power Hydrogen Arcjet"; IEPC-93-126; 23rd AIAA/AIDAA/DGLR/JSASS International Electric Propulsion Conference, September 1993.
18. I. Boyd, M.A. Cappelli and D.R. Beattie; "Monte Carlo and Experimental Studies of Nozzle Flow in a Low-Power Hydrogen Arcjet"; AIAA-93-2529 29th AIAA/SAE/ASME/ASEE Joint Propulsion Conference, June 1993.
19. M.A. Cappelli and P.V. Storm; "Interior Plasma Diagnostics of Arcjet Thrusters"; AIAA-94-2654; 25th AIAA Plasmadynamics and Lasers Conference, June 1994.

20. M. Ishii and K. Kuriki; "Optical and Analytical Studies of Arc Column in DC Arcjet"; AIAA-87-1086; 19th AIAA/DGLR/JSASS International Electric Propulsion Conference, May 1987.
21. D.M. Zube and R.M. Myers; "Nonequilibrium in a Low Power Arcjet Nozzle"; AIAA-91-2113; 27th AIAA/SAE/ASME/ASEE Joint Propulsion Conference, June 1991.
22. W.J. Harris, E.A. O'Hair, L.L. Hatfield and M.D. Grimes; "Static Pressure Measurements in a 30 kW Class Arcjet"; AIAA-91-2457; 27th AIAA/SAE/ASME/ASEE Joint Propulsion Conference, June 1991.
23. K. Talley, W. Elrod and F.M. Curran; "Static Pressure Measurements of the NASA-Lewis 1.2-kW Arcjet"; AIAA-92-3111; 28th AIAA/SAE/ASME/ASEE Joint Propulsion Conference, July 1992.
24. F.M. Curran and D.H. Manzella; "The Effect of Electrode Configuration on Arcjet Performance"; NASA TM 102346, 1989.
25. P.V. Storm and M.A. Cappelli; "Axial Emission Diagnostics of a Low Power Hydrogen Arcjet Thruster"; IEPC-93-219; 23rd AIAA/AIDAA/DGLR/JSASS International Electric Propulsion Conference, September 1993.
26. D.H. Oza, R.L. Greene and D.E. Kelleher; "Collisional Broadening of the Balmer- $\alpha$  Transition of H and He<sup>+</sup> in Plasmas"; *Phys. Rev. A*, **37**, no. 2, pp. 531-536, 1988.
27. H.R. Griem; "*Plasma Spectroscopy*"; McGraw-Hill, Inc., New York, 1964.
28. L.M. Biberman and G.E. Norman; "Continuous Spectra of Atomic Gases and Plasma"; *Soviet Physics Uspekhi*, **10**, pp. 52-90, 1967.
29. A.T.M. Wilbers, G.M.W. Kroesen, C.J. Timmermans and D.C. Schram; "The Continuum Emission of an Arc Plasma"; *J. Quant. Spectrosc. Radiat. Transfer*, **45**, pp. 1-10, 1991.
30. W.G. Vincenti and C.H. Kruger, Jr.; "*Introduction to Physical Gas Dynamics*"; Robert E. Krieger Co., New York, 1965.
31. B. van der Sijde, J.J.A.M. van der Mullen, and D.C. Schram; "Collisional Radiative Models in Plasmas"; *Beitr. Plasmaphys.*, **24**, pp. 447-473, 1984.
32. T. Holstein; "Imprisonment of Resonance Radiation in Gases II"; *Phys. Rev.*, **83**, p. 1159, 1951.
33. L.C. Johnson; "Approximations for Collisional and Radiative Transitions Rates in Atomic Hydrogen"; *Astrophys. J.*, **174**, pp. 227-236, 1972.
34. W.L. Wiese; "Line Broadening"; *Plasma Diagnostic Techniques*, R.H. Huddlestone and S.C. Leonard, eds., Academic Press, New York, 1965.
35. C.R. Vidal, J. Cooper and E.W. Smith; "Hydrogen Stark Broadening Tables"; *The Astrophysical Journal Supplement Series*, No. 214, **25**, pp. 37-136, 1973.
36. D.E. Kelleher, W.L. Wiese, V. Helbig, R.L. Greene and D.H. Oza; "Advances in Plasma Broadening of Atomic Hydrogen"; *Phys. Scripta*, **T47**, pp. 75-79, 1993.
37. W.L. Wiese, D.E. Kelleher and D.R. Paquette; "Detailed Study of the Stark Broadening of Balmer Lines in a High-Density Plasma"; *Phys. Rev. A*, **6**, p. 1132, 1972.
38. F.M. Curran, T.W. Haag and J.F. Raquet; "Arcjet Cathode Phenomenon"; NASA Technical Memorandum 102099, 1989.
39. J.K. Koester; "Analytical and Experimental Studies of Thermionically Emitting Electrodes in Contact with Dense Seeded Plasmas"; Ph.D. Thesis, California Institute of Technology, 1970.
40. CRC Handbook of Chemistry and Physics, 73rd Ed.; CRC Press Inc., Boca Raton, FL, 1992.
41. W.L. Bade and J.M. Yos; "Theoretical and Experimental Investigation of Arc Plasma-Generation Technology"; Part II, Vol. 1, ASD-TDR-62-729, AVCO Corp., 1962.
42. W. Finkelnburg and H. Maecker; "Electric Arcs and Thermal Plasma"; Translation from Handbuch der Physik, Bd. 22, Gasentladungen II, 1956.

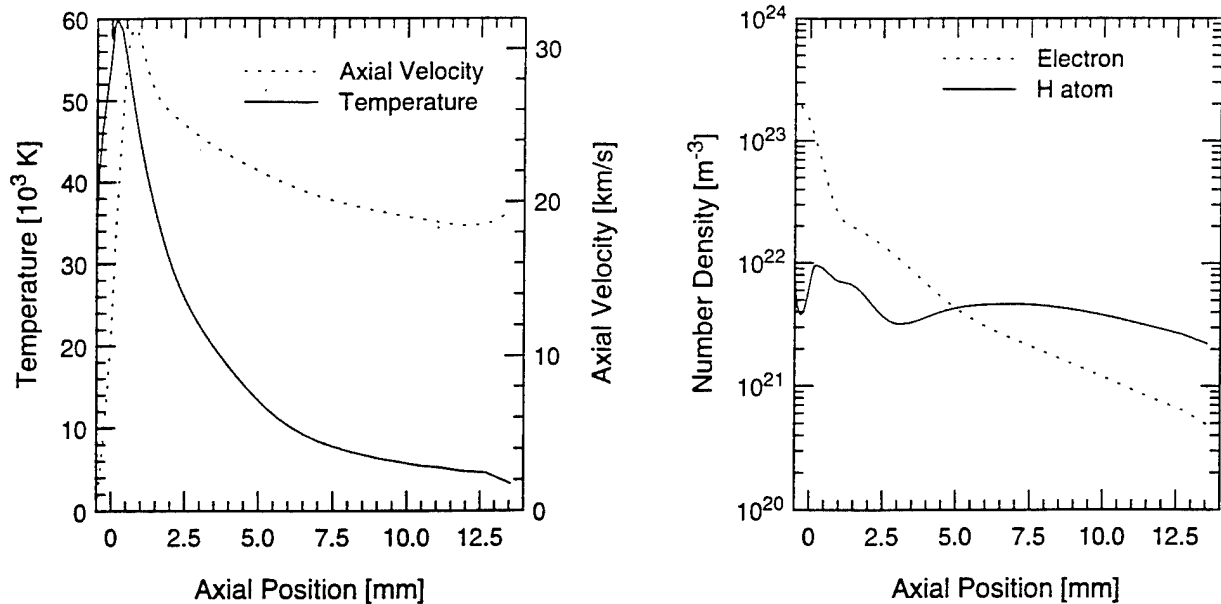


Figure 1. Axial properties  $T$ ,  $u_z$ ,  $n_H$  and  $n_e$  on the 5 kW arcjet centerline from a one-fluid MHD code (Butler and King, Olin Aerospace Company) at a specific power of 220 MJ/kg.

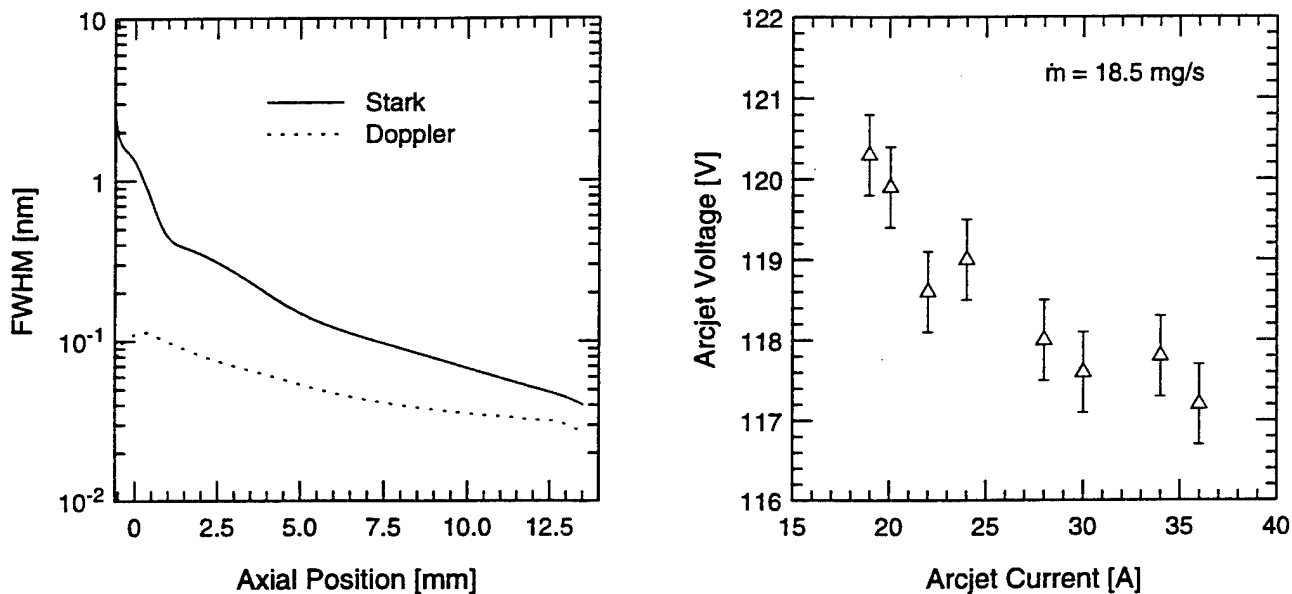


Figure 2. A comparison between the Stark and Doppler broadening of  $H_{\alpha}$  along the axis of the 5 kW arcjet.

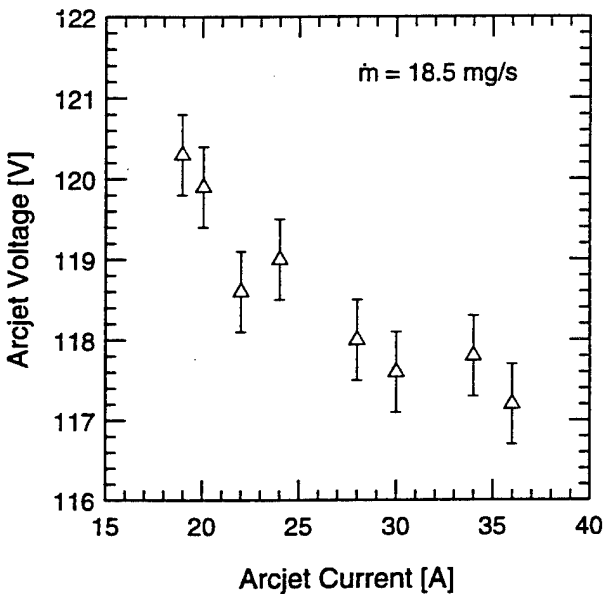


Figure 3. Current-voltage characteristics of the 5 kW arcjet at a mass flow rate of 18.45 mg/s.

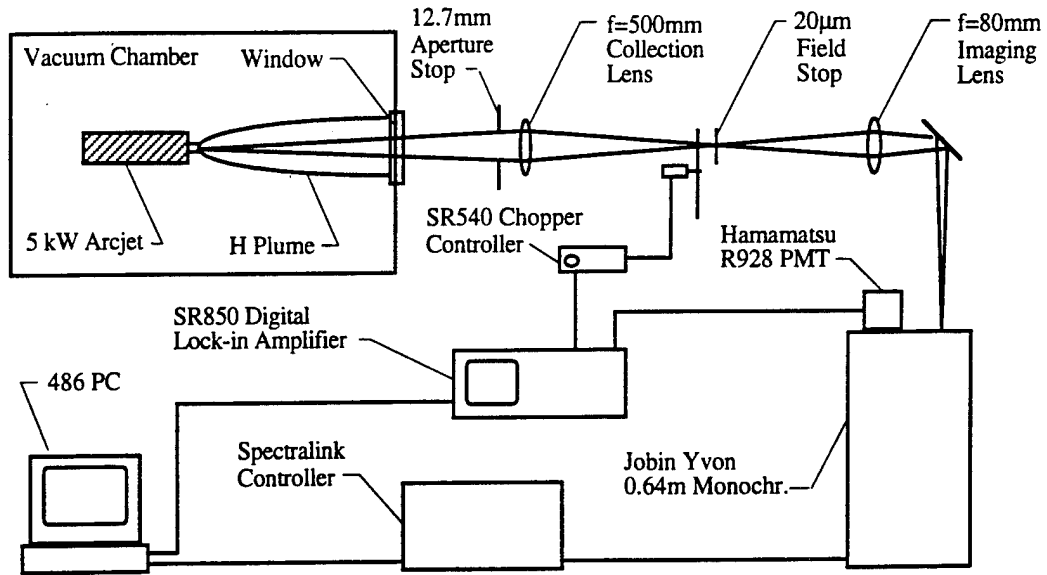


Figure 4. Schematic diagram of the axial emission experimental setup.

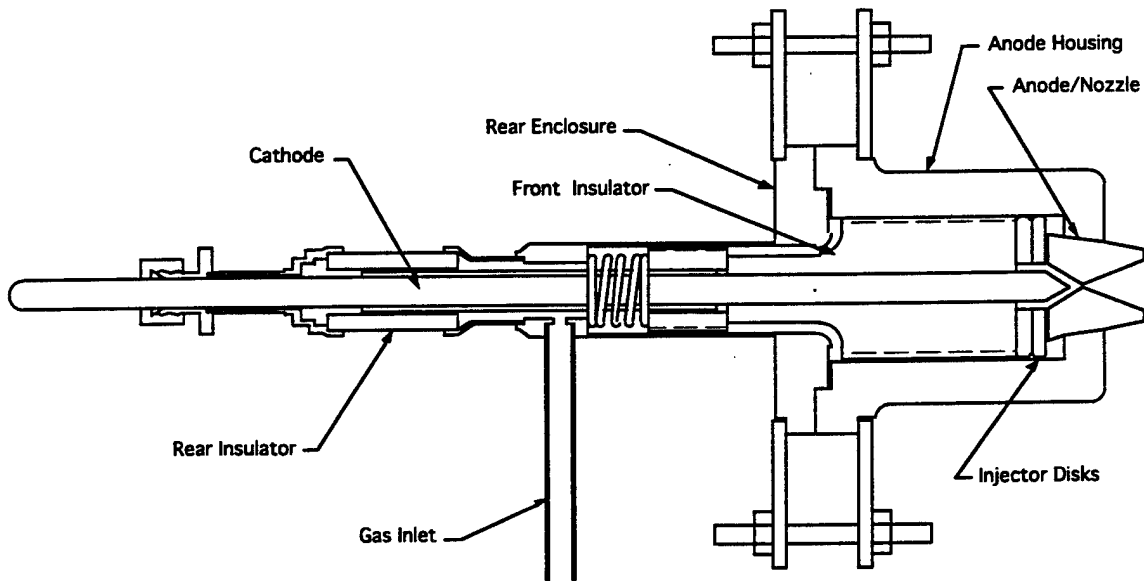


Figure 5. The NASA LeRC 5 kW arcjet.

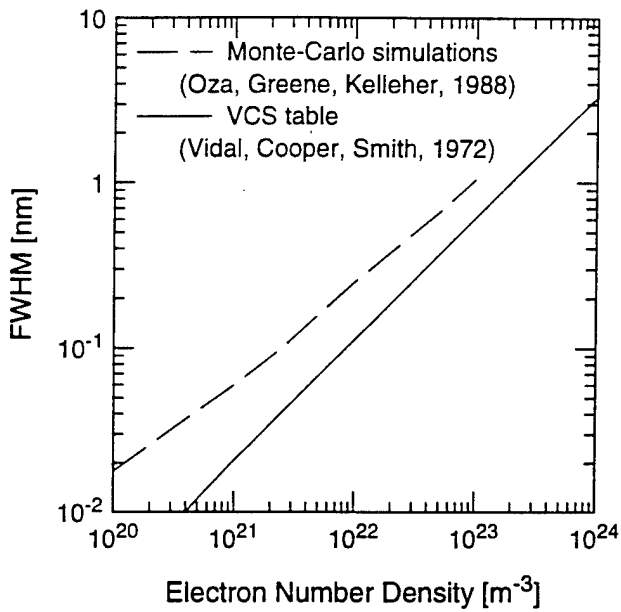


Figure 6. The Stark broadening of  $H_{\alpha}$  showing the discrepancy between the static ion calculations by Vidal, Cooper and Smith (solid) and the more recent dynamic ion Monte-Carlo simulations by Oza, Greene and Kelleher (dashes).

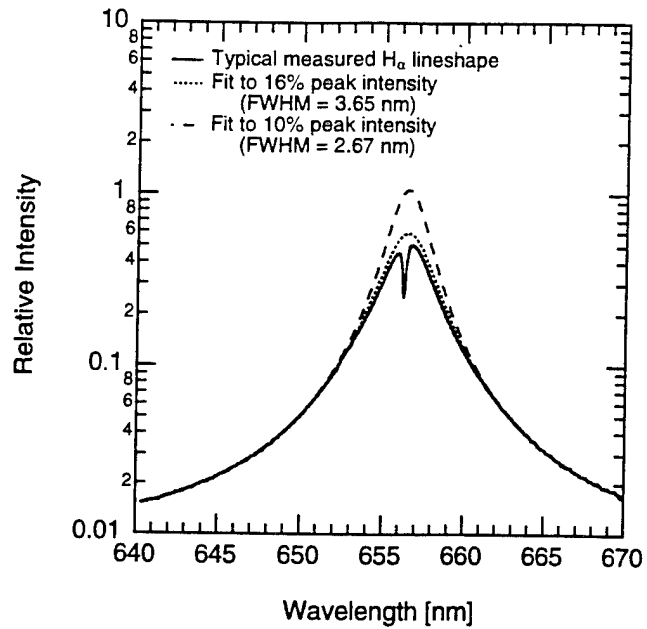


Figure 7. Typical measured  $H_{\alpha}$  lineshape with best fit Lorentzian functions to the linewings. The best fits differ in how much of the linewings are used in the fitting procedure as indicated by the percentage of the peak intensity used in the fitting. The difference in FWHM of nearly forty percent corresponds to a difference in electron number density of nearly seventy percent.

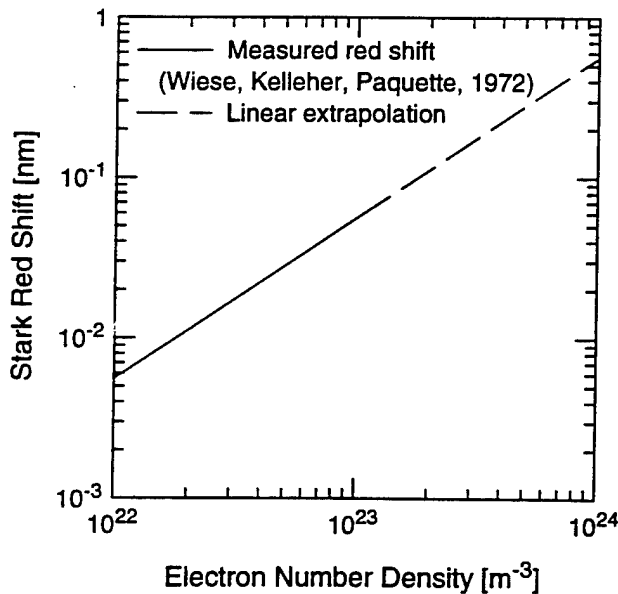


Figure 8. Stark red shift of  $H_{\alpha}$  as a function of electron number density. The dashed line is a linear extrapolation of the data of Wiese, Kelleher and Paquette.<sup>37</sup>

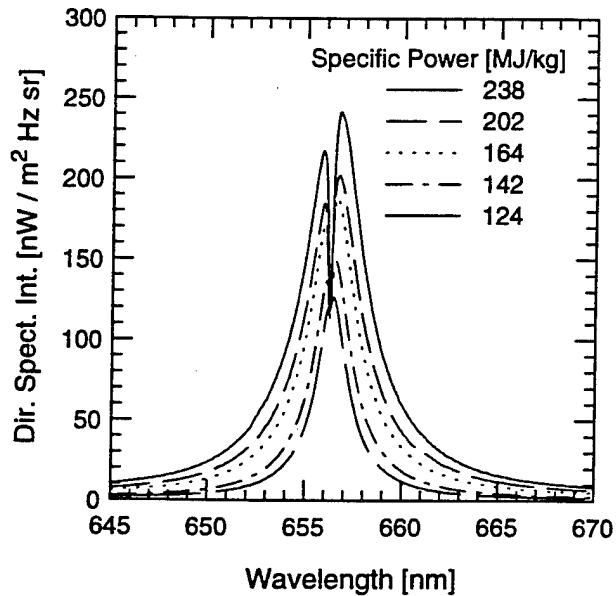


Figure 9. Measured centerline axial emission spectra of  $H_{\alpha}$  at different specific powers for the 5 kW arcjet showing the reabsorption dip near line center.

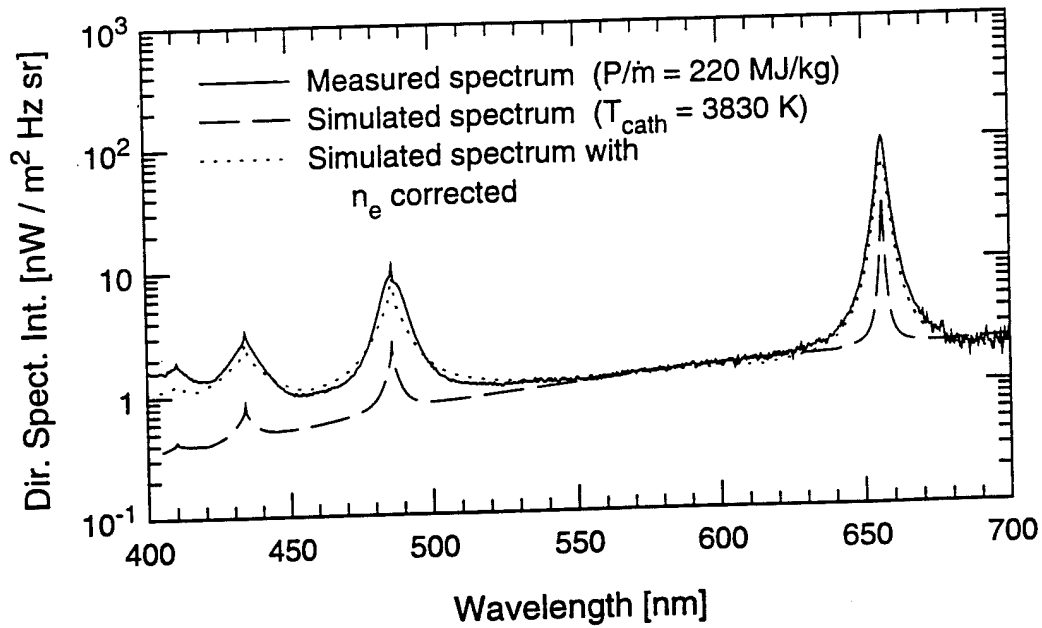


Figure 10. A comparison between the measured (solid) and calculated (dashes, dots) axial emission spectra of the 5 kW arcjet for a specific power of 220 MJ/kg. The dashed line is the calculated spectrum using the axial properties from Figure 1 and a cathode temperature of 3830 K. The dotted line is a calculated spectrum using a corrected electron number density and a cathode temperature of 3400 K.

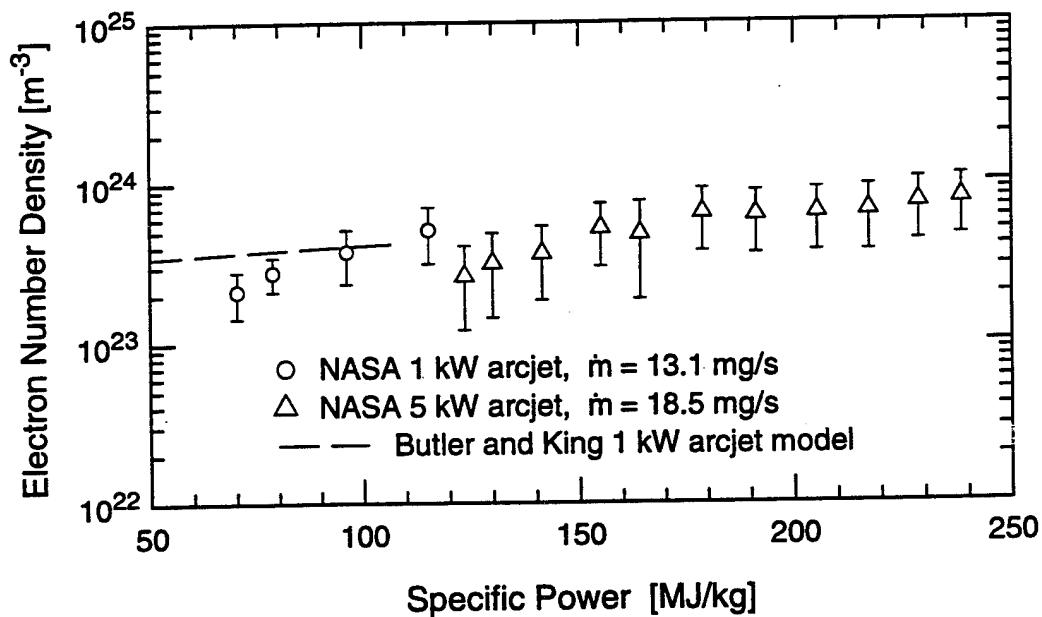


Figure 11. Measured near-cathode electron number density as a function of specific power for both the 1 kW and 5 kW arcjets. The dashed line gives the peak near-cathode electron density in the 1 kW MHD model of Butler and King.<sup>2,3</sup>

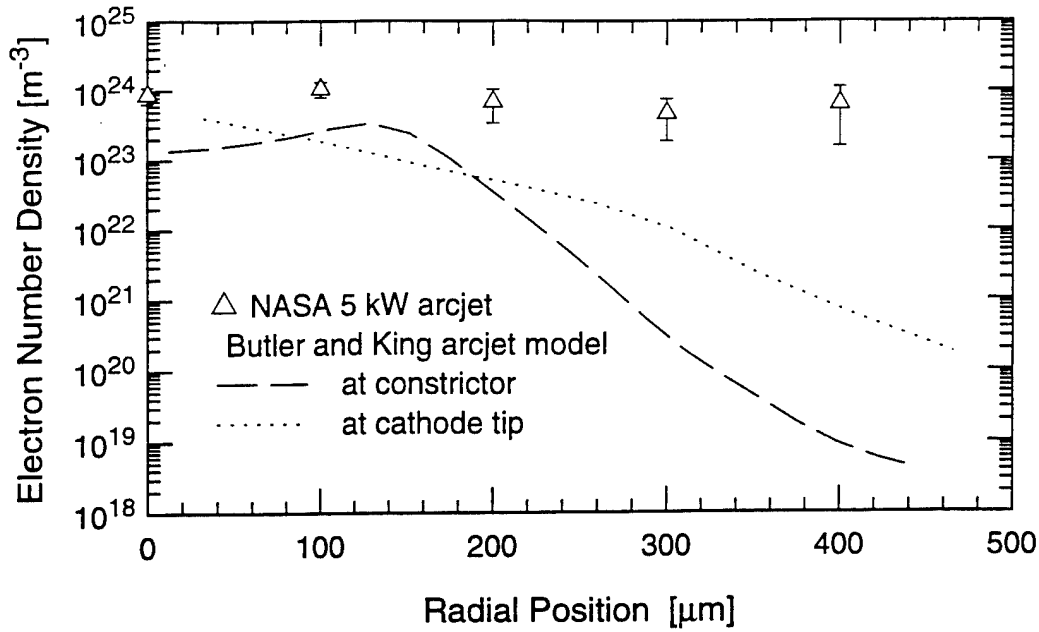


Figure 12. Measured near-cathode electron number density as a function of radial position for the 5 kW arcjet at a specific power of 238 MJ/kg. The dashed and dotted lines are model predictions by Butler and King<sup>2,3</sup> at the arcjet constrictor and cathode tip respectively.

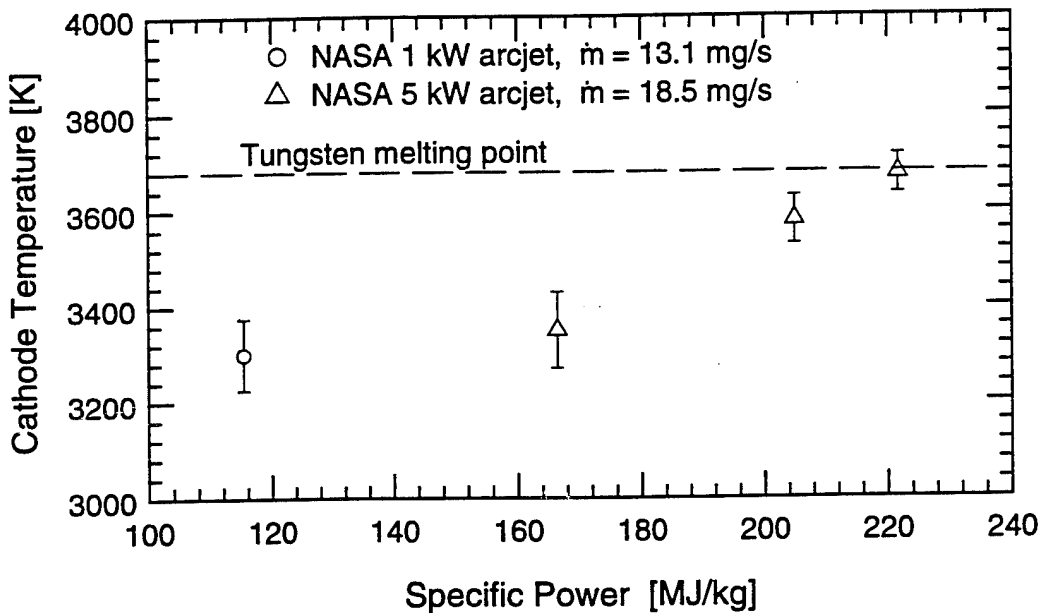


Figure 13. Measured cathode temperature as a function of arcjet specific power for both the 1 kW and 5 kW arcjets. The error bars correspond only to the statistical error of the fitting.



**AIAA - 95 - 1956**

**Raman Scattering Measurements of  
Molecular Hydrogen in an Arcjet  
Thruster Plume**

D.R. Beattie and Mark A. Cappelli

High Temperature Gasdynamics Laboratory  
Department of Mechanical Engineering  
Stanford University  
Stanford, California

**26th AIAA Plasmadynamics and Lasers  
Conference  
June 19-22, 1995/San Diego, CA**

# RAMAN SCATTERING MEASUREMENTS OF MOLECULAR HYDROGEN IN AN ARCJET THRUSTER PLUME

Doug R. Beattie\* and Mark A. Cappelli\*\*

High Temperature Gasdynamics Laboratory  
Department of Mechanical Engineering  
Stanford University  
Stanford, CA 94305-3032

## Abstract

*Raman scattering measurements of molecular hydrogen density and temperature were made in the plume of a 1 kW-class hydrogen arcjet thruster. Pulsed-laser excitation was used to improve the signal-to-noise ratio in this high-background environment. Quantum-limited detection was achieved through the use of gated photon counting and a high-power Nd:YAG laser. Radial profiles of rotational temperature and density at the exit plane were measured for 5 power levels. In all cases the profiles were asymmetric about the arcjet centerline. The rotational temperatures were compared with the translational temperatures of atomic hydrogen from LIF studies and found to be significantly lower. This result suggests that this flow, like the cold flow, is not in translational-rotational equilibrium.*

## Introduction

Arcjet thrusters are a type of electric-powered rocket which can be used for propulsion of space vehicles. They offer higher exhaust velocities than conventional chemical rockets; hence they require less propellant mass to deliver a given impulse. For certain missions, arcjets offer a good compromise between the often conflicting requirements of small size and low mass for the thruster and propellant combined. They are now being commercially employed in station-keeping roles on communication satellites.

There is a desire to increase both the thermal efficiency and exhaust velocities of current designs in order improve cost effectiveness and allow for use in a wider range of missions. Furthermore, there is interest in developing higher thrust versions which could be used in applications such as orbit transfer. Such improvements will depend partly on a better understanding of the plasma and gas dynamic processes undergone in the arcjet nozzle.

Currently both numerical analysis and experimental studies are being used to investigate flow properties in low-power arcjet thrusters. Attempts at modelling the plasma flow in hydrogen arcjet thrusters use both continuum (Butler et al. 1994, Miller and Martinez-

Sanchez 1993) and Monte Carlo techniques (Boyd et al. 1994). These models are useful in understanding the various loss mechanisms in an arcjet, including anode radiation, ionization, dissociation and other frozen-flow losses. Numerical models with accurate predictive capabilities will also be very helpful by allowing parametric studies to be performed much more easily than by testing prototypes in the laboratory. However, experimental measurements of relevant physical parameters in both the nozzle and plume are needed to validate these models. Of particular interest are density, temperature and velocity measurements of atomic hydrogen (H) and molecular hydrogen (H<sub>2</sub>).

Recent studies have relied primarily on optical diagnostics such as emission, absorption, and fluorescence. Optical techniques have the potential advantages of high spatial resolution and minimal perturbation to the flow field and most efforts have probed atomic hydrogen because of the large number of transitions in the visible spectrum. These experiments have included measurements of: H velocity and translational temperature using laser induced fluorescence (LIF) of the H<sub>α</sub> Balmer line (Liebeskind et al. 1993), H density using vacuum ultraviolet absorption (Manzella and Cappelli 1992) and multiphoton LIF (Pobst et al. 1995), and H temperature and electron density using emission (Storm and Cappelli 1994).

\* Research Assistant

\*\* Associate Professor, Member AIAA

Copyright © 1995 by Stanford University. Published by the American Institute of Aeronautics and Astronautics, Inc. with permission.

Molecular hydrogen (like other homonuclear, diatomic molecules) does not undergo radiative transitions between rotational or vibrational levels in the ground electronic state since it does not have a dipole moment. As a result, one can not use emission, absorption or fluorescence techniques to study these energy states. Until now, measurements of H<sub>2</sub> properties have been limited to spatially averaged absorption measurements (Pollard 1992) and density and temperature measurements in the distant plume using mass sampling spectroscopy (Pollard 1993). However, numerical simulations (Butler et al. 1994) have predicted that ~95% of the mass flow at the exit plane is molecular hydrogen so it is important to have experimental data on H<sub>2</sub> exit-plane properties.

The research described in this paper involved making measurements of molecular hydrogen properties in the plume of a hydrogen arcjet thruster. Spontaneous Raman scattering was chosen as a suitable technique for making spatially resolved measurements of the ground electronic state of H<sub>2</sub>. Raman scattering is a linear, inelastic, two-photon scattering process. It can be used to measure the density of various rotational and vibrational levels, allowing calculation of the total H<sub>2</sub> density and the rotational and vibrational temperatures. Measurements of the Doppler shift of the scattered light can provide the velocity distribution function, which gives both the bulk velocity and the translational temperature. The primary disadvantage of Raman scattering is the very low signal levels involved. Typical scattering cross sections are 10<sup>-33</sup> m<sup>2</sup>, or about 1000 times smaller than Rayleigh (elastic) scattering cross sections. As a result, the data collection process is generally very slow and it can be difficult to detect the signal in a luminous background, such as an arcjet thruster plume.

In this study, the population of various rotational levels was measured, giving the rotational temperature and density. Initial measurements (Beattie and Cappelli 1992) were made in the plume of a cold-flowing arcjet thruster. These flow conditions were well suited to developing both the experimental and numerical methods. Exit-plane profiles showed strong two-dimensionality in the flow, and also a moderate degree of asymmetry about the axis. The measured rotational temperatures on centerline were significantly higher than expected for isentropic flow, suggesting that the flow was not in rotational-translational equilibrium. Comparison of the results with Monte Carlo numerical simulations (Boyd et al. 1994) confirmed this result. Good agreement was obtained between experimental and modeling results for density and rotational temperature profiles by using a slightly lower value of the rotational relaxation rate than the accepted values. Axial profiles of density were also measured at various back pressures. Shock structure was vis-

ible downstream of the exit plane, and the shock behavior with changing pressure was consistent with gas dynamic theory and the simulation results.

## Theory

The Raman effect is a linear, inelastic, two-photon scattering process. An incident photon of frequency  $\nu_0$  scatters off a particle, causing a transition in the particle from the initial state  $i$  to a final state  $f$ . Since the system energy is conserved, the scattered photon must be shifted in energy correspondingly:

$$\begin{aligned}\epsilon_{\text{mol},i} + \epsilon_{\nu,i} &= \epsilon_{\text{mol},f} + \epsilon_{\nu,f} \\ \Delta\epsilon_{\nu} &= -\Delta\epsilon_{\text{mol}},\end{aligned}\quad (1)$$

where  $\epsilon_{\text{mol}}$  and  $\epsilon_{\nu}$  are the energy of the molecule and photon respectively. In the harmonic oscillator-rigid rotor approximation, the molecular energy can be written as:

$$\epsilon_{\text{mol}} = \epsilon_{\text{trans}} + \epsilon_{\text{rot}} + \epsilon_{\text{vib}} + \epsilon_{\text{elec}} + \epsilon_{\text{nucl}}.\quad (2)$$

The Raman transitions under consideration here all begin and end in the ground electronic state. Furthermore, changes in the translational and nuclear energy components as a result of the Raman scattering process are small. Hence the changes in  $\epsilon_{\text{mol}}$  can be approximated as changes in the rotational and vibrational states, allowing Eq. (1) to be written as:

$$\Delta\epsilon_{\nu} = -\Delta\epsilon_{\text{mol}}(\nu, J).\quad (3)$$

For a diatomic molecule, the selection rules are  $\Delta J = 0, \pm 2$  and  $\Delta v = 0, \pm 1$ , where  $\Delta J = J_f - J_i$  and  $\Delta v = v_f - v_i$ . The case of  $\Delta J = 0$  and  $\Delta v = 0$  is actually Rayleigh scattering. Scattering is designated as purely rotational when  $\Delta J = \pm 2$  and  $\Delta v = 0$ , purely vibrational when  $\Delta J = 0$  and  $\Delta v = \pm 1$ , and rotational-vibrational when  $\Delta J = \pm 2$  and  $\Delta v = \pm 1$ .

Theoretical Raman spectra were calculated for H<sub>2</sub> in equilibrium at a given temperature and density. The Raman energy shifts were taken from the experimentally-measured values of Veirs and Rosenblatt (1987) for pure rotational, vibrational and rotational-vibrational transitions from  $v_i = 0$  and  $J_i = 0$  through  $J_i = 5$  (6 for Q branch). These measurements are in excellent agreement with the quantum mechanical calculations of Wolniewicz (1983), differing by less than one part in 10<sup>5</sup>.

The H<sub>2</sub> Raman line shape is primarily determined by Doppler and collisional effects (Rahn et al. 1991). At the low pressures in these experiments, the transitions will be primarily Doppler broadened. The Doppler width for Raman scattering is different than for emission or

absorption, since two photons are involved. By solving the equations of conservation of energy and momentum, Weber (1973) shows that the Doppler width is:

$$\Delta v_{\text{FWHM}} = \frac{2}{c} \left( 2 \ln \frac{2kT}{m_{\text{mol}}} \right)^{\frac{1}{2}} \left[ 4(v_0^2 + v_0 \Delta v_R) \sin^2 \frac{\theta}{2} + \Delta v_R^2 \right]^{\frac{1}{2}} \quad (4)$$

where  $\theta$  is the angle between the incident and scattered light ( $\theta = 180^\circ$  implies forward scattering),  $\Delta v_R$  is the Raman frequency shift, and FWHM denotes the full-width at half maximum.

Raman cross sections for transitions from  $v_i = 0$  and  $J_i = 0$  through  $J_i = 3$  were calculated by Ford and Browne (1973) using quantum mechanical evaluations of the dynamic polarizability. Their results are in good agreement with previous experimental measurements and calculations. The cross sections were obtained at the excitation wavelength of interest using their 8<sup>th</sup> order expansion in wavelength. Cross sections for states  $J_i = 4$  and higher were not available, so they were estimated from the  $J_i = 3$  value taking into account the  $v_R^3$  frequency dependence.

In a typical Raman experiment, the incident photons are provided by a laser beam at a rate  $\dot{N}_L$  and light scattered into a solid angle  $d\Omega$  is collected from a beam segment of length  $l$ . The rate of Raman photons scattered for a transition from the initial state  $i$  to the final state  $f$  is:

$$\dot{N}_{i,f} = \dot{N}_L l n_0 \frac{n_i}{n_0} \left( \frac{d\sigma}{d\Omega} \right)_{i,f} d\Omega \quad (5)$$

where  $\dot{N}_L$  is the incident laser photon rate,  $n_0$  is the molecular number density,  $n_i/n_0$  is the population fraction in the initial state, and  $(d\sigma/d\Omega)_{i,f}$  is the differential Raman cross section for the transition from  $i$  to  $f$ .

The population fractions  $n_i/n_0$  were calculated assuming the gas was in local thermodynamic equilibrium (LTE) with the molecules obeying Boltzmann statistics, in which case:

$$\begin{aligned} \frac{n_i}{n_0} &= \frac{g_i e^{-\epsilon_i/kT}}{\sum_j g_j e^{-\epsilon_j/kT}} \\ &= \frac{g_i e^{-\epsilon_i/kT}}{q} \end{aligned} \quad (6)$$

where  $q$  is the molecular partition function. Neglecting interactions between all energy modes except rotational and nuclear, the total molecular wavefunction for  $\text{H}_2$  may be expressed as follows:

$$\psi_{\text{total}} = \psi_{\text{trans}} \psi_{\text{vib}} \psi_{\text{elec}} \psi_{\text{rot,nucl}} \quad (7)$$

which implies:

$$\epsilon_{\text{total}} = \epsilon_{\text{trans}} + \epsilon_{\text{vib}} + \epsilon_{\text{elec}} + \epsilon_{\text{rot,nucl}} \quad (8)$$

Hence the partition function can be factored as follows:

$$q = q_{\text{trans}} q_{\text{elec}} q_{\text{vib}} q_{\text{rot,nucl}} \quad (9)$$

allowing the population fraction for a particular state of an energy mode to be calculated independently of the other modes. For example, the population fraction in the vibrational state  $v$  is:

$$\frac{n(v)}{n_0} = \frac{g_{\text{vib}}(v) e^{-\epsilon_{\text{vib}}(v)/kT}}{\sum_v g_{\text{vib}}(v) e^{-\epsilon_{\text{vib}}(v)/kT}} \quad (10)$$

which only requires knowledge of the vibrational energy levels and degeneracies. The vibrational populations were calculated using the harmonic-oscillator approximation with  $\Delta\epsilon_{\text{vib}}(v=0 \rightarrow v=1)$  from Wolniewicz (1983) used as the vibrational energy constant. The error introduced by making the harmonic approximation is small at the temperatures involved in this study, since most of the molecules are in the ground vibrational state (>95% at  $T < 2000$  K). The rotational energies were taken from a 6 parameter fit to experimental data provided by Jennings et al. (1985). These energy levels agree to better than 1 part in  $10^4$  with the previously mentioned results of Veirs and Rosenblatt (1987) and Wolniewicz (1983). The electronic partition function was taken as unity. Furthermore, all measurements taken were integrated over essentially all translational velocities, so the translational partition function can be neglected.

Unlike the other energy modes, the rotational and nuclear modes interact, so their populations may not be calculated independently. A hydrogen nucleus (proton) is a fermion with spin of  $I = 1/2$ . As a result, the wavefunction of an  $\text{H}_2$  molecule must be antisymmetric with respect to interchange of the two nuclei. This property results in a restriction on the symmetry of the rotational wavefunction. For  $\text{H}_2$  in the ground electronic state, the electronic wavefunction is symmetric. In addition, the translational and vibrational wavefunctions are both symmetric. The only components of  $\psi_{\text{total}}$  which can be antisymmetric are  $\psi_{\text{nucl}}$  and  $\psi_{\text{rot}}$ . There are 4 possible nuclear spin states of the 2 nuclei: 3 symmetric states with parallel spins (often referred to as ortho-hydrogen), and 1 antisymmetric state with opposed spins (para-hydrogen). The rotational wavefunctions are symmetric for even  $J$  and antisymmetric for odd  $J$ . Hence there are only two ways of satisfying the antisymmetric constraint on the total wavefunction: (i) coupling a symmetric nuclear spin state (ortho) with an antisymmetric rotational state (odd  $J$ ) or (ii) coupling the antisymmetric nuclear spin state (para) with a symmetric rotational state (even  $J$ ).

The rotational-nuclear partition function is calculated as follows:

$$q_{\text{rot.nucl}} = \sum_{J=0}^{\infty} g_{\text{nucl}} g_{\text{rot}} e^{-\varepsilon_{\text{nucl}}/kT} \quad (11)$$

where  $g_{\text{rot}}$  is the rotational degeneracy ( $2J + 1$ ),  $g_{\text{nucl}}$  is the nuclear degeneracy (3 for odd  $J$ , 1 for even  $J$ ), and the nuclear state energy  $\varepsilon_{\text{nucl}}$  is neglected. The nuclear degeneracy ratio of 3:1 (ortho-para) results in a 3:1 statistical weighting of the odd-even  $J$  states. At temperatures above 300 K, the upper rotational states are sufficiently populated in equilibrium that the ortho-para ratio is in fact 3:1. At lower temperatures, the population increasingly fills the  $J = 0$  state, and the equilibrium ortho-para ratio decreases. In the limit as  $T$  approaches 0, the equilibrium ortho-para ratio also approaches 0.

Using the previously outlined techniques, the predicted signal from  $\text{H}_2$  at reference conditions ( $T = 300 \text{ K}$ ,  $P = 101\,325 \text{ Pa}$ ) is shown in Figure 1 for various rotational and/or vibrational transitions from  $v_i = 0$ . The plot shows the intensity versus wavelength for excitation by a 2 W laser at 532 nm, with  $l = 2 \text{ mm}$ ,  $d\Omega = 0.024 \text{ sr}$ , and a detection system efficiency (detected photons per collected photon) of  $\eta_{\text{sys}} = 0.005$ . The Rayleigh line is shown for comparison, though it is  $\sim 1000$  times more intense than the strongest Raman transition. The lowest 4 rotational states are shown, since they are the only ones with a significant population at this temperature. The pure rotational transitions, near the Rayleigh line, are the most intense at up to  $6000 \text{ photon s}^{-1}$ . However the slightly weaker pure vibrational transitions near 680 nm were used in these experiments for two reasons. First, they are well separated from the laser wavelength, which makes it easier to separate them from elastically scattered light due to both Rayleigh scattering and reflections off the arcjet and chamber walls. Second, since the various transitions are close together they can be measured in a single, short spectral scan. These transitions are shown in more detail in Figure 2. To indicate how these features might appear with typical instrument resolution, the spectrum was also convolved with a triangular function of 0.2 nm FWHM. Under these conditions, all the peaks are resolved except  $J = 0$  and  $J = 1$ . However, only the wings of these two lines overlap and the centerline intensity is unaffected by the adjacent transition. Table 1 shows a summary of these calculations, including the transition wavelengths, cross sections and intensities. The Q-branch transitions are highlighted and Rayleigh scattering information is included for comparison.

In order to determine if Raman scattering is a feasible technique for use in the arcjet plume, Raman spectra were calculated for the estimated flow conditions. The average exit-plane density was estimated at  $1 \times 10^{22} \text{ m}^{-3}$  using  $6000 \text{ m s}^{-1}$  as a typical mass-averaged

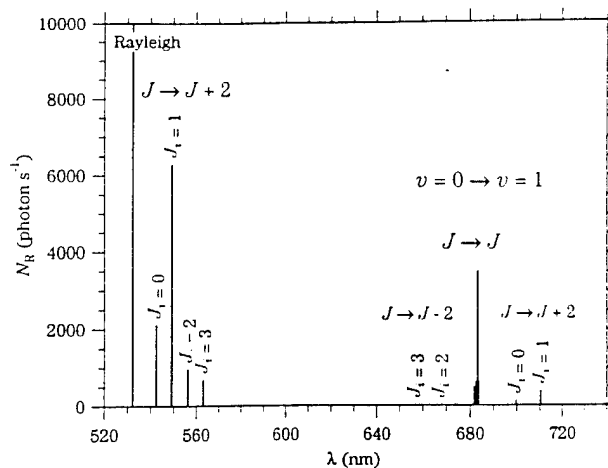


**Figure 1** Raman intensity versus wavelength for various rotational and/or vibrational transitions from  $\text{H}_2$  at reference conditions.

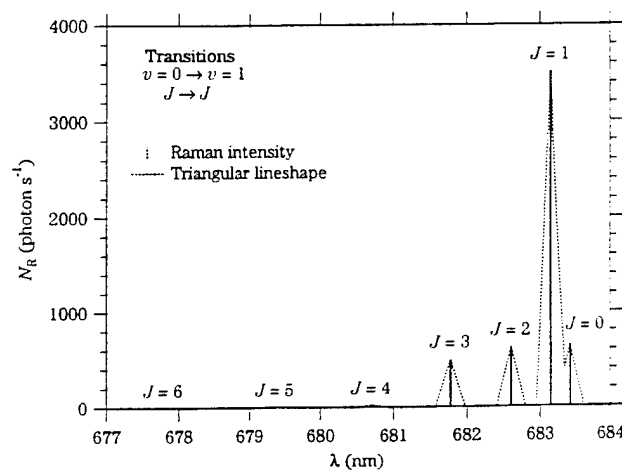


**Figure 2** Raman intensity versus wavelength for pure vibrational transitions under the same conditions as Figure 1.

exhaust velocity. The rotational temperature was estimated to be 1500 K based on the absorption measurements of Pollard (1993). Using these conditions, the spectrum shown in Figure 3 was calculated using the same setup parameters as for the reference calculation. The maximum estimated signal level is  $0.6 \text{ photon s}^{-1}$  from the  $J = 3$  transition. At these higher temperatures, the population is spread out over more rotational levels, with significant population in all 7 of the rotational states shown. The coupling of the rotational degeneracy to the nuclear spin degeneracy is evident from the alternating high-low intensity of the odd-even transitions. These very low signal estimates suggest that detection of the Raman scattering will be difficult, especially in the highly luminous background of the plume. Long collection periods will likely be required in order to accumulate statistically significant data.

**Table 1** Summary of Raman transition data at reference conditions using an incident wavelength of 532.1 nm, with the Q-branch transitions highlighted.

$v_i$	$v_f$	$J_i$	$J_f$	$\lambda$ (nm)	$\Delta E_R/hc$ ( $m^{-1}$ )	$n_i/n_0$	$\sigma$ ( $10^{-33} m^2$ )	$\dot{N}_R$ ( $s^{-1}$ )
0	0	0	2	542.326	35437	0.128	3.292	2115.4
0	0	1	3	549.258	58709	0.657	1.914	6295.7
0	0	2	4	556.204	81446	0.117	1.635	960.3
0	0	3	5	563.102	103470	0.092	1.485	682.5
0	1	0	0	683.421	416120	0.128	1.000	642.5
0	1	1	1	683.145	415528	0.657	1.067	3509.1
0	1	2	2	682.595	414349	0.117	1.065	625.7
0	1	3	3	681.777	412590	0.092	1.079	495.8
0	1	4	4	680.695	410259	0.004	1.084	23.1
0	1	5	5	679.359	407370	0.001	1.090	5.5
0	1	6	6	677.782	403945	0.000	1.098	0.1
0	1	0	2	699.515	449785	0.128	0.201	128.9
0	1	1	3	710.201	471294	0.657	0.117	383.6
0	1	2	4	720.646	491703	0.117	0.032	18.5
0	1	3	5	730.725	510842	0.092	0.021	9.9
0	1	2	0	667.263	380686	0.117	0.023	13.6
0	1	3	1	656.805	356824	0.092	0.032	14.6
0	0	0	0	532.100	0	0.128	109.403	70310.4
0	0	1	1	532.100	0	0.657	111.182	365710.2
0	0	2	2	532.100	0	0.117	111.462	65460.9
0	0	3	3	532.100	0	0.092	112.522	51714.8

## Experiment

The arcjet thruster uses an electric arc to heat propellant to high temperatures, often 10 000 to 20 000 K. The hot gases are then expanded through a Laval nozzle. The arc passes from the cathode to the nozzle walls, which act as the anode. The arcjet nozzle is machined from a tungsten alloy containing 98% W and 2% Th. Both the converging and diverging sections are conical, with half angles of 30° and 20° respectively. The nozzle diverging section has a 225:1 area ratio relative to the 0.64 mm diameter throat. The cathode is machined from a rod of the same alloy, with a tip angle matching that of the converging section. The cathode is installed by placing it in contact with the converging section, then pulling it 0.7 mm back. A drawing of the nozzle is shown in Figure 4. The anode is held by a stainless-steel anode housing which is bolted to the anode body. The cathode is insulated from the housing with a boron nitride sleeve. The hydrogen is injected tangentially through two small passages in the injector disk upstream of the cathode tip. The swirl imparted by this injection mechanism is believed to help stabilize the arc, primarily during startup.

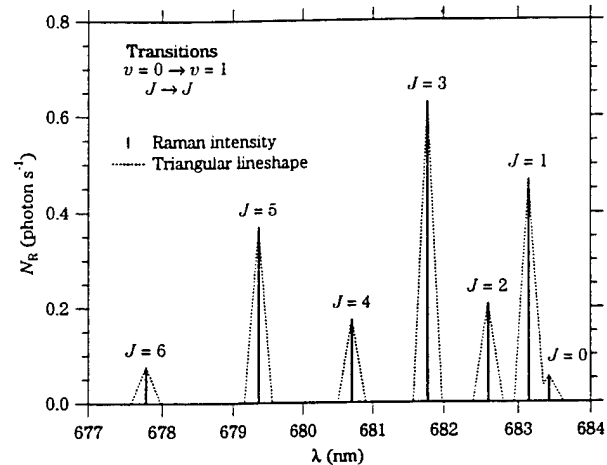


**Figure 3** Predicted Raman intensity versus wavelength at the exit plane of the arc-ignited thruster.

The arcjet used for these experiments was a 1kW class NASA laboratory hydrogen thruster. The thruster was operated in a vacuum chamber 1.09 m long and 0.53 m in diameter with optical access through 75 mm diameter ports. It was mounted on a two-axis axial and radial translation stage. Twelve optical ports were located at 30° intervals around the circumference of the tank, with additional ports in the endwall. The tank was evacuated by two Roots blowers backed by mechanical roughing pumps with a total capacity of 1.2  $m^3 s^{-1}$ . This system was capable of maintaining a back pressure of  $43 \pm 2$  Pa while flowing 13.3  $mg s^{-1}$  hydrogen.

In the previous cold flow experiments (Beattie and Cappelli 1992, Boyd et al. 1994, Beattie 1995) a CW laser was used. However, in order to improve the signal-to-noise ratio (SNR), a pulsed laser excitation scheme was chosen here. The Nd:YAG laser used was a Spectra Physics DCR-1 flashlamp-pumped, solid-state model. The output was frequency doubled using a type II KDP crystal, and the 532 nm light was separated using two dichroic filters. When operating at a 10 Hz repetition rate, the laser was capable of producing 200 mJ pulses at 532 nm with a 10 ns length.

Initially, the laser beam was sent axially into the arcjet through a port in the chamber endwall, as in the cold-flow experiments. However, the beam intensity at nozzle was so high that each laser pulse created a tungsten plasma and after a relatively short period of time, the nozzle was visibly eroded by the laser. In order to allow full laser energy to be utilized, the setup was modified to send the laser beam radially into the arcjet plume. The laser was sent in through a port 30° from vertical and directly out through the opposite port (Figure 5).

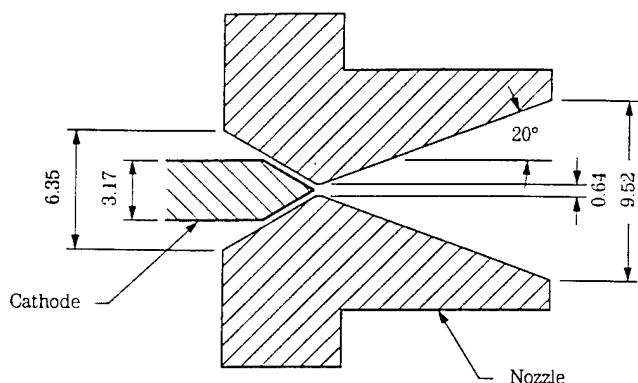


**Figure 4** Drawing of the 1 kW-class arcjet nozzle and cathode, showing key dimensions in mm.

The scattered light was collected at  $\theta = 120^\circ$  through a port located in the same circumferential plane as the laser at optical table level, and was focused onto a spectrometer entrance slit with an achromatic two-lens system as shown in Figure 6. The collection lens ( $f = +400$  mm,  $d = 76$  mm) was limited to  $f/5.7$  by the port geometry. The focusing lens ( $f = +600$  mm,  $d = 76$  mm) was chosen to match the spectrometer  $f$ -number. The spatial resolution was 2 mm in the radial direction, determined by the slit height, and 0.25 mm in the axial direction, determined by the slit width. The spectrometer was a 1.0 m focal length  $f/8.7$  single-pass Czerny-Turner design (Jarrell Ash 78-466). The grating was an 1800 line/mm holographic model with high efficiency from 400 to 1000 nm. A long-pass filter (Schott OG 590) was placed before the entrance slit to further reduce the intensity of collected laser light to negligible levels ( $10^8$ ). The spectrometer slits were  $400 \mu\text{m}$  giving a spectral resolution of  $\sim 0.2$  nm.

Light was detected at the exit slits with a Hamamatsu R928 photomultiplier tube (PMT) which had an efficiency of 6% at 680 nm and was operated at 1000 V. The output was amplified by an integral socket/preamplifier assembly (Hamamatsu C716-01) and sent to a photon counter (SRS 400). The counter was triggered by the laser using a photodiode. The 15 ns gate width was as narrow as possible to maximize the background rejection while still being wide enough to capture the peak of the signal pulse including jitter. The gate delay was first set approximately by simultaneously monitoring the counter input signal and the gate output on a two-channel oscilloscope. To set it more accurately, the count rate was recorded for a constant level of pulsed-light input to the detector. The delay was then scanned over the time-frame of interest and set at the position of the maximum count rate.

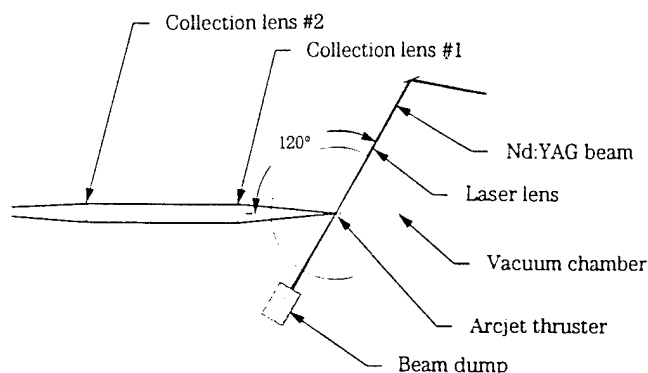


**Figure 5** Schematic diagram of laser and collection optics (front view).

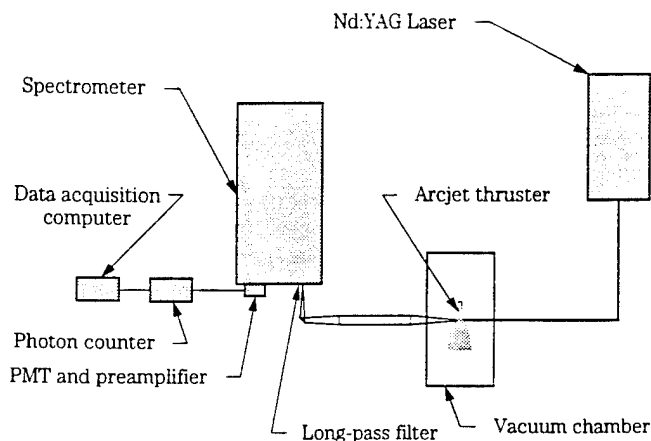


**Figure 6** Schematic diagram of experimental apparatus (plan view)

The counter was gated to the laser pulse using a photodiode. Counts are only accumulated when the counter is gated. The photon pulse height distribution peaked at  $\sim 300$  mV and the lower level discriminator was set to 100 mV. The spectrometer was scanned over the spectral region of interest and the photon counter output was recorded on a 486 computer using SRS 440 software.

The system was calibrated for absolute efficiency by measuring the Raman scattering from stagnant  $\text{H}_2$  at a known temperature and pressure. In order to account for the different efficiency at each transition, the relative efficiency versus wavelength was measured using a tungsten strip lamp. This second calibration was necessary since the transitions from  $J = 4$  through 6 were too weak at room temperature to be accurately measured.

## Results and Analysis

Given the low signal levels expected in the arc-ignited flow, it was feasible to make measurements at only a few spatial positions. Since arcjet performance is

determined entirely by the exit plane properties, data was collected as close to the exit as possible. Measurements were taken at 5 radial locations each 2 mm apart. With spatial resolution of 2 mm radially, this mesh covered the entire exit plane with no overlapping of segments. The arcjet was positioned at  $z = +4.0$  mm and the data acquisition program was started. The signal was recorded for 4000 laser pulses ( $\sim 400$  s) at each of the 5 positions across the exit plane.

Radial profiles in the arcjet plume were taken at 5 power levels: 800, 900, 1000, 1200, and 1400 W. With the hydrogen mass flow at  $13.3 \text{ mg s}^{-1}$ , the corresponding specific power levels were from  $60 \text{ MJ kg}^{-1}$  to  $106 \text{ MJ kg}^{-1}$ . A plot of the Raman signal versus radial position for the 900 W case is shown in Figure 7. The signal levels ranged from under 300 photons ( $0.7 \text{ photon s}^{-1}$ ) from state  $J = 1$  to 5 photons ( $0.01 \text{ photon s}^{-1}$ ) from  $J = 6$ . One notable feature is that the data is not symmetrical about  $z = 0$ . This asymmetry was observed at all power levels, although to varying degrees. In order to determine if this effect was systematic, one data set was taken by scanning the arcjet up for some  $J$  values and down for the others. However, there was no correlation between the scan direction and the asymmetry. Furthermore, the plume emission provided confirmation that the arcjet was properly centered. The plume emission that was measured simultaneously with the Raman scattering using the CW gate is shown in Figure 8 for the 900 W case. Gaussian curves were fitted to the emission to check the centering and in all cases the center of the fit was within  $50 \mu\text{m}$  of  $z = 0$ . The emission intensity varied with  $J$  depending on whether the Raman transition wavelength coincided with any  $\text{H}_2$  emission lines.

The first step in the analysis was to correct the data for possible saturation effects, which arise when consecutive photons overlap within the temporal resolution of the photon counting electronics (Beattie 1995). This correction was negligible except in the calibration scans, where the  $J = 1$  peak was reduced  $\sim 20\%$  by saturation. Next, the contribution of the CW signal to the gated counts was subtracted, using the measured CW rejection ratio of  $6.4 \times 10^6$ . This amount was no more than 4 counts at the 1400 W power level and less than 1 count at 800 W. With signal levels typically 40 to 200 counts, the largest source of error was the statistical variation in  $N_R$ , with the SNR equal to  $\sqrt{N_R}$ . The raw data was normalized by the laser power and relative efficiency at each transition. Then a best fit was performed to the corrected data using a function which assumed that the flow was in local thermodynamic equilibrium (LTE) with rotational population distributions dictated by a rotational temperature. The two parameters in this fit (LTE fit) were the  $\text{H}_2$  tem-

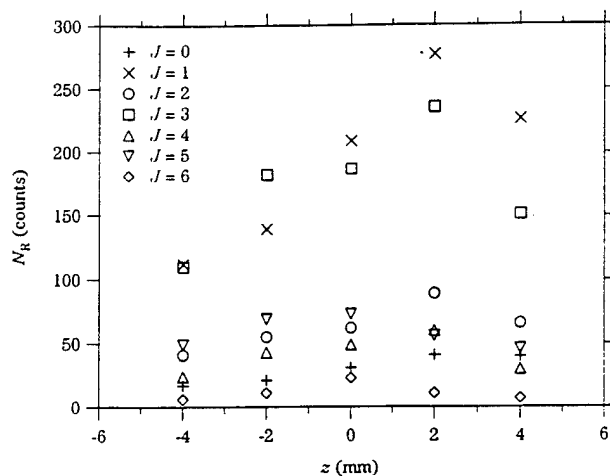


Figure 7 Raman signal versus radial position at 900 W power.

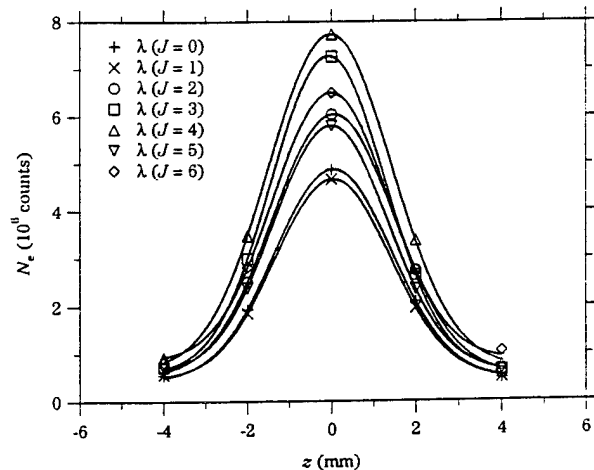
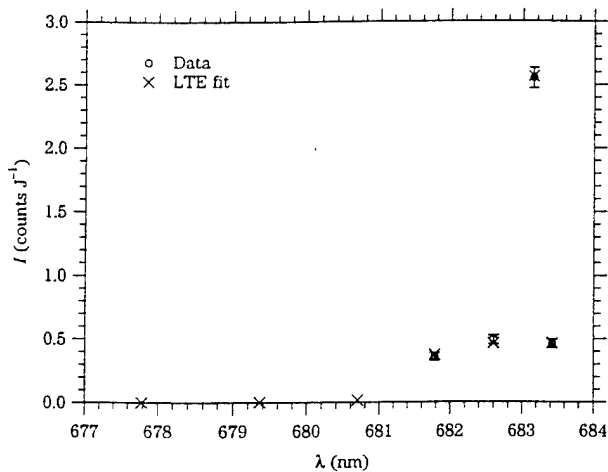


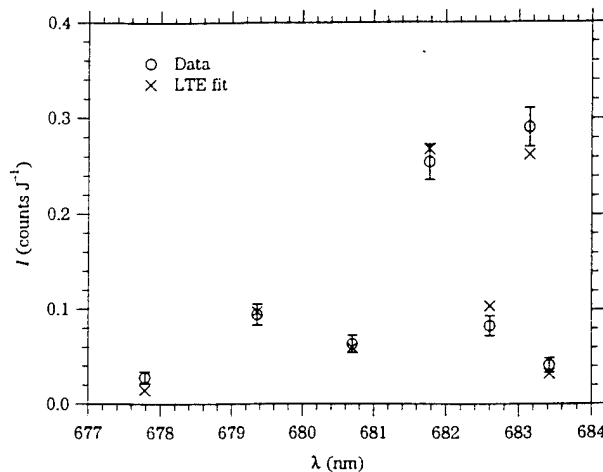
Figure 8 Plume emission signal measured simultaneously with the Raman signal shown in Figure 7.

perature and density. For the data presented here, states  $J = 0$  through 3 were used for calibration and states  $J = 0$  through 6 were used in the plume.

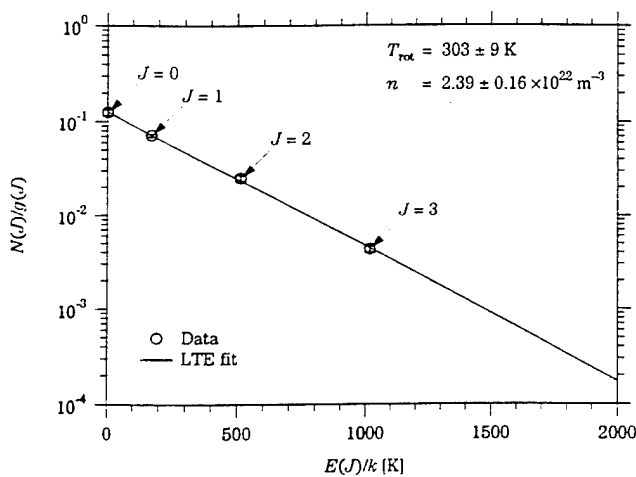
The corrected calibration data and LTE fit intensities are plotted as a function of wavelength in Figure 9 and in a Boltzmann plot in Figure 10. The data in Figure 9 is normalized by the laser pulse energy in Joules (J). The excellent agreement is primarily due to the good SNR afforded by the relatively high density at 100 Pa. The LTE fit temperature of  $303 \pm 9 \text{ K}$  is consistent with the measured room temperature of 300 K. The intensity of the transitions from  $J = 4$  through  $J = 6$  are shown for the LTE fit, but were not measured because of their relative weakness at this temperature.



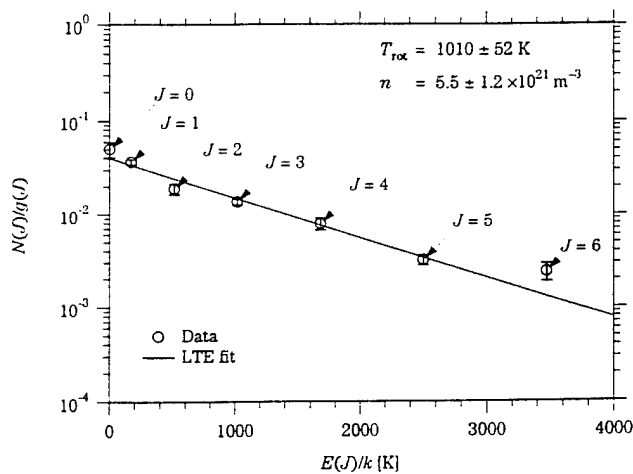
**Figure 9** Normalized Raman signal versus wavelength from calibration data.



**Figure 11** Normalized Raman signal versus wavelength measured at  $x = 2$  mm and  $z = 0$  mm while operating at  $P = 900$  W.



**Figure 10** Boltzmann plot of rotational population fractions from Figure 9.



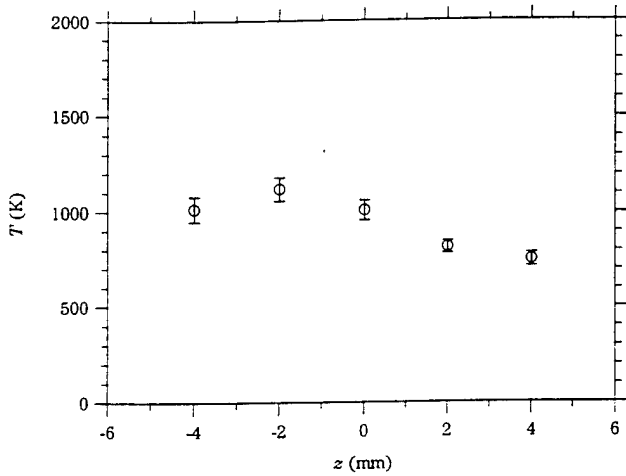
**Figure 12** Boltzmann plot of data in Figure 11, showing the measured density and rotational temperature, along with the calculated pressure.

Figure 11 shows a plot of the corrected data from Figure 7 at  $z = 0$  mm along with the results of the LTE fit. As an indication of how weak the scattering process is, the normalized peak signal of  $0.3 \text{ photon J}^{-1}$  corresponds to 1 detected photon for every  $10^{19}$  laser photons. The corresponding Boltzmann plot of the data is shown in Figure 12. This data was typical in that all but 2 or 3 points fell within one standard error of the intensity fit. For data following a Poisson distribution, one would expect measurements to lie within one standard error 68% of the time (for large  $N$ ). Thus the observed agreement of the data with the fit is quite reasonable.

The temperature profile across the arcjet exit plane is plotted in Figure 13 for the 900 W case. There is a relatively small variation in temperature across the exit

plane, ranging from 750 to 1120 K. The asymmetry that was apparent in the raw data is also evident here, with the peak temperature located at  $z = -2$  mm, rather than along the centerline as expected. The asymmetry appears again in the density profile shown in Figure 14, except that the peak density is located at  $z = +2$  mm. The shape is more peaked than for temperature, with the maximum density slightly more than double the minimum.

The temperature profiles measured at the 5 power levels are plotted in Figure 15. Similar asymmetries are evident to varying degrees in all cases. The maximum temperature always occurs at either  $z = -2$  or  $z = -4$  mm. The temperatures generally rise across the entire exit plane as the power is increased. This behavior is illustrated in Figure 16, where the maximum measured



**Figure 13** Rotational temperature versus radial position for the 900 W power level.

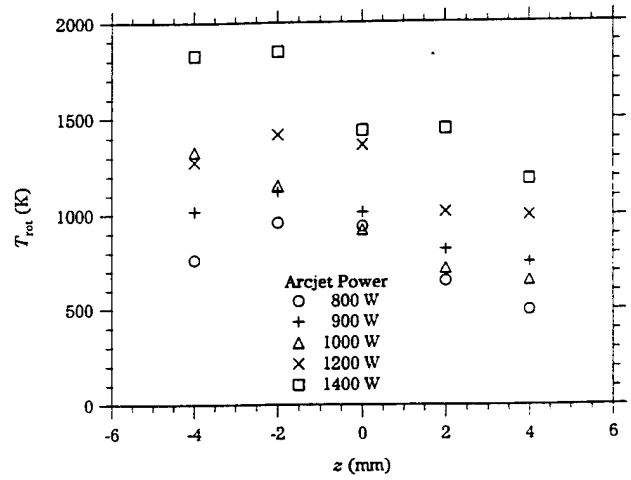


**Figure 15** Rotational temperature versus radial positions for 5 power levels.

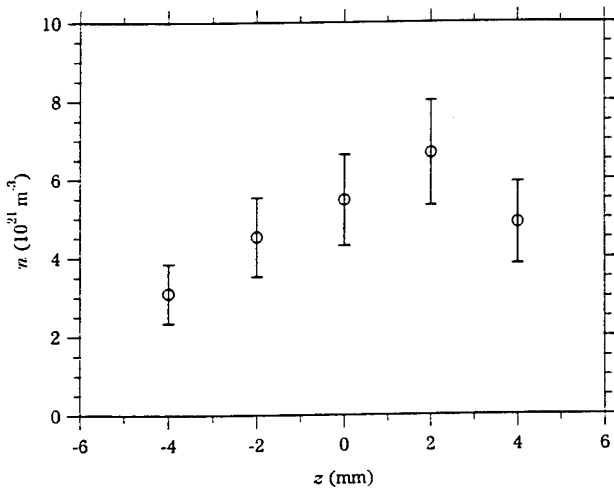


**Figure 14**  $H_2$  density versus radial position for the 900 W power level.

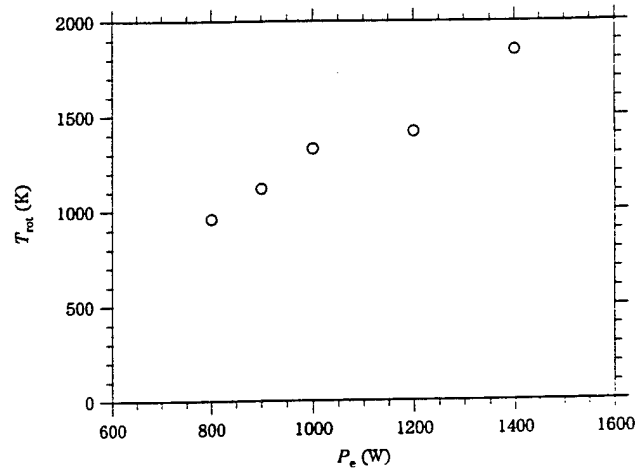


**Figure 16** Maximum rotational temperature versus arcjet power level.

temperature is plotted as a function on arcjet power. The maximum temperature was chosen instead of the center-line temperature in order to allow a consistent quantity to be compared between profiles of varying shape. The results range from  $T_{\max} = 960$  K at 800 W to 1850 K at 1400 W, with a relatively smooth upward trend associated with increasing power.

The corresponding density profiles are plotted in Figure 17. Again, the profiles were all asymmetric, with the maximum density at  $z = +2$  mm except for the 800 W power level. The densities range from  $2.8 \times 10^{21}$  to  $8.8 \times 10^{21} \text{ m}^{-3}$ , all below the predicted value of  $9 \times 10^{21} \text{ m}^{-3}$ . This difference is not surprising, since that prediction was based on the assumption that the exhaust was 100%  $H_2$  at a uniform velocity.

## Discussion

The  $H_2$  rotational temperatures were compared to previous experimental results. The H translational temperature was previously measured on the same facility using LIF and emission of the Balmer  $\alpha$  line. In the LIF study (Liebeskind et al. 1993), the mass flow rate was reported as  $13.7 \text{ mg s}^{-1}$  (versus  $13.3 \text{ mg s}^{-1}$  here) and the power levels were 870, 1000, and 1500 W. This LIF data was re-analyzed to account for Stark broadening (Storm and Cappelli 1995) and the resulting temperatures are significantly lower than the originally published data. The emission spectra were collected with a flow of  $13.3 \text{ mg s}^{-1}$  and  $P = 1500$  W, and were Abel inverted to give spatially resolved data. Figure 18 shows a comparison of the exit plane temperatures from Raman (1400 W), LIF (1500 W), and emission. The re-analyzed LIF results show the most peaked temperature distribution, reaching a maximum of 3400 K on axis, and in agreement with

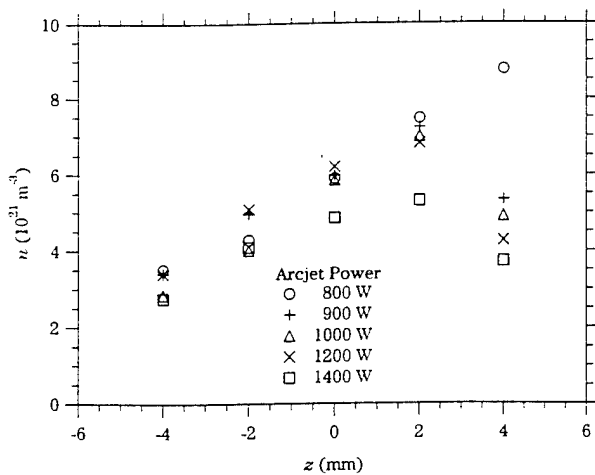


**Figure 17** Density versus radial positions for 5 power levels.

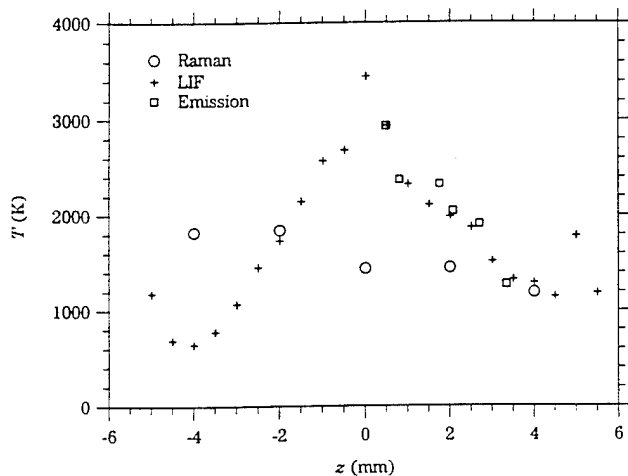


**Figure 18** Comparison of temperature versus radial position from Raman scattering, LIF, and emission for  $P \approx 1500$  W.

the more recent emission measurements of temperature. The Raman temperatures are the lowest of all, except near the edges, where all methods give similar values. However, the Raman temperatures are consistent with the absorption measurements of Pollard (1993) which gave  $T_{\text{rot}} = 1500$  K averaged across the exit plane.

These temperature measurements suggest the arc-ignited flow is not in rotational-translational equilibrium. This result is not entirely unexpected, since the cold-flow also showed significant rotational non-equilibrium. At the higher temperatures in the arc-ignited case, the rotational collisional number  $Z_{\text{rot}}$  decreases which should bring the flow closer to equilibrium. However, the density is roughly an order of magnitude lower, which will have a counteracting effect by reducing the number of collisions. The lower rotational temperatures can potentially be explained by considering whether  $\text{H}_2$  should be in rotational equilibrium as it diffuses to the centre. The

number of collisions an  $\text{H}_2$  molecule would undergo while moving from the nozzle wall to the center is proportional to  $Kn^{-1}$ . The mean-free path was estimated for  $\text{H}_2$  in  $\text{H}_2$  (since the flow is predominantly  $\text{H}_2$ ) using the tabulated value at room temperature and scaling as  $n^{-1}$ . At the throat  $\lambda = 0.6 \mu\text{m}$ , so  $Kn^{-1} \approx 500$ . Since  $Z_{\text{rot}} \approx 60$  at 2000 K, then  $Kn^{-1} \gg Z_{\text{rot}}$  and the flow is likely near rotational equilibrium. However, at the exit plane  $\lambda \approx 500 \mu\text{m}$  and  $Kn^{-1} \approx 10$ , so  $Kn^{-1} \ll Z_{\text{rot}}$ . Hence near the exit plane the density is sufficiently reduced that  $\text{H}_2$  molecules could be transported to the center without undergoing enough collisions to maintain rotational-translational equilibrium. Molecules colliding with the wall are expected to equilibrate at the wall temperature which has been estimated as  $\sim 1700$  K (Butler et al. 1994). Hence the walls provide a source of  $\text{H}_2$  with a rotational temperature comparable to that measured in the flow.

## Summary

Raman scattering measurements of  $\text{H}_2$  density and temperature were made at the exit plane of a 1 kW-class hydrogen arcjet thruster. Unlike in the cold-flow studies reported previously, pulsed-laser excitation was used in this study to improve the SNR in this high-background environment. Quantum-limited detection was achieved through the use of gated photon counting and a high-power Nd:YAG laser. Radial profiles of rotational temperature and density at the exit plane were measured for 5 power levels. In all cases the profiles were asymmetric about the arcjet centerline. The temperature profiles were compared with the translational temperatures of H from LIF studies and the bulk temperature from continuum simulations. The rotational temperatures were significantly lower than the other results, implying the flow is not in translational-rotational equilibrium. This finding is not so surprising, since results from the cold-flow studies and simple calculations indicate that rotational equilibrium is unlikely under cold-flow conditions. These results also suggest that the predictive capabilities of numerical simulations of such flows would be enhanced by incorporating a rotational energy transfer mechanism.

## Acknowledgements

This research was supported by the Air Force Office of Scientific Research, with partial support from the Olin Aerospace Company and Norton Company. We would also like to acknowledge the NASA Lewis Research Center for providing the arcjet and power processing unit.

## References

- Beattie, D.R. "Raman scattering measurements of molecular hydrogen in an arcjet thruster plume." Ph.D. Thesis, Mechanical Engineering Department, Stanford University, 1995.
- Beattie, D.R. and M.A. Cappelli. "Molecular hydrogen Raman scattering in a low power arcjet thruster." AIAA Paper, 28<sup>th</sup> AIAA/SAE/ASME/ASEE Joint Propulsion Conference, July 1992.
- Boyd I.D., D.R. Beattie, and M.A. Cappelli. "Numerical and experimental investigations of low-density supersonic jets of hydrogen." *Journal of Fluid Mechanics*, **V 280**, P 41-67, 1994.
- Butler G.W., A.E. Kull, and D.Q. King. "Single fluid simulations of low power hydrogen arcjets." AIAA Paper 94-2870, 30<sup>th</sup> AIAA/ASME/SQE/ASEE Joint Propulsion Conference, June 1994a.
- Ford A.L. and J.C. Browne. "Rayleigh and Raman Cross Sections for the hydrogen molecule." *Atomic Data*, **V 5**, P 305, 1973.
- Jennings D.E., L.A. Rahn, and A. Owyong. "Laboratory measurement of the S(9) pure rotation frequency." *Astrophysical Journal*, **V 291**, L 15-L 18, 1985.
- Liebeskind J.G., R.K. Hanson, and M.A. Cappelli. "Laser-induced fluorescence diagnostic for temperature and velocity measurements in a hydrogen arcjet plume." *Applied Optics*, **V 32**, P 6117-6127, 1993.
- Manzella D.H. and M.A. Cappelli. "Vacuum ultraviolet absorption measurements in a hydrogen arcjet." AIAA Paper 92-3564, 28<sup>th</sup> AIAA/SAE/ASME/ASEE Joint Propulsion Conference, July 1992.
- Miller, S. and M. Martinez-Sanchez. "Non-equilibrium numerical simulation of radiation-cooled arcjet thrusters." Paper IEPC 93-218, 23rd International Electric Propulsion Conference. September 1993.
- Pobst, J., I. Wysong, and R. Spores. "Laser induced fluorescence of ground state hydrogen atoms in an arcjet plume." Paper AIAA-95-1973, 26th Plasma-dynamics and Lasers Conference, June 1995.
- Pollard, J.E. "Arcjet diagnostics by XUV absorption spectroscopy." AIAA Paper 92-2966, 23<sup>rd</sup> AIAA Plasma Dynamics and Lasers Conference. July 1992.
- Pollard, J.E. "Arcjet plume studies using molecular beam mass spectrometry." Paper IEPC 93-132, 23rd International Electric Propulsion Conference. September 1993.
- Rahn L.A., R.L. Farrow, and G.J. Rosasco. "Measurement of the self-broadening of the H<sub>2</sub> Q(0-5) Raman transitions from 295 K to 1000 K." *Physical Review A*, **V 43**, N 11, P 6075-6088, 1991.
- Storm P.V. and M.A. Cappelli. Private communication, 1994.
- Veirs D.K. and G.M. Rosenblatt. "Raman line positions in molecular hydrogen: H<sub>2</sub>, HD, HT, D<sub>2</sub>, DT and T<sub>2</sub>." *Journal of Molecular Spectroscopy*, **V 121**, P 401-419, 1987.
- Weber, A. "High resolution Raman studies of gases." *The Raman Effect: Vol. 2*, edited by A. Anderson. Marcel Dekker, New York, 1973.
- Wolniewicz, L. "The  $X^1\Sigma_g^+$  state vibration-rotational energies of the H<sub>2</sub>, HD, and D<sub>2</sub> molecules." *Journal of Chemical Physics*, **V 78**, P 6173-6181, 1983.



AIAA 95-1957

**Spectral Imaging of the Arcjet  
Electrode Region**

D. Berns, P. V. Storm, M. A. Cappelli

*High Temperature Gasdynamics Laboratory  
Department of Mechanical Engineering  
Stanford University  
Stanford California*

**26th AIAA Plasmadynamics and Lasers  
Conference  
June 19-22, 1995/San Diego, CA**

# Spectral Imaging of the Arcjet Electrode Region

D.H.Berns\*, P.V.Storm†, and M.A. Cappelli‡

*High Temperature Gasdynamics Laboratory  
Department of Mechanical Engineering  
Stanford University*

## Abstract

Arc-electrode interaction is the main determinate of arcjet lifetime and one of the key determinates of performance. The position of the arc and the geometry of the arc attachment at both the cathode and anode govern the electrode material temperature profiles and power transfer efficiency to the propellant. The electrode temperature profiles control thruster lifetime due to material loss and deformation. The energy transfer from the arc to the propellant determines the performance potential of the arcjet. Therefore, knowledge of the physical nature of the arcjet electrode region is quite important for prediction of arcjet lifetime and performance. These concerns are important for arcjet use in satellite propulsion as well as their use as plasma sources for materials processing. The development of a non-intrusive in-situ measurement technique for on-axis spectral imaging of the electrode region of arcjets is presented herein. A large field of view and high spatial resolution are achieved. This technique allows measurement of both cathode and anode temperatures, cathode spot size, and may provide anode attachment geometry determination in certain cases.

## Introduction

The performance of arcjet thrusters as plasma sources for materials processing and their performance as electric thrusters for satellite propulsion depends on several key factors, of which electrode erosion and arc-electrode interaction are important.

Arcjet thruster use has increased over the past five years due to improvements in design and testing. The present use of arcjets for satellite propulsion has expanded the operating realm of these devices and has increased the desire for further understanding of the electrode erosion processes and plasma-electrode interaction. Measurement of electrode temperatures and arc attachment is difficult due to the harsh thermal and chemical environment in these regions. Previous studies have been conducted where various in-situ measurements were obtained for arc attachment and cathode temperatures. Segmented anodes were used to measure arc anode-attachment for different types of arcjet geometries [1-4]. In these studies information was obtained showing that the arc anode-attachment can either be

diffuse when the attachment is downstream of the nozzle throat in a low pressure region, or the arc attachment can be a constricted-spot attachment when the attachment is upstream of the nozzle throat in the high pressure region. However, questions remain as to the disruption of the arc caused by anode segmentation. Static pressures have also been measured for several different arcjet geometries [5-7]. Imaging of the electrode region of an exposed cathode plasma device similar to an arcjet has been performed on-axis and normal to the flow direction [8]. This study was at higher powers and with larger electrode geometry's than normally used with state-of-the-art arcjets. Axial emission measurements have also been presented for both low and medium power arcjets [9-12]. From these measurements various parameters were calculated including cathode temperature and electron number densities within the arcjet.

The purpose of the work presented herein was to develop a non-intrusive in-situ measurement technique for on-axis spectral imaging of the electrode region of a conventional arcjet. This technique has several advantages over previous measurement techniques. It provides a large field of view and high spatial resolution over the entire electrode region. The cathode and most of the

---

\* Research Assistant

† Research Assistant, Member AIAA

‡ Associate Professor, Member AIAA

anode can be viewed simultaneously. This technique allows measurement of both cathode and anode temperatures, and cathode spot size. This measurement technique is flexible and can be used with any size of arcjet or arcjet-type of device. This method allows the measurement of the anode throat temperature which has not been done with axial emission measurements. The anode throat size can also be inferred from the images. This allows a monitoring technique for throat closure, which can be an operating limitation in the smaller geometry, higher specific power arcjets of the present.

The method presented here is similar to experiments performed on higher power arcjets which helped to illustrate the effectiveness of regenerative heating in arcjet nozzles [13].

### Experimental Setup

The experimental setup is shown in Figure 1. The measurements were performed in 1.09m x 0.56 m diameter stainless steel vacuum chamber maintained at a background pressure of 0.4 Torr by mechanical roughing pumps backed by 1250 cfm blowers. The arcjet observed was a typical NASA Lewis modular arcjet design used and described previously [9-11]. The arcjet nozzle had a throat diameter of 0.635 mm with a 20 degree half angle divergence section leading to an exit diameter of 9.5 mm (225 area ratio), see Figure 2. The arcjet cathode was machined from a 1/8" diameter thoriated tungsten rod with a conical tip at a 30 degree half angle. The cathode was set approximately 0.45 mm from the anode/nozzle constrictor.

A high-resolution (12  $\mu\text{m}$  per pixel - 384 x 578 pixel area) CCD camera coupled with a tele-microscope was used for these measurements. Optical access to the arcjet was acquired through a 3" window downstream of the arcjet exit plane in the vacuum facility end flange. The end-on view of the arcjet provided optical access to the cathode tip and the diverging side of the anode/nozzle. The CCD camera and the tele-microscope were the major components of this system. The tele-microscope is a Questar Corporation, Model DR1 magnifying device. The device has a focal range of 36" to 96" with magnification of 17x (at 36") and 7x (at 96"). The advantage of this device for this application was its large field width, 10mm (at 36") and 23mm (at 96"). With other lenses and attachments the magnification could be increased. The CCD camera used is a Model # TE/CCD-576/UV, temperature controlled, Princeton

Instruments Inc. design. The camera has 14 bit A/D conversion, and exposure time range of 5ms-23 hours, a readout rate with 100kHz capability, and a shutter time of 5-6ms. Based on the knowledge of the spectrum, see Figure 3, a 700nm, 10 nm bandwidth, and an 810nm, 10 nm bandwidth interference filter, were chosen such that the cathode emission could be isolated from the hydrogen lines and the continuum emission due to free electrons in the plasma. These interference filters only pass radiation within the wavelength window of the filter.

Light emitted from the arcjet was collected by the tele-microscope through a series of redirecting mirrors. The tele-microscope was adjusted such that the focal plane was at the cathode-anode throat region of the arcjet. The light exiting the tele-microscope was then focused onto the photo-sensitive array in the CCD camera. For a given arcjet operating level, the appropriate exposure time (controlled by the camera shutter speed) was chosen such that the array was not saturated but a significant signal was obtained. The image was converted to a set of digital signals (one value for each pixel of the array) within the detector/controller and the signals were then stored on a P.C. for post-processing. Images were acquired for several specific power levels (input power/propellant flow rate). Intensity calibration was performed with a tungsten filament lamp, placed at the position of the arcjet, whose temperature was determined by a single color Minolta Cyclops 152 optical pyrometer (iterating on emissivity).

It was determined that two separate images were required in order to gain information about both the cathode and anode temperatures. The dynamic range of the camera limited the overall temperature range which could be measured in a given image. The first set of images taken were to capture the phenomenon occurring at the cathode. These images do not provide much useful information about the anode beyond radii of about 2 mm from the centerline. This data was used to calculate all of the cathode properties presented in this paper. Another set of data were then taken where both the cathode and anode were captured. At each operating level, the cathode shutter speed was adjusted so that the radiation emitting from the cathode tip could be captured without saturating the CCD array. Directly following this captured image, the camera exposure time was increased so that a large enough signal could be obtained from the radiation emitting from the

anode, while the cathode region in the image was saturated. Only 3 arcjet operating levels were investigated with this second method and the data presented in this paper pertaining to these images is used to provide information about the anode.

### Results

In order to obtain in-situ images of the cathode and anode surfaces it is necessary to utilize a narrow wavelength region which is minimally obstructed by plasma emission. Axial emission measurements previously performed on the same arcjet have revealed that continuum (bremsstrahlung) and hydrogen emission dominate most of the visible spectrum, with the exception being at long wavelengths. This observation is shown in Figure 3, where the axial emission along the arcjet centerline has been simulated. The solid curve is the spectral intensity resulting from thermal graybody emission of the cathode, assuming a cathode temperature of 4000 K and emissivity of 0.4. The other curves are the results of simulating the continuum and atomic hydrogen plasma emission. The simulation consists of an integration of the one-dimensional radiative transfer equation along the arcjet centerline, using the cathode graybody emission as the initial condition. Plasma properties along the arcjet centerline were taken from the arcjet code of Butler et al., [14] or calculated using a non-equilibrium collisional-radiative model. This simulation is described in detail in Ref. [9]. It is evident from Figure 3 that in the spectral region beyond the H-alpha line, the continuum emission is a small fraction of the cathode thermal emission. For this reason, two wavelengths were chosen in this region to examine the thermal emission from the electrodes, namely at 700 nm and 810 nm. Although longer wavelengths may further reduce the continuum emission, these were not selected due to loss of sensitivity of the CCD camera. Finally, thermal emission from the anode surface, which is at a much lower temperature than the on-axis cathode, is also expected to be unobstructed by plasma radiation. Far off-axis continuum radiation from the plasma will be negligible due to a drop in electron number density by several orders of magnitude.

The cathode images were obtained during arc operation by acquiring the continuous radiation emitted from the high temperature cathode tip. From these images, the cathode radial temperature distribution and the cathode spot size

could be measured. The cathode temperature was calculated from comparison of the cathode tip local radiation, again for various arcjet operation levels, with calibrated data obtained from a tungsten arc lamp. Given the temperature distribution, other properties can be determined such as the current density distribution along the cathode, the cathode spot size, and electric field in front of the cathode.

As stated above, the temperatures were obtained from calibration of a graybody source at known temperature. The CCD signal was converted to graybody intensity ( $W/m^3Sr$ ) using the calibration. This graybody intensity was then converted to a blackbody intensity using an emissivity of 0.4. The temperature was then calculated from the blackbody intensity using the equation which relates these two values, the Planck distribution.

$$I_{\lambda,b}(\lambda, T) = \frac{2hc_0^2}{\lambda^5 \left[ \exp\left(\frac{hc_0^2}{\lambda kT} - 1\right) \right]}$$

$$I_{\lambda,b}(\lambda, T) = \text{black body intensity (W/m}^3\text{Sr)}$$

$$h = \text{plank constant}$$

$$\lambda = \text{wavelength (m)}$$

$$c_0 = \text{speed of light}$$

Due to the lack of information on tungsten emissivity at temperatures higher than 2600 K, a constant of 0.4 was used. This assumption will introduce slight errors in the temperature calculation. If accurate emissivity data were available it would be possible to iterate on the temperature to get more precise values.

Figure 4 illustrates a typical temperature profile obtained from an image of the cathode at a specific power of 101.2 MJ/kg (9.76 Amps, 146.2 Volts, 14.106 mg/s  $H_2$  flow). The profile is a cross-section through the center of the nozzle. The centerline ( $r=0.0$ ) is a local center, determined by choosing the location of the peak temperature, and does not necessarily correspond to the exact geometric center of the cathode tip. This choice of  $r=0.0$  is the method used for all figures. The errors in temperature have been calculated to be approximately  $\pm 80$  K near the cathode (from centerline out to a radius of about 0.3 mm) and  $\pm 200$  K in the anode regions (beyond radius of 0.3 mm).

Figure 5 shows the calculation of current density for the temperature profile shown in Figure 4. Two current densities are shown in this figure,

the current density for a purely thermionic emitting cathode and the current density for a field-enhanced thermionically emitting cathode. Previous researchers, [15] have suggested that the cathodes in these types of devices emit electrons based on the principle of field-enhanced thermionic emission, where the electric field at the cathode surface acts to reduce the potential barrier at the surface. Field-enhanced thermionic emission is governed by the equation [16,17]:

$$J_{th} = AT_c \exp \left[ \frac{-e}{kT_c} \left( \phi_w - \left( \frac{eE}{4\pi\epsilon_0} \right)^{1/2} \right) \right]$$

$$A = \text{constant} = 1.202 \times 10^6 \text{ Am}^{-2} \text{ K}^{-2}$$

$$\phi_w = \text{work function} = 4.5 \text{ V (pure tungsten)}$$

$$E = \text{electric field}$$

Purely thermionic emission is governed by the same equation where  $E=0$ . The work function assumed for pure tungsten [18] was based on previous experiments which showed that the thorium in the cathode migrates out of the cathode tip and after short operation times the cathode tip is left with virtually no thorium [15]. This cathode had been run extensively, therefore, it was expected that the cathode tip was pure tungsten.

Based on the temperature distributions it is possible to calculate the current density at each radial location where there is a temperature value. The integral of current density times the differential area gives the total enclosed current. The electric field is then changed through iteration until the total enclosed current matches the measured current of the arcjet.

Figure 6 contains a summary of the data obtained from the set of cathode images. The peak temperatures range from 4000-4200 K. As stated above, the measurement error on these temperatures is  $\pm 80\text{K}$ . These values are above the melting point of tungsten which could be due to the fact that the cathode tip is expected to be molten and the molten pool could be at a superheated temperature. The electric fields calculated are on the order of  $3.0 \times 10^8 \text{ V/m}$ . The error on these values was calculated to be  $\pm 1.0 \times 10^8 \text{ V/m}$ . These electric fields are on the same order of magnitude as values previously reported, [10,15,19]. These fields can be shown to be order-of-magnitude-correct by looking at what cathode fall voltage arises with these field magnitudes. As an example, for the data presented in Figure 5, the electron number density in front of the cathode is expected to be approximately  $4.0 \times 10^{23} \text{ m}^{-3}$  [9]. If a plasma temperature of 10,000 K is assumed, the debye

length is approximately  $1.0 \mu\text{m}$ . Assuming the plasma sheath thickness in front of the cathode is on the order of the debye length, the cathode fall voltage would be on the order of 4 Volts. This agrees well with what is expected for high pressure discharges [20].

It should be noted that these field magnitudes should be considered as upper limits to what might actually exist. Fields in excess of  $10^7 \text{ V/m}$  start to distort the potential barrier at the electrode to the extent that electron tunneling through the barrier becomes significant [21]. This tunneling phenomenon, commonly referred to as field emission, becomes important when the thickness of the barrier approaches the wavelength of the free electrons in the tungsten electrode. In essence, the mechanism for current transfer from cathodes in these arcjets may be more complicated than previously thought [15,19].

The cathode spot diameters were inferred from the current density profiles. The radial distance at which the current density dropped to less than one percent of the centerline value was used as the cutoff for the spot diameter, or the diameter of the arc attachment at the cathode tip. These values have an accuracy of approximately  $\pm 100 \mu\text{m}$ .

The second set of data is presented in Figures 7 and 8. The temperature profile reflects a set of images centered around viewing the cathode and then the anode with sequential images at the same arcjet operating condition. The data images are then converted to intensities and then temperatures in the same manner as presented earlier in this paper for the first set of experiments. Figure 7 illustrates the calculated temperature profile across the entire electrode region for arcjet operation at 100.2 MJ/kg (9.92 Amps, 153.0 Volts, 15.15 mg/s  $\text{H}_2$  flow). The position of the anode throat is tagged in the figure to help illustrate how the temperature distributions relate to the geometry of the nozzle. The peak temperature is 3760 K which is about 200 degrees less than the previous data showed. It is suspected that this difference, along with the apparent increased width of the throat region, is caused by differences in the electrode geometries between the two sets of data. This newer data was taken after the arcjet had been run for a considerable amount of time since the first set of data. The nozzle throat did not appear to be circular any more. Disassembly of the arcjet, which had not been done by the time this paper was written, is required to determine this.

Figure 8 is a close-up view of the anode region of Figure 7. The edges of the nozzle inner diameter

(ID) and outer diameter (OD) are tagged to help show the location of the temperatures at the nozzle features. It can be seen that the anode temperature ranges from 1300-1400 K at the outer edges, to 2000 K near the nozzle throat. These values are probable upper limits to the temperature distribution since reflections to/from the interior surface of the nozzle are not taken into account in the calculation of relative intensity at a given radial location. Presently, a radiation reflectance model incorporating view factors is being formulated which will allow for this correction. This correction requires knowledge of the angular and temperature dependence of the spectral emissivity.

The anode temperature is slowly increasing in the outer regions of the nozzle as it is followed towards the throat. Closer to the throat, there is a rapid increase in temperature as the profile narrows and eventually becomes the cathode temperature profile. However, the radius at which the temperature starts to rapidly increase is larger than the throat radius. This may correspond to the anode arc attachment position. In Figure 8, this radius is approximately 0.3175 mm, which corresponds to an axial location of 3.918 mm downstream of the throat (1/3 of the distance from the throat to the nozzle exit).

Images were also obtained for the same hydrogen flowrate and currents of 8 Amps and 6 Amps. For these arcjet operation levels the temperature profiles have the same shape but show an overall decrease in anode temperatures.

### Conclusions

A method was presented which allows for non-intrusive temperature measurement of the entire electrode region of an arcjet thruster during operation. This method provides accurate wide-scale temperature measurement over a range of approximately 1000-4000 K

From the temperature profiles, other properties can be inferred such as electric field in front of the cathode, cathode arc-attachment spot size, and anode-attachment position. It was found that field-enhanced thermionic emission at the cathode tip is necessary to obtain the operating currents for these types of devices. The electric fields in front of the cathode calculated from these experiments range from  $3-4 \times 10^8$  V/m. These electric fields should be considered as upper limits due to the fact that at these high field magnitudes, field emission may be the mechanism for electron emission from the cathode surface. The

cathode peak temperatures ranged from 4000-4200 K which would suggest a superheated molten cathode tip. The cathode arc-attachment spot size was on the order of 600  $\mu\text{m}$  in diameter. Typical anode temperatures for these types of devices operating in the 100 MJ/kg specific power range are approximately 1300 K near the nozzle exit and increase to 2000 K near the nozzle throat.

### Acknowledgments

This work was supported in part by NASA Lewis Research Center, and the United States Air Force Office of Scientific Research.

### References

1. Curran, F.M., *et al.*, "Performance Characterization of a Segmented Anode Arcjet Thruster," AIAA 90-2582, (also NASA TM 103227), July 1990.
2. Curran, F.M. and Manzella, D.H., "The effect of Electrode Configuration on Arcjet Performance," NASA TM 102346, 1989.
3. Sankovic, J.M. and Berns, D.H., "Performance of a Low-Power Subsonic-Arc-Attachment Arcjet Thruster," AIAA 93-1898, June 1993.
4. Berns, D.H. and Sankovic, J.M., "Investigation of a Subsonic-Arc-Attachment Thruster Using Segmented Anodes," AIAA 93-1899, June 1993.
5. Berns, D.H., Heberlein, J., Zelesnik, D. and Sankovic, J.M., "Internal Nozzle Parameters of a Subsonic-Anode-Attachment Medium-Power Hydrogen Arcjet," AIAA 94-3248, June 1994.
6. Harris, W.J., *et al.*, "Static Pressure Measurements in a 30 kWe Class Arcjet," AIAA-91-2457, June 1991.
7. Talley, K., Elrod, W., and Curran, F.M., "Static Pressure Measurements of the NASA-Lewis 1.2 kW Arcjet," AIAA-92-3111, July 1992.
8. Zhou, X., Berns, D.H. and Heberlein, J., "Investigation of Arc-Cathode Interaction," AIAA 94-3129, June 1994.
9. Storm, P.V. and Cappelli, M.A., "Axial Emission Diagnostics of a Low Power Hydrogen Arcjet Thruster," IEPC-93-219, September 1993.

10. Storm, P.V. and Cappelli, M.A., "Axial Emission Measurements on a Medium-Power Hydrogen Arcjet Thruster," AIAA 94-2743, June 1994.
11. Storm, P.V. and Cappelli, M.A., "Interior Plasma Diagnostics of Arcjet Thrusters," AIAA-94-2654, June 1994.
12. Ishii, M. and Kuriki, K., "Optical and Analytical Studies of Arc Column in DC Arcjet," AIAA-87-1086, May 1987.
13. Hoskins, W.A., Butler, G.W., and Kull, A.E., "A Comparison of Regenerative and Conventional Arcjet Performance," AIAA 94-3124, June 1994.
14. Butler, G.W., Kull, A.E., and King, D.Q., "Numerical Simulations of Hydrogen Arcjet Performance," IEPC-93-249, September 1993.
15. Curran, F.M. and Haag, T.W., "Arcjet Cathode Phenomena," JANNAF Propulsion Meeting, 1989, (also NASA TM 102009).
16. Koester, J.K., "Analytical and Experimental Studies of Thermionically Emitting Electrodes in Contact with Dense Seeded Plasmas"; Ph.D. Thesis, C.I.T., 1970.
17. Cobine, J.D., Gaseous Conductors, Dover Publications, New York, 1958.
18. CRC Handbook of Chemistry and Physics, 73rd Ed., CRC Press Inc., Boca Raton, FL, 1992.
19. Bade, W.L. and Yos, J.M., "Theoretical and Experimental Investigation of Arc Plasma Generation Technology," AVCO Corp., 1962.
20. Finkelnburg, W. and Maecker, H., "Electric Arcs and Thermal Plasmas," Translation from Handbuch der Physik, Bd. 22, Gasentladungen II, 1956.
21. Bardeen, J. , "Flow of Electrons and Holes in Semiconductors," Handbook of Physics, sect. 8, ch.6, pg. 79, McGraw Hill, 1967.

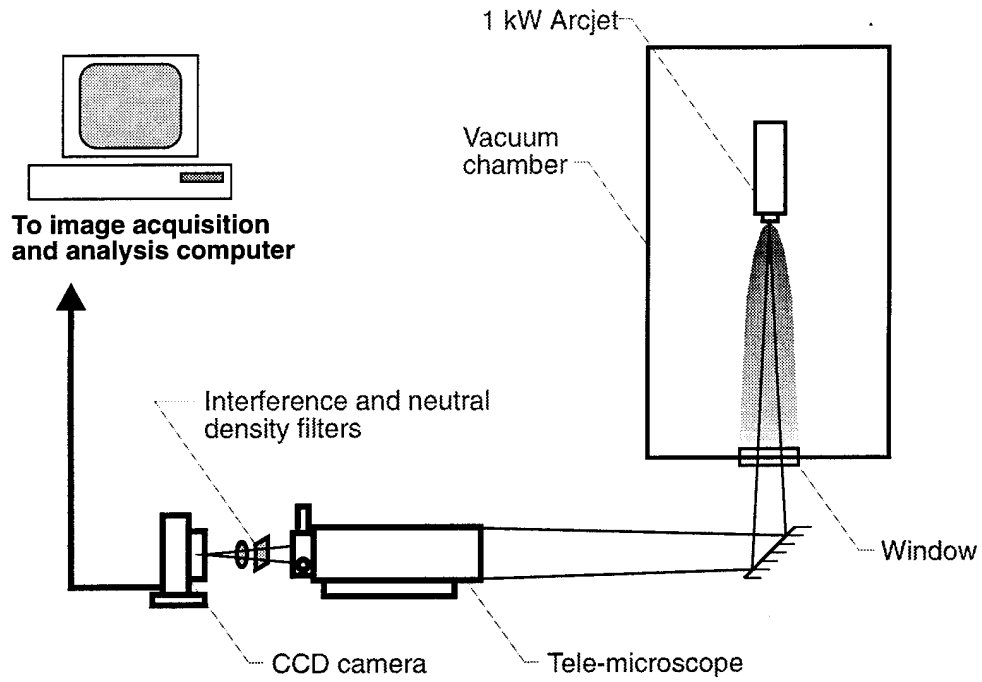


Figure 1. Experimental Setup

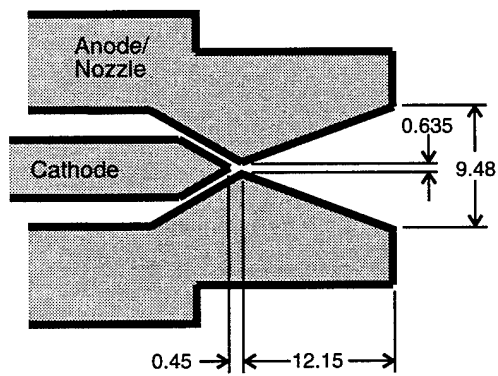


Figure 2. Arcjet Electrode Geometry

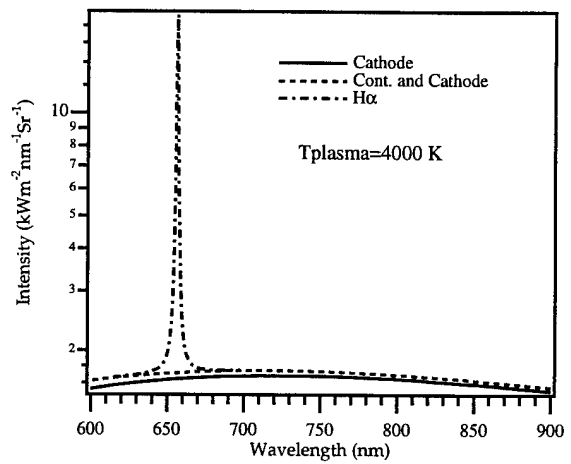


Figure 3. Calculated spectrum comparing cathode thermal emission, plasma continuum emission, and H $\alpha$  line in measurement region.

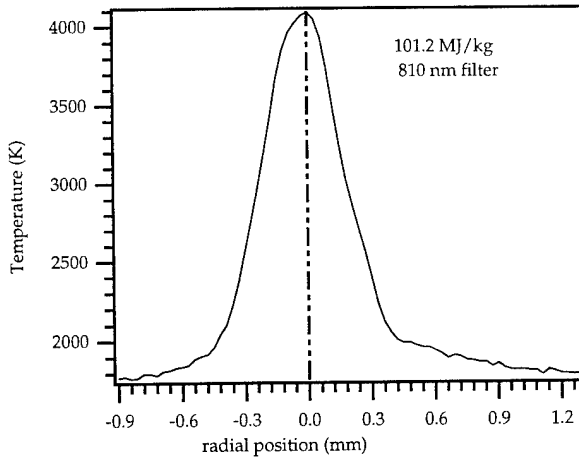


Figure 4. Image showing radial temperature distribution. Arcjet operated at 101.2 MJ/kg.

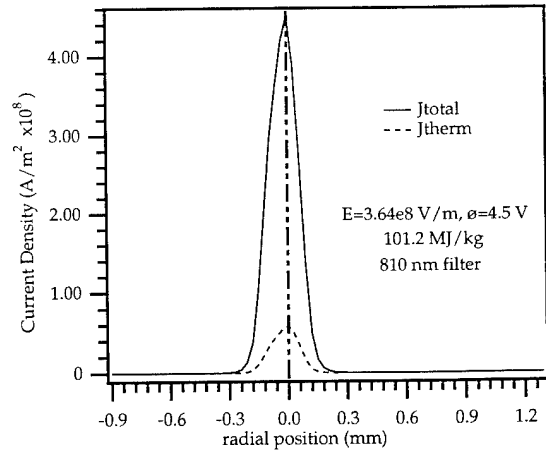


Figure 5. Current density profile obtained from temp. profile of Figure 4, showing results for pure thermionic emission and field-enhanced emission.

P/mdot (MJ/kg)	Cutoff Filter (nm)	Potential (Volts)	Current (Amps)	Therm. Current (Amps)	Electric Field (V/m)	Spot Diameter ( $\mu\text{m}$ )	Peak Temperature (K)
101.2	810	146.20	9.760	1.093	3.64E+08	510	4090
101.2	810	146.30	9.760	1.029	3.79E+08	570	4054
102.6	810	145.90	9.920	1.286	3.21E+08	540	4167
102.9	700	146.15	9.935	1.232	3.33E+08	570	4092
102.9	700	146.15	9.928	1.143	3.55E+08	540	4097
106.7	810	151.00	9.970	1.262	3.24E+08	600	4064
115.5	810	146.30	9.960	1.434	2.90E+08	600	4146
117.4	700	140.80	9.925	1.244	3.26E+08	600	4095
118.1	810	141.60	9.926	1.274	3.24E+08	570	4154
119.5	700	143.15	9.935	1.237	3.21E+08	630	4032
130.3	810	136.95	9.910	0.964	3.98E+08	600	4061
131.0	700	137.50	9.920	1.442	2.76E+08	660	4052
Avg=580							

\* Used 4.5V for work function of tungsten

Figure 6. Summary of data obtained from first set of experiments, targeting cathode region.

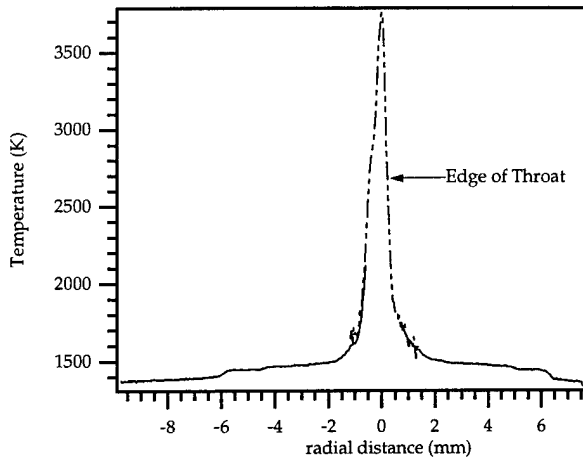


Figure 7. Temperature profile for entire electrode region. Arcjet operated at 100.2 MJ/kg

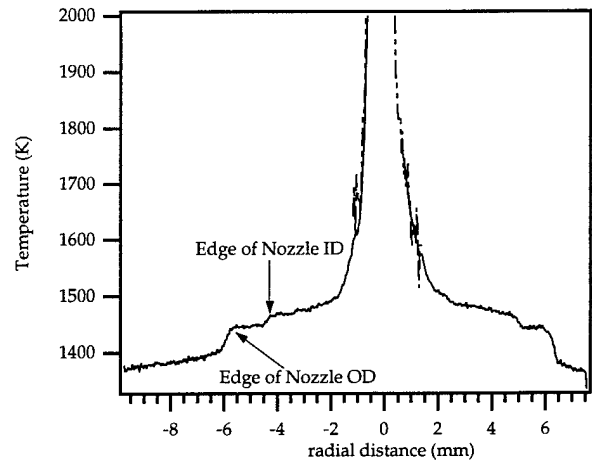


Figure 8. Anode region of temperature profile shown in Figure 7.



**AIAA-95-1960**

**High Spectral Resolution Emission Study Of A  
Low Power Hydrogen Arcjet Plume**

P. V. Storm and M. A. Cappelli

High Temperature Gasdynamics Laboratory  
Department of Mechanical Engineering  
Stanford University  
Stanford, California

**26th AIAA Plasmadynamics and Lasers  
Conference**

**June 19-22, 1995 / San Diego, CA**

# HIGH SPECTRAL RESOLUTION EMISSION STUDY OF A LOW POWER HYDROGEN ARCJET PLUME

P. Victor Storm\* and Mark A. Cappelli†

*High Temperature Gasdynamics Laboratory  
Department of Mechanical Engineering  
Stanford University  
Stanford, California, USA*

## Abstract

*An experimental investigation of the plasma plume of a 1 kW class radiatively-cooled hydrogen arcjet thruster is presented. The line-of-sight emission of the Balmer alpha line is measured at several radial positions using a high resolution monochromator and photon counting detection. The line-of-sight spectra are deconvolved radially into Voigt profiles, from which radial distributions of translational temperature and electron number density are determined. Absolute intensity calibration is also performed providing radial distributions of atomic hydrogen  $n=3$  excited state number density. Electron temperature profiles are calculated using a non-equilibrium collisional-radiative model. The hydrogen translation temperature displays good agreement with previous measurements. The electron number density profiles are consistent with Langmuir probe measurements made downstream of the exit plane. The results of the model indicate that the plasma at the nozzle exit plane is strongly recombining.*

## I. Introduction

Measurements of plasma plume properties, such as temperature, density and velocity of the various species, have recently been a very useful means of investigating arcjet performance and evaluating arcjet models. These measurements can be broadly divided into two categories: intrusive and non-intrusive. Intrusive techniques, such as mass spectrometry<sup>1</sup> and electrostatic probe measurements,<sup>2,4</sup> are relatively easy to perform and interpret, but have the obvious disadvantage that the detecting device may alter the plume characteristics and therefore the properties of the plume being measured. To avoid this apparent problem, non-intrusive techniques tend to be optical in nature: emission, absorption, fluorescence, Raman scattering, etc. In the strictest sense only radiative emission is truly non-intrusive; however, these other optical techniques are generally considered non-intrusive since their effect on the plasma is to locally redistribute the populations of atomic or molecular states, while having a negligible effect on the species overall density, momentum and kinetic energy.

Spatially resolved techniques, such as laser-induced fluorescence,<sup>5,6</sup> electron beam fluorescence<sup>7</sup> and Raman spectroscopy,<sup>8</sup> have been demonstrated very useful for measuring local plasma temperature, density and velocity. However, these techniques have the drawback that they are not simple to perform due to a number of possible reasons: low signal levels, poor signal-to-noise ratios, saturation effects, etc. On the other hand, line-of-sight optical techniques, such as absorption and emission, are considerably simpler to perform and can yield a wealth of information about the plasma properties. Absorption measurements performed to date in the plume of an arcjet include VUV absorption on atomic hydrogen and XUV absorption on  $\text{NH}_3$  and  $\text{H}_2$  for determining ground state number densities.<sup>9,10</sup> Several plume emission studies have been undertaken on a number of different propellants for the measurement of temperature, velocity and electron number density.<sup>11-16</sup>

Line-of-sight optical techniques offer the advantage of simplicity to perform but the disadvantage that the data must be deconvolved to produce true radial profiles. In previous optical studies of the arcjet plume the spectral data taken at different chords is Abel-inverted to obtain true radial

\* Research Assistant, Student Member AIAA

† Professor, Member AIAA

profiles. Although this analysis technique produces reasonably accurate results, except near the centerline where the inversion operation suffers a singularity, in the strictest sense it is not applicable to the arcjet plume due to the radial velocity component. This radial velocity produces Doppler shifts on the order of 0.01 nm at visible wavelengths. With a poor spectral resolution, say worse than 0.01 nm, the radial Doppler shift will not be resolvable and use of the Abel inversion may be justified. However, at higher spectral resolution the radial Doppler shift should be taken into account and the Abel inversion should be avoided to obtain the most accurate results. Failure to take the radial Doppler shift into account may lead to an over-estimation of the linewidths and therefore an over-prediction of the translational temperature and/or electron number density.

To replace the Abel inversion, a shell technique may be used to deconvolve the line-of-sight spectra into radial properties. This technique consists of segmenting the plume into annular shells, one shell for each radial position at which the emission spectrum was taken. Plume properties are assumed to be radially symmetric and uniform within each shell, and the plasma is assumed to be optically thin. The properties of each shell are found by taking into account the contribution to the line-of-sight emission spectra, including the radial velocity Doppler shift, from the surrounding shells. By separating the spectral contribution from each shell and deconvolving the instrument broadening, plasma properties such as atomic translational temperature, electron number density and atomic hydrogen excited state number density are determined as a function of radial position.

This paper describes high spectral-resolution emission studies of a 1 kW hydrogen arcjet plume. Emission spectra of the hydrogen Balmer alpha line were recorded 1 mm downstream of the arcjet exit plane at several transverse chords, using a 1 m monochromator with an 1800 groove/mm holographic grating. A spectral resolution of 0.006 nm was measured with an exit slit width of 10  $\mu\text{m}$ . This high resolution enabled very precise lineshape measurements, permitting the deconvolution of the Gaussian and Lorentzian linewidths and the subsequent determination of the atomic hydrogen translational temperature and electron number density. The arcjet operating conditions were chosen to facilitate a comparison between these measurements and previous temperature measurements in the arcjet plume.

## II. Experiment

The experimental setup is shown in Figure 1. The vacuum facility consisted of a 1.09 m x 0.56 m diameter stainless steel chamber maintained at a background pressure of 0.3 torr by two mechanical pumps and two 1250 CFM blowers. The arcjet was a 1 kW class radiatively-cooled laboratory type thruster designed and built by NASA Lewis Research Center. The tungsten nozzle consisted of a 0.64 mm diameter constrictor and a 20 degree half-angle diverging section to an exit plane area ratio of 225. The tip of the 2% thoriated tungsten cathode was approximately 0.69 mm upstream of the nozzle constrictor. Details of the vacuum facility and arcjet have been given elsewhere.<sup>5</sup>

The collection optics consisted of four lenses and two stops aligned normal to the arcjet axis. A 400 mm focal length (f.l.) achromat lens was used to collimate light from the arcjet plume through a 76 mm diameter window on the side of the vacuum chamber. The collimated beam was focused onto a 20  $\mu\text{m}$  field stop using a 100 mm f.l. achromat. With a transverse magnification of the collection optics of 0.25, the field stop defined the radial resolution at the arcjet exit plane of 80  $\mu\text{m}$ . The image at the field stop was re-collimated using a 280 mm f.l. plano-convex lens, and then focused onto the entrance slit of a Jarrell-Ash 1.0 m monochromator with a 600 mm f.l. achromat. Since the distance between the vacuum chamber and the monochromator was fixed by other constraints, the four lens system provided focusing and alignment flexibility. Each lens was mounted on translation stages for precise alignment of the optical system.

The monochromator contained a 100 mm wide holographic grating with 1800 grooves/mm, providing an ideal spectral resolution of 0.0036 nm. However, using 10  $\mu\text{m}$  slits, the measured resolution was 0.006 nm. The narrow entrance slit acted as the field stop in the horizontal direction, providing an axial resolution at the arcjet of 19  $\mu\text{m}$ , neglecting diffraction effects. With diffraction effects included the minimum axial resolution was approximately 25  $\mu\text{m}$ .

An aperture stop was placed in front of the first collection lens to stop down the collection volume, thereby increasing the depth of focus. The experiments were performed with an aperture of 28 mm giving a collection  $f/\#$  of 14.3 and a depth of focus of 0.32 mm. As a result of the relatively small aperture stop, field stop and monochromator slit widths, the signal level was reduced to the point where photon counting was chosen as the form of signal detection. Detection at the exit slit was

performed with a Hamamatsu R928 PMT at a cathode supply voltage of 1000 V. The output was amplified by a Hamamatsu C716-01 integral socket/preamplifier and routed to a Stanford Research Systems SR400 photon counter, gated continuously. To eliminate unwanted background light, an  $H_{\alpha}$  interference filter with a bandpass of 10 nm was placed at the entrance slit of the monochromator. The maximum signal at the  $H_{\alpha}$  linecenter was approximately  $4 \times 10^4$  photons per second. Signal noise consisted primarily of PMT dark noise, which was below 600 photons per second.

Line-of-sight emission scans of  $H_{\alpha}$  were performed 1.0 mm from the nozzle exit plane at six to twelve different chords for four different arcjet power levels from 0.8 kW to 1.4 kW. The mass flow rate of  $H_2$  was fixed at 13.3 mg/s. Absolute intensity calibration was performed using an 18 A tungsten filament lamp placed at the location of the arcjet. The temperature of the lamp was determined with a Minolta Cyclops 152 optical pyrometer.

### III. Analysis

Due to the radial velocity component, the Abel inversion is strictly not applicable to the arcjet plume. Instead a shell technique is used to deconvolve the line-of-sight spectra at the various chords into radial properties. This procedure, which can be understood with the aid of Figure 2, consists of segmenting the plume into annular shells, one shell for each radial position at which the emission spectrum was taken. All properties in the plume are assumed to be radially symmetric and uniform within each shell, and the plasma is assumed optically thin, which is a valid assumption for the non-resonant  $H_{\alpha}$  transition. Thus the line-of-sight emission spectrum of  $H_{\alpha}$  at a given chord will be a superposition of the  $H_{\alpha}$  spectra from the innermost shell at that chord and all outer-lying shells, with the relative intensities weighted by the optical path lengths, as determined by the radii of the shell boundaries. The spectral lineshape from each shell is taken to be a Voigt lineshape consisting of a Doppler-broadened Gaussian and a Stark-broadened Lorentzian. The spectra from the outer shells are appropriately Doppler shifted due to the component of the radial velocity in the direction of the emission. The radial velocity profile is obtained from the LIF velocity measurements of Liebeskind et al.<sup>5</sup> Thus, for example, the line-of-sight emission spectrum from the chord of observation shown in Figure 2 is assumed to consist of a large central unshifted Voigt function and four smaller Voigt functions, two shifted to shorter wavelengths and two shifted to longer wavelengths.

Assuming that the spectral emission lineshapes from the two outer shells are known, then by fitting the measured emission spectrum with the assumed superposition of five Voigt functions, the Voigt parameters of the inner shell can be determined. The translational temperature and electron number density in the inner shell is then determined from the Gaussian and Lorentzian components of the Voigt lineshape. Furthermore, the number density of the  $n=3$  excited state of atomic hydrogen can also be determined from the total integrated line intensity. In this manner, one first determines the properties in the outer shell and then moves inwards, adding two Voigt functions with each additional shell, until the properties of all shells are determined. Since the analysis starts with a single Voigt function fit at the outermost shell, errors will propagate towards the inner shells. Hence it is desirable to start with an emission spectra taken far away from the arcjet centerline where the signal is quite low.

Since this analysis method assumes radial symmetry, it is important to precisely locate the origin before applying the shell technique. This was achieved by taking line-of-sight emission spectra on both sides of the arcjet centerline. The integrated intensity of each spectrum was calculated and plotted as a function of measured position. This plot was found to be very symmetric and the line of symmetry was taken to be the centerline of the arcjet.

The emission spectral lineshape for each shell is assumed to be a Voigt function, which is the convolution of a Gaussian and Lorentzian lineshape,

$$\phi_V(\nu) = \phi_G(\nu) * \phi_L(\nu) \quad (1)$$

where

$$\phi_G(\nu) = \frac{2}{\Delta\nu_G} \left( \frac{\ln 2}{\pi} \right)^{1/2} \exp \left[ -4 \ln 2 \left( \frac{\nu - \nu_0}{\Delta\nu_G} \right)^2 \right] \quad (2)$$

and

$$\phi_L(\nu) = \frac{1}{2\pi} \left[ \frac{\Delta\nu_L}{(\nu - \nu_0)^2 + (\Delta\nu_L/2)^2} \right] \quad (3)$$

The translational temperature of the emitting species is related to the Gaussian width by the Doppler broadening formula

$$\Delta\nu_G = \nu_0 \left( \frac{8 \ln 2 kT}{m c^2} \right)^{1/2} \quad (4)$$

where  $m$  is the atomic mass. This equation is strictly only applicable to a single line. The  $H_\alpha$  transition contains fine-structure which has a significant effect on the Doppler broadening at temperatures below 10,000 K. Figure 3 shows the relationship between  $\Delta v_G$  and temperature for a single  $H_\alpha$  line (Eqn. 4) and for the  $H_\alpha$  transition with the fine-structure included. The inclusion of fine-structure is necessary to correctly determine the temperature at the arcjet exit plane. One drawback of this, however, is that at temperatures below 1000 K the actual Doppler-broadened  $H_\alpha$  lineshape is not well approximated by a single Gaussian function and this leads to large uncertainty in the measured translational temperature.

The electron number density is related to the Lorentzian width by Stark broadening. The most recent Stark broadening calculations which include dynamic ion effects<sup>17</sup> have shown that the hydrogen Stark broadening tables of Vidal, Cooper and Smith<sup>18</sup> are not accurate for  $H_\alpha$  at electron number densities below  $10^{17} \text{ cm}^{-3}$ . Therefore, instead of using the VCS tables, the electron number densities are determined from an empirical approximation to the recent dynamic ion Stark broadening calculations in the range of electron number densities from  $10^8 \text{ cm}^{-3}$  to  $3 \times 10^{13} \text{ cm}^{-3}$ . These calculations at low electron number density include the effects of fine structure, and agree extremely well with measurements made by saturation Doppler-free spectroscopy<sup>17</sup> in the range of  $n_e$  from  $5 \times 10^8 \text{ cm}^{-3}$  to  $10^{11} \text{ cm}^{-3}$ . The approximation is given (in SI units) by

$$\Delta\lambda_L = 3.4 \times 10^{-31} n_e^{1.014} \quad (5)$$

where  $\Delta\lambda_L$  is the FWHM in wavelength units. This approximation fits the dynamic ion calculations to within 10 percent over the range of electron number densities from  $10^{10} \text{ cm}^{-3}$  to  $3 \times 10^{13} \text{ cm}^{-3}$ . Although the Stark lineshape of  $H_\alpha$  is not truly Lorentzian, it is a reasonably good approximation and introduces errors of less than 10 percent in the electron density. This is not the case for the other Balmer lines, however, which is the primary reason for using  $H_\alpha$  in this study.

The atomic hydrogen  $n=3$  excited state number density is determined from the total integrated line intensity as follows. The spectral emission coefficient is given by

$$\epsilon_v = \frac{hv}{4\pi} n_3 A_{32} \phi(v) \quad (6)$$

where  $\phi(v)$  is the normalized lineshape function. Assuming the plasma to be optically thin, the total integrated line intensity from the optical path  $l$  is

$$\begin{aligned} I &= \int l \epsilon_v(v) dv \\ &\approx \frac{hv}{4\pi} l n_3 A_{32} \int \phi(v) dv \\ &= \frac{hv}{4\pi} l n_3 A_{32}. \end{aligned} \quad (7)$$

Through the tungsten filament lamp calibration, the photon flux to the PMT is related to the spectral intensity, which in turn is related to  $n_3$  using Eqn. 7.

A correct determination of the plasma properties from the  $H_\alpha$  lineshape must take into account the instrument broadening. The measured line-of-sight emission lineshape at the  $j^{\text{th}}$  chord can be written as

$$\phi(v)_{j, \text{ meas.}} = \phi(v)_{\text{instr.}} * \sum_{k \geq j} \phi(v)_{\text{shell } k} \quad (8)$$

where  $\phi(v)_{\text{instr.}}$  is the instrument broadened lineshape. The sum is taken over shell  $j$  and all outer shells, as shown in Fig. 2. The instrument broadening lineshape was measured using diffusely scattered light from a HeNe laser, and the slit function was assumed to be identical at the HeNe wavelength of 632.8 nm and the  $H_\alpha$  wavelength of 656.3 nm. To simplify the deconvolution of the instrument broadening from the measured spectra, the slit function was fit to a Voigt lineshape. The fit, which was surprisingly good, produced Gaussian and Lorentzian FWHMs of  $0.134 \text{ cm}^{-1}$  and  $0.022 \text{ cm}^{-1}$  respectively. Since all lineshapes are assumed to be Voigt functions, the total line-of-sight emission lineshape can be written as

$$\begin{aligned} \phi_{j, \text{ meas.}} &= \phi_{\text{instr.}} * \sum_{k \geq j} \phi_{k, \text{ actual}} \\ &= \sum_{k \geq j} (\phi_{\text{instr.}} * \phi_{k, \text{ actual}}) \\ &= \sum_{k \geq j} (\phi_G * \phi_L)_{\text{instr.}} * (\phi_G * \phi_L)_{k, \text{ actual}} \\ &= \sum_{k \geq j} (\phi_{G, \text{ instr.}} * \phi_{G, k \text{ actual}}) * (\phi_{L, \text{ instr.}} * \phi_{L, k \text{ actual}}) \\ &= \sum_{k \geq j} (\phi_{G, k \text{ apparent}} * \phi_{L, k \text{ apparent}}) \\ &= \sum_{k \geq j} \phi_{k, \text{ apparent}} \end{aligned} \quad (9)$$

where the  $v$ -dependence has been dropped from the lineshape functions for clarity. The slit function clearly broadens all contributing shells in the same manner. After the shell technique is applied to determine the apparent Voigt function from each shell, the effects of instrument broadening is removed from the FWHMs using

$$\Delta v_{G,k}^2 \text{ actual} = \Delta v_{G,k}^2 \text{ apparent} - \Delta v_{G,instr.}^2 \quad (10)$$

and

$$\Delta v_{L,k} \text{ actual} = \Delta v_{L,k} \text{ apparent} - \Delta v_{L,instr.} \quad (11)$$

which can easily be derived from the convolution of two Gaussians and two Lorentzians, respectively.

Having obtained electron number density and  $n=3$  excited state H-atom number density profiles, the electron temperature profile is determined using a non-equilibrium collisional-radiative model, applied at each radial position. Since this model has been described previously in great detail,<sup>19,20</sup> only a brief summary will be given here. The model consists of a rate equation for each excited state of hydrogen. The equation includes electron collisional excitation, de-excitation and ionization processes, three-body and radiative recombination, and spontaneous emission. The stationary state approximation is assumed for the excited states since the characteristic time scale for convection is small compared to those for collisional and radiative processes. For example, the rate equation for the  $n=3$  excited state can be written as

$$\begin{aligned} 0 = & n_e \sum_{j \neq 3} n_j K_{j3} - n_e n_3 \sum_{j \neq 3} K_{3j} \\ & - n_e n_3 K_{3c} + n_e^3 \beta_{c3}^{(3)} + n_e^2 \beta_{c3}^{(r)} \\ & + \sum_{j > 3} n_j \gamma_{j3} A_{j3} - n_3 \sum_{j < 3} \gamma_{3j} A_{3j} \end{aligned} \quad (12)$$

where  $\gamma$  is a radiation escape factor which can account for radiation trapping, and quasi-neutrality,  $n_{H^+} = n_e$ , is assumed. The appropriate number of levels to be included in the model is determined by Debye shielding of the hydrogen atom by the free electrons; however, as this would require typically 100 or more levels, it was decided to limit the number of levels to 50 to improve computational speed. This restriction has an insignificant effect on the results since the total population of the neglected states is small compared to the lower states. The rate equations for the excited states are coupled to the equation of state

$$p = \frac{1}{f_{\text{diss}}} \left( \sum_j n_j + n_{H^+} \right) kT + n_e kT_e \quad (13)$$

where the hydrogen dissociation fraction is given by

$$f_{\text{diss}} = \frac{\sum_j n_j + n_{H^+}}{\sum_j n_j + n_{H^+} + n_{H_2}} \quad (14)$$

The coupled equations are solved for  $n_j$  ( $j=1..50$ ) as a function of radial position, given the total pressure, dissociation fraction, electron number density, hydrogen translational temperature and electron temperature. As a first approximation, the exit plane pressure is taken to be a constant 2.25 torr, which corresponds approximately to the near-centerline exit plane pressure of the arcjet model of Butler et al.<sup>21</sup> The dissociation fraction is taken to be a constant 5%, consistent with the results of  $H_2$  Raman scattering at the nozzle exit.<sup>8</sup> The electron temperature is varied until the collisional-radiative model predicts the measured  $n=3$  number density. In this manner, exit plane electron temperature profiles are obtained.

The collisional-radiative model incorporates a radiation escape factor,  $\gamma_{ij}$ , into each spontaneous emission term. This factor is taken to be unity for all non-resonance transitions since the plasma is optically thin to this radiation. However, the ground state population of hydrogen is typically  $10^4$  or more times greater than the next most populated level; therefore, the plasma is less likely to be optically thin to resonance radiation. To determine the appropriate escape factor for resonance transitions, the optical thickness at line center can be estimated from the absorption coefficient

$$\begin{aligned} k_{1j}(\lambda_0) &= \frac{hc}{\lambda_0} n_1 B_{1j}^{\lambda} \phi_{1j}^{\lambda}(\lambda_0) \\ &= \frac{g_j}{g_1} \frac{\lambda_0^4}{8\pi c} n_1 A_{j1} \phi_{1j}^{\lambda}(\lambda_0) \\ &\approx \frac{g_j}{g_1} \frac{\lambda_0^4}{8\pi c} \frac{n_1 A_{j1}}{\Delta\lambda_{1j}} \end{aligned} \quad (16)$$

For example, on the  $3 \rightarrow 1$  transition,  $\lambda_0 \cong 102.6$  nm,  $A_{31} \cong 5.6 \times 10^7$  s<sup>-1</sup>, and  $\Delta\lambda_{13} \cong 4 \times 10^{-3}$  nm. With a typical ground state density of  $5 \times 10^{20}$  m<sup>-3</sup>, the mean optical path length is 1.0 mm. This is sufficiently small to consider the plasma optically thick to resonance radiation. Hence, the escape factors for resonance transitions are set to zero to account for resonance radiation trapping.

#### IV. Results

Figure 4 shows the arcjet current-voltage characteristics for the four operating conditions used in this study. These conditions were chosen to match exit plane LIF and Raman studies<sup>5,8</sup> on the same arcjet. A typical  $H_{\alpha}$  emission spectrum is shown in Fig. 5 along with the best fit, which for this spectrum consists of a sum of seven Voigt functions. Note that

the radial velocities produce Doppler shifts that are smaller than the broadening of the lines; hence, the seven Voigt profiles are closely spaced and appear as a single line. It would be incorrect, however, to assume that fitting the spectrum with a single Voigt function would produce accurate results.

Figures 6 to 8 show the radial profiles of hydrogen translational temperature, electron number density and hydrogen  $n=3$  number density determined using the shell technique and the analysis described above. To avoid a cluttered appearance, error bars have been omitted from the temperature and electron number density plots. The measured Voigt 'a' parameter is also shown, in Fig. 9, and appears to be relatively independent of the arcjet power but has a very distinctive radial dependence which peaks at about 1.0 mm from the arcjet centerline. This profile reflects the fact that the translational temperatures appear to peak on the centerline, whereas the electron number densities peak away from the centerline.

#### Atomic Hydrogen Translational Temperature

The translational temperatures shown in Fig. 6 display an approximately linearly decreasing trend with radius as well as with arcjet power. The 1.4 kW case is compared in Fig. 10 with LIF translational temperature<sup>5</sup> and Raman scattering  $H_2$  rotational temperature<sup>8</sup> measurements made on the same arcjet at the same operating condition. While the  $H_2$  rotational temperatures are lower than the H-atom translational temperatures due to non-equilibrium, the LIF and emission temperatures are expected to be identical. The discrepancy can be explained by the fact that the LIF results assumed that Stark broadening of the  $H_\alpha$  line was negligible at the nozzle exit. The present emission measurements have shown that this is not the case, as demonstrated by the Voigt 'a' parameter in Fig. 9. The LIF measurements were subsequently re-analyzed taking into account Stark broadening, and the results are shown in Fig. 11. Having made this correction, the agreement in the translational temperatures is very good, and the measurements are in reasonably good agreement with the arcjet model prediction of Butler et al.,<sup>21</sup> shown as the dashed line. This agreement is significant since the translational temperature is an important indicator of arcjet efficiency, and as such, it is often used as a basis for evaluating arcjet models.

#### Electron Number Density

The measured electron number densities of Fig. 7 display an increasing trend with arcjet power, which is not surprising since a higher degree of ionization with

specific power is expected. With radial position, the electron density first increases from the centerline to a peak which depends on arcjet power, and then drops exponentially to the edge of the plume. This exponential drop can be understood by the near linear decrease in temperature with radial position, resulting in an exponential decrease in ionization fraction. The reason for the central dip in electron number density is not known; however we speculate that it is a result of an increasing electron temperature and a relatively flat electron mole fraction, or partial pressure, profile near the centerline.

Few other measurements of electron number density versus radial position have been performed in a hydrogen arcjet plume. Hoskins et al. determined electron number density in the plume of a 10 kW hydrogen arcjet using a collisional-radiative model and measured line intensities of the first nine Balmer series lines.<sup>12</sup> More recently, Gallimore et al. used a Langmuir probe to measure electron density 20 mm downstream of the nozzle exit plane of the identical arcjet used in this study.<sup>4</sup> The results of these two studies are compared to the present results in Fig. 12. Electron number densities in the plume of the 10 kW arcjet are higher than the 1 kW arcjet due to the higher exit plane pressure and degree of ionization with arcjet power. The results of Gallimore et al. are lower than the present measurements by an order of magnitude due to the measurements being taken 20 mm downstream of the nozzle exit. The axial drop in density is in agreement with centerline electron number density measurements made by Zube and Messerschmid at 1.6 kW with simulated hydrazine and at 750 W with ammonia propellant.<sup>15</sup>

#### Hydrogen Excited State Number Density

The atomic hydrogen  $n=3$  excited state number density profiles, shown in Fig. 8, display the same trends as the electron number densities in Fig. 7. For all but the lowest power level, the densities dip at the arcjet centerline and drop off exponentially away from the centerline. Furthermore, at a given radial position the densities drop approximately exponentially with arcjet power. The similarity between the  $n=3$  excited state hydrogen number density and the electron number density is not surprising since in the recombining plasma there is a strong coupling between the hydrogen ions and excited state atoms. The  $n=3$  density is primarily a result of atoms cascading down from the higher lying excited states and the continuum ions.

## Electron Temperature

The electron temperatures at the arcjet exit plane were calculated using the non-equilibrium collisional-radiative model described above. The results, shown in Fig. 13, indicate that the electron temperature is approximately linearly dependent on arcjet power and radial position, in a manner similar to the hydrogen translational temperature. The former trend is consistent with the increased joule heating with arcjet specific power. The latter observation indicates that the characteristic time for electron energy transport by conduction and ambipolar diffusion is larger than the residence time of the electrons in the arcjet nozzle.

A comparison of the electron temperature between the present work and the Langmuir probe measurements 20 mm downstream of the nozzle exit by Gallimore et al.<sup>4</sup> is given in Fig. 14. While the electron temperatures at the exit plane are peaked at the arcjet centerline, the profiles downstream are flat and lower by nearly a factor of two. The flattening of the temperature profile is largely due to thermal conduction of the electron translational energy. The lower temperature of the downstream profile can be accounted for by gasdynamic expansion, radiative energy losses (bremsstrahlung radiation), and collisional energy transfer to the heavy species.

Two significant notes should be made at this point concerning the assumptions of non-equilibrium and optically thick resonance radiation. The non-equilibrium assumption was tested by performing an equilibrium calculation at the exit plane. Using the measured values of  $n_3$  and  $n_e$ , and assuming thermodynamic equilibrium, the required H-atom pressure at the nozzle exit is greater than  $10^{10}$  atmospheres. This unphysical result indicates that the  $n=3$  excited state is over-populated in comparison to thermodynamic equilibrium. Hence the plasma at the nozzle exit is clearly in a state of recombination.

Finally, to test the effect of the resonance radiation trapping, the electron temperatures were also calculated using the collisional-radiative model with optically thin resonance radiation. The resulting temperatures show the same power and radial dependence, but are typically twice the magnitude of those shown in Fig. 13. These results could be used as an upper limit on the electron temperature; however, Hoskins et al. have shown that model calculations assuming optically thick Lyman radiation match very well to measured populations for the lower excited states.<sup>12</sup> The correct electron temperatures are therefore more likely to be near those presented in Fig. 13.

## V. Summary and Conclusions

Emission spectra of the Balmer alpha transition of atomic hydrogen were recorded 1.0 mm downstream of the exit plane of a 1 kW hydrogen arcjet perpendicular to the arcjet axis. A spectral resolution of 0.006 nm was obtained using a 1.0 m monochromator with an 1800 groove/mm holographic grating and 10  $\mu\text{m}$  slits. The spectra, taken at several different chords, were deconvolved using a shell technique. By avoiding the Abel inversion, the Doppler shift due to the radial velocities could be accounted for in the analysis. Assuming an optically thin plasma, an apparent Voigt lineshape function was found for the  $H_\alpha$  emission from each shell. The instrument broadening was deconvolved from these apparent lineshapes to produce actual lineshapes which were characteristic of the plasma properties at the radii of the shells. Radial profiles of atomic hydrogen translational temperature and electron number density were determined from the Gaussian and Lorentzian component widths of the Voigt lineshapes. Furthermore, using a tungsten filament lamp absolute intensity calibration, the integrated line intensities were related to the  $n=3$  excited state number density of atomic hydrogen.

Radial profiles of translational temperature, electron number density and  $n=3$  excited state hydrogen number density were obtained at four arcjet power levels and compared to previously obtained measurements and modeling results. The translational temperatures display a roughly linear decrease with radial position and arcjet power. The temperature profile at 1.4 kW is in excellent agreement with the temperature obtained by LIF on the same arcjet after a Stark broadening correction is taken into account.

The electron and hydrogen excited state number density profiles display a central dip and exponential decrease with both radial position and arcjet power. There have been few direct measurements of electron number density in the near plume of a hydrogen arcjet. However, the measured densities are approximately an order of magnitude greater than those 20 mm downstream of the nozzle exit as measured using a Langmuir probe, and this axial dependence is in agreement with emission measurements performed on ammonia and simulated hydrazine arcjets.

Electron temperature profiles were determined from the measured plasma properties using a 50-level non-equilibrium collisional-radiative model, coupled to the equation of state. The resulting temperatures are linearly dependent on both radial position and

arcjet power, consistent with the measured hydrogen translational temperature at the arcjet exit plane.

### Acknowledgments

This work was supported in part by the Air Force Office of Scientific Research under grant No. F49620-92-J-0449 with M. Birkan as monitor. Partial support was provided by Olin Aerospace Company. Special acknowledgment is also given to NASA Lewis Research Center for supplying the arcjet thruster and power supply.

### References

1. J.E. Pollard; "Arcjet Plume Studies using Molecular Beam Mass Spectrometry"; Aerospace Corp. Report ATR-93(8344)-5, October 1993.
2. L.M. Carney and T.G. Keith; "Langmuir Probe Measurements of an Arcjet Exhaust"; *J. Propulsion* 5, no. 3, 287 (1989).
3. H.A. Habiger, M. Auweter-Kurtz and H.L. Kurtz; "Electrostatic Probes for the Investigation of Arc Driven Electric Propulsion Devices"; IEPC-93-124; 23rd AIAA/AIDAA/DGLR/JSASS International Electric Propulsion Conference, September 1993.
4. A.D. Gallimore, S.W. Kim, J.E. Foster, L.B. King, F.S. Gulczinski; "Near and Far-field Plume Studies of a 1 kW Arcjet"; AIAA-94-3137; 30th AIAA/ASME/SAE/ASEE Joint Propulsion Conference, June 1994.
5. J.G. Liebeskind, R.K. Hanson and M.A. Cappelli; "Laser-Induced Fluorescence Diagnostic for Temperature and Velocity Measurements in a Hydrogen Arcjet Plume"; *J. Applied Optics* 32, no. 30, 6117 (1993).
6. W.M. Ruyten, D. Burtner and D. Keefer; "Laser-Induced Fluorescence Measurements on the Plume of a 1 kW Arcjet Operated on Simulated Ammonia"; IEPC-93-127; 23rd AIAA/AIDAA/DGLR/JSASS International Electric Propulsion Conference, September 1993.
7. J.A. Pobst, J.H. Schilling, F.M. Lutfy, D.A. Erwin and R.A. Spores; "Arcjet Diagnostics using Current Modulation Velocimetry and Pulsed Electron Beam Fluorescence"; AIAA-94-2742; 30th AIAA/ASME/SAE/ASEE Joint Propulsion Conference, June 1994.
8. D.R. Beattie and M.A. Cappelli; "Raman Scattering Measurements of Molecular Hydrogen in an Arcjet Thruster Plume"; To be presented as paper AIAA-95-1956 at the 26th Plasmadynamics and Lasers Conference, June 1995.
9. D.H. Manzella and M.A. Cappelli; "Vacuum Ultraviolet Absorption in a Hydrogen Arcjet"; AIAA-92-3564; 28th AIAA/SAE/ASME/ASEE Joint Propulsion Conference, July 1992.
10. J.E. Pollard; "Arcjet Diagnostics by XUV Absorption Spectroscopy"; Aerospace Corp. Report ATR-92(8441)-5, February 1993.
11. D.H. Manzella, F.M. Curran, R.M. Myers and D.M. Zube; "Preliminary Plume Characteristics of an Arcjet Thruster"; AIAA-90-2645; 21st AIAA/DGLR/JSASS International Electric Propulsion Conference, July 1990.
12. W.A. Hoskins, A.E. Kull and G.W. Butler; "Measurement of Population and Temperature Profiles in an Arcjet Plume"; AIAA-92-3240; 28th AIAA/SAE/ASME/ASEE Joint Propulsion Conference, July 1992.
13. W.M. Ruyten, D. Burtner and D. Keefer; "Spectroscopic Investigation of a Low-Power Arcjet Plume"; AIAA-93-1790; 29th AIAA/SAE/ASME/ASEE Joint Propulsion Conference, June 1993.
14. D.M. Zube and M. Auweter-Kurtz; "Spectroscopic Arcjet Diagnostics Under Thermal Equilibrium and Nonequilibrium Conditions"; AIAA-93-1792; 29th AIAA/SAE/ASME/ASEE Joint Propulsion Conference, June 1993.
15. D.M. Zube and E.W. Messerschmid; "Spectroscopic Temperature and Density Measurements in a Low Power Arcjet Plume"; AIAA-94-2744; 30th AIAA/ASME/SAE/ASEE Joint Propulsion Conference, June 1994.
16. H.A. Habiger, M. Auweter-Kurtz and H.L. Kurtz; "Investigation of Arc Jet Plumes with Fabry-Perot Interferometry"; AIAA-94-3300; 30th AIAA/ASME/SAE/ASEE Joint Propulsion Conference, June 1994.
17. D.E. Kelleher, W.L. Wiese, V. Helbig, R.L. Greene and D.H. Oza; "Advances in Plasma Broadening of Atomic Hydrogen"; *Phys. Scripta*, T47, 75 (1993).
18. C.R. Vidal, J. Cooper and E.W. Smith; "Hydrogen Stark Broadening Tables"; *The Astrophysical Journal Supplement Series* 25 no. 214, 37 (1973).
19. P.V. Storm and M.A. Cappelli; "Axial Emission Diagnostics of a Low Power Hydrogen Arcjet Thruster"; IEPC-93-219; 23rd AIAA/AIDAA/DGLR/JSASS International Electric Propulsion Conference, September 1993.
20. P.V. Storm and M.A. Cappelli; "Axial Emission Measurements on a Medium Power Hydrogen Arcjet Thruster"; AIAA-94-2743; 30th AIAA/ASME/SAE/ASEE Joint Propulsion Conference, June 1994.
21. G.W. Butler, A.E. Kull and D.Q. King; "Single Fluid Simulations of Low Power Hydrogen Arcjets"; AIAA-94-2870; 30th AIAA/ASME/SAE/ASEE Joint Propulsion Conference, June 1994.

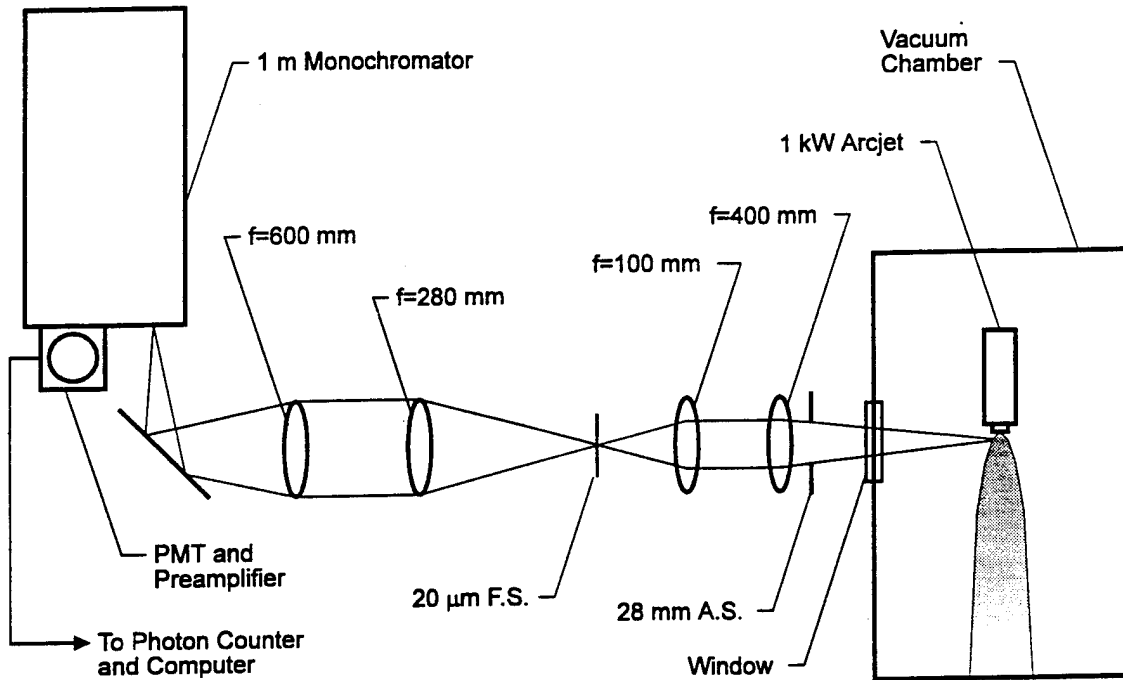


Figure 1. Schematic diagram of the radial emission experimental setup.

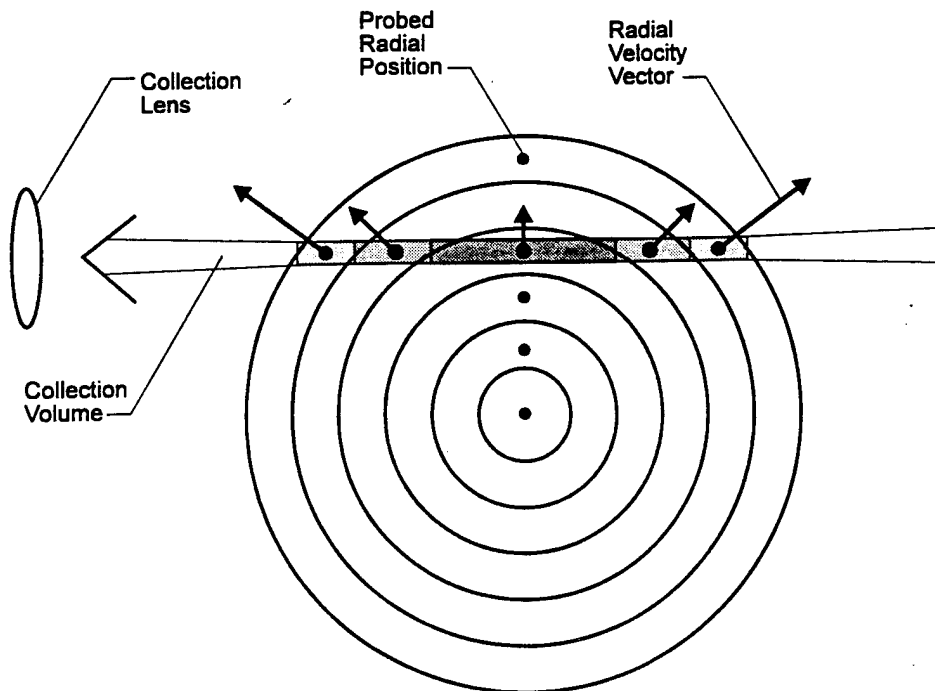


Figure 2. Schematic cross-section of plasma plume showing application of shell method for analysis of line-of-sight emission.

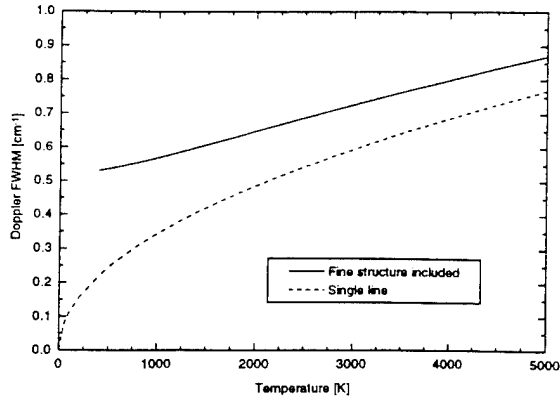


Figure 3. Doppler broadening of  $H_{\alpha}$  showing the increase in linewidth when fine structure is taken into account.

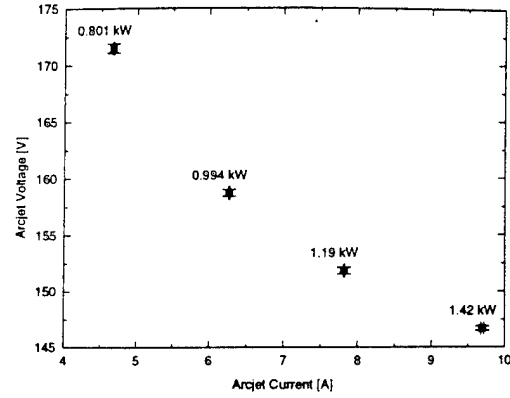


Figure 4. Arcjet current and voltage operating points. The mass flow rate was 13.3 mg/s.

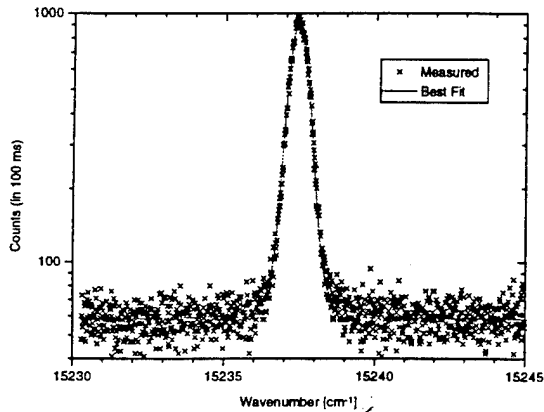


Figure 5. Typical radial emission spectrum of  $H_{\alpha}$  with best fit sum of seven Voigt functions.

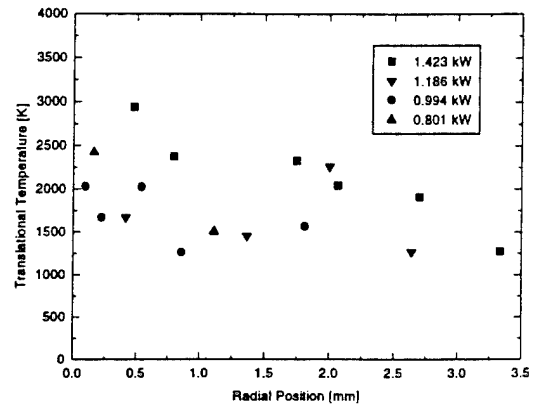


Figure 6. Atomic hydrogen translational temperature at arcjet exit plane. The typical error is approx.  $\pm 400$  K.

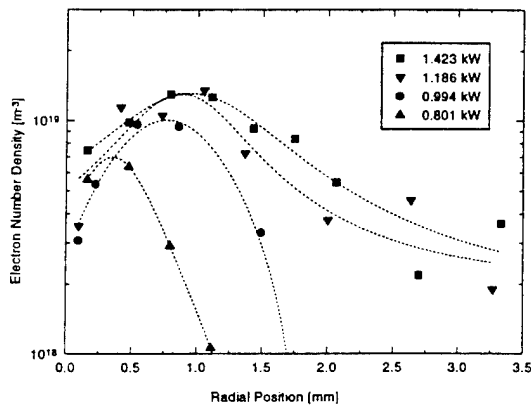


Figure 7. Electron number density at arcjet exit plane. The typical error is approximately  $\pm 20\%$ .

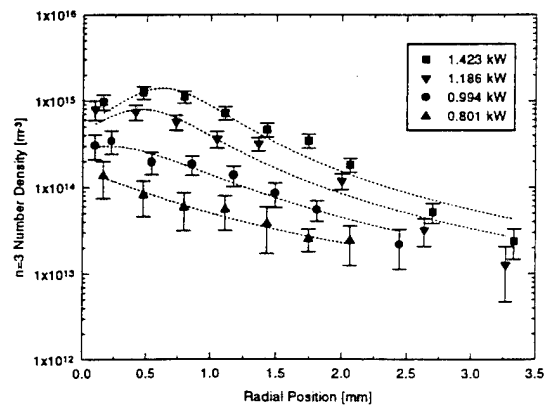


Figure 8. Atomic hydrogen  $n=3$  excited state number density at arcjet exit plane.

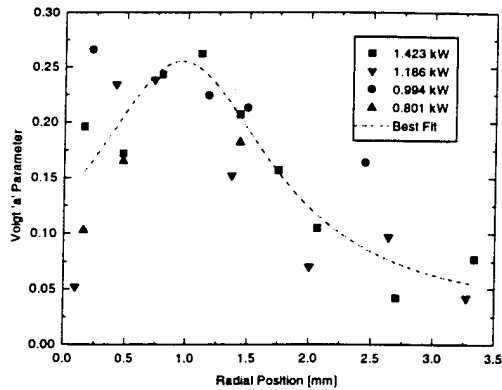


Figure 9. Voigt 'a' parameter at arcjet exit plane. The typical error is approximately  $\pm 25\%$ .

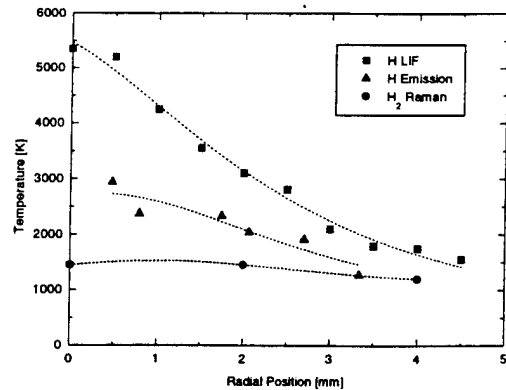


Figure 10. A comparison of exit plane temperatures at an arcjet power of approximately 1.4 kW.

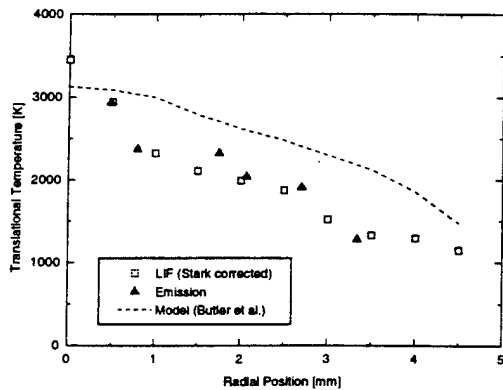


Figure 11. A comparison of measured and modeled exit plane hydrogen translational temperatures at a power level of approx. 1.4 kW. The LIF measurements from Ref. 5 have been corrected to take into account Stark broadening. The model results are from Ref. 21.

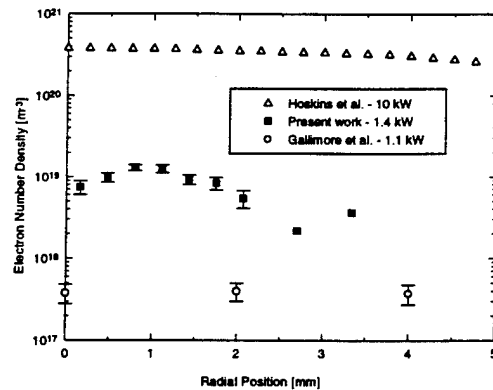


Figure 12. A comparison of measured electron number densities in the arcjet plume. The error bars are omitted for the data points at 2.7 and 3.3 mm because the errors are greater than 100 percent.

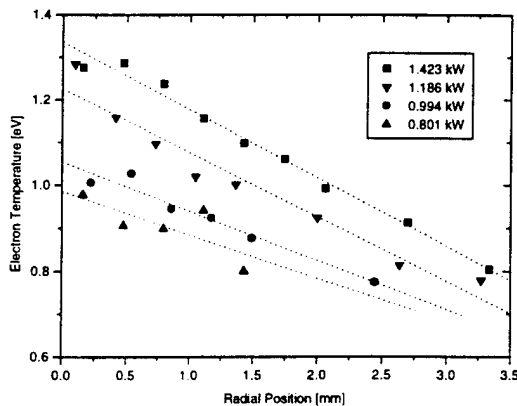


Figure 13. Electron temperature at arcjet exit plane calculated using a non-equilibrium collisional-radiative model.

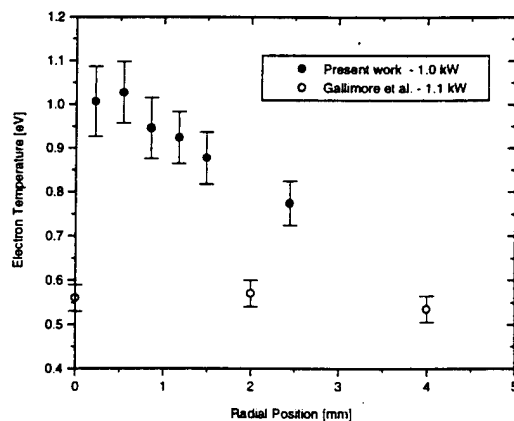


Figure 14. A comparison of electron temperatures in the arcjet plume. Those of Gallimore et al. (Ref. 4) were performed using a Langmuir probe 20 mm downstream of the exit plane.



**AIAA-95-1969**

**LIF Lineshape Analysis of the Xenon  
 $6s[3/2]_2^o - 6p[3/2]_2$  and  $6s[3/2]_1^o - 6p[1/2]_0$   
Transitions in a Glow Discharge**

**R.J. Cedolin, R.K. Hanson, and M.A. Cappelli**

**High Temperature Gasdynamics Laboratory  
Department of Mechanical Engineering  
Stanford University  
Stanford, California**

**26th AIAA Plasmadynamics and Lasers  
Conference  
June 19-22, 1995/San Diego, CA**

# LIF LINESHAPE ANALYSIS OF THE XENON $6s[3/2]_2^0 - 6p[3/2]_2$ AND $6s[3/2]_1^0 - 6p[1/2]_0$ TRANSITIONS IN A GLOW DISCHARGE

R.J. Cedolin\*, R.K. Hanson†, and M.A. Cappelli‡

High Temperature Gasdynamics Laboratory  
Department of Mechanical Engineering  
Stanford University  
Stanford, CA 94305-3032

## Abstract

*Laser induced fluorescence lineshape measurements of excited state neutral xenon have been used as diagnostic tools in a DC discharge. Using tunable semiconductor diode lasers, the spectral broadening of the  $6s[3/2]_1^0 - 6p[1/2]_0$  (828.0 nm) transition by the resonant interaction of its lower level with ground state xenon was investigated to compare to low pressure resonance broadening theory. Kinetic temperatures of xenon in the discharge were derived from the Doppler broadening of the same transition as well as from that of the  $6s[3/2]_2^0 - 6p[3/2]_2$  transition at 823.2 nm. The resonance broadening was found to be in near agreement with the theory at number densities below  $5 \times 10^{22} \text{m}^{-3}$  but appears to depart from the theory for higher number densities. This study is part of a program to develop laser-based diagnostic techniques for xenon plasmas appropriate for the application to thrusters which use xenon as a propellant. These electric propulsion thrusters are planned for use in satellite station-keeping and orbit transfer.*

## Introduction

We present an investigation into the resonance broadening of xenon using analyses of the spectral lineshapes of two excited state electronic transitions. Xenon's  $6s[3/2]_1^0$  level is resonantly coupled to the ground state causing resonance broadening to be an important broadening mechanism for the  $6s[3/2]_1^0 - 6p[1/2]_0$  transition. The nearby  $6s[3/2]_2^0$  level is metastable, so transitions from it, including  $6s[3/2]_2^0 - 6p[3/2]_2$ , are broadened mainly by the Doppler effect. A tunable AlGaAs semiconductor diode laser is used as the spectroscopic tool to probe a xenon plasma produced by a weak discharge. Transitions from the ground state of xenon, as in all inert gases, are inconvenient to probe as they are deep in the ultraviolet. Transitions from the lower lying excited levels, however, are accessible with diode lasers. Diode lasers are compact, inexpensive sources capable of providing narrow lasing linewidths ( $\sim 10 \text{MHz}^1$ ) which facilitates the resolution of the hyperfine-split lineshapes encountered in these xenon plasmas.

As a rare gas with low ionization potential and high molecular weight, xenon is the logical propellant in both Kaufmann-type ion thrusters<sup>2</sup> as well as for use in Hall accelerators such as the stationary plasma thruster<sup>3</sup> and

the anode layer thruster. Nonintrusive measurements of parameters in the exhausts of these satellite thrusters are needed to lend insight into the physical processes controlling their operation. Optical diagnostic techniques have been successfully developed and applied in the past to study various plasma properties in electric propulsion devices. LIF of singly ionized xenon in the plume of a stationary plasma thruster has been used to obtain ion velocities from the Doppler lineshift.<sup>4</sup> However, to determine further plasma parameters from lineshape analyses of xenon transitions, a thorough understanding of the underlying hyperfine splitting and of the dominant broadening mechanisms is required.<sup>5</sup>

The spectral lineshape of a transition between a species' energy levels is determined by the environment. Several different factors can affect this lineshape and give rise to a broadening and/or shift of the spectral line. If a broadening mechanism is well understood, accurate lineshape measurements can be used for quantitative determination of the environmental parameter responsible for the broadening. This is the case for Doppler broadening which can be used as a measure of the kinetic temperature. In general, spectral broadening caused by collisional interactions is less well understood.

Resonance broadening, where the species probed can efficiently exchange energy with interacting species, is a type of pressure broadening. Theoretical treatments of low pressure resonance broadening produce a fairly uncomplicated result. The linewidth is shown to be

\* Research Assistant

† Professor; Associate Fellow AIAA

‡ Associate Professor; Member AIAA

independent of temperature and linearly dependent on the species number density and the oscillator strength of the resonant transition.<sup>6</sup> The strong resonant transitions of the noble gases allow for the study of pure resonance broadening, uncomplicated by non-resonant collisional interactions. Emission studies of resonance broadening have been complicated by non-Gaussian velocity distributions of highly excited states in the direct-current (DC) discharge plasmas investigated.<sup>7,8</sup> The resonance state is lower lying than the states essentially studied by emission, though. Atoms in the resonance level of Ne have been shown to have a velocity distribution very close to that of the ground level<sup>9</sup> meaning absorption lineshapes derived from probing the resonance level are not distorted by these discharge effects. Using helium<sup>10</sup> and neon,<sup>11</sup> absorption experiments in a weak discharge have been used to verify the resonance broadening theory. But, little work has been done with the heavier inert gases.

Laser induced fluorescence (LIF) effectively measures the absorption lineshape by monitoring the fluorescence from a small region following absorption of a probe laser beam. The spectrally narrow laser is tuned across the absorption feature to allow for an accurate reconstruction of a spectral lineshape representative of the plasma conditions. The high spatial resolution of single-point laser induced fluorescence is essential in probing nonuniform plasma environments such as those encountered in electric propulsion devices.

### Theory

As a relatively heavy element, xenon's atomic spectrum is fairly complex. A partial energy level diagram for neutral xenon is shown in Figure 1.<sup>12</sup> The conventional Racah notation for the inert gases is used to denote the levels investigated. The two transitions probed in this work, the  $6s[3/2]_2^0 - 6p[3/2]_2$  ( $^3P_2 - ^1D_2$ ) transition at 823.2 nm, and the  $6s[3/2]_1^0 - 6p[1/2]_0$  ( $^3P_1 - ^3P_0$ ) transition at 828.0 nm, are indicated. These transitions arise from the first two excited states of xenon. The lowest excited state,  $6s[3/2]_2^0$ , is metastable; transitions to ground are optically forbidden by quantum mechanical selection rules. The neighboring  $6s[3/2]_1^0$  level, however, is coupled to the ground state by the resonant 147 nm transition. This is a configuration common to all inert gases.

This study into the resonance broadening of the Xe  $6s[3/2]_1^0 - 6p[1/2]_0$  transition is complicated by the larger number of hyperfine-split lines than present in the lighter inert gases. The levels shown on the energy level diagram in Figure 1 are the fine structure components due to electron spin-orbit interactions. Transitions between

these displayed energy levels are hyperfine-split into several components. The isotopic and nuclear spin effects contributing to this hyperfine splitting were described in a previous paper.<sup>5</sup> This splitting decomposes the  $6s[3/2]_2^0 - 6p[3/2]_2$  transition into twenty-one lines. A sample LIF trace of this transition is shown in Figure 2. The positions and relative intensities of the twenty-one hyperfine-split lines contributing to the six distinct LIF peaks are shown within the scan. The structure of the  $6s[3/2]_1^0 - 6p[1/2]_0$  transition is less complicated being comprised of only twelve lines. The positions and relative intensities of these twelve hyperfine-split lines are shown within a sample LIF lineshape in Figure 3. The separation of the hyperfine components for this transition is also much smaller.

The sample LIF traces are measures of the fluorescence excitation lineshape. The interaction of a laser beam with a plasma may involve the excitation of some atoms to a higher quantum state. Excitation is more likely to occur if the laser is tuned to the energy difference,  $h\nu_{12}$ , between this upper state and the original lower state. This interaction can be investigated by either monitoring the resulting reduction in laser power following propagation through the plasma (absorption process), or by monitoring the subsequent spontaneous emission of line radiation as the resulting excited state relaxes to a lower state (laser induced fluorescence process). Monitoring the fluorescence as the laser is tuned over the transition measures the fluorescence excitation lineshape and is favored for the higher spatial resolution that it affords in plasma parameter determination. The spatial resolution for LIF is determined by the intersection of the laser beam with the optical collection volume. Absorption offers only the measurement of properties that are averaged over the entire beam path through the plasma.

The measured fluorescence signal is given by:<sup>13</sup>

$$S_f = \eta_d \alpha_c h c \nu_{12} A N_2 \quad (1)$$

where  $\eta_d$  is the efficiency of the detection system,  $\alpha_c$  takes into account factors involving the collection system, and  $A$  is the Einstein coefficient for spontaneous emission of the detected radiation. For low laser intensities, a rate equation analysis shows that the upper level population  $N_2$  and thus the fluorescence signal is linear with  $I_\nu$  at steady state:

$$N_2 \propto I_\nu B_{12} \phi_\nu \quad (2)$$

Here  $I_\nu$  is the spectral irradiance (intensity) at frequency  $\nu$  and  $B_{12}$  is the Einstein stimulated absorption coefficient.  $\phi_\nu$  is the transition's spectral lineshape which accounts for the variation of the absorption or laser excitation with frequency. The spectral lineshape is determined by the plasma environment of the absorbing atoms, so an

accurate measurement of the lineshape function can lead to the determination of plasma parameters.

The measured fluorescence excitation lineshape is not necessarily equivalent to the spectral lineshape. The spectral lineshape is an intrinsic property of the absorbers whereas the fluorescence excitation lineshape is the variation in the detected fluorescence signal with frequency as the laser is tuned across the absorption line feature. If the laser excitation significantly perturbs the populations in the coupled levels, it is said to be saturating the transition and the fluorescence signal will be a nonlinear function of laser intensity. In cases where the laser intensity is much below the saturation level, and the laser linewidth is small compared to the measured linewidth, the fluorescence excitation lineshape will reflect the spectral absorption lineshape as given by equations 1 and 2.

Mechanisms that broaden the spectral lineshape can be classified as either homogeneous or inhomogeneous. Homogeneous mechanisms affect each atom equally. For a single transition, the atoms all have the same transition frequency  $\nu_{a0}$  and are thus indistinguishable. Inhomogeneous broadening, conversely, arises from a spread in  $\nu_0$ , the individual transition frequencies, about the linecenter frequency  $\nu_{a0}$ . Similar atoms are distinguished by these slightly different  $\nu_0$ 's. The overall response of an inhomogeneously broadened lineshape can be understood as the sum of the individual responses of a number of spectral packets.<sup>14</sup> A spectral packet is a group of atoms with a certain transition frequency  $\nu_0$ . The most common example of inhomogeneous broadening, and one pertinent to plasma studies, is Doppler broadening. Doppler broadening reflects the fact that the absorbing species is distributed in velocity according to the kinetic temperature,  $T_{kin}$ . The velocity distribution determines the spread of  $\nu_0$  about  $\nu_{a0}$  through the Doppler effect. When the absorbing species is characterized by a Maxwellian velocity distribution, Doppler broadening results in a Gaussian distribution of the  $\nu_0$  and hence a Gaussian spectral lineshape with Doppler halfwidth (FWHM):<sup>15</sup>

$$\Delta\nu_D = \nu_{a0} \sqrt{\frac{8kT_{kin} \ln 2}{Mc^2}} \quad (3)$$

Homogeneous broadening mechanisms do not distinguish between different atoms but broaden the response from all atoms equivalently. Collisional interactions between the absorbers and other particles in the plasma homogeneously broaden the spectral lineshape. These include interactions with charged particles (Stark broadening) and uncharged particles (van der Waals broadening) and result in a Lorentzian profile with halfwidth  $\Delta\nu_L$  within the framework of the Lorentz theory.<sup>16</sup> Natural or lifetime broadening also contributes

to  $\Delta\nu_L$ . Natural broadening is a consequence of Heisenberg's uncertainty principle.<sup>17</sup> The finite lifetimes of quantum states imply uncertainties in their energies. These uncertainties result in a homogeneous lineshape broadening for transitions between states.

Collisional or pressure broadening arises from the perturbation of the energy levels involved in the spectral transition by an interaction with a nearby particle. The broadening depends on the density of the perturbing species. When an excited atom can undergo a resonant energy exchange with a perturber, it is subject to resonance broadening. The resonant energy exchange can be understood, in connection with natural broadening, as causing a reduction in the lifetime of the excited state. Strong interactions with ground state atoms of the same kind can make this phenomenon significant. This is the case for the xenon  $6s[3/2]_1^0 - 6p[1/2]_0$  transition and corresponding transitions in all noble gases. Resonance broadening depends also on the efficiency or strength of the energy exchange through the oscillator strength  $f$ .

From statistical considerations, long range interactions dominate the broadening of spectral lines. The long-range interactions are described by an expansion of the potential  $V$  in negative powers of  $r$ ,  $C_n r^{-n}$ , with  $r$  the distance between the radiating atom and the perturber.<sup>18</sup> The important terms include the familiar  $r^{-2}$  linear Stark effect, the quadratic Stark effect with  $n=4$ , and the dipole-dipole  $n=6$  term for the van der Waals or dispersion forces between any two particles.

The resonance interaction ( $n=3$ ) is a dipole-dipole interaction of a longer range than the van der Waals interaction. The impact theory of line broadening produces a simple expression for the resonance halfwidth (FWHM):<sup>6</sup>

$$\Delta\bar{\nu}_{res} = k_{jj'} \cdot \frac{\pi/8}{(2\pi c)^2} \cdot \frac{e^2 f_{res}}{\epsilon_0 m_e \bar{\nu}_{res}} N \quad (4)$$

predicting a linear dependence on number density. Here,  $\bar{\nu}_{res}$  is the wavenumber of the resonant transition and  $f_{res}$  its absorption oscillator strength.  $k_{jj'}$  is a constant determined by the quantum numbers  $j$  and  $j'$  of the ground and resonance level. For all noble gases,  $j=0$  and  $j'=1$ . The accepted theoretical value is  $k_{01}=1.53$ .<sup>7</sup>

The oscillator strength for the resonant 147 nm  $5p^6(1S_0) - 6s[3/2]_1^0$  transition is  $f_{res}=0.260$ .<sup>19</sup> Equation 4 gives a resonance width of  $6.17 \times 10^{-21}$  MHz·m<sup>3</sup>·atom<sup>-1</sup> or 198 MHz·torr<sup>-1</sup> at 300 K. The total Lorentzian halfwidth for the  $6s[3/2]_1^0 - 6p[1/2]_0$  transition,  $\Delta\nu_L$ , should then be composed of this resonance broadening plus the natural broadening contribution. The Lorentzian halfwidth should approach the natural linewidth at zero density. The natural linewidth for the

$6s[3/2]_1^0 - 6p[1/2]_0$  transition including the upper level contribution<sup>20</sup> as well as that from the resonance level is 49 MHz.

The dispersion contribution ( $n=6$ ) to the Lorentzian broadening is neglected. The van der Waals broadening is of the same order across transitions between the same manifolds of fine structure levels.<sup>21</sup> The measured value<sup>22</sup> of  $24 \text{ MHz}\cdot\text{torr}^{-1}$  for the  $6s[3/2]_2^0 - 6p[3/2]_2$  transition then gives an idea of the relative importance of the van der Waals broadening as compared to the  $n=3$  resonance component of  $198 \text{ MHz}\cdot\text{torr}^{-1}$  for the  $6s[3/2]_1^0 - 6p[1/2]_0$  transition. Furthermore, it has been shown with impact theory that the dispersion contribution does not simply add to the resonance broadening.<sup>23</sup> For a resonant component more than twice as great as the dispersion contribution, the dispersion contribution can be neglected.

Local electric and magnetic fields can also homogeneously broaden and shift spectral lines through a further Stark and Zeeman splitting of the fine and hyperfine structure. In the results reported here, we do not include the effects of an applied electric field since the Stark splitting of the transitions studied is small in comparison to the broadening encountered. In the discharge studied, there are no applied magnetic fields.

If both Doppler broadening and homogeneous mechanisms are significant, each spectral packet is then taken as a group of atoms with a certain transition frequency within one homogeneous linewidth  $\Delta\nu_L$  of a specified  $\nu_0$ .<sup>24</sup> All atoms within a spectral packet will have the same homogeneous response. The resulting lineshape is a convolution of the Gaussian and Lorentzian lineshapes. This convolution can be expressed in terms of the Voigt function  $V(a,x)$  with the lineshape given by:<sup>25</sup>

$$\phi(\nu) = \frac{\sqrt{4 \ln 2 / \pi}}{\Delta\nu_D} V(a, x). \quad (5)$$

Here  $x$  is a normalized frequency (i.e.  $x=0$  at linecenter), and the Voigt 'a' parameter gives the relative importance of homogeneous versus inhomogeneous broadening:

$$a \equiv \sqrt{\ln 2} \frac{\Delta\nu_L}{\Delta\nu_D}. \quad (6)$$

For the two xenon transitions studied, each hyperfine-split line contributing to the lineshape has its own Voigt profile and the entire lineshape is composed of the sum of these twenty-one or twelve separate Voigt profiles.

### Experiment

The plasma source for this study is a simple hollow electrode DC discharge. It is a version of a commercially

available gas spectrum tube (Central Scientific Company) modified to have a 1 cm square cross-section and gas flow capability. The current is varied between 0.75 and 2.0 mA to provide adequate signal at higher pressures while avoiding electrode sputtering at lower pressures. Xenon is metered through the discharge at 0.5 to 1 sccm. A 590 k $\Omega$  ballast resistance is used. The pressure is measured just downstream of the discharge by a capacitance manometer baratron absolute pressure transducer (MKS Instruments) of 0.5% accuracy. During each scan the pressure is recorded and verified to be within  $\pm 0.5\%$  of the set pressure. A thermocouple bead of 0.6 mm diameter is positioned against the glass to monitor the temperature on the outer wall of the discharge.

The tunable light sources used are AlGaAs semiconductor diode lasers (Mitsubishi 5415N-01 for 823.2 nm 5415R-01 for 828.0 nm). The laser system (ILX Lightwave) involves a thermoelectrically cooled diode mount (LDM-4412), controlled by a temperature controller (LDT-5910B), and a current source (LDX-3620). The lasers are coarsely tuned to the transition of interest by adjusting the temperature. To tune over the transition with finer resolution, the injection current to the diode is modulated externally with a function generator. The transition is found with the help of a wavemeter (Burleigh WA-10) which measures the frequency of laser light.

A schematic of the experiment is shown in Figure 4. To prevent back reflections from affecting the laser operation, both beams first pass through an optical isolator. A portion of each beam is then split off to enable the frequency to be monitored. The remainder of the two beams are joined onto a coincident path through the discharge. A motorized rotating polarizer is used to keep the intensity far below the saturation intensity appropriate to the specific transition and discharge conditions. The saturation intensities were found to be about  $190 \mu\text{W}/\text{m}^2$  for 823.2 nm and about  $2.3 \text{ mW}/\text{m}^2$  for 828.0 nm at 1 torr. The laser intensity was kept at a level calculated to give only about a 1-2% reduction in the peak absorption from saturation.

The laser output is collimated by a lens in the diode mount into a 5x2 mm beam. The beam enters the discharge upright near the LIF collection side to minimize radiative trapping. A silicon photodiode monitors the beam intensity which passes through the discharge. The fluorescence from the beam intersecting the collection volume is collected at right angles to the incident beam. A half-meter monochromator (Jarrell-Ash) is used as a set spectral filter and passes light over the entire transition while the laser frequency is varied. The LIF is detected by a photomultiplier tube (Hamamatsu R928) operated at

1000 V. The PMT current is converted to a voltage across a 15 k $\Omega$  load resistor. Phase-sensitive detection is used to discriminate between the fluorescence and the background emission. A lock-in amplifier (SRS 850) is locked to the frequency of an optical chopper operating at 1 kHz. The low laser intensities used result in a low signal-to-background ratio requiring the use of a long time constant ( $\tau=0.3,3$  s) and scan times from 5 to 30 minutes. The absorption signal on the photodiode detector is also chopped so a second lock-in amplifier (SRS 530) is needed.

The laser frequency is monitored with the use of a fiber ring interferometer. This device is basically a four-port directional fiber coupler with one output fed back into an input. At resonant frequencies, the circulating intensity destructively interferes with the entering light, causing a minimum in the throughput.<sup>26</sup> The fiber ring interferometer was calibrated with a 2 GHz etalon and found to have a free spectral range of  $178.4 \pm 4$  MHz. The light is focused into the fiber with a laser-fiber coupler and the fiber output is focused onto a detector using a similar device.

It has been found that, for short scans (seconds) the laser tunes near linearly but for the longer LIF scans performed here, the tuning rate becomes nonlinear. This nonlinearity is likely caused by small temperature fluctuations. To accurately track the frequency, a device such as a fiber ring interferometer with a small free spectral range is necessary.

The 823.2 nm laser is tuned first and the resulting LIF lineshape, the absorption signal, and the interferometer output are recorded. The interferometer is then connected to the laser-fiber coupler for the second laser, the monochromator is dialed up to 828.0 nm, and the process is repeated for the second lineshape with the discharge continually operating at the same conditions. For the first two discharge conditions, 0.3 and 4.0 torr, the beams were first coupled into a single-mode 1x2 fiber splitter (Gould) with one portion going to the interferometer and the other portion to the discharge. The additional noise added by the splitter was unacceptable so the experiment was redesigned to that shown in Figure 4.

Sample data taken with the 823.2 nm laser is shown in Figure 5. The absorption trace is used to calculate the intensity incident on the collection volume to normalize the LIF data. The absorption never exceeded 5%. The interferometer data is then used to transform the LIF data into frequency space. The twenty-one (or twelve) theoretical lines are individually broadened and the resulting intensities added to construct an excitation spectrum similar to the LIF data. The data is introduced to a  $\chi^2$  minimization curve fitting procedure that optimizes  $T_{kin}$  and the Lorentzian halfwidth  $\Delta v_L$  to most closely

match the data. The line positions and relative intensities are fixed, with the overall amplitude, a linear baseline,  $T_{kin}$ , and  $\Delta v_L$  being the parameters to the fit. For the 828.0 nm data, the  $T_{kin}$  may be fixed to the value resulting from the 823.2 nm fit or to the thermocouple temperature or may remain as a parameter to the fit.

## Results

Figure 2 shows LIF results for a scan taken in a sealed xenon spectrum tube for the  $6s[3/2]_2^o - 6p[3/2]_2$  (823.2 nm) transition. The output of the curve fitting procedure is overlaid onto the data with the fit residual displayed below it. The Voigt 'a' parameter of 0.24 is representative of all discharge conditions investigated and illustrates the dominance of Doppler broadening for this transition. The resulting Doppler halfwidth implies a kinetic temperature of 325 K in the discharge.

Corresponding LIF results for the  $6s[3/2]_1^o - 6p[1/2]_0$  (828.0 nm) transition are shown in Figure 3.  $T_{kin}$  was fixed at 325 K from above for this fit. A much higher Voigt 'a' parameter here demonstrates the importance of resonance broadening for this transition. In Figure 6, LIF data taken at three different discharge pressures are displayed to illustrate the dependence of the resonance broadening on pressure.

Measurements of both lineshapes were taken at five different discharge conditions. At one condition, 2.7 torr, an extra measurement of the  $6s[3/2]_1^o - 6p[1/2]_0$  lineshape was made to give an idea of the scatter in consecutive measurements. The second scan was taken with a higher time constant and a correspondingly longer scan time.

Table 1 presents the results for the temperature from three different sources:  $\Delta v_D$  from the curve fits of the  $6s[3/2]_2^o - 6p[3/2]_2$  and  $6s[3/2]_1^o - 6p[1/2]_0$  lineshapes, and the thermocouple measurement of the wall temperature. Also given for each condition are the Voigt 'a' parameter result from the curve fit of the  $6s[3/2]_1^o - 6p[1/2]_0$  lineshape and rough indications of the signal-to-noise (S/N) ratios of the lock-in amplifier output for each scan.

The discrepancy in temperature is the largest uncertainty in determining the resonance broadening. The statistical errors in the fits are in general smaller than the size of the markers in Figure 7 which displays the results for  $\Delta v_L$  for the  $6s[3/2]_1^o - 6p[1/2]_0$  transition. With the ideal gas relation,  $T_{kin}$  must be used to convert the pressure to number density for this figure. For the 0.3, 0.9 and 1.5 torr measurements, the Voigt 'a' parameter for this transition is low enough for the lineshape to give a reasonable measure of  $T_{kin}$ . So for one set of points in

**Table 1.** Temperature measurements.

p (torr)	0.3	0.9	1.5	2.7	2.7	4.0
$T_{kin}(823)$ (K)	323	331	370	288		379
$T_{kin}(828)$	297	302	288	268	259	172
$T_{wall}$	291	294	298	299	297	296
$a_{828}$	0.2	0.38	0.42	0.96	0.99	1.1
S/N 823	100	50	12	50		25
S/N 828	200	100	20	36	100	50

Figure 7,  $T_{kin}$  was a parameter to the fit of the  $6s[3/2]_1^o - 6p[1/2]_0$  lineshape at 0.3, 0.9 and 1.5 torr. At 2.7 and 4.0 torr, the temperature in the fit was set at the wall temperature. For the second set of points,  $T_{kin}$  was set to the result from  $\Delta v_D$  of the  $6s[3/2]_2^o - 6p[3/2]_2$  lineshape for all discharge conditions. In each case, the temperature used in the fit is also used to convert the pressure to number density. The result from resonance broadening theory is included as the solid line intersecting the natural linewidth at zero density. A parabolic curve fit of the data, weighted according to the signal-to-noise ratio, is also included to give an idea of the trend.

### Discussion

From Figure 2 it is evident that the structure of the  $6s[3/2]_2^o - 6p[3/2]_2$  transition is well understood. The residuals are all within 1% of the peak height. This understanding translates into a very accurate modeling of the measured LIF lineshape. This is necessary since plasma parameter determination is very sensitive to the lineshape. The kinetic temperatures measured with this lineshape agree to within 10% with those using the  $6s[3/2]_1^o - 6p[1/2]_0$  transition and with the thermocouple measurement for the 0.3, 0.9 and 2.7 torr discharge operating conditions (Table 1). However they agree less well at the 1.5 and 4.0 torr conditions. At these conditions, the LIF signal was notably more noisy (see Table 1). The accuracy of the temperature measurement is seen to be very dependent on the quality of the LIF signal. The discharge power is greater at higher pressures to provide adequate signal so more discharge heating should be expected. But, considering that the wall temperature does not increase significantly and that the higher quality 2.7 torr trace agrees with the wall temperature, it is unlikely that the kinetic temperature of the xenon atoms in the discharge is as elevated as the  $6s[3/2]_2^o - 6p[3/2]_2$  lineshapes at 1.5 and 4.0 torr suggest.

The temperature resulting from the curve fitting procedure has been found to be very sensitive to small disagreements in the positions and relative heights of the three larger outlying peaks in the  $6s[3/2]_2^o - 6p[3/2]_2$  lineshape. These discrepancies cause the curve fitting procedure to incorrectly alter parameters in searching for the minimum of  $\chi^2$  (sum of residual points squared). To mitigate this effect, the relative positions of the major line making up each of these three outlying peaks is shifted in the fit procedure to match the data. It has been found that the line at  $0.054 \text{ cm}^{-1}$  generally needs to be shifted 0.5-1.5% outward; the line at  $-0.071 \text{ cm}^{-1}$ , 0.9-1.8% outward; and the line at  $-0.043 \text{ cm}^{-1}$ , 0.2-1% outward. The consistent component of these required shifts may be a result of a small error in the constants for the calculation of the hyperfine splitting, in the free spectral range of the interferometer, or a combination of these two effects.

The hyperfine line separation for the  $6s[3/2]_1^o - 6p[1/2]_0$  transition is less than the broadening circumventing the problems described in the previous paragraph. The confidence in the accurate modeling of the lineshape can be transferred over from the  $6s[3/2]_2^o - 6p[3/2]_2$  transition as well as being taken from the results in Figures 3 and 6. Figure 3 shows curve fit residuals of less than 1% again demonstrating the accurate modeling of the lineshape. The lineshape for 0.3 torr in Figure 6 reveals some of the underlying structure displaying the agreement with the hyperfine line positions. The lack of peak separation makes the curve fitting of the  $6s[3/2]_1^o - 6p[1/2]_0$  transition much less sensitive to small errors in the relative line positions and heights. This translates into excellent agreement of the kinetic temperature measurement from its Doppler halfwidth with the discharge wall temperature (Table 1). Where Doppler broadening is dominant, 'a' < 0.5, these two temperature measurements agree to within 5%. As the Voigt 'a' increases, signaling the growing predominance of resonance broadening, the merit of the temperature from the Doppler broadening decreases. This becomes evident for the 2.7 torr case and especially for the 4.0 torr case.

The results for the Lorentzian halfwidth in Figure 7 exhibit a departure from the resonance broadening theory. Taking the temperature measurement results into account, the higher quality traces (0.3, 0.9 and 2.7 torr) are probably conservatively correct to within 10% with the noisier conditions (1.5 and 4.0 torr) producing less accurate halfwidths. The relative difference on Figure 7 resulting from using alternate temperature measurements gives an idea of the quality of the signal. For the higher quality signals, using the alternate temperature measurement makes only a small difference in the

position of the data point. The large change in the result for the noisier lineshapes from using the temperature from the  $6s[3/2]_2^o - 6p[3/2]_2$  Doppler halfwidth is a manifestation of their poor quality. The agreement of the two consecutive measurements of the  $6s[3/2]_1^o - 6p[1/2]_0$  Lorentzian halfwidth at 2.7 torr demonstrate the reproducibility of the measurement if there is adequate signal.

At the lower number densities the Lorentzian broadening is in agreement with the theory within the uncertainties of the measurement. But, the data at higher densities indicate that the resonance broadening becomes nonlinear with measured halfwidths being less than that predicted by the theory. This trend is shown in Figure 7 by the dashed line.

Nonlinearities in measured resonance broadening have been previously reported. Lindsay et al. found that the resonance broadening in neon is linear up to densities of  $2 \times 10^{23} \text{ m}^{-3}$  but becomes nonlinear at higher densities in a manner similar to the xenon data presented here.<sup>11</sup> Lindsay et al. also report an indication of a nonlinearity for helium beginning at a higher number density than for neon.<sup>11,10</sup>

One of the explanations that Lindsay et al. propose for the nonlinearity is the breakdown of the validity of the impact approximation upon which the low pressure resonance broadening theory (Equation 4) relies. The impact approximation is often used at much higher pressures than encountered here for broadening from the van der Waals forces. However the resonance interaction is a much longer range interaction.

The impact approximation is valid when the collision duration is much smaller than the time between collisions or:<sup>6</sup>

$$\Delta v_L \ll N^{1/3} \bar{v} \quad (7)$$

with  $\bar{v} \propto M^{-0.5}$ . As the atomic mass increases, the impact approximation becomes less valid. This would suggest, as was observed, that the nonlinearity for neon would occur at lower number densities than for helium.<sup>11,10</sup> It would be expected that the approximation would break down at number densities a factor of  $\sqrt{M_{Xe}/M_{Ne}} = \sqrt{131 \text{amu}/20 \text{amu}} = 2.6$  lower than the breakdown point for neon, at about  $0.8 \times 10^{23} \text{ m}^{-3}$ . This is in rough agreement with the data in Figure 7. This suggests that the breakdown of the validity of the impact approximation is a reasonable explanation for the nonlinearities observed.

Another explanation Lindsay et al. propose is a non-Maxwellian velocity distribution for atoms in the resonance state: the state probed by LIF. This is not

apparent from the temperature results for this transition. With the exception of the 4.0 torr condition, the measured Doppler widths imply kinetic temperatures for atoms in the resonance state which agree well with the wall temperature. Furthermore, the curve fits of the  $6s[3/2]_1^o - 6p[1/2]_0$  transition result in Doppler widths lower than expected at the higher number densities. This should cause the resulting Lorentzian halfwidth to be slightly larger--not smaller--than in actuality. So a non-Maxwellian velocity distribution cannot explain the nonlinearities observed.

### Conclusions

The small data set taken for the resonance broadening of the xenon  $6s[3/2]_1^o - 6p[1/2]_0$  transition indicates a nonlinearity of the Lorentzian halfwidth at number densities greater than about  $0.5 \times 10^{23} \text{ m}^{-3}$ . This is in disagreement with the low pressure resonance broadening theory which is based upon the impact approximation. But, the nonlinearity is consistent with previous investigations into the resonance broadening of the lighter inert gases. The breakdown of the validity of the impact approximation is found to be a possible explanation for the observed nonlinearity. At lower number densities, the broadening here is found to be in agreement with the theory within the uncertainty of the experiment. To further test the low pressure resonance broadening theory, more data should be taken at number densities on the order of  $10^{22} \text{ m}^{-3}$ . The predominance of Doppler broadening at these densities would, however, affect these results.

The more complicated structures of the xenon lineshapes make linewidth measurements necessarily more difficult and less precise than for the lighter inert gases. An understanding of the underlying hyperfine splitting and the appropriate broadening mechanisms has been translated into an ability to accurately model the lineshapes. This has led to the determination of plasma parameters from the information contained within the complex lineshapes.

It is found that the accuracy with which the linewidths can be measured can be seriously compromised by an increased amount of noise in the data trace. The separation of the  $6s[3/2]_2^o - 6p[3/2]_2$  lineshape into distinct peaks makes it especially prone. But, for a high quality trace, this transition has been shown to produce kinetic temperature measurements with about a 10% accuracy.

Kinetic temperature measurements using the  $6s[3/2]_1^o - 6p[1/2]_0$  lineshape in the regime where Doppler broadening is predominant have been found to be more accurate. The lack of separation of the lineshape

into distinct peaks makes it less sensitive to small irregularities in the data. In electric propulsion devices, the kinetic temperatures are higher than those encountered in this study and the pressures are lower, making resonance broadening insignificant. Stark broadening may be more significant in these environments but both transitions will be similarly affected. This would make the  $6s[3/2]_1^0 - 6p[1/2]_0$  transition a more appropriate choice for use in measurements on electric propulsion devices.

### Acknowledgments

This work was supported by the United States Air Force Office of Scientific Research.

### References

- J.C. Camparo, "The Diode Laser in Atomic Physics," *Contemp. Phys.* **26**(5), 443 (1985).
- F.M. Curran, J.S. Sovey, and R.M. Myers, "Electric Propulsion: An Evolutionary Technology," *Acta Astronautica* **29**(9), 651 (1993).
- J.M. Sankovic, J.A. Hamley, and T.W. Haag, "Performance Evaluation of the Russian SPT-100 Thruster at NASA LeRC," IEPC-93-094, 23rd International Electric Propulsion Conference (Sept. 1993).
- D. Manzella, "Stationary Plasma Thruster Ion Velocity Distribution," AIAA-94-3141, 30th Joint Propulsion Conference (June 1994).
- R.J. Cedolin, R.K. Hanson, and M.A. Cappelli, "Semiconductor Laser Diagnostics for Xenon Plasmas," AIAA-94-2739, 30th Joint Propulsion Conference (June 1994).
- H.G. Kuhn and E.L. Lewis, "Resonance Broadening of Spectral Lines," *Polarisation, Matière et Rayonnement*, ed. La Société Française de Physique, (Paris: Presses Universitaires de France, 1969) 341.
- A.R. Malvern, A.C. Pinder, D.N. Stacey, and R.C. Thompson, "Self-broadening in singlet spectral lines of helium," *Proc. R. Soc. Lond. A* **371**, 259 (1980).
- A. Atiola, B.C. Gibson-Wilde, A.C. Lindsay, J.L. Nicol, and I.B. Whittingham, "Temperature dependence of self-broadening at low densities in singlet spectral lines of helium," *J. Phys. B* **21**, 249 (1988).
- P.E.G. Baird, K. Burnett, R. Damaschini, D.N. Stacey, and R.C. Thompson, "Resonance broadening in neon at low densities," *J. Phys. B* **12**, L143-6 (1979).
- A.C. Lindsay, J.L. Nicol, D.N. Stacey, and P.E.G. Baird, "Absorption measurements of resonance broadening in helium," *J. Phys. B* **22**, L303 (1989).
- A.C. Lindsay, J.L. Nicol, and D.N. Stacey, "Linear absorption measurements of pressure broadening in neon," *J. Phys. B* **24**, 4901 (1991).
- C.E. Moore, "Atomic Energy Levels," Vol. 3, National Bureau of Standards Circular 467 (Washington: 1958).
- R.P. Lucht, in *Laser Spectroscopy and its Applications*, ed. L.J. Radziemski et al. (New York: Marcel Dekker, 1987).
- A. Yariv, *Quantum Electronics*, 3rd ed. (New York: John Wiley and Sons, 1989).
- W. Demtröder, *Laser Spectroscopy* (New York: Springer-Verlag, 1981).
- A. Corney, *Atomic and Laser Spectroscopy* (New York: Oxford University Press, 1986) 242.
- S. Gasiorowicz, *Quantum Physics* (New York: John Wiley and Sons, 1974) 366.
- H.G. Kuhn, F.R.S., *Atomic Spectra* (New York: Academic Press, 1969).
- W.F. Chan, G. Cooper, X. Guo, G.R. Burton, and C.E. Brion, "Absolute optical oscillator strengths for the electronic excitation of atoms at high resolution. III. the photoabsorption of argon, krypton and xenon," *Phys. Rev. A* **46**, 1, 149 (1992).
- M.R. Bruce, W.B. Layne, C.A. Whitehead, and J.W. Keto, "Radiative lifetimes and collisional deactivation of two-photon excited xenon in argon and xenon," *J. Chem. Phys.* **92**, 5, 2917 (1990).
- D.F.T. Mullamphy, G. Peach and I.B. Whittingham, "Self-broadening of singlet lines of helium," *J. Phys. B* **24**, 3709 (1991).
- K. Tachibana, N. Kitagawa, and H. Harima, "Detection of Excited Atoms and Measurement of Electron Excitation Coefficients for Rare-Gases by Using Near-Infrared Diode Lasers," Proceedings of the Third Workshop on Radiation Detectors and Their Uses (1988) 45.
- E.L. Lewis, "Self-broadening and oscillator strengths in the rare gases," *Proc. Phys. Soc.* **92**, 817 (1967).
- A. Siegman, *Lasers* (Mill Valley, CA: University Science Books, 1986) 158.
- M. Mitchner and C.H. Kruger, Jr., *Partially Ionized Gases* (New York: John Wiley and Sons, 1992) 70.
- L.F. Stokes, M. Chodorow, and H.J. Shaw, "All-single mode fiber resonator," *Opt. Lett.* **7**, 6, 288 (1982).

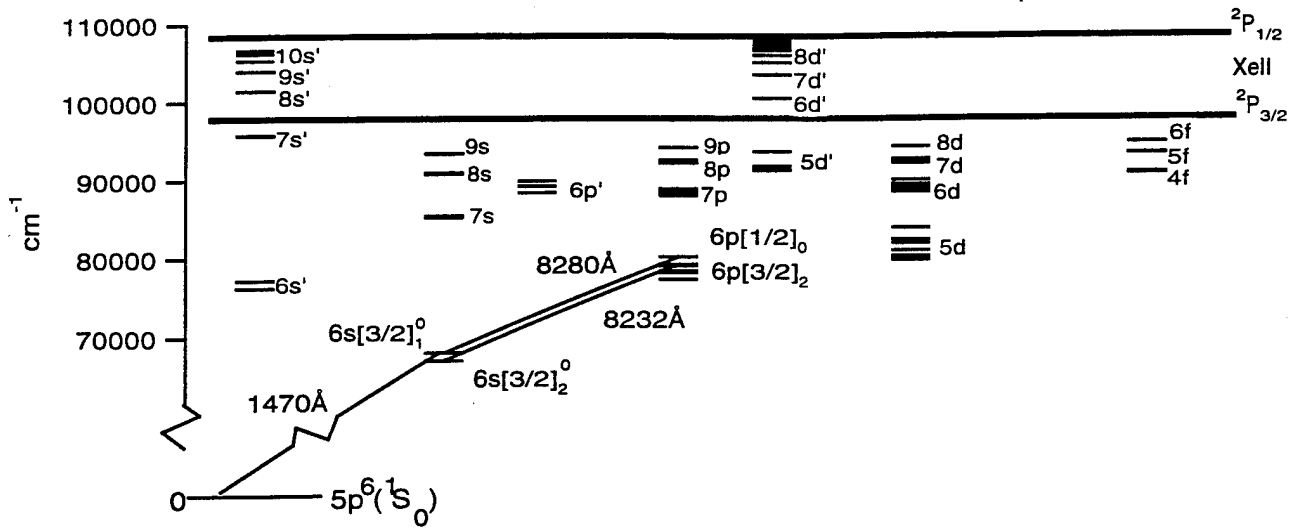


Figure 1. Xenon energy level diagram.

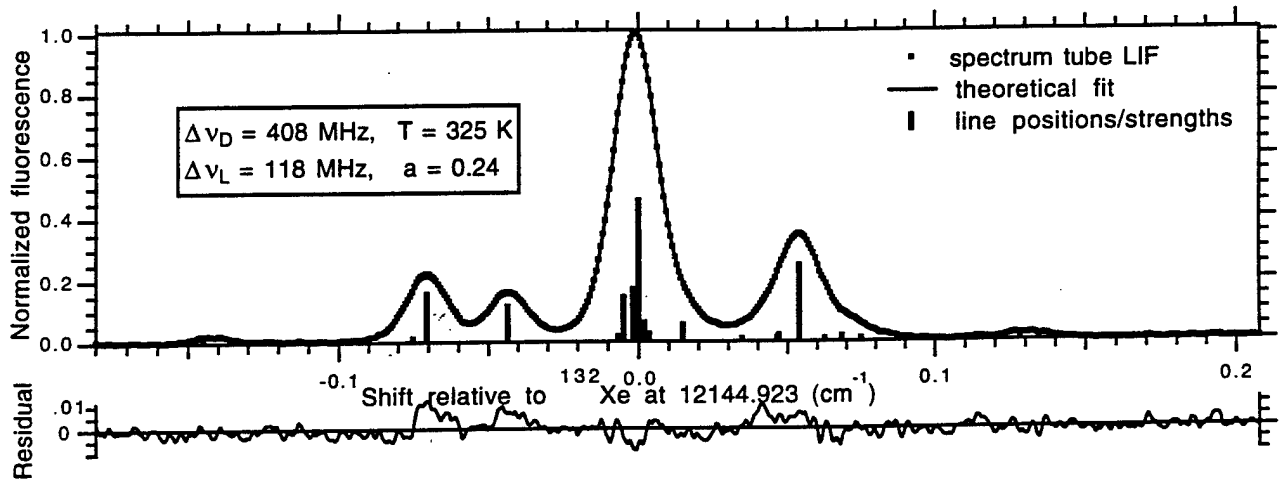


Figure 2. LIF excitation spectrum for the  $6s[3/2]_2^0 - 6p[3/2]_2$  transition.

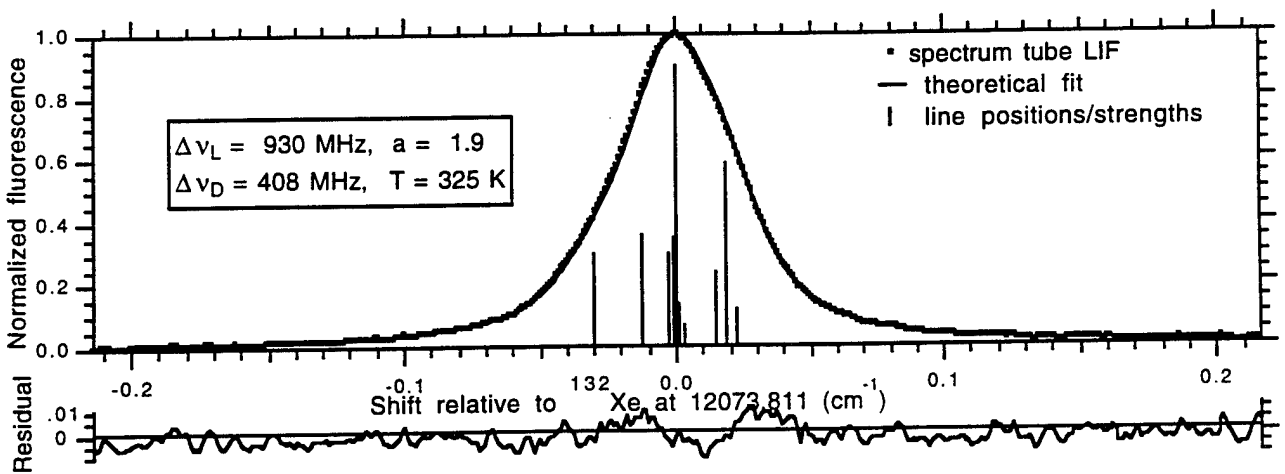


Figure 3. LIF excitation spectrum for the  $6s[3/2]_1^0 - 6p[1/2]_0$  transition.

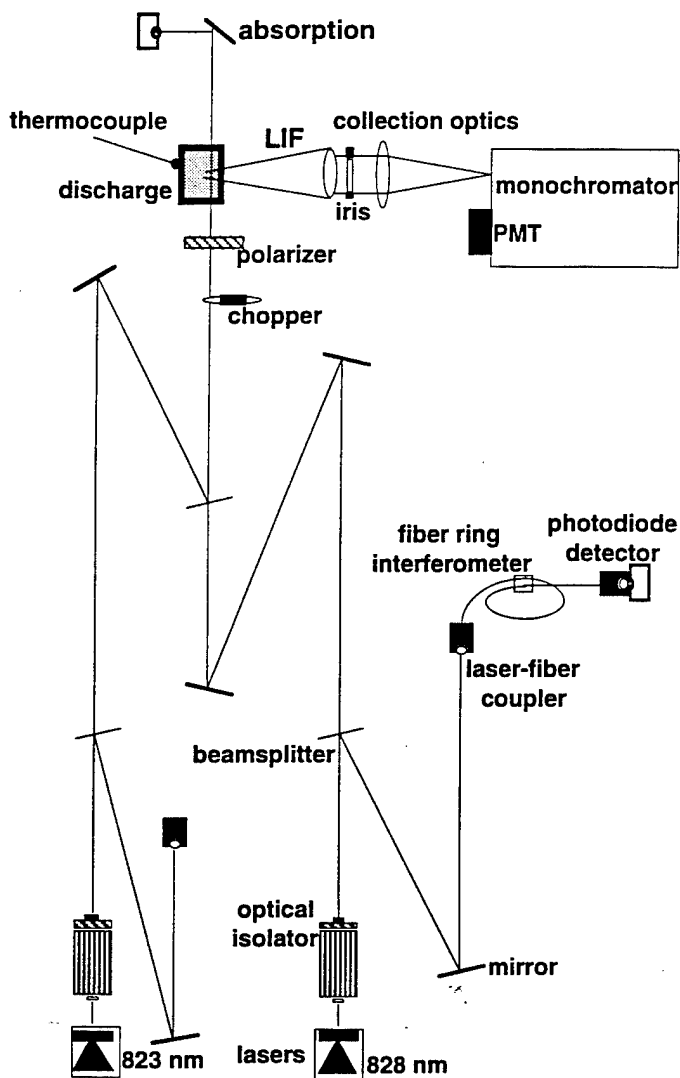


Figure 4. LIF setup.

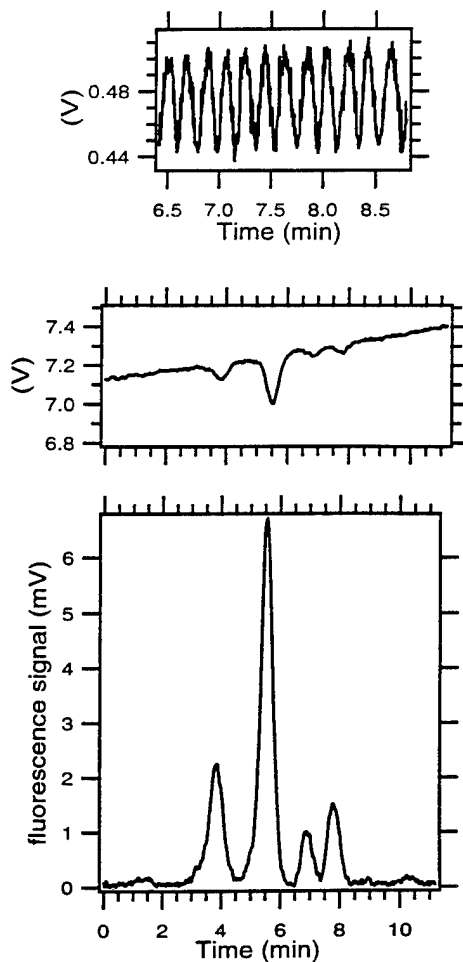


Figure 5. Sample data: ring throughput, absorption, LIF.

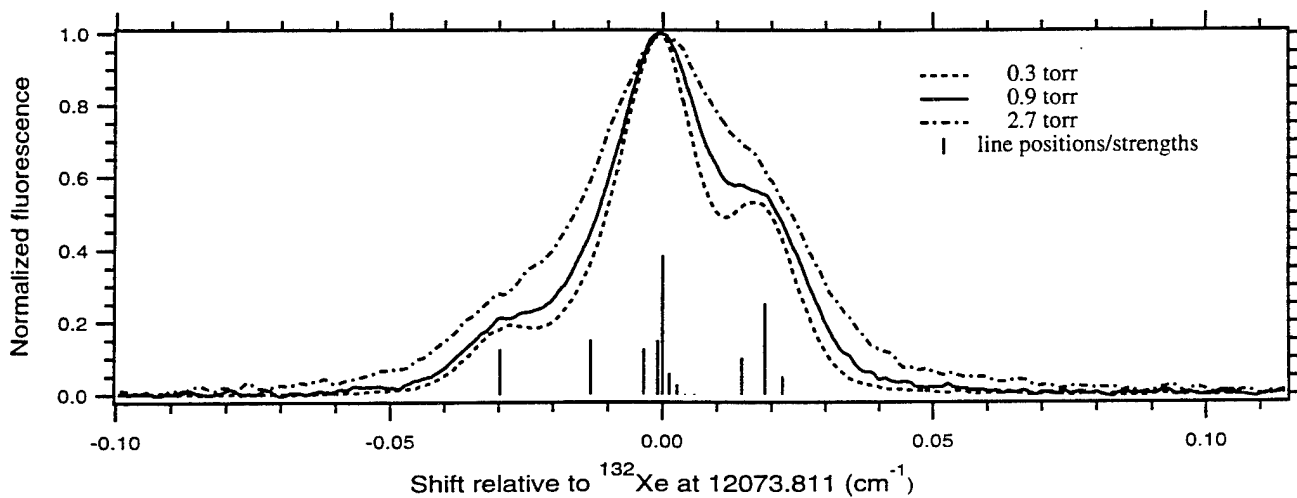


Figure 6.  $6s[3/2]_i^o - 6p[1/2]_o$  LIF lineshapes for different pressures.

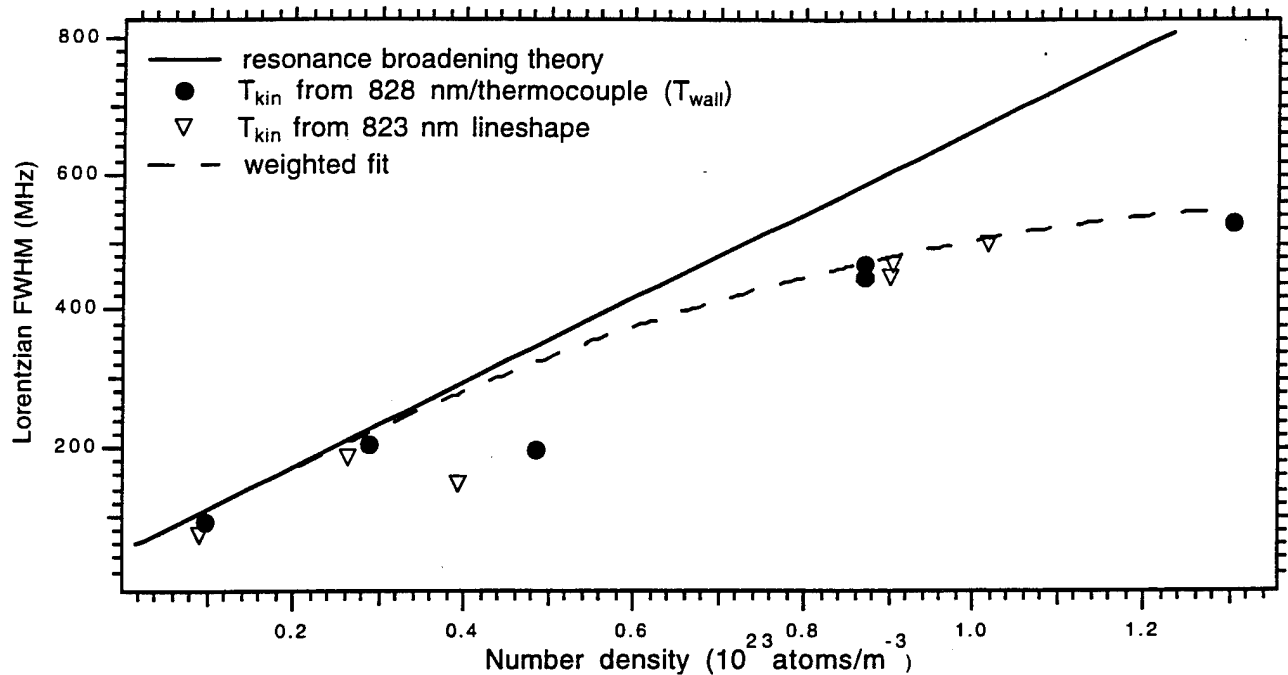


Figure 7.  $6s[3/2]_1^0 - 6p[1/2]_0$  measured Lorentzian halfwidths compared to low pressure resonance broadening theory.



**AIAA-95-2381**

**Laser-Induced Fluorescence Measurements  
Within An Arcjet Thruster Nozzle**

P. V. Storm and M. A. Cappelli

High Temperature Gasdynamics Laboratory  
Department of Mechanical Engineering  
Stanford University  
Stanford, California

**31st AIAA/ASME/SAE/ASEE  
Joint Propulsion Conference and Exhibit  
July 10-12, 1995 / San Diego, CA**

# LASER-INDUCED FLUORESCENCE MEASUREMENTS WITHIN AN ARCJET THRUSTER NOZZLE

P. Victor Storm\* and Mark A. Cappelli†

*High Temperature Gasdynamics Laboratory  
Department of Mechanical Engineering  
Stanford University  
Stanford, California, USA*

## Abstract

*An investigation of the feasibility of laser-induced fluorescence (LIF) measurements within the nozzle of a 1 kW class radiatively-cooled hydrogen arcjet thruster is presented. Calculations of the fluorescence signal, signal-to-background ratio and fluorescence saturation limits indicate that LIF of the atomic hydrogen Balmer-alpha transition is attainable to within a few millimetres of the nozzle throat. Fluorescence measurements were performed with an Ar<sup>+</sup>-pumped cw ring dye laser using DCM dye. Axial velocities were determined from the Doppler shift of the H<sub>α</sub> linecenter; however the limited scanning range of the dye laser did not permit the accurate determination of atomic hydrogen translation temperature. Velocity profiles are presented along the arcjet centerline and radially at the exit plane and three axial positions within the nozzle. Translation temperature was measured at the exit plane. The results demonstrate that LIF is a feasible means of measuring velocity, and potentially temperature, in the plasma flowfield within the thruster nozzle.*

## I. Introduction

As arcjet thrusters have advanced from laboratory devices to in-flight operational thrusters for satellite north-south station-keeping, there has been a significant increase in interest in improving arcjet efficiency and operating range. These improvements will be obtained primarily through advanced analytical modeling of arcjets; however, the validation of the models can only be performed by comparison with experimental measurements of operating parameters and plasma properties. During the past several years a number of optical diagnostics have been developed to investigate properties in the plasma plume of the arcjet. Among these diagnostics, laser-induced fluorescence (LIF) has proven to be very useful due to its linearity, very good spatial resolution and specie specific nature. Plasma plume properties have been measured using LIF on a number of different arcjet propellants. Liebeskind et al.<sup>1</sup> measured atomic hydrogen temperature and velocity

at the exit plane of a 1 kW hydrogen arcjet thruster. The same group investigated slip velocity in the plasma plume by performing LIF on helium in a helium-seeded hydrogen arcjet.<sup>2</sup> Ruyten and Keefer<sup>3</sup> measured velocity in an argon plume of a 0.3 kW arcjet, and Ruyten et al.<sup>4</sup> performed LIF on atomic hydrogen and nitrogen to measure velocity in a 1 kW arcjet plume using simulated ammonia as the propellant. Recently, Pobst et al.<sup>5</sup> measured ground state atomic hydrogen density, temperature and velocity profiles at the exit plane of a 1 kW hydrogen arcjet using pulsed two-photon LIF.

Although LIF has been successfully applied as a plasma plume diagnostic, it has never been used to investigate plasma properties within the arcjet due to geometric constraints and reduced signal-to-background ratios. To date, only emission has been used as an optical diagnostic to probe the nozzle interior. By observing the emission through small holes in the anode, Zube and Myers<sup>6</sup> obtained rotation, vibration and excitation temperatures as well as electron number densities at a few axial locations within a 1 kW arcjet running on a propellant of simulated hydrazine. Hargus et al.<sup>7</sup> performed similar

\* Research Assistant, Student Member AIAA

† Associate Professor, Member AIAA

measurements on a 30 kW arcjet with ammonia as the propellant. Using quartz glass rings rather than holes in the anode, Tahara et al.<sup>8</sup> performed a comprehensive study of the emission from the interior of a 10 kW water-cooled nitrogen arcjet thruster. A few emission studies have been performed in the constricted arc region of the thruster. Glocker and Auweter-Kurtz<sup>9</sup> observed the emission through a small quartz window in the nozzle throat of a 10 kW hydrogen arcjet. Abel-inverted profiles of electron temperature and atomic hydrogen excitation temperature were obtained from the continuum and hydrogen line emission, respectively. Zube and Auweter-Kurtz<sup>10</sup> extended this study to simulated hydrazine propellant and included electron number density measurements from the linewidth of the Balmer-beta line. By investigating the emission along the axis of the arcjet, Storm and Cappelli measured electron number densities in the near-cathode region of 1 kW and 5 kW hydrogen arcjets.<sup>11,12</sup> A summary of arcjet interior diagnostics is given in Ref. 13.

This paper describes a preliminary investigation of the use of laser-induced fluorescence for spatially resolved velocity measurements within a 1 kW hydrogen arcjet nozzle. The arcjet operating conditions have been chosen to facilitate a comparison between these measurements and arcjet modeling results of Butler et al.<sup>14</sup> A few measurements of velocity and temperature were performed at the exit plane for comparison with previous LIF<sup>1,5</sup> and emission<sup>15</sup> measurements performed at the exit plane of the same or a similar arcjet.

## II. Fluorescence Modeling

To determine the potential applicability of laser-induced fluorescence to the plasma in the interior of the arcjet nozzle, several calculations have been performed. The LIF signal intensity from the Balmer alpha transition in atomic hydrogen was simulated at different axial positions in the arcjet. A collisional-radiative model of atomic hydrogen was developed which includes stimulated emission and absorption terms on the  $H_\alpha$  transition, as well as the usual collisional and spontaneous radiative terms on all transitions. The model, without the stimulated emission terms, is described in detail in Storm and Cappelli;<sup>11</sup> therefore only the additional stimulated emission terms will be described here. Rate equations for the  $n=2$  and  $n=3$  excited states contain, in addition to those terms described in Ref. 11, stimulated terms of the form  $n_2 B_{23} I_l(\lambda)$  and  $n_3 B_{32} I_l(\lambda)$  where  $B_{23}$  and  $B_{32}$  are the Einstein B coefficients on the  $H_\alpha$

transition, and  $I_l(\lambda)$  is the incident laser intensity. The simulations were performed at the unshifted linecenter of the  $H_\alpha$  transition,  $\lambda=656.28$  nm. Laser beam properties were taken to be those of a typical cw ring dye laser pumped by a 5 W Argon ion laser. A beam waist of 200  $\mu\text{m}$  and laser power of 10 mW to 500 mW at line center were assumed.

The effect of the stimulated emission terms in the collisional-radiative model is to raise the  $n=3$  number density above that which would exist in the absence of these terms. This excess  $n=3$  population determines the strength of the LIF signal relative to the background emission from the same volume of plasma. However, to estimate a realistic LIF signal-to-background ratio, the background emission is scaled by an effective optical path length, which was taken to be the diameter of the nozzle. The diameter was originally chosen because the initial intention was to observe the LIF signal through holes in the side of the nozzle. This estimate would result in a worst-case signal-to-background prediction since in reality the emission falls off quickly away from the arcjet centerline. The simulated LIF signal-to-background ratio is shown as a function of axial position and laser power in Figure 1. The axial position is defined to be zero at the arcjet exit plane and negative towards the nozzle throat. As expected, the higher emission in the interior of the arcjet results in a much reduced LIF signal-to-background ratio than at the exit plane. Even at the exit plane, however, the signal-to-background ratio is still below unity, which is the reason why the laser beam is mechanically chopped and phase sensitive detection is used in practice. Since a typical lock-in detection system has a dynamic reserve of approximately 60 dB (signal-to-noise ratio of  $10^{-3}$ ), one should therefore expect to detect the LIF signal as far as 8 mm into the nozzle with a typical laser power of 100 mW.

Apart from the signal-to-background ratio, two other critical issues include the signal level itself and the saturation limit. The LIF signal intensity was calculated from the excess  $n=3$  population describe above. The results are shown as a function of axial position and laser power in Figure 2. The signal intensities are normalized to unity at the exit plane for the 500 mW laser power case. Due to the increased quenching rate at the higher pressures experienced in the nozzle interior the LIF signal drops. Measurements performed by Liebeskind et al. at the exit plane with a 30 mW laser power indicate that signal levels two orders of magnitude smaller may be detectable.<sup>16</sup> This would indicate that fluorescence measurements could feasibly be made up to 8 mm into

the nozzle interior, close to the axial position where the signal-to-background limitation begins. With higher laser power the measurements may be extended inward toward the throat, provided that saturation is not reached.

The calculated saturation behavior at the exit plane and at  $z = -8$  mm is demonstrated in Figure 3. Note that the LIF intensities for the latter axial position have been increased by a factor of 200 to show both curves on the same plot. This figure clearly shows that while saturation at the exit plane is reached well below a laser power of 50 mW, the onset of saturation is significantly delayed in the arcjet interior and is not evident up to a laser power of almost 200 mW near the constrictor. This indicates that increased laser power may be used in the nozzle interior to help offset the loss of LIF signal intensity and the reduced signal-to-background ratio.

### III. Experiment

The experimental setup is shown in Figure 4. The vacuum facility consisted of a 1.09 m x 0.56 m diameter stainless steel chamber pumped by two mechanical pumps and 1250 CFM blowers through 15 cm pipe.

The fluorescence excitation laser was a Spectra Physics model 380A cw ring dye laser pumped by a Spectra Physics Stabilize 2016 argon-ion laser in multi-line mode. The dye laser was operated with DCM dye which has broad absorption and emission bands centered around 500 and 650 nm, respectively, making this dye particularly suitable for the Balmer alpha excitation of hydrogen at 656.28 nm. Dye laser output up to 200 mW was obtained with a pump laser power of 4 W in all lines. Scanning the ring dye laser was performed with a tunable, piezoelectrically driven intracavity etalon. The high voltage to the piezoelectric was supplied by a Burleigh model RC-43 programmable ramp generator. The maximum scanning range was 75 GHz, or approximately 0.1 nm; however, in practice this was reduced by roughly 30 percent due to laser mode instability. Scanning of the dye laser could not be performed continuously. Instead, the laser jumped axial modes, at 200 MHz spacing, as the etalon was being scanned. This, however, was inconsequential as the axial mode spacing was considerably less than one percent of the  $H_\alpha$  linewidth.

A fraction of the excitation laser beam from the dye laser was split off and sent to a Thorlabs model PDA50 photodiode detector and a Burleigh model

WA-10 wavemeter to monitor the laser intensity and wavelength. The main beam was expanded to approximately 40 mm in diameter by a -25 mm focal length (f.l.) plano-concave lens and then collimated using a 750 mm f.l. achromat lens. The collimated beam was then focused at the arcjet using a 700 mm f.l. achromat. Optical access was provided by a 76 mm diameter quartz window on the endplate of the chamber, aligned axially with the arcjet. By expanding the beam before focusing, the Gaussian beam waist was reduced to 15  $\mu\text{m}$ , and the depth of focus was 0.50 mm. The laser was directed axially into the plasma in order to probe the interior of the arcjet nozzle and to use the nozzle as a beam dump. As a result of the axial excitation, the axial velocity component was measured from the Doppler shift of the line.

Two different configurations were used for the collection optics as shown in Figure 4. For the exit plane measurements, the collection optics axis was aligned normal to the arcjet and excitation optics axes, and access into the vacuum chamber was provided by a 76 mm diameter window on the side of the chamber. For these measurements the collection optics consisted of a 400 mm f.l. achromat collimating lens followed by a 600 mm f.l. achromat focusing lens. A 20  $\mu\text{m}$  field stop defined the spatial resolution in the axial direction to be approx. 13  $\mu\text{m}$ . Photodetection was accomplished with a Hamamatsu R928 photomultiplier tube (PMT) at a cathode supply of 1000 V, enclosed in a light-tight housing. A 10 nm bandwidth  $H_\alpha$  interference filter was mounted to the entrance of the PMT housing to eliminate unwanted background light. Finally, to prevent saturation of the PMT, a neutral density filter of optical density 2.0 was placed in front of the field stop.

In the second configuration, used for the detection of fluorescence within the arcjet nozzle, optical access was provided by a 76 mm diameter window on the endplate of the vacuum chamber, adjacent to the window used for the excitation laser beam. In this configuration the optical axis was aligned at 16 degrees to the beam axis. A single 400 mm f.l. achromat lens was used for collection and focusing, yielding a transverse magnification of 0.84. The PMT and  $H_\alpha$  filter were identical to those of the previous configuration; however to account for lower fluorescence signal levels within the arcjet, the field stop and neutral density filters were both changed. The field stop was a rectangular pinhole 350  $\mu\text{m}$  high by 150  $\mu\text{m}$  wide, yielding a spatial resolution in the axial direction at the arcjet of approximately 0.6 mm. The increased height of the field stop was desired to

minimize large fluctuations in the fluorescence signal due to laser beam steering or directional fluctuations in the dye laser. The large size of the field stop required neutral density filters totaling an optical density of 3.2 to prevent saturating the PMT.

The output signal of the photomultiplier tube was sent to a Stanford Research Systems SR850 DSP lock-in amplifier. Since the fluorescence signal was considerably smaller than the background emission, phase-sensitive detection was performed by mechanically chopping the excitation beam near the dye laser at a frequency of 1.5 kHz. Signal noise near the chopping frequency was digitally filtered in the lock-in amplifier using a low-pass filter with a time constant of 1 s and a roll-off of 24 dB/oct. With such a long time constant, scans across the  $H_\alpha$  line were performed in a minimum of 100 s. Noise at the chopping frequency, due primarily to scattered laser light in the arcjet, could not be filtered and therefore was the limiting factor in obtaining a fluorescence signal. Outputs of the ramp generator and photodiode detector were simultaneously recorded through analog input channels of the lock-in amplifier in order to calibrate for wavelength and normalize the scans by laser intensity.

The arcjet, shown in cross-section in Figure 5, was a radiatively-cooled 1 kW class laboratory type thruster designed and built at NASA Lewis Research Center. The tungsten nozzle consisted of a 0.635 mm diameter, 0.25 mm long constrictor and a 12.1 mm long diverging section at a half angle of 20 degrees. With a design area ratio of 225, the exit plane diameter was 9.53 mm. The tip of the 2% thoriated tungsten cathode was originally set approximately 0.45 mm upstream of the nozzle constrictor; however, with erosion of the cathode, this value may now be somewhat larger.

In these experiments the arcjet was operated at a constant power of 1.49 kW and a fixed  $H_2$  mass flow rate of 14.2 mg/s according to the factory calibration of the mass flow controller. The background chamber pressure was maintained at approximately 0.35 torr. By translating the arcjet axially and radially, fluorescence was obtained along the arcjet centerline as well as radially at several axial positions. Measurements were made to within 1.5 mm downstream of the arcjet throat, at which point the LIF signal became lost in the background of scattered laser light.

## IV. Analysis

A typical LIF scan at the arcjet exit plane centerline is shown in Figure 6. The recorded fluorescence signal from the lock-in amplifier was divided by the photodiode output to account for variations in the laser power during each scan. The wavenumber scale was determined from the ramp generator output and the recorded scan endpoints from the wavemeter. As is evident in this figure, the typical scanning range was approximately  $1.7 \text{ cm}^{-1}$ , which was not sufficient to scan the linewings even at the exit plane where the line is the narrowest. The linecenter, however, could be accurately determined by fitting the lineshape with either a Gaussian or Voigt profile. The axial velocity is determined from the shift of the linecenter,  $\Delta v$ , from a stationary reference according to

$$\frac{u_z}{c} = \frac{\Delta v}{v_0}$$

The stationary reference frequency,  $v_0$ , was obtained from Liebeskind et al.<sup>1</sup>

A previous emission study of this arcjet found that accurate plasma temperature determination based on the Doppler width of the  $H_\alpha$  line must take into account Stark broadening of the line.<sup>15</sup> However, due to the limited scanning range of the dye laser, not enough of the linewings could be measured to accurately fit a free Voigt profile to the measured lineshape. This limitation precluded the accurate determination of temperature within the arcjet nozzle, where electron number densities have not been measured. At the exit plane, however, electron number density profiles have been previously measured<sup>15</sup> and this permitted fixing the Lorentzian component width to allow a "forced" Voigt fit of the lineshape. This best fit is shown in Figure 6. The Gaussian component width of the Voigt fit is directly related to the translational temperature of the  $n=2$  excited state of atomic hydrogen, duly taking into account the fine structure of the  $H_\alpha$  lineshape as described in Ref. 15.

## V. Results

The saturation behavior was investigated at the exit plane centerline and is shown in Figure 7. The fluorescence signal shows a linear dependence with laser power up to at least 100 mW. This measured saturation curve can not be compared directly to the simulated saturation curve of Figure 3 since the laser power was measured at the exit aperture of the dye

laser and will be very different from the incident laser power in the plasma. Nevertheless, as the simulation demonstrated that saturation is less detrimental in the interior of the nozzle than at the exit plane, it was safely assumed that saturation was not a problem below 100 mW of laser power. The exit plane and nozzle interior measurements were performed at laser powers of approximately 30 mW and 80 mW respectively.

#### Exit Plane Measurements

Figures 8 and 9 show the measured axial velocity and translation temperature at the arcjet exit plane. Since this study was intended to concentrate on the interior region of the nozzle, only a few measurements were performed at the exit plane. These measurements are compared to other LIF<sup>1,5</sup> and emission<sup>15</sup> studies performed on the same type of arcjet, as well as the modeling results of Butler et al.<sup>14</sup>

The radial profiles of axial velocity at the exit plane display the same trends but vary between experiments by up to 25 percent. These variations may be due in part to the slight differences in arcjet operating conditions or back pressures between the different experiments. Results of the present study are lower than the other experimental measurements, but not out of line with the model results.

In the case of the translational temperature profiles, the present results agree very well with both the arcjet model and emission measurements on the same arcjet. The temperature measurements of Liebeskind et al. are believed to be in error on the high side due to neglecting the Stark broadening of the  $H_{\alpha}$  line.<sup>17</sup> It has been speculated that the two-photon LIF measurements of translation temperature of Pobst et al. may be lower due to translational non-equilibrium between the ground state and first excited state of atomic hydrogen at the exit plane.<sup>5</sup>

#### Axial Measurements

Measurements of axial velocity as a function of axial position along the arcjet centerline are given in Figure 10. As was previously stated, the axial position is defined as zero at the exit plane and negative into the nozzle. The centerline velocity is seen to drop monotonically from a peak of approximately 17.5 km/s at 1.3 mm downstream of the throat to around 12 km/s at the exit plane. Since no other measurements of velocity have been made within the arcjet nozzle, the results are only compared to the arcjet model of Butler et al.,<sup>14</sup> including an older version of the model which did not incorporate mass diffusion. There is remarkably good agreement

between the measurements and the model which includes diffusion, indicating the importance of mass diffusion in the modeling work. More evidence to support this conclusion can be found in Ref. 17. The only significant discrepancy between the model and measurements appears in the three data points closest to the throat of the arcjet. It is here where the measurements have the largest uncertainty due to the loss of LIF signal and the increased background noise.

As explained above, the translational temperature could not be determined accurately within the arcjet nozzle due to the Stark broadening of the  $H_{\alpha}$  transition. Nevertheless, for the purpose of interest, "uncorrected" temperatures were determined by neglecting the Stark contribution to the linewidth and assuming the measured FWHM to be entirely Doppler broadened. The results are presented in Figure 11 along with the modeled temperatures. Although one should not attempt to read too much into this comparison, it is interesting to note that these uncorrected temperatures display the same axial trend as the modeled temperatures.

#### Radial Measurements

Radial profiles of the axial velocity were measured at three axial positions within the nozzle, (-2.54, -5.08, -6.35 mm) and are shown in Figure 12. The LIF signal intensities drop off very fast with radial position, indicating a rapid radial decrease in the  $n=2$  excited state number density. This loss in signal restricted the measurement domain to within approximately 2 mm of the arcjet centerline. The dashed lines in the figure are the model results at the same axial locations as the measurements. The measurements and the model show remarkably good agreement, although the measured velocities are somewhat greater than those of the model away from the arcjet centerline. The results indicate that while the centerline velocity decreases axially, the axial velocities away from the arcjet centerline increase with axially position. Since most of the mass convection occurs in the outer region, the total kinetic energy of the flow is clearly increasing downstream, as expected.

## VI. Summary and Conclusions

A feasibility study was performed to investigate the use of laser-induced fluorescence as a diagnostic technique to measure velocities and temperatures within an arcjet nozzle. The fluorescence of the  $H_{\alpha}$  transition of atomic hydrogen was simulated using a collisional-radiative model of the plasma with

stimulated emission and absorption terms in the rate equations for the  $n=2$  and  $n=3$  states. Fluorescence signal intensity, signal-to-background ratio and saturation behavior were calculated as a function of laser power and axial position in the arcjet. The results indicate that detectable signal levels and adequate signal-to-background ratios are achievable along the axis of the arcjet up to a few millimetres of the nozzle throat. It was shown that saturation was less detrimental in the arcjet interior than at the exit plane, thereby permitting an increase in laser power to offset the loss of LIF signal.

Laser-induced fluorescence measurements on the  $H_{\alpha}$  transition of atomic hydrogen were performed at the exit plane and within the nozzle of a 1 kW arcjet. The laser excitation system consisted of an  $Ar^{+}$ -pumped scanning ring dye laser with DCM dye producing up to 200 mW of cw output at 656.28 nm. Axial velocities were determined from the Doppler shift of the linecenter relative to a stationary reference. Translational temperatures were obtained at the exit plane by fitting the measured LIF lineshapes with Voigt profiles whose Lorentzian components were fixed by previously measured electron number densities.<sup>15</sup> Due to Stark broadening of the  $H_{\alpha}$  line, accurate translational temperature measurement within the nozzle could not be performed.

Measurements of translational temperature at the arcjet exit plane are in very good agreement with the arcjet model and previous emission measurements. Discrepancies exist, however, with the other LIF temperature measurements, but explanations have been suggested based on differences in the measurement or analysis technique. Measurements of axial velocity at the exit plane are in reasonable agreement with the model and previous LIF measurements, considering the slightly different operating conditions: power, propellant mass flow, tank back pressure, and perhaps arcjet throat diameter and cathode gap.

Axial velocities were measured along the axis of the arcjet from the exit plane to within 1.5 mm of the nozzle throat. These measurements agree very well with the arcjet model and suggest that mass diffusion is an important process to be included in the model. The axial velocities were also measured as a function of radial position at three axial locations in the nozzle and were found to be in good agreement with the model results.

The use of laser-induced fluorescence as a diagnostic for measuring axial velocity within the

nozzle of a hydrogen arcjet thruster has been demonstrated. Improved scanning capabilities may provide better lineshape resolution, leading to the determination of atomic translational temperature and perhaps electron number density in the expanding plasma. Plans are underway to perform a more comprehensive study to map the velocity flowfield at various arcjet specific energies.

## Acknowledgments

This work was supported in part by the Air Force Office of Scientific Research under grant No. F49620-92-J-0449 with M. Birkan as monitor. Partial support was provided by Olin Aerospace Company. Special acknowledgment is also given to NASA Lewis Research Center for supplying the arcjet thruster, and G.W. Butler of Olin-Aerospace for providing the arcjet modeling results.

## References

1. J.G. Liebeskind, R.K. Hanson and M.A. Cappelli; "Laser-Induced Fluorescence Diagnostic for Temperature and Velocity Measurements in a Hydrogen Arcjet Plume"; *J. Applied Optics* 32, no. 30, 6117 (1993).
2. J.G. Liebeskind, R.K. Hanson and M.A. Cappelli; "LIF Measurements of Species Velocities in an Arcjet Plume"; IEPC-93-131; 23rd AIAA/AIDAA/DGLR/JSASS International Electric Propulsion Conference, September 1993.
3. W.M. Ruyten and D. Keefer; "Characterization of Electric Thruster Plumes using Multiplexed Laser Induced Fluorescence Measurements"; AIAA-92-2965; 28th Joint Propulsion Conference, July 1992.
4. W.M. Ruyten, D. Burtner and D. Keefer; "Laser-Induced Fluorescence Measurements on the Plume of a 1 kW Arcjet Operated on Simulated Ammonia"; IEPC-93-127; 23rd AIAA/AIDAA/DGLR/JSASS International Electric Propulsion Conference, September 1993.
5. J.A. Pobst, I.J. Wysong and R.A. Spores; "Laser Induced Fluorescence of Ground State Hydrogen Atoms at Nozzle Exit of an Arcjet Thruster"; AIAA-95-1973; 26th AIAA Plasmadynamics and Lasers Conference, June 1995.
6. D.M. Zube and R.M. Myers; "Nonequilibrium in a Low Power Arcjet Nozzle"; AIAA-91-2113; 27th AIAA/SAE/ASME/ASEE Joint Propulsion Conference, June 1991.
7. W. Hargus, M. Micci and R. Spores; "Interior Spectroscopic Investigation of the Propellant Energy Modes in an Arcjet Nozzle"; AIAA-94-3302; 30th AIAA/ASME/SAE/ASEE Joint Propulsion Conference, June 1994.

8. H. Tahara, N. Uda, K. Onoe, Y. Tsubakishita and T. Yoshikawa; "Discharge Features in a Steady-State Nitrogen Arcjet Engine with an Expansion Nozzle"; *IEEE Transactions on Plasma Science* 22, no. 1, 58 (1994).
9. B. Glocker and M. Auweter-Kurtz; "Numerical and Experimental Constrictor Flow Analysis of a 10 kW Thermal Arcjet"; AIAA-92-3835; 28th AIAA/SAE/ASME/ASEE Joint Propulsion Conference, July 1992.
10. D.M. Zube and M. Auweter-Kurtz; "Spectroscopic Arcjet Diagnostics Under Thermal Equilibrium and Nonequilibrium Conditions"; AIAA-93-1792; 29th AIAA/SAE/ASME/ASEE Joint Propulsion Conference, June 1993.
11. P.V. Storm and M.A. Cappelli; "Axial Emission Diagnostics of a Low Power Hydrogen Arcjet Thruster"; IEPC-93-219; 23rd AIAA/AIDAA/DGLR/JSASS International Electric Propulsion Conference, September 1993.
12. P.V. Storm and M.A. Cappelli; "Axial Emission Measurements on a Medium Power Hydrogen Arcjet Thruster"; AIAA-94-2743; 30th AIAA/ASME/SAE/ASEE Joint Propulsion Conference, June 1994.
13. M.A. Cappelli and P.V. Storm; "Interior Plasma Diagnostics of Arcjet Thrusters"; AIAA-94-2654; 25th AIAA Plasmadynamics and Lasers Conference, June 1994.
14. G.W. Butler, A.E. Kull and D.Q. King; "Single Fluid Simulations of Low Power Hydrogen Arcjets"; AIAA-94-2870; 30th AIAA/ASME/SAE/ASEE Joint Propulsion Conference, June 1994.
15. P.V. Storm and M.A. Cappelli; "High Spectral Resolution Study of a Low Power Hydrogen Arcjet Plume"; AIAA-95-1960; 26th AIAA Plasmadynamics and Lasers Conference, June 1995.
16. J.G. Liebeskind, private communication.
17. G.W. Butler, I.D. Boyd and M.A. Cappelli; "Nonequilibrium Flow Phenomena in Low-Power Hydrogen Arcjets"; To be presented as paper AIAA-95-2819 at the 31st AIAA/ASME/SAE/ASEE Joint Propulsion Conference, July 1995.

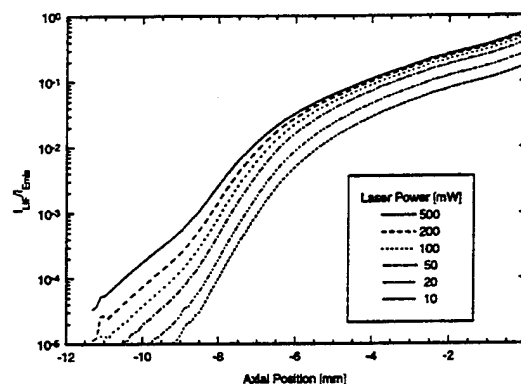


Figure 1. Simulated signal-to-background ratio on the arcjet centerline for various laser powers. The axial position origin is at the arcjet exit plane and negative position indicates into the arcjet nozzle.

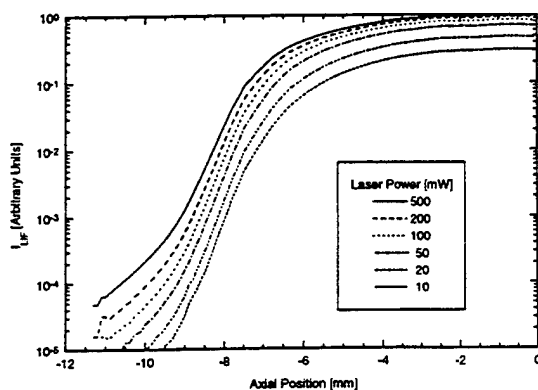


Figure 2. Simulated LIF relative signal intensity on the arcjet centerline.

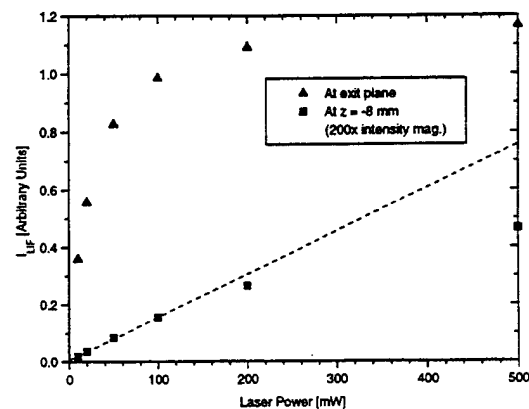


Figure 3. Simulated saturation behavior at the exit plane and in the nozzle interior.

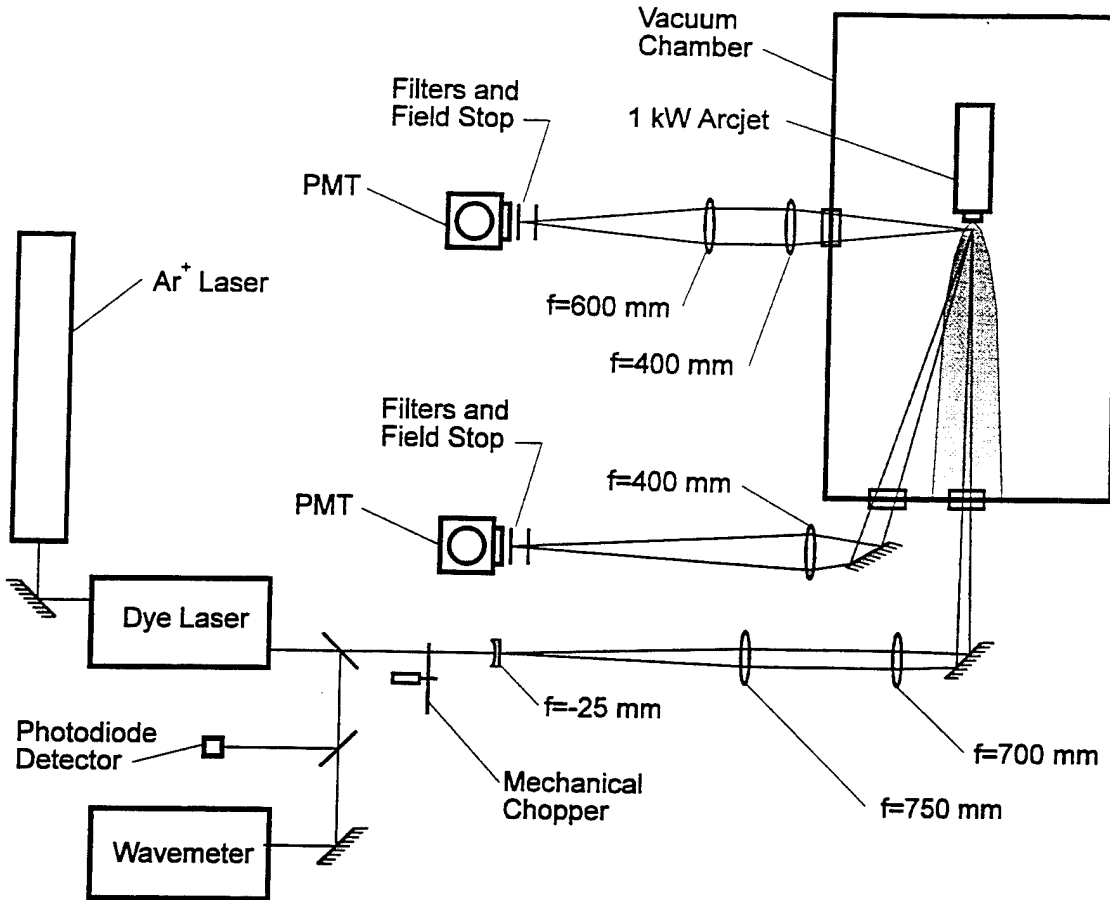


Figure 4. Schematic diagram of the experimental setup.

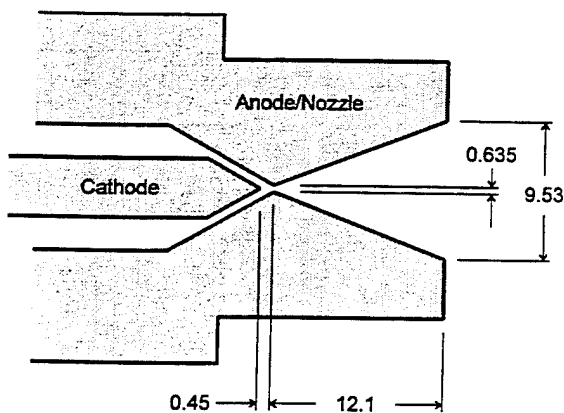


Figure 5. Cross-section of the 1 kW arcjet thruster nozzle (not to scale). All dimensions are in mm.

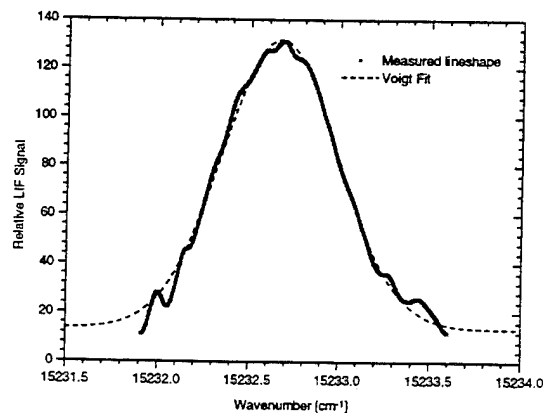


Figure 6. Typical LIF scan of  $H_{\alpha}$  at the arcjet exit plane centerline and best fit "forced" Voigt function.

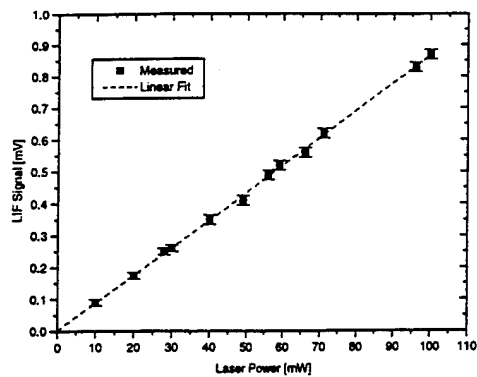


Figure 7. LIF saturation behavior at the arcjet exit plane centerline.

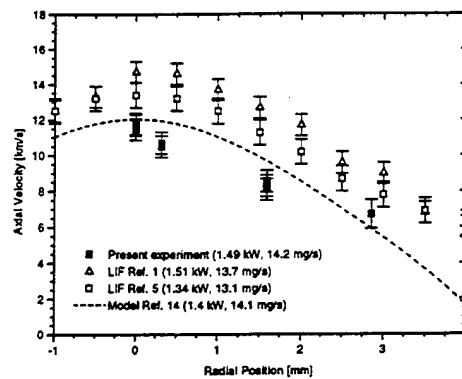


Figure 8. Axial velocity at the arcjet exit plane.

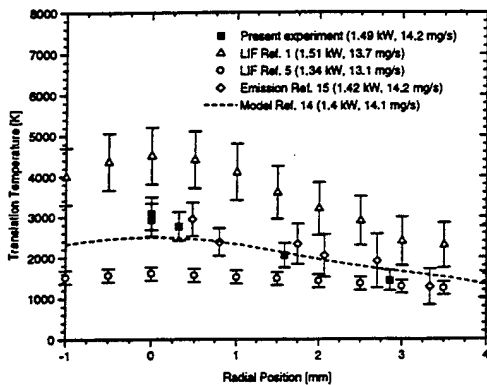


Figure 9. Translational temperature at the arcjet exit plane.

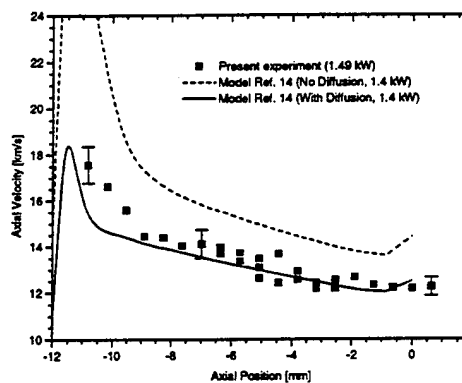


Figure 10. Axial velocity along the arcjet centerline.

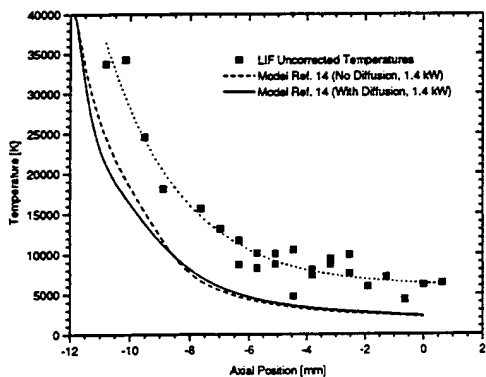


Figure 11. Translational temperature (uncorrected for Stark broadening) along the arcjet centerline.

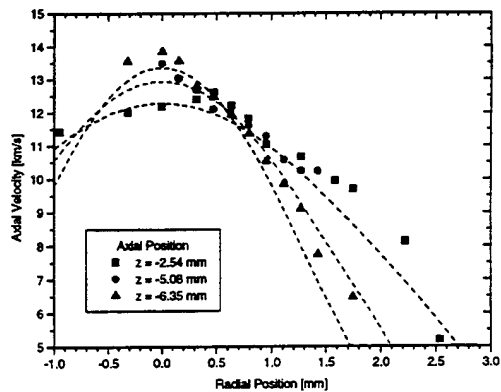


Figure 12. Radial profiles of axial velocity at three axial locations within the arcjet nozzle. The errors are typically  $\pm 0.6$  km/s. The dashed lines are the arcjet model (with diffusion) results at the same axial locations as the measurements.



**AIAA 95-2818**

**Pressure Measurements in the Plume  
of a Low Power Arcjet Nozzle**

W.A. Hargus, Jr. and M.A. Cappelli  
High Temperature Gasdynamics Laboratory  
Mechanical Engineering  
Stanford University

**31st AIAA/ASME/SAE/ASEE  
Joint Propulsion Conference and Exhibit  
July 10-12, 1995/San Diego, CA**

# Pressure Measurements in the Plume of a Low Power Arcjet Nozzle

William A. Hargus, Jr.<sup>†</sup> and Mark A. Cappelli<sup>‡</sup>  
High Temperature Gasdynamics Laboratory  
Mechanical Engineering Department  
Stanford University  
Stanford, CA 94305

## Abstract

Pitot pressure measurements were performed for both cold and arc heated flows with several probe geometries. Resulting measurements were compared to numerical models available in the literature. These models included a direct simulation Monte Carlo model (DSMC) of cold flow and a magnetohydrodynamic (MHD) model of arc heated flow. Cold flow pitot pressures exhibited complex behavior not completely described by the model. Since differing probe geometries resulted in variations of certain flow features, some of the observed phenomena may be due probe-flow interactions and, or rarefied gas effects. The ability to locate a shock in the plume both predicted by the DSMC model and previously observed by Raman spectroscopy, shows that the cold flow probes were capable of resolving major flow features. The pitot pressure measurements of arc heated flow agreed well with the results calculated from the MHD model, but corrections for rarefied flow would indicate that the model over predicts temperature. In addition, plume center line temperatures were determined from pressure measurements using laser induced fluorescence velocity data available in the literature.

## Introduction

Due to their high specific impulse and moderate thrust levels, arcjet thrusters are playing an increasing role in satellite propulsion. Existing and planned applications include arcjet thrusters for stationkeeping and on-orbit maneuvering. Low power hydrazine arcjets are now in use on the TelStar IV class of communications satellites and the first space test of a high power arcjet will be launched in 1996 under the Air Force ESEX program [1,2]. Arcjet technology is steadily improving as our understanding of the physics governing their operation increases. Efforts that combine both experimental and theoretical studies are necessary in order to build reliable models of

arcjet performance that can be then used as design tools for next generation thrusters.

These next generation thrusters will extend the envelope of low power arcjet operation to higher specific impulse. This paper is motivated by the need to measure arcjet flow properties that can be used to verify the predictions of performance models. In this paper, we discuss the results of pitot pressure measurements in the plume of a low power arcjet thruster.

There have been only a few reported studies that have used pitot probes to understand the behavior of electrothermal thruster plumes. A study performed by the McDonnell Corporation in the 1960's examined the impact pressure on a pitot probe in the plume of several 30 kW class hydrogen arcjets [3]. A more recent study by Penko, et al., examined the plume of a nitrogen resistojet with a pitot probe for verification of direct simulation Monte Carlo (DSMC) and Navier Stokes continuum models [4]. To our knowledge, no such measurements have been published on low power hydrogen arcjets. Therefore, pressure measurements with several

---

<sup>†</sup> Student Member AIAA

<sup>‡</sup> Member AIAA

Copyright © 1995. Published by the American Institute of Aeronautics and Astronautics for the 31st Joint Propulsion Conference

pitot probe geometries were performed for both cold and arc heated flows in the plume of a low power arcjet. The results were compared to arcjet models available in the current literature. These include DSMC calculations [5] for unignited (no arc) hydrogen flow, and a magnetohydrodynamic (MHD) continuum model [6] for ignited flow in an arcjet of the same geometry. These results also complement the many non-intrusive spectroscopic studies that have been performed on this low power hydrogen arcjet plume that have provided measurements of velocity [7-9], translational temperature [7,10], rotational temperature [5,11], and hydrogen number density [5,11].

## Apparatus

### Thruster and Test Facility

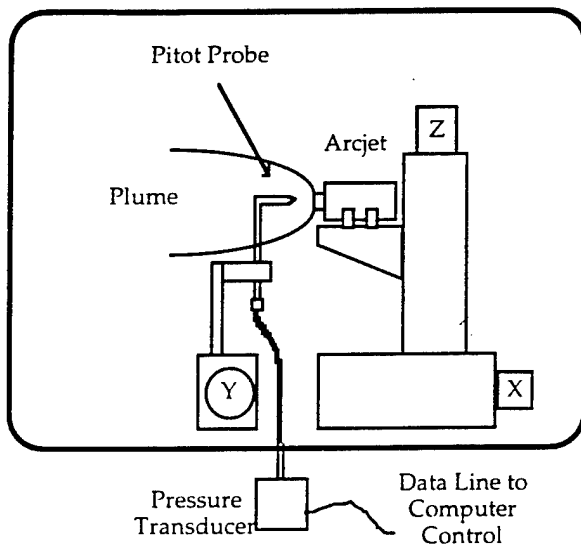


Figure 1. Test facility and experimental setup. The arcjet is mounted on a two-axis translation system with the probe mounted on a third.

The thruster and Stanford arcjet facility have been discussed in detail elsewhere in the literature [7-11], and they are only briefly described here. The arcjet used here is the standard 1 kW class NASA Lewis thruster [12], operating on hydrogen for this study. The nozzle has a 0.64 mm throat diameter with a 20° expansion half angle and an area ratio 225. The arcjet was mounted on a two-axis translational system within a 0.6 meter diameter, 1.1 meter

long vacuum tank. The vacuum facility was evacuated by two Roots blowers backed by mechanical roughing pumps for a combined pumping speed of 1200 l/s. In order to take measurements throughout the volume of interest, the probe was mounted on an additional translation stage. The mass flow for all tests was measured by a Unit Instruments hydrogen calibrated mass flow controller.

### Experimental Set Up

As shown in Figure 1, the arcjet was placed on a mount providing vertical and horizontal motion. Motion in the remaining radial axis was provided by placing the pitot probe on a third translation stage. The pressure within the pitot probe test volume was measured by use of a 0-17,000 Pa MKS capacitance manometer. All three translation stages and the pressure sensor were computer controlled and monitored. The result was a near automation of the data acquisition process and uniformity of test procedure.

Figure 2 shows the two pitot probe tips used for the cold flow studies. Both probes were 0.875 inches (22.2 mm) in length and 0.25 inches (6.4 mm) in diameter. The sharp probe had a cone angle of 9.5° while the blunt probe had a radius of curvature of 0.25 inches (6.4 mm). Both probe tips shown in Figure 2 were machined from brass and soldered onto stainless steel tubing that formed the body of the probe. Figure 3 shows the probe tip used for arc heated pitot pressure measurements. The copper hot flow probe was 1.125 inches (28.6 mm) in length and 0.625 inches (15.9 mm) in diameter; the larger size necessary for a water coolant jacket that surrounded the 0.125 inch (3.18 mm) diameter inner copper tubing (not shown) that connected the probe to the pressure transducer. The water cooling is necessary for the probe to survive in the near plume environment during arc heated flow. The probe tip also was attached to a copper collar-body assembly with the required coolant connections. For all probes, the opening at the tip was 0.020 inches (0.51 mm) in diameter.

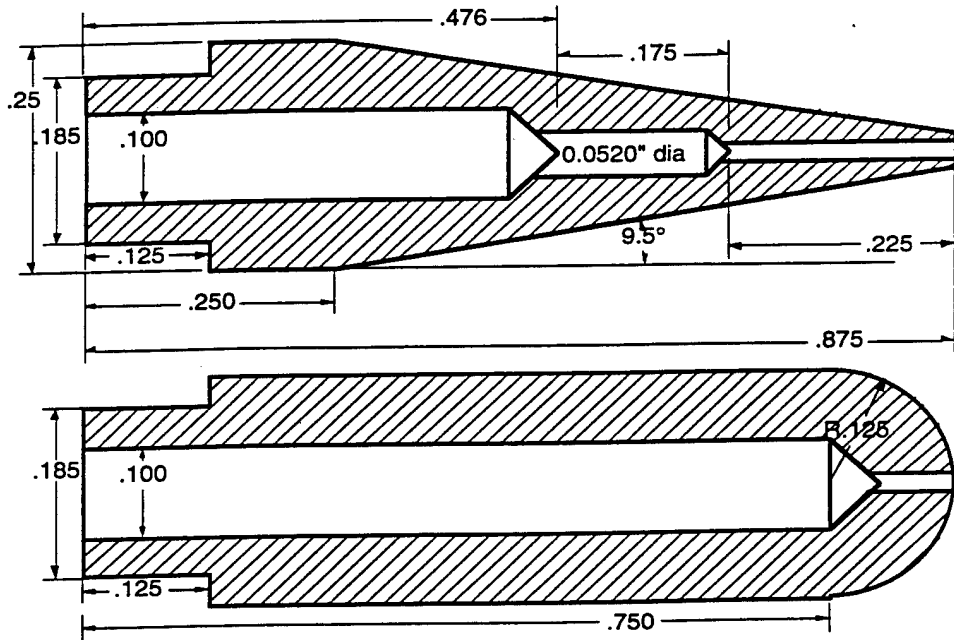


Figure 2. Sharp and blunt tips of the Pitot probes used for cold flow measurements. Note that the dimensions are in inches.

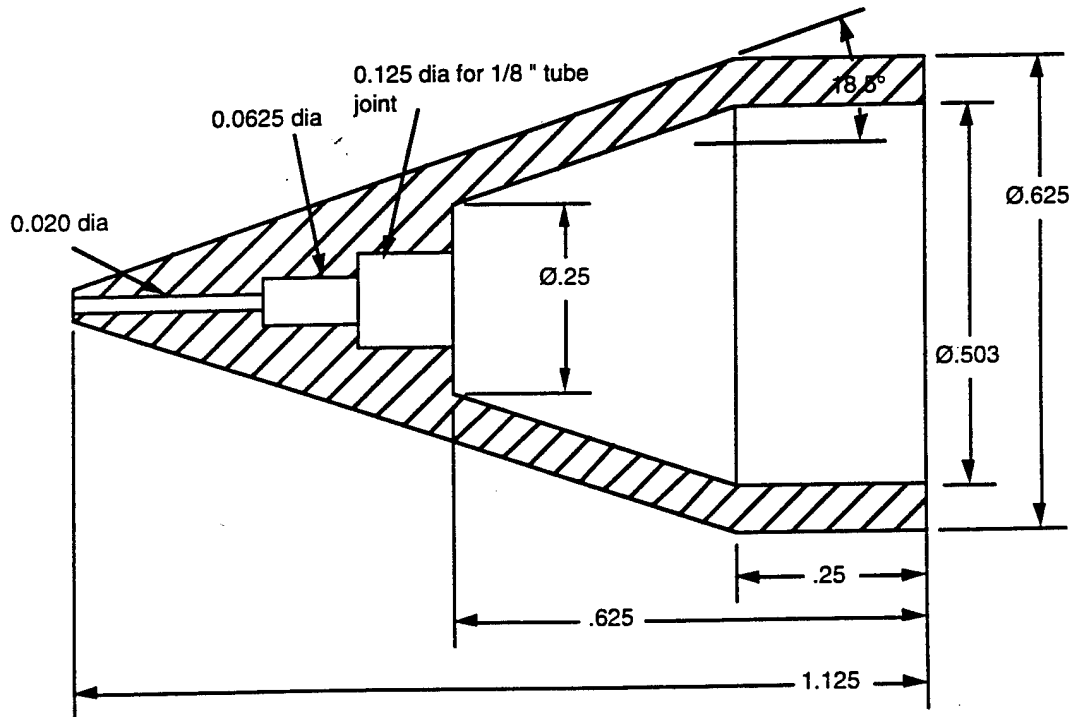


Figure 3. Probe tip for arc heated flow measurements. The diameter of this probe is greater than that of the cold flow probes in order to allow a water jacket to cool the probe while it is in the plume. Note that the dimensions are in inches.

## Normal Shock Calculations

When pitot probes are utilized in supersonic flows, a bow shock will form in front of the probe. The pressure actually measured by the pitot probe is the stagnation pressure after the shock. For continuum flow the shock strength is given by Saad [13] to be

$$\frac{P_{oy}}{P_{ox}} = \frac{\left[ \frac{2kM^2 - (k-1)}{k+1} \right]^{-1/(k-1)}}{\left[ \frac{(k+1)M^2}{2 + (k-1)M^2} \right]^{k/(k-1)}} \quad \{1\}$$

where  $M$  is the freestream Mach number,  $k$  is the ratio of specific heats,  $P_{oy}$  is the stagnation pressure after the shock, and  $P_{ox}$  is the stagnation pressure before the shock. With a root finder, Equation 1 can be used to determine the Mach number from pitot pressure measurements. However, a value of the stagnation pressure prior to the shock is required. If this information is taken from the results of a model, it is often necessary to calculate local stagnation pressures from static pressures.

$$\frac{P_o}{P} = \left[ 1 + \frac{k-1}{2} M^2 \right]^{\frac{k}{k-1}} \quad \{2\}$$

where  $P$  is the static pressure and  $P_o$  is the local stagnation pressure. Note that the Mach number is defined by.

$$M = \frac{V}{\sqrt{kRT}} \quad \{3\}$$

where  $V$  is the velocity of the gas,  $T$  is the local gas temperature, and  $R$  is the appropriate gas constant.

## Results and Analysis

### Cold Flow

Two series of tests were performed with the arcjet unignited. The first of these cold flow studies used the sharp probe. A blunt probe was later employed to insure a normal shock in front of the probe. All tests, except one, were performed at a mass flow rate of 14.2 mg/s. One test with the blunt probe tip was performed at 7.1 mg/s. In all tests, a background pressure of 40 Pa was maintained.

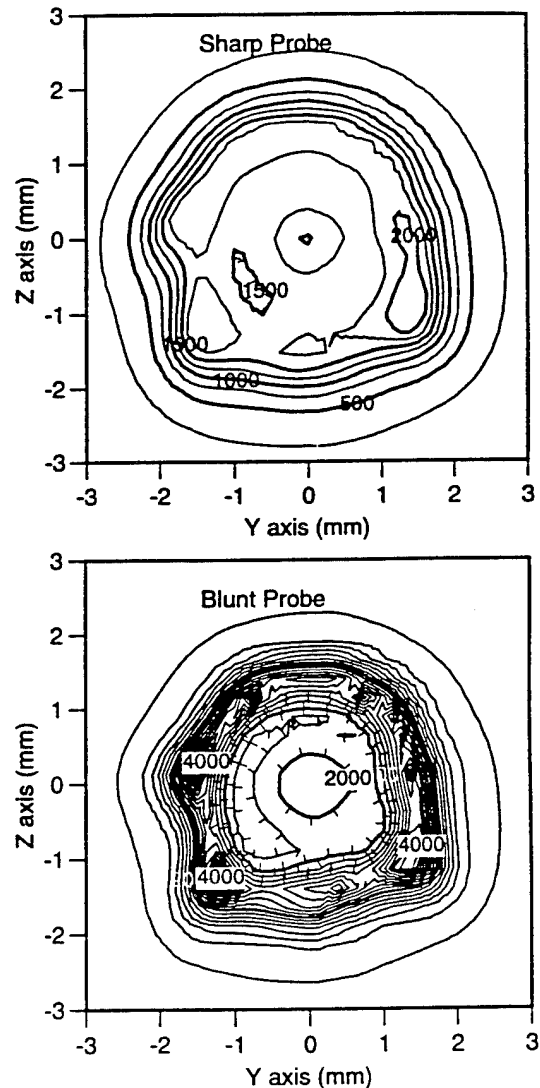


Figure 4. Sharp and blunt probe pressure contours at exit plane in Pascals. Note the large annular structure seen with the blunt probe. Note that the scales are the same.

Figure 4 shows the pitot pressure contours for the sharp and blunt probes 0.5 mm from the exit plane. The contours are similar in that a relatively small central core of similar shape and size is the most significant feature. In both cases, the core is unsymmetric in a similar manner. Examination of the arcjet has shown that the interior of the nozzle is not perfectly smooth and that a number of small irregularities are visible approximately in the lower left quadrant of the nozzle where the greatest lack of circular symmetry is visible in Figure 4.

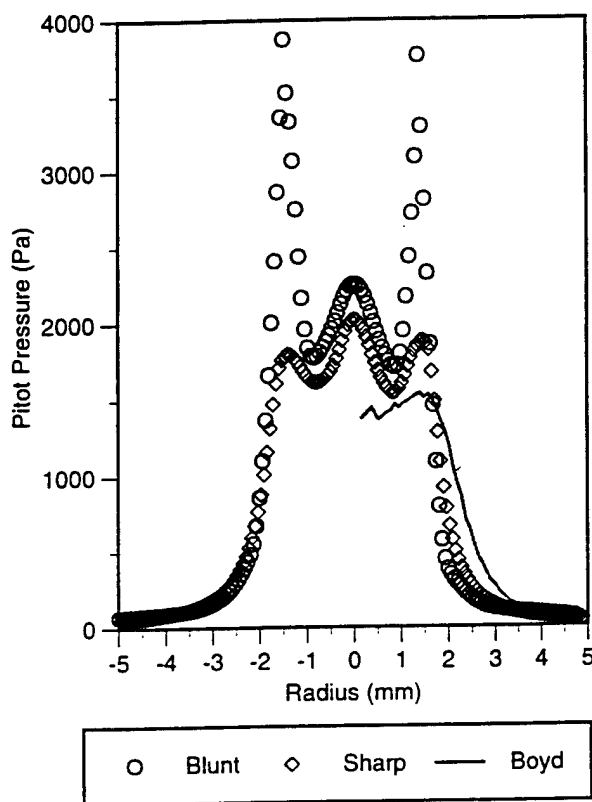


Figure 5a. Pitot pressure cross-sections; measured and predicted. All experimental cross-sections taken in the vertical from Figure 4.

The most important difference in the measurements of each probe are the unanticipated set of high pressure annular regions more clearly shown in Figure 5a. These regions may represent the extent of the large viscous boundary layer that develops during the expansion. If this is true, then the central core represents a nearly isentropic flow. A measurement with the blunt probe at a

significantly lower mass flow rate (see Figure 5b) appears to reinforce this reasoning. In this test, the lower mass flow rate case, this annular region of higher pressure is closer to the center of the flow and is slightly wider. There are several differences between the sharp and blunt probe results in Figure 5a. In the core region, there is a difference in pitot pressure of approximately 300 Pa. This difference is attributed to rarefied gas effects. The lower pressure given by the sharp probe is thought to be more accurate since the measured pitot pressures in rarefied flows have been found to be higher than the true stagnation pressures behind a normal shock. Corrections for rarefied gas effects are known to be available in the literature, but were not used in this study [4]. The difference between the pressures measured by the sharp and blunt probe in the annular region is yet unexplained.

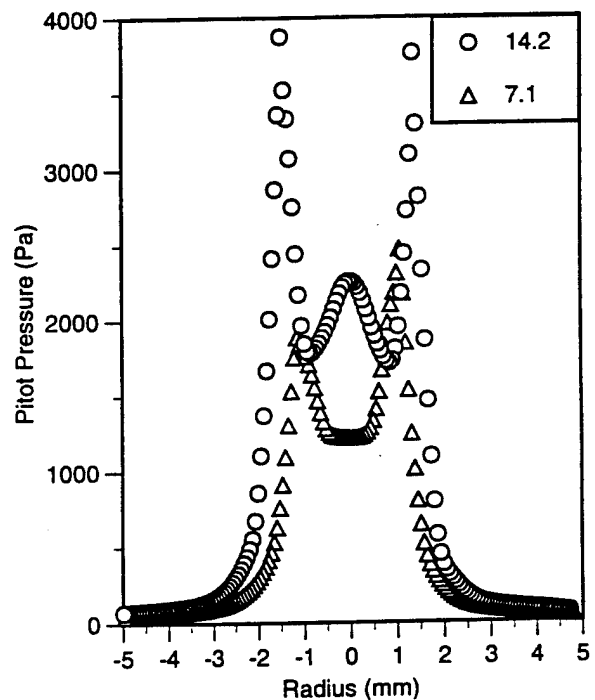


Figure 5b. Pitot pressure cross-section at reduced mass flow of 7.1 mg/s compared to standard test procedure of 14.2 mg/s. Central cross-sections taken along the vertical axis of Figure 4 with the blunt probe.

Figure 5a also shows the calculated pitot pressure from DSMC data from Boyd et al. for this nozzle with the same run conditions [4], but not corrected for rarefied gas effects. Continuum shock results computed from the DSMC data exhibit a wider pitot pressure profile than do the experimental results. In the core of the flow, the numerical model is also much flatter than the experimental results. However, the DSMC result exhibits several of the distinctive features seen in the experimental cross-sections including the higher pressure annular region. Note however, that the central peak does not appear to be captured by the pitot pressure extracted from the DSMC calculations. Note also that the lower mass flow rate data does not show a maximum in the pitot pressure along the arcjet centerline.

The Mach number of the flows can be determined from the experimental pitot pressure cross-sections if the stagnation pressure of the flow is known as a function of radial location. The shock strength is then known and a simple root finder can be used to determine Mach number, given the ratio of specific heats [13]. The results of the DSMC model were converted to stagnation pressures as a function of radial position using Equation 2. These results along with the measured pitot pressures and Equation 1 were then used to determine radial values of the Mach number shown in Figure 6. The ratio of specific heats used was 1.4 which corresponds to fully excited translational and rotational modes, but assumes the vibrational modes are unexcited. The calculated Mach numbers generally agree well with the Mach numbers determined from the model results. The flat portion in the core appears to be an isentropic region of the flow with the wings of the profile corresponding to the viscous boundary layer. The results from the blunt probe exhibit a dip at the edge of the core corresponding to the location of the apparent annulus of high pitot pressure. Elsewhere, the two probes agree closely. At a radius of approximately 3.75 mm, the root finder was no longer able to converge to a finite Mach number. Examination of the data showed that the pitot pressures were higher than the model's local stagnation pressures.

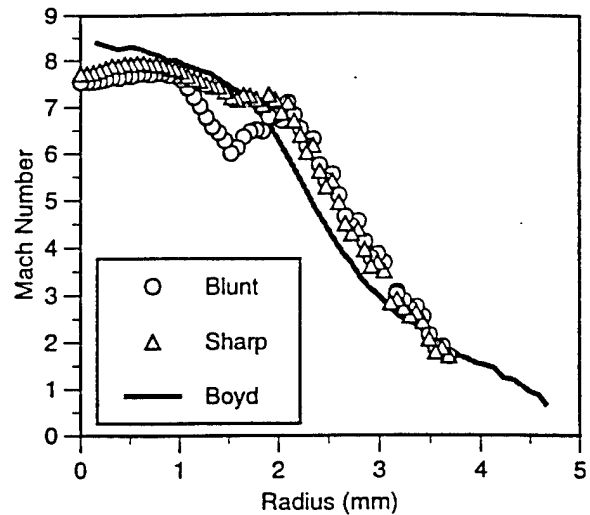


Figure 6. Calculated Mach numbers compared to Mach numbers calculated from the DSMC results of Boyd et al.

Figure 7 shows the plume pitot pressure field for distance of approximately 15 mm downstream of the exit plane. In both cases, we see the high pressure annulus extending into the plume and the central core pitot pressure dropping until a strong shock is encountered at a location 12 to 14 mm downstream. This shock location agrees with the shock location predicted and measured by Boyd et al., as shown in Figure 8. The axial pitot pressures of the sharp and blunt probes are overlaid by the number density of the first excited hydrogen vibrational state as measured by Raman spectroscopy and predicted by the DSMC model [5]. Agreement is quite good with the DSMC model predictions, especially for the sharp probe. Close examination of Figure 7, reveals that the blunt probe appears to retard the shock. Hence, the more abrupt pressure rise also seen in Figure 8. Therefore, it must be noted that the shock location derived from the pitot probe location remains somewhat ambiguous due to probe perturbation of the flow. Also, the number densities measured by Raman scattering represent an average over a probe volume that 4 mm in length along the axial direction.

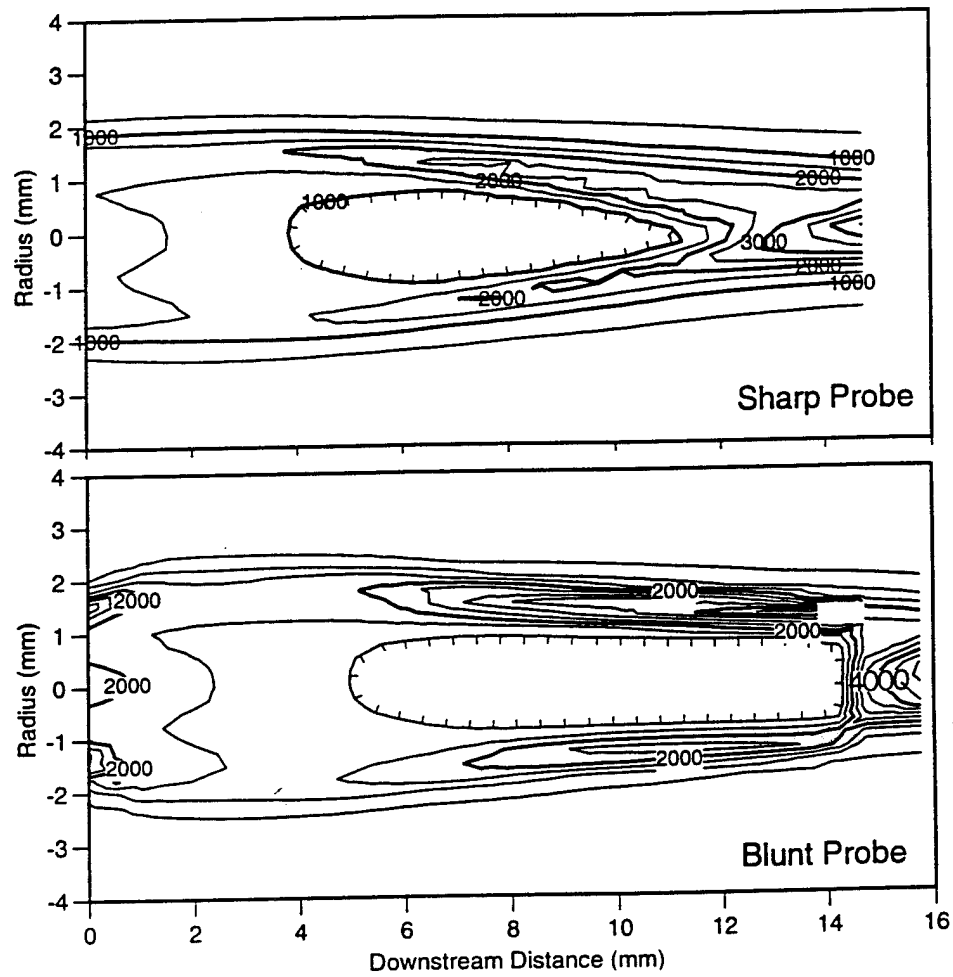


Figure 7. Plume pitot pressure fields for sharp and blunt probes. Pitot pressures contours are in Pascals. Note the more abrupt pressure rise in the case of the blunt probe.

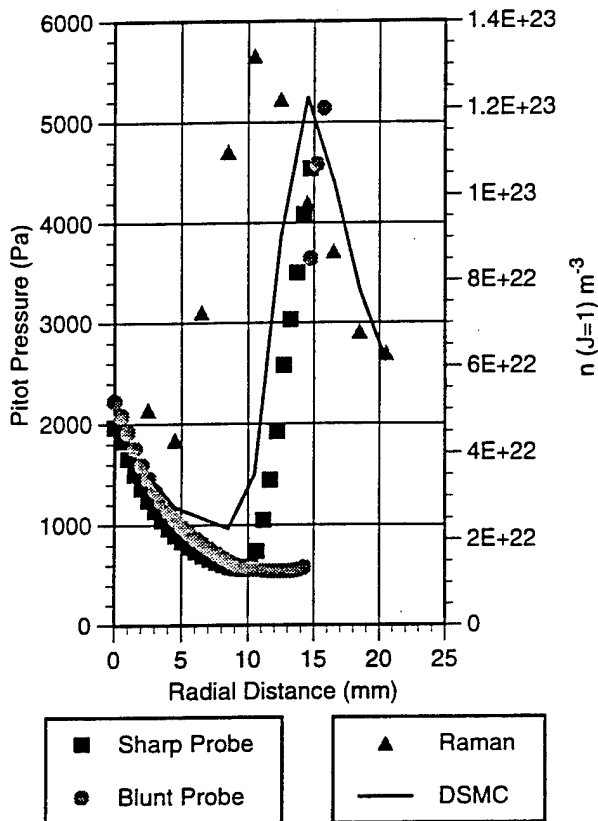


Figure 8. Shock location measured with sharp and blunt probes compared with results from Boyd et al.

### Arc Heated Flow

The second portion of this study concentrated on pitot pressure measurements in the arc heated flow. The power for most of the tests performed was approximately 1.50 kW; however, a number of other powers varying from 1.4 to 0.9 kW were also examined. In all tests, the mass flow rate was 14.2 mg/s and a background pressure of 40 Pa was maintained.

Figure 9 shows the pitot pressure contour 0.5 mm from the exit plane for a power of 1.50 kW. Unlike the cold flow exit plane data, there is a distinct lack of structure in the hot flow pressure contour. It is smooth and symmetric. This is further illustrated in the cross-section

pitot pressure profile for various input powers in Figure 10. The profile is very smooth and lacks the distinctive high pressure annulus found in the cold flow measurements. If the plume centerline pitot pressures are plotted as a function of specific power, as in Figure 11, a linear trend is seen. The data extrapolates to a zero power point which is near in agreement with the cold flow pitot pressures measured and the calculated pitot pressures from the DSMC model.

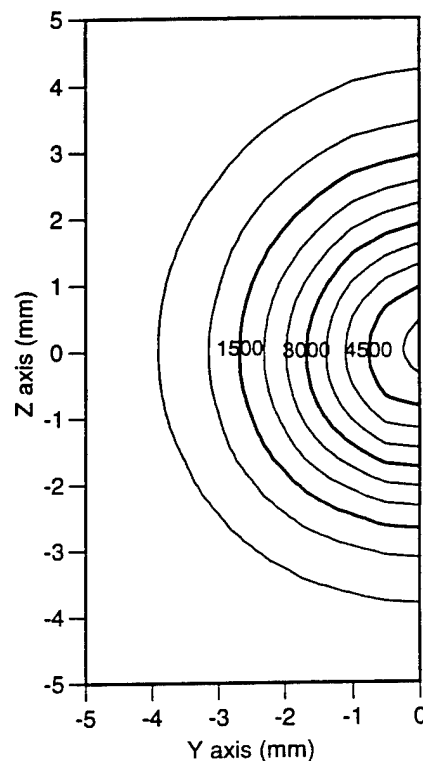


Figure 9. Arc heated exit plane pitot pressure contour for a power of 1.50 kW. Pitot pressures are labeled in Pascals.

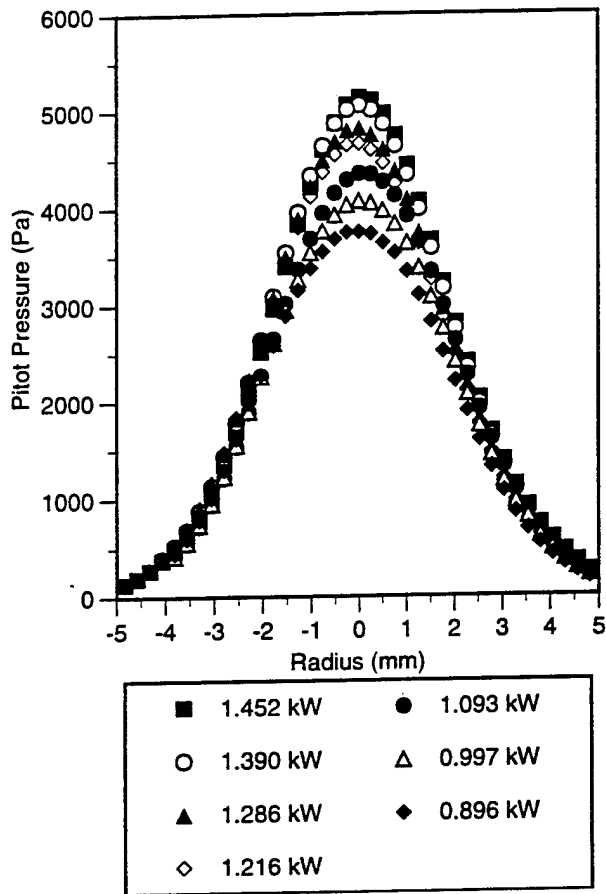


Figure 10. Pitot pressure profiles at a variety of powers.

Figure 12 compares the pitot pressure cross-section for an arcjet power of 1.39 kW to the calculated pitot pressures from MHD model simulations [6]. The model simulations are for an arcjet of similar geometry and mass flow at a power of 1.4 kW [6]. The pitot pressure was calculated using three different ratios of specific heats; the first (1.40) to simulate no vibrational excitation, the second (1.33) to simulate full vibrational excitation, and the third (1.25) to simulate vibrational over-excitation by a factor of two. If effects due to rarefied flow are neglected, there is very good agreement between the experimental data and the model. The peak pitot pressure is bracketed by the pitot pressures calculated from the model results. There may be evidence of vibrational over-excitation in the wings. We note that in all measurements reported here, no attempt was made to align the probe axis to be parallel to the flow vector. The small error bars placed on the experimental data points in Figure 12 represent the maximum error likely in the measured pitot pressures due to flow angle assuming purely conical flow.

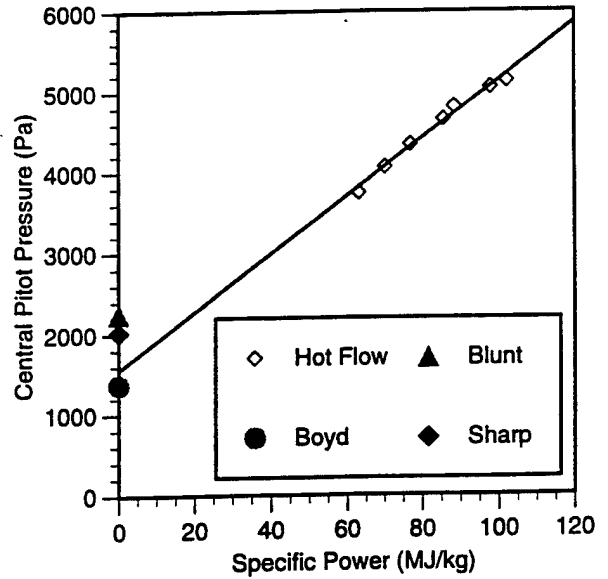


Figure 11. Center pitot pressure variation with specific power and cold flow data including results taken from the DSMC results of Boyd et al.

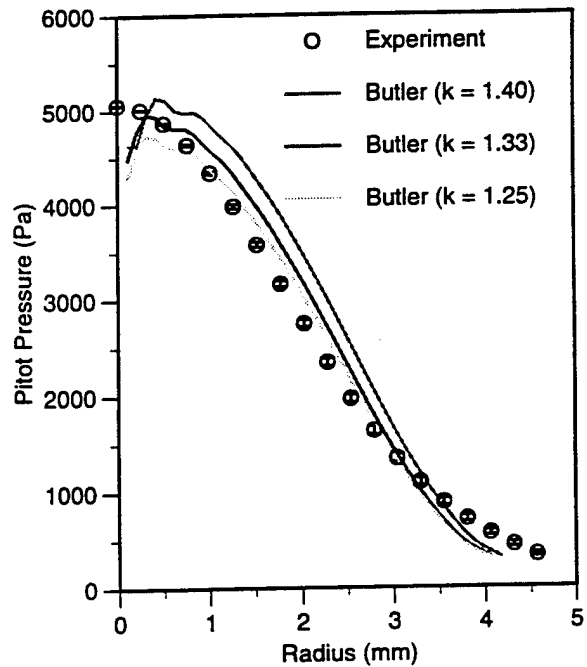


Figure 12. Comparison of pitot pressures measured and calculated from the MHD model results of Butler et al. using several values of the ratio of specific heats at a power of 1.4 kW. Note small error bars on experimental data points

If, as in the cold flow, the model stagnation pressures are used to calculate a shock strength, the local Mach number may be determined from the measured pitot pressures. Figure 13 shows the resulting Mach numbers using the pitot pressures and assuming fully excited vibrational state ( $k = 1.33$ ) compared to the Mach numbers from the MHD code. The agreement is good and shows that the results are self consistent. Similar to the cold flow analysis, the root finder was not able to converge on a Mach number beyond a radius of approximately 3.25 mm. In this region, analysis of the data showed that the MHD model stagnation pressures were slightly less than the measured pitot pressures.

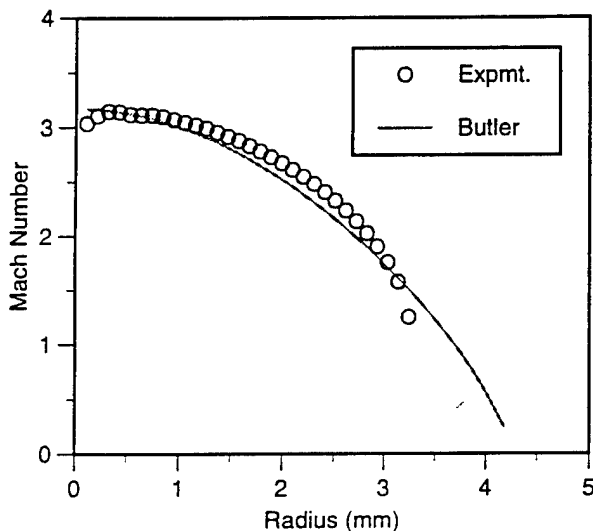


Figure 13. Comparison of calculated and predicted Mach numbers from the MHD model of Butler et al. for a power of 1.4 kW. Calculated using  $k = 1.33$  corresponding to fully excited translational, rotational, and vibrational energy modes.

Figure 14 shows the plume pitot pressure field for a power of 1.50 kW. Unlike the cold flow plume, the arc heated plume is devoid of complex structures and slowly decays in all directions. It is symmetric and there is no evidence of a shock in the first 25 mm downstream of the exit plane. Assuming that the plume core flow is isentropic, the pitot pressure along the center line can be used to determine plume temperatures. The procedure

is to use a constant stagnation pressure, equal to the maximum calculated at the exit plane by the MHD model, and the measured pitot pressure. Assuming full vibrational excitation ( $k = 1.33$ ), these quantities allow us to determine the local Mach number from Equation 1. Using reliable axial velocity data for the same arcjet (at a slightly lower power of 1.43 kW) from Liebeskind et al. [7], a temperature can be extracted from the calculated Mach number by use of Equation 3. The resulting temperatures are plotted in Figure 15 along with laser-induced fluorescence (LIF) based temperatures also measured by Liebeskind, et al. [7]. As seen in this figure, the LIF temperatures are higher than those determined from the pitot pressure measurements. However, it has recently been discovered that Stark broadening of the laser-probed transition was not taken into account in the study of Ref. [7]. Correcting for Stark broadening, which will be significant only at the higher apparent temperatures, would lower the LIF temperatures at the exit plane to values that would be in close agreement with the temperatures inferred from the measured pitot pressure [10]. Further downstream from the exit plane, the agreement between the two temperatures is certainly apparent. At a distance 18 mm downstream of the exit plane, Liebeskind et al. found evidence of a shock. No evidence of a shock was found in the plume pitot pressure field. It is not certain whether this is due to the perturbation of the probe in the plume flow, or to the slightly higher power level studied here (1.50 versus 1.43 kW).

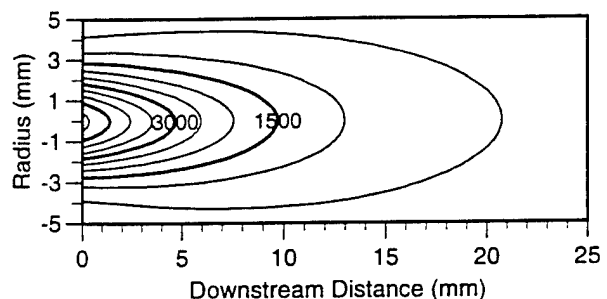


Figure 14. Arc heated plume pitot pressure field at a power of 1.5 kW. Pitot pressures are in Pascals.

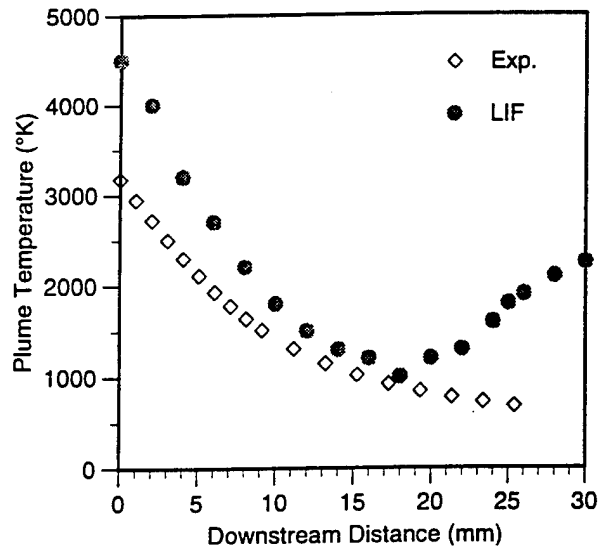


Figure 15. Temperature calculations in the plume compared to measured LIF temperatures from Liebeskind et al. Note that calculated temperatures do not show evidence of a shock.

### Conclusions

The cold flow pitot pressure measurements and differences due to differing probe geometry illustrate the complexity of these low density nozzle and plume flows, and the difficulties in interpreting such measurements. The available results from the DSMC model suggest that the flow has a core that is not quite as wide as that predicted. Although the higher pitot pressure annular regions were predicted by the model at much smaller magnitudes, the distinct structure seen in the contours and profiles of pitot pressures is likely magnified by the combination of the rarefied and highly viscous nature of the flow. The ability to locate a shock in the plume in agreement with both the DSMC calculations and Raman spectroscopy measurements of density shows that these probes are capable of resolving major flow features. In addition, the Mach number calculations show consistency between the model and measurements, especially those of the sharp tip probe.

The arc heated probe was able to survive in the exit plane and plume indefinitely and provided measurements of pitot pressure for a range of input powers. Results for a power of 1.4 kW compared very well with the MHD model predictions that were available in the

literature. The calculated and measured pitot pressures matched closely, but no corrections were made for rarefied gas effects. If a rarefied correction is found to be necessary, this would imply that the calculated pitot pressures of the MHD model are high; the result of an under predicted shock strength. The cause of this could be a lower than actual Mach number resulting from an overly high temperature. This particular question needs to be addressed carefully if the model is to be verified. Also, pressure measurements allowed for an estimate of the axial variation in the plume temperature. These temperatures were in general agreement with those measured by LIF and emission spectroscopy, however, there was no evidence of any shock structure from the probe measurements, in contrast with the measurements of temperature by LIF.

This study has demonstrated that a relatively simple experimental technique can provide a number of important insights into a complex propulsion device as well as the complex models attempting to describe it. However, there are obvious drawbacks, in that it is difficult to directly compare measured pitot pressures with flow properties predicted by the models. As a future project, a mass flux probe is planned to determine local mass flux across the exit plane. Using the reliable velocity data available in the literature, it will be possible to determine the density of the flow as a function of radius for direct comparison to current cold and hot flow models.

### Acknowledgments

This work was supported in part by the Air Force Office of Scientific Research. The authors are grateful to NASA Lewis for providing the arcjet and power processing unit. W.A.H. Jr. was supported under the Air Force Palace Knight Program. The authors also wish to thank Iain Boyd of Cornell University and Bill Butler of Olin Aerospace Company for access to the results of the their numerical simulations of arcjet flows.

### References

1. Smith, W.W. et al., "Low Power Hydrazine Arcjet Qualification," Paper IEPC 91-148, 22nd International Electric Propulsion Conference, Viareggio, Italy, Oct. 1991.

2. Sutton, A. "Overview of the Air Force ESEX Flight Experiment," Paper IEPC 93-057, 23rd International Electric Propulsion Conference, Seattle, WA, Sept. 1993.
3. Van Camp, W.M., D.W. Esker, R.J. Checkly, W.G. Duke, J.C. Crouton, S.E. Merrifield, and R.A. Williamson, "Study of Arc-Jet Propulsion Devices: Final report," NASA CR-54691, McDonnell Report E368, Mar. 1966.
4. Penko, P.F., I.D. Boyd, D.L. Meissner, and K.J. DeWitt, "Pressure Measurements in a Low Density Nozzle Plume for Code Verification," Paper AIAA 91-2110, 27th Joint Propulsion Conference, Sacramento, CA, June, 1991
5. Boyd, I.A., D.R. Beattie, and M.A. Cappelli, "Numerical and Experimental Investigations of Low-Density Supersonic Jets of Hydrogen," *Journal of Fluid Mechanics*, Vol. 280, pp 41-67, 1994.
6. Butler, G.W, I.D. Boyd, and M.A. Cappelli, "Nonequilibrium Flow Phenomenon in Low Power Hydrogen Arcjets" AIAA -95-2819, 31st Joint Propulsion Conference, San Diego, CA, July, 1995.
7. Liebeskind, J.G., R.K. Hanson, and M.A. Cappelli, "Laser-Induced Fluorescence Diagnostic For Temperature and Velocity Measurements in a Hydrogen Arcjet Plume," *Journal of Applied Optics*, Vol. 32, No. 30, Oct., 1993.
8. Liebeskind, J.G., R.K. Hanson, and M.A. Cappelli, "Flow Diagnostics of an Arcjet Using Laser-Induced Fluorescence," AIAA 92-3243, 28th Joint Propulsion Conference, July 6-8, Nashville, TN, 1992.
9. "Plume Characteristics of an Arcjet Thruster," AIAA 93-2530, 29th Joint Propulsion Conference, June 28-30, Monterey, CA, 1993.
10. Storm, P.V. and M.A. Cappelli, "High Spectral Resolution Emission Study of a Low Power Hydrogen Arcjet Plume," AIAA-95-1960, 26th AIAA Plasma Dynamics and Lasers Conference, San Diego, CA, June 19-23, 1995.
11. Beattie, D.R. and M.A. Cappelli, "Raman Scattering Measurements of Molecular Hydrogen in an Arcjet thruster Plume," AIAA-95-1956, 26th AIAA Plasma Dynamics and Lasers Conference, San Diego, CA, June 19-23, 1995.
12. F.M. Curran and T.W. Haag, "Extended Life and Performance Test of a Low Power Arcjet, AIAA-88-3106, 24th Joint Propulsion Conference, New York, NY 1988.
13. Saad, M.A., *Compressible Fluid Flow*, Prentice-Hall Inc., Englewood Cliffs, NJ, 1985.



**AIAA-95-2819**

**NON-EQUILIBRIUM FLOW PHENOMENA IN LOW  
POWER HYDROGEN ARCJETS**

G. W. Butler  
Olin Aerospace Company  
Redmond, WA

Iain D. Boyd  
School of Mechanical and Aerospace Engineering  
Cornell University  
Ithaca, NY

Mark A. Cappelli  
Department of Mechanical Engineering  
Stanford University  
Stanford, CA

**31st AIAA/ASME/SAE/ASEE  
Joint Propulsion Conference and Exhibit  
July 10-12, 1995/San Diego, CA**

# NON-EQUILIBRIUM FLOW PHENOMENA IN LOW POWER HYDROGEN ARCJETS

G.W. Butler\*  
Olin Aerospace Company  
Redmond, Washington

Iain D. Boyd\*\*  
School of Mechanical and Aerospace Engineering  
Cornell University  
Ithaca, NY

Mark A. Cappelli+  
Department of Mechanical Engineering  
Stanford University  
Stanford, CA

## Abstract

Low power arcjet thrusters are high specific impulse, high specific energy, electric propulsion devices that are now used for north-south satellite stationkeeping. Simple mission considerations indicate that the efficiency of these devices must increase to remain competitive with next generation electric propulsion devices. Numerical performance models can assist in this effort by providing tools to evaluate present performance and new concept designs. To be useful, however, these tools must correctly model the physics of ohmic dissipation, chemical reactions, gasdynamic expansion, and energy transport to and across the anode surface. This paper discusses the sensitivity of model predictions to the description of nonequilibrium transport processes and chemical phenomena within low power hydrogen arcjets. Simulation results are obtained using a continuum-based single fluid description of the flow and with a particle-based Monte Carlo method. Optical measurements of temperatures, velocities, and hydrogen number densities are used to assess the model predictions. Improved descriptions of ohmic dissipation, chemical nonequilibrium, and transport properties throughout the arcjet flow field are necessary to improve the accuracy of numerical methods and satisfactorily represent thruster performance.

## I. Introduction

Low power arcjet thrusters ( $\leq 2$  kW) are high specific impulse, high specific energy, electric propulsion devices that are now used for north-south satellite stationkeeping. At present, low power arcjets operate on hydrazine decomposition products and

generate a specific impulse ( $I_{sp}$ ) in the 500-600 second range with thrust efficiencies of approximately 30-35%. Future mission scenarios require that the stationkeeping roles of present low power arcjets expand to provide orbit maneuvering capability and some limited number of repositioning events. For the arcjet, this will require even higher  $I_{sp}$ s which, in turn, operate at higher specific energies ( $P/\dot{m}$ , where  $P$  is power and  $\dot{m}$  is mass flow rate) while maintaining or improving thrust efficiency. The present day technology, however, is limited by the anode material's ability to withstand the

\* Staff Engineer, Member AIAA

\*\* Assistant Professor, Member AIAA

+ Associate Professor, Member AIAA

high thermal fluxes characteristic of such high P/m operation.

A simple mission analysis<sup>(1)</sup> indicates that  $I_{sp}$ s on the order of 700 seconds will be required for the arcjet to maintain its competitive advantage over other electric propulsion thrusters. Figure 1 presents a schematic of the physics at work within a conventional arcjet thruster. The discharge has been traditionally considered as a wall and vortex stabilized arc. The arc emanates from the cathode, passes through the constrictor, and attaches in a diffuse (nondestructive) manner along the expanding portion of the nozzle which also serves as the anode. The propellant is injected upstream of the cathode tip with an azimuthal component of velocity. The resultant swirl promotes arc stability and acts to reduce heat transfer to the upstream anode surfaces. The propellant "merges" with the arc as it passes from the plenum through the constrictor, into the expanding portion of the nozzle, and finally to ambient space. The merging of the arc with the propellant gas is a complex and continuous process. No distinct boundary between arc and non-arc fluid can be drawn.

Flight qualified low power arcjets have conical converging-diverging nozzles with constrictor diameters on the order of 0.05 cm, nominal expansion angles of 20°, and exit diameters of 0.35 cm. The physical characteristics of the arcjet flow field vary from a nearly fully ionized plasma at temperatures in excess of 20,000 K near the cathode tip to a relatively cold, weakly ionized plasma (1000–2000 K) at the anode surface. Moreover, velocities vary from approximately 10 km/sec on centerline to zero at the wall. Considering the magnitude of these parameters and small geometric length scales, it is clear that the arcjet's performance depends largely on nonequilibrium transport processes. The more important of these processes are discussed below.

The shaded zones of Figure 1 identify regions of the discharge in which one physical process may be considered dominant. The principal activity in Zone 1 is the dissipation of electrical energy via collisions of electrons with the neutral and ionized propellant. Some of the ions produced in this region migrate to the cathode with sufficient energy to maintain the discharge. The bulk of the current is made up of electrons which travel through the propellant under the influence of the electric field to the anode. Along the way they are continually decelerated by collisions with their heavier neighbors and continually accelerated by the imposed electric field. In Zone 2, this process results in a

substantial increase in the bulk temperature of the plasma. This situation changes dramatically as the plasma leaves the constrictor and enters Zone 3 which is characterized by decreasing field strengths and rapid gas dynamic expansion of the plasma. Thermal energy exchange between the electrons and other species thus falls dramatically so that this region is dominated by the evolution of energy from recombination reactions. The principle process in Zone 4 is then the conversion of this internal energy to kinetic energy through gas dynamic expansion processes. In this zone, viscous dissipation and heat transfer at the anode surface act to reduce the benefits of the expansion process.

The most obvious area for improvement in arcjet performance is in the management of energy transport to and from the plasma. In particular, much needs to be understood about the transport processes that govern heat transfer to the anode and the conversion of chemical-to-kinetic energy. Numerical models can assist in this regard by providing guidance for critical design decisions. The accuracy of such design tools weighs heavily on their ability to correctly model the underlying physics.

State-of-the-art arcjet performance models provide solutions to the magnetohydrodynamic equations using Navier-Stokes (NS) solvers combined with Maxwell's equations to represent ohmic dissipation ( $P_{\Omega}$ ) and the resulting plasma motion.<sup>(2,3,4,5,6)</sup> Although these approaches typically demonstrate good agreement between measured and predicted exit plane velocities, they do not adequately replicate thruster performance over a sufficient range of operating conditions to support thruster design. We interpret this to mean that the analytical and experimental description of the energy transport within the arcjet needs further refinement.

Another modeling approach which has demonstrated merit and future potential is the direct simulation Monte Carlo (DSMC) method of Bird.<sup>(7)</sup> This approach has been used to predict the exit plane  $H_2$  population and temperature of a NASA LeRC  $H_2$  arcjet running in the cold-flow mode (no arc). These predictions compared favorably to data obtained with spontaneous Raman scattering<sup>(8)</sup> and demonstrate that the DSMC approach faithfully represents nonequilibrium transport of mass, momentum, and energy in such flows. Present DSMC development efforts, including possible hybrid schemes (e.g., DSMC/particle-in-cell codes) are now focusing on the simulation of ohmic dissipation and electron

diffusion to provide a more complete description of the arcjet physics.

The objective of this paper is to investigate the sensitivity of model predictions to the description of nonequilibrium transport processes and chemical phenomena within the arcjet. To accomplish this, NS and DSMC simulation results will be compared with corresponding velocity, temperature, and species data obtained in the exhaust of a low power hydrogen arcjet. Directions for future model development evolve naturally from these comparisons.

## II. Technical Approach

### Overview

We compare predictions of the NS performance model of Reference 2 with optical emission, laser induced fluorescence (LIF), and spontaneous laser Raman scattering to gauge the sensitivity of the steady state solution to the most important transport processes and the unequilibrated internal energy modes. The numerical simulations addressed power levels from 0.6 kW to 1.4 kW at a fixed  $\dot{m}$  of 14 mg/sec to overlap, as close as possible, the data taken using a low power NASA LeRC arcjet operating on  $H_2$ .<sup>(9,10)</sup> The NS solution provides the plasma and anode boundary conditions for a DSMC calculation similar to that performed in Reference 8.

The starting point for the DSMC calculations was chosen to be at a location in the arcjet nozzle where the effects of ohmic heating were thought to be significantly diminished. This was necessary since the DSMC model does not include the effects of externally imposed fields or ohmic dissipation. Figure 2 shows the centerline ratio of ohmic dissipation ( $P_{\Omega}$ ) to total energy as a function of axial distance for power levels of 600 W and 1400 W and  $\dot{m}=14$  mg/sec. The DSMC starting point was chosen to be at  $Z=0.55$  mm from the constrictor inlet, or approximately 0.05 mm downstream of the constrictor exit. At this location, the NS solution would estimate that approximately 75% of the ohmic power has been dissipated. However, as will be discussed below, the remaining 25% proved more important than originally anticipated.

The strength of the DSMC model is that it provides a good representation of the transport of mass, momentum, and energy. Finally, although both models make use of the same Arrhenius reaction mechanism, the DSMC approach tracks the translational, rotational, and vibrational states and corresponding temperatures,

$T_{trans}$ ,  $T_{rot}$ , and  $T_{vib}$  of the reactants while the NS model assumes instantaneous equilibration of all internal modes at the local temperature. A description of the numerical schemes and the experimental set up follow.

### Navier Stokes Solver

The NS solver used here is based on a single-fluid hydrodynamic description of the flow field. The format of the hydrodynamic solution has been described in detail previously. The kernel of the code is a nonsteady, two-dimensional, axisymmetric, finite volume hydrodynamics algorithm developed at Los Alamos National Laboratory.<sup>(11)</sup> A detailed discussion of the underlying numerical method may be found in References 2 and 11. Briefly, a computational cycle begins with a two phase Lagrangian sweep over the cells which is followed by a remapping to the fixed Eulerian grid.

In Phase 1 of the Lagrangian sweep, changes in the fluid dynamic state of the fluid are assumed to take place at fixed composition. Plasma transport properties are estimated at designated intervals using the method described by Yos.<sup>(12)</sup> Thermodynamic properties are calculated as needed using high temperature curve fits in JANNAF format.<sup>(13)</sup> The state of the individual mass elements is initially associated with computational cells at the top-of-cycle. From this state, they are acted upon by the various hydrodynamic forces and energy exchange processes. These processes include the effects of pressure gradients, thermal conduction, viscous dissipation, and ohmic dissipation (including the influence of electron pressure gradients in Ohm's Law). Phase 2 of the Lagrangian calculation evaluates the contributions of diffusion and chemical reaction at fixed hydrodynamic state. The change in species concentration and energy is determined cell-by-cell as discussed in Reference 2. Changes in bulk momentum due to these processes are neglected. In the final Eulerian portion of the cycle, the field is remapped to the stationary grid according to the Reynold's transport theorem.

The continuum boundary conditions are specified in the following way. The composition, density, and energy are specified along the inflow boundary and the velocity of the incoming gas is set to match the specified mass flow rate. The arc current is made up entirely of electrons. Its distribution and associated magnetic field are specified along the cathode. The exit plane of the arcjet is considered a fixed pressure

boundary. A constant, low pressure condition is set to insure a continuous expansion to space conditions. This is the simplest condition to apply since the exit flow is supersonic near the centerline and subsonic near the anode. The magnetic field is set to zero at the outflow boundary to force current attachment within the arcjet. The axis of the arcjet is considered a line of symmetry for all parameters.

Finally, no mass transport (except electrons) is permitted across the anode-plasma boundary, the anode is considered non-catalytic, and a no-slip condition is enforced. The value for the magnetic field is set by requiring the current to be normal to the non-neutral anode surface. This condition means that the anode is an equipotential surface. There are no other restrictions on either the current density or the magnetic field. The current attachment process is considered to be collisionally dominated and the losses due to the anode sheath are neglected. To further simplify the calculations, the effects of ionic recombination and anode work function at the surface are also neglected in the calculation of energy transport to the anode. A steady state anode temperature distribution is then determined (see Reference 6) to provide time-dependent estimates for temperatures along the plasma-anode boundary.

### DSMC Approach

A computer program based on the direct simulation Monte Carlo method (DSMC) for application to electric propulsion is under development at Cornell University.<sup>(7)</sup> The DSMC technique models gas flow at the molecular level using particles that are stored in the computer. Collisions are computed statistically using concepts from kinetic theory. The DSMC code used in this study<sup>(14)</sup> is implemented efficiently on a Cray C90 computer and has been verified directly against experimental data for neutral flows in small thrusters operating on nitrogen, helium, and hydrogen.<sup>(8,15,16)</sup> For the present application, extensions of the code are required for relaxation of high-temperature hydrogen, and for inclusion of electrons. Models are implemented for relaxation of the rotational and vibrational modes based on previous studies.<sup>(17,18)</sup> Chemical reactions include dissociation-recombination of molecular hydrogen and ionization-recombination of atomic hydrogen. The dissociation model and method for handling three-body reactions are described in Reference 18. Every effort has been made to use similar chemical reaction rates in the DSMC and single-fluid NS codes.

In the present study, plasma effects are handled in a simplistic way. While electrons are given particle

velocities representative of their mass and energy, they are constrained to move through the flow field with the average ion velocity determined in each cell. This approach provides a first-order simulation of ambipolar diffusion and ensures charge neutrality at the macroscopic level. However, this method omits two important plasma effects. The first is the diffusion of electrons. With the present scheme, the electrons are generally convected with velocities lower than the real physics would demand. This aspect will lead to the DSMC code predicting electron number densities that are too large. The second shortcoming of the present approach is the omission of ohmic heating. This is expected to be an important factor in the overall energy balance of the arcjet flows. This aspect should result in the temperatures predicted by the DSMC code being too low.

In general, when particles collide with the nozzle wall they are reflected diffusely assuming full energy accommodation. The profile of temperature along the nozzle is taken from the single-fluid NS computation. When ions collide with the wall they are neutralized. When electrons collide with the wall they are removed from the simulation.

An inlet plane profile for the DSMC simulation is provided by the single-fluid NS computation for a particular power level and mass flow rate. Remember that the single-fluid NS code models a single temperature that assumes all thermal modes are in thermodynamic equilibrium. For all cases considered, the temperature of the plasma on the centerline is in excess of 18,000 K and a small amount of hydrogen molecules are still undissociated. In the real physical situation, molecular hydrogen cannot exist with such a large vibrational temperature. This is reflected in the DSMC simulations which cannot maintain these high values for the vibrational mode. Due to vibration-dissociation coupling, molecules in high vibrational levels are dissociated preferentially.<sup>(18)</sup> In the DSMC simulation, this leads to a rapid decrease in the vibrational temperature close to the inlet plane. With this exception, all other macroscopic properties from the single-fluid continuum simulation are accurately reproduced by the DSMC calculation at the inlet plane.

The DSMC calculations proceed from the inlet plane out beyond the nozzle exit plane into the near field plume expansion. This allows more direct comparison with many of the experimental measurements that are taken a short distance into the

plume from the nozzle exit. The expansion process is assumed to occur into a perfect vacuum.

### Experimental Set Up

The data for the model comparisons included measurements of hydrogen atom translational temperature and electron number density by optical emission spectroscopy, hydrogen atom velocity and translational temperature by laser-induced fluorescence, and molecular hydrogen number density and rotational temperature by spontaneous laser Raman scattering.

The vacuum facility consisted of a 1.09 m x 0.56 m diameter stainless steel chamber maintained at a background pressure of 0.3 torr during arcjet operation. The arcjet was a 1 kW class radiatively-cooled laboratory type thruster designed and built by NASA Lewis Research Center. Figure 3 provides a schematic of the arcjet. The tungsten nozzle consisted of a 0.64 mm diameter constrictor and a 20 degree half-angle diverging section to an exit plane area ratio of 225. The tip of the 2% thoriated tungsten cathode was approximately 0.69 mm upstream of the nozzle constrictor. Details of the vacuum facility and arcjet have been given elsewhere.<sup>(9)</sup>

### Optical Emission Measurements

In this section, we briefly review the measurements of exit plane temperature and electron number density obtained by optical emission spectroscopic analysis of the hydrogen alpha ( $H_{\alpha}$ ) transition. A detailed description of this diagnostic has been given elsewhere<sup>(10)</sup>

A system consisting of four lenses and two stops was used to image  $H_{\alpha}$  plasma emission from the arcjet exit plane onto the entrance slit of a high resolution (0.006 nm) monochromator. The imaging optics defined a radial resolution at the arcjet exit plane of 80  $\mu\text{m}$ . The narrow entrance slit and optics defined (10  $\mu\text{m}$ ) defined an axial resolution of approximately 25  $\mu\text{m}$ . The collection f# was 14.3, and the depth of focus was 0.32 mm. The signal level was reduced by the use of a small aperture and monochromator slit width, necessary to define high spatial and spectral resolution, to the point where photon counting was chosen as the form of signal detection. Detection at the exit slit was performed with a photomultiplier tube (PMT), the output of which was amplified and routed to a continuously gated photon counter. To eliminate unwanted background light, a 10 nm bandpass  $H_{\alpha}$  interference filter was placed at the entrance slit of the monochromator. The maximum signal at the  $H_{\alpha}$  linecenter was approximately  $4 \times 10^4$  photons per

second. Signal noise consisted primarily of PMT dark noise, which was below 600 photons per second. This quantum-limited detection scheme allowed us to make accurate radially-resolved measurements of  $H_{\alpha}$  emission lineshapes.

Line-of-sight emission scans of  $H_{\alpha}$  were performed 1.0 mm from the nozzle exit plane at six to twelve different chords for a range of arcjet powers and P/m. Due to the radial velocity component, an Abel inversion is strictly not applicable to the arcjet plume. Instead, a shell technique is used to deconvolve the line-of-sight spectra at the various chords into radial properties. This procedure consists of segmenting the plume into annular shells, one shell for each radial position at which the emission spectrum was taken. All properties in the plume are assumed to be radially symmetric and uniform within each shell, and the plasma is assumed optically thin, which is a valid assumption for the non-resonant  $H_{\alpha}$  transition. Thus the line-of-sight emission spectrum of  $H_{\alpha}$  at a given chord will be a superposition of the  $H_{\alpha}$  spectra from the innermost shell at that chord and all outer-lying shells, with the relative intensities weighted by the optical path lengths, as determined by the radii of the shell boundaries. The spectral lineshape from each shell is taken to be a Voigt lineshape consisting of a Doppler-broadened Gaussian and a Stark-broadened Lorentzian. The spectra from the outer shells are appropriately Doppler shifted due to the component of the radial velocity in the direction of the emission. The radial velocity profile is obtained from the LIF velocity measurements of Liebeskind et al.<sup>(9)</sup> In this manner, one first determines the properties in the outer shell and then moves inwards, adding two Voigt functions with each additional shell, until the properties of all shells, related to the Gaussian and Lorentzian contributions (as discussed below) are determined.

The translational temperature of the emitting species is determined from the Gaussian width contribution (which is a manifestation of Doppler broadening) to the Voigt profile within any shell. Fine structure of the  $H_{\alpha}$  transition and instrumental broadening is accounted for. The electron number density is related to the Lorentzian width by Stark broadening. The most recent Stark broadening calculations which include dynamic ion effects<sup>(19)</sup> have shown that that the hydrogen Stark broadening tables of Vidal, Cooper and Smith<sup>(20)</sup> are not accurate for  $H_{\alpha}$  at electron number densities below  $10^{17} \text{ cm}^{-3}$ . Therefore, instead of using the VCS tables, the electron number densities are determined from an empirical approximation to the recent dynamic ion Stark broadening calculations in the range of electron number densities from  $10^8 \text{ cm}^{-3}$  to  $3 \times 10^{13} \text{ cm}^{-3}$ .

### Laser-Induced Fluorescence Measurements

Laser-induced fluorescence (LIF) excitation of the  $H_{\alpha}$  transition is used to measure both hydrogen atom velocity and translational temperature. Below is a brief description of the experimental approach. The reader is referred to References 9 and 21 for a more detailed description of the theory and experimental method.

In the LIF approach, an argon-ion laser-pumped ring-dye laser source, tunable over the range of 656.43 - 656.53 nm is used to selectively excite the  $H_{\alpha}$  transition. For exit plane property measurements, the laser beam was expanded to approximately 40 mm in diameter, collimated, and then focussed along the plume axis (into the arcjet, through a quartz window on the endplate of the chamber, aligned axially with the arcjet). At the exit plane, the beam waist was reduced to 15  $\mu\text{m}$ , and the depth of focus was 0.50 mm. Fluorescence emission was collected along a direction normal to the arcjet axis, through a quartz window on a side-port of the chamber, and directed onto a PMT. A 10 nm bandwidth  $H_{\alpha}$  interference filter was mounted to the entrance of the PMT housing to eliminate unwanted background light. As a result of the axial excitation, the axial velocity component was measured from the Doppler shift of the fluorescence excitation lineshape. The translational temperature was obtained from the Doppler width of the line. The linewidth is partially broadened by the Stark effect associated with the free electrons, and so a correction to the measured width is made in order to account for this broadening mechanism using either the exit plane electron number densities measured by optical emission spectroscopy (described above), or the calculated axial variation in the electron number density from the single-fluid NS model.

For measurements of arcjet flow properties through LIF spectroscopy within the nozzle, fluorescence emission was collected through a window on the endplate of the vacuum chamber, adjacent to the window used for the excitation laser beam. In this configuration the collection optical axis was aligned at 16.3 degrees to the beam axis. A single lens defining a magnification of approximately unity was used for collection and focussing, and a rectangular pinhole, 350  $\mu\text{m}$  high by 150  $\mu\text{m}$  wide, defined the spatial resolution in the axial direction. In this configuration, neutral density filters totaling an optical density of 3.2 were placed in front of the PMT, to prevent saturation of the detector because of the strong intrinsic plasma emission. For both the exit plane and internal nozzle flow studies, the fluorescence signal was considerably smaller than the background emission. As a result, phase-sensitive

detection was performed by mechanically chopping the excitation beam near the dye laser at a frequency of 1.5 kHz.

### Spontaneous Raman Scattering

Spontaneous Raman scattering was used to measure molecular hydrogen number density and rotational temperature. Details of this diagnostic strategy applied to arc-heated hydrogen flows have been discussed in other publications.<sup>(21)</sup> In previous cold flow experiments<sup>(8)</sup> a cw laser was used. However, in order to improve the signal-to-noise ratio in the arc-heated case, a pulsed, frequency-doubled Nd:YAG laser operating at 532 nm, was chosen as the excitation source. The laser was capable of producing 200 mJ pulses with a 10 ns pulse length at a 10 Hz repetition rate.

In order to allow full laser energy to be utilized, the experiment was designed to send the laser beam radially into the arcjet plume near the exit plane. The scattered light was collected at  $120^{\circ}$  from the incident laser direction through a port located in the same circumferential plane as the laser at optical table level, and was focused onto the entrance slit of the same scanning monochromator that was used in the emission studies (described above) with an achromatic two-lens system. The collection lens was limited to an  $f\#$  of 5.7 by the port geometry. The focusing lens was chosen to match the spectrometer  $f\#$ . The spatial resolution was 2 mm in the radial direction, determined by the monochromator slit height, and 0.25 mm in the axial direction, determined by the slit width. A long-pass filter was placed before the entrance slit to further reduce the intensity of collected laser light to negligible levels. The spectrometer slits were 400  $\mu\text{m}$  in width, giving a spectral resolution of 0.2 nm. Light was detected using the same PMT and photon counting electronics as in the emission studies. In this case however, the counter was triggered by the laser using a photodiode. The 15 ns gate width was as narrow as possible to maximize the background rejection while still being wide enough to capture the peak of the signal pulse.

The system was calibrated for absolute efficiency by measuring the Raman scattering from stagnant  $H_2$  at a known temperature and pressure. In order to account for the different efficiency at each transition, the relative efficiency versus wavelength was measured using a tungsten strip lamp. This second calibration was necessary since the transitions from  $J = 4$  through 6 were too weak at room temperature to be accurately measured. Hydrogen number densities are obtained by comparing the measured scattered intensities to the

absolute calibration. Rotational temperatures are obtained by fitting the intensities of the individual  $\Delta J = 0$  rotational transitions within the  $v=0$  to  $v=1$  vibrational manifold to a Boltzmann plot, accounting for effects associated with the coupling between the rotational and nuclear wavefunctions of molecular hydrogen.<sup>(8)</sup>

### III. Results of the Investigation

Three major topics are addressed in this section. The first is the prediction of velocities at the exit plane and within the arcjet. The second is the prediction of  $H_2$  number densities at the exit plane, and finally, the third is the prediction of energy transport and associated temperatures within the arcjet plasma.

#### Arcjet Velocities

Figure 4 presents a comparison of NS and DSMC predictions of axial velocities at the arcjet exit plane with corresponding LIF measurements. DSMC estimates are shown by the solid line, NS solutions by the dashed lines and LIF data by the filled circles. The NS solutions bracket the experimental uncertainties in mass flow rates and power. The results of NS simulations at 1.48 kW and 14 mg/sec differed very little from the 1.40 kW case and are not plotted here. Generally speaking, the agreement between experiment and simulation is remarkably good in both the profile shape and magnitude. Furthermore, the fact that the DSMC and the NS prediction are similar for the same operating condition suggests that the effects of ohmic heating on the centerline velocity are not significant. Note, however, the NS solutions show a significant sensitivity as  $\dot{m}$  varies from 13.1 to 14 mg/sec. Also, the DSMC method and the NS solutions are notably different near the nozzle wall. Although seemingly insignificant, this near wall discrepancy in the axial velocity between the DSMC approach and the NS solutions may have a considerable affect on the computed performance, since a large fraction of the mass is convected out of the nozzle within an annulus close to the wall. The difference between the DSMC approach, NS solution, and LIF data near the anode may be attributed in part to the differences in the DSMC method's handling of momentum transport and in part due to fact that the DSMC and experimental results are taken approximately 1 mm downstream of the exit plane.

Figure 5 carries the comparison of axial velocities up into the nozzle toward the constrictor region and increasing ohmic dissipation. The agreement between experiment and simulation is again exceptional,

particularly when one considers the difficulty of this LIF measurement and the complexity of the calculations. Differences are notable from the starting point of the DSMC calculation,  $Z=0.55$  mm, to approximately  $Z=2.50$  mm. Note that the rate of ohmic heating decreases by an order of magnitude over this distance (Figure 2). The discrepancy between NS and DSMC calculations reflect this change. For values of  $Z$  greater than 2.5 mm the differences between simulation and experiment are not significant.

Figure 6 presents a summary of predicted and measured centerline velocities at the arcjet exit. Powers ranged from 0.6 kW to 1.48 kW for a nominal  $\dot{m}$  of 14 mg/sec. The corresponding change in  $P/\dot{m}$  was from 45 to 110 MJ/kg. As shown, the overall agreement between simulation and experiment remains good in both trend and magnitude. The small differences between NS and DSMC simulation results again underscore the hypothesis that ohmic heating does not significantly affect the centerline velocity predictions.

#### $H_2$ Number Densities

The purpose of the comparisons presented here is to demonstrate potential differences in the way mass transport is treated by the NS and DSMC approaches, as well as to compare simulation results to experiment. Figure 7 presents a direct comparison of NS and DSMC predictions of  $H_2$  exit plane number densities without the complication of ohmic heating. These NS simulations were started from  $Z=0.55$  mm (the same as the DSMC simulations) using the full upstream NS solution as a starting point, but with the ohmic dissipation term turned off for the remaining solution. All other solution parameters remained the same. As shown, the number density profiles are of the same order of magnitude (actually within a factor of two), but differ considerably in shape across the nozzle exit plane. In comparison to the DSMC model, the NS model appears to allow a greater  $H_2$  diffusion rate toward the centerline. Unlike the DSMC results, which peak off center, the resulting NS profile has significantly less radial structure and a distinct maximum near the arcjet centerline. One possible explanation for the differences between NS solutions and the DSMC approach evident in Figure 7 is in the treatment of molecular diffusion over the range of conditions encountered in the expansion process. Another explanation lies in the solution for the temperature field which is affected by a number of complicated factors, for example gas-surface interactions and catalytic surface phenomenon. The NS predictions for this same case show higher temperature at the walls than on the centerline while the DSMC

approach generates a translational temperature that is high on centerline and at the wall. A distinct minimum is shown at about the location of the maximum in the  $H_2$ , a radial location of approximately 2.5 mm.

Figure 8 presents a comparison of predicted  $H_2$  number density with Raman scattering data taken at 1400 W and  $\dot{m} = 14$  mg/sec. Considering the difficulty of the measurement, the comparisons between experiment and simulation are again satisfactory. We note that the NS simulations shown in this figure are for the case where ohmic heating is continued throughout the expansion to the exit plane. With ohmic heating "turned on," the NS and DSMC results are similar in both magnitude and trend. This agreement is considered to be fortuitous, now evident only because of the more direct comparison that was made in Figure 7.

Although it is difficult to anticipate what the DSMC model would predict if ohmic heating was accounted for, it is likely that the densities would be reduced because of the higher temperatures. The DSMC simulations would therefore be expected to be closer in magnitude to the experimental measurements. At the moment, the Raman data fall below both predictions by about a factor of two. Note also that the point of maximum number density in the experimental profile peaks off center. This is attributed to a misalignment of the cathode, and is consistent with a measured rotational temperature profile that peaks opposite the side of the maximum in number density. It is clear that more refined measurements are needed in order to draw specific conclusions concerning profile shapes.

### Energy Transport

The previous two sections have shown that the NS and DSMC predictions of axial velocity and the  $H_2$  mass distribution, at least for the cases posed here, are comparable. Furthermore, they do not differ significantly from experimental data taken in the arcjet exit plane. This observation suggests that differences between measured and predicted performance could be significantly improved by better modelling of energy transport within the arcjet. In this section, NS and DSMC predictions of plasma temperatures (energies) will be compared with LIF and Raman scattering measurements. This comparison leads directly to conclusions concerning the importance of ohmic heating and the appropriate treatment of internal energy modes.

LIF temperature measurements at the exit plane of an  $H_2$  arcjet operating at 1.48 kW and 14 mg/sec are

shown in Figure 9. The solid and dashed lines indicate values predicted by the NS and DSMC models while the filled circles represent the LIF data. There are three important points to note here:

1. The NS model has only one temperature since it assumes an infinite relaxation rate for the internal modes.
2. The DSMC simulation does not include the effects of ohmic dissipation beyond  $Z=0.55$  mm.
3. The LIF temperature is that associated with the  $n=3$  electronically excited hydrogen atom ( $H^*$ ).

The NS prediction for the temperature profile is characterized by higher temperatures than those measured near the anode and lower than those measured on centerline. In general, the NS solution follows the DSMC prediction for vibrational temperature ( $T_{vib}$ ). It is interesting to note that the DSMC prediction for  $T_{vib}$  tracks the experimental data quite well in both shape and magnitude. If  $P_\Omega$  were in fact negligible, one could argue that the vibrational modes of  $H_2$  are loosely equilibrated with the lower electronically excited H states. With consideration given to non-negligible  $P_\Omega$ , one would expect (with sufficient electron-heavy collisions) that all the DSMC temperatures would be somewhat elevated. The effect on the distribution of internal energy between translation, rotation, and vibration is not yet understood.

Figure 10 presents a comparison of the NS solution without  $P_\Omega$  beyond  $Z=0.55$  mm and the DSMC results shown in Figure 9 (repeated here). The change in NS temperature is dramatic. The centerline NS temperature approaches  $T_{tran}$ , indicating an extremely rapid depletion of the rotational and vibrational energy. Figure 11 presents the corresponding picture of the total energy distribution. In this figure the NS solution with and without  $P_\Omega$  are compared with DSMC predictions of the energy density distribution at the arcjet exit plane.  $P_\Omega$  increases the predicted NS energy density by a factor of approximately 4 near the anode and by a factor of 2 on centerline. The resulting profile is nearly flat across the exhaust flow. In contrast, the nonequilibrium DSMC results indicate nearly a factor of 5 increase over the NS solution without  $P_\Omega$  beyond  $Z=0.55$  mm and a factor of 2.5 over the full NS solution.

Figure 12 extends the temperature comparisons upstream toward the constrictor. In this figure the various simulation temperatures are compared with LIF measurements along the axis of an arcjet operating at 1400 W and 14 mg/sec. The scatter of the LIF measurements are indicative of the difficulty of the measurement. The data generally support the final predicted expansion values. It is apparent from this figure that the NS and DSMC approaches reach these exit plane values via greatly different paths. Starting at  $Z=0.55$  mm, the DSMC temperatures at first fall precipitously and then gradually decrease to the exit plane. Over the same axial distance, the NS solution is as much as 10,000 K higher. From the previous discussion, this difference comes about as a result of the ohmic dissipation (not included in the DSMC simulation). It is not until the ohmic dissipation rate falls below the relaxation rate (e.g.,  $Z > 8.5$  mm) that the NS temperature falls below  $T_{vib}$ . The predicted energy distribution will be thus be different for the NS and DSMC approaches throughout the expansion process

Figures 13.a and 13.b provide a comparison of predicted temperatures and measured values of rotational temperature ( $T_{rot}$ ) at the arcjet exit plane. In these figures, the computations were performed for powers of 600 W and 1400 W and the available experimental data is for powers of 800 and 1400 W respectively. The data generally agree in magnitude and overlap the DSMC predictions at both experimental power levels. They do not, however, mimic the simulation's peaks and valleys. Note, however, that the difficulty of the experimental measurement combined with the uncertain effects of  $P_{\Omega}$  and other non-equilibrium phenomena make conclusions concerning profile shapes somewhat tenuous.

A summary view of exit plane temperatures for  $P/\dot{m}$  ranging from 40-to-100 MJ/kg is presented in Figure 14. The measured values (filled squares) are data taken by optical emission. The solid and dashed lines, respectively, represent the NS and DSMC temperature predictions. As the power level increases (at fixed  $\dot{m}$ ), the measured temperatures transition from values very near the predicted  $T_{rot}$  toward values very near the predicted  $T_{vib}$ , overlapping the temperature predicted by the NS code. At the lower power levels the NS solver underpredicts the amount of energy stored in vibrational modes and overpredicts energy contributed to translation. As the applied power increases, the influence of  $P_{\Omega}$  increases in the later portions of the expansion, driving the population of the vibrational levels toward, and eventually above, the fully equilibrated NS values. The observed data trend

suggests that the optical emission and LIF temperatures approach the DSMC predicted  $T_{vib}$  as the applied power increases. The measured temperature values are everywhere greater than either  $T_{trans}$  or  $T_{rot}$ . Just how the influence of increased  $P_{\Omega}$  in the expansion process will affect the DSMC predictions of internal mode temperatures (energies) is still known.

A clear message from this discussion is that a significant amount of energy may be frozen in vibrational states, and is therefore unavailable for conversion to thrust. The NS solutions indicate the importance of including  $P_{\Omega}$  in the vicinity of the anode, but greatly overpredict the relaxation of the internal energy modes. On the other hand, the DSMC solutions do not represent  $P_{\Omega}$ , but do attempt to track the nonequilibrium distribution of internal energy. A comparison of measured  $I_{sp}$  and performance predictions based on the present simulations support these observations. In Figure 15,  $I_{sp}$  data taken at NASA LeRC on the same thruster configuration for  $\dot{m} = 11.2$  and 16.2 mg/sec are plotted for  $P/\dot{m}$ s ranging from 60 MJ/kg to 145 MJ/kg. Both NS and DSMC predictions fall within 10% of the measured values. Ideally, the predicted values of  $I_{sp}$  at  $\dot{m} = 14$  mg/sec should fall somewhere between the two data sets shown. Based on the previous discussion, our conclusion is that the DSMC approach underpredicts performance due largely to the neglect of  $P_{\Omega}$  in the expansion, while the NS solution overpredicts performance due to far too rapid equilibration of internal energy modes.

#### IV. Summary

We have set out using a direct simulation Monte Carlo approach and a continuum based Navier-Stokes solver to investigate the sensitivity of low power hydrogen arcjet performance predictions to the modelling choices of nonequilibrium transport and chemical phenomena. Optical measurements over a wide range of operating conditions have provided velocity, temperature, and hydrogen molecule number density data to anchor and support the simulation results.

We have reached several conclusions concerning state-of-the-art performance models:

1. Agreement between measured and predicted exit plane parameters is an important requirement. A good comparison, however, does not necessarily mean that energy transport has been modeled correctly throughout the flow field.

2. A favorable comparison of exit plane velocity profiles, especially at a single operating condition, is not an adequate measure of merit for state-of-the-art models.
3. Differences in hydrogen number density profiles resulting from the DSMC and NS descriptions of mass transport were not significant for the length or time scales considered in this study. Although the exit plane magnitudes were similar, the variation in profile shapes are indicative of differences in the models and should be explored further.
4. Ohmic dissipation is important throughout the arcjet flow field and cannot be neglected.
5. The internal energy modes (e.g., vibration) are most likely not in local thermal equilibrium and must be appropriately modelled to correctly predict performance.
6. Further refinements in the measurement of temperatures (energies) and number density are needed to validate numerical models of nonequilibrium phenomena.
7. The DSMC approach shows promise, particularly with improved modeling of the plasma phenomena and further refinement of the relaxation and chemical kinetic models.
8. Performance predictions based on state-of-the-art single fluid models would benefit from a simple, physically consistent treatment for the relaxation of vibrational energy modes.

#### Acknowledgments

Support for IDB was provided by the Air Force Office of Scientific Research under Grant F49620-94-1-0328. MAC was provided partial support for this work through the Air Force Office of Scientific Research and Olin Aerospace Company.

#### REFERENCES

1. Butler, G.W., Cassady, R.J., and King, D.Q., "Directions for Arcjet Technology Development," AIAA Paper 94-2652, 25th AIAA Plasmadynamics and Lasers Conference, Colorado Springs, CO, June 20-23, 1994.
2. Butler, G.W., Kashiwa, B.A., and King, D.Q., "Numerical Modeling of Arcjet Performance," AIAA 21<sup>st</sup> Fluid Dynamics, Plasma Dynamics and Lasers Conference, Seattle, WA, June 18-20, 1990.
3. Butler, G.W. and King, D.Q., "Single and Two Fluid Simulations of Arcjet Performance," AIAA Paper 92-3104, AIAA/SAE/ASME/ASEE 28<sup>th</sup> Joint Propulsion Conference and Exhibit, Nashville, TN, July 6-8, 1992.
4. Miller, S. and Martinez-Sanchez, M., "Nonequilibrium Numerical Simulation of Radiation-Cooled Arcjet Thrusters," 23<sup>rd</sup> International Electric Propulsion Conference, Seattle, WA, Sept. 13-17, 1993.
5. Rhodes, R. and Keefer, D., "Modeling Arcjet Space Thrusters," AIAA Paper No. 91-1994, AIAA/SAE/ASME/ASEE 27<sup>th</sup> Joint Propulsion Conference, June 24-26, 1991, Sacramento, Calif.
6. Butler, G.W., Kull, A.E., and King, D.Q., "Numerical Simulations of Hydrogen Arcjet Performance," 23<sup>rd</sup> International Electric Propulsion Conference, September 13-16, Seattle, Washington, 1993.
7. G.A. Bird, *Molecular Gas Dynamics and Direct Simulation of Gas Flows*, Oxford University Press, 1994.
8. Boyd, I.D., Beattie, D.R., and Cappelli, M.A., "Numerical and experimental investigations of low-density supersonic jets of hydrogen," *J. Fluid Mech.* **280**, 1994, pp. 41-67.
9. J.G. Liebeskind, R.K. Hanson and M.A. Cappelli, "Laser-Induced Fluorescence Diagnostic for Temperature and Velocity Measurements in a Hydrogen Arcjet Plume"; *J. Applied Optics* **32**, no. 30, 6117 (1993).
10. P.V. Storm and M.A. Cappelli, "High Spectral resolution Study of a Low-Power Hydrogen Arcjet Plume"; AIAA-95-1960; 26th AIAA Plasmadynamics and Lasers Conference, June 1995.

## REFERENCES

11. Addressio, F.L., et al, "Caveat: A Computer Code for Fluid Dynamics Problems with Large Distortion and Internal Slip," LA-10613-MS, Rev. 1, UC-905, Los Alamos National Laboratory, May 1992.
12. Yos, J.M., "Transport Properties of Nitrogen, Hydrogen, Oxygen, and Air to 30,000K," AVCO Corporation Technical Memorandum RAD-TM-63-7, Contract AF33(616)-7578, Task 73603, March, 1963.
13. McBride, B.J. and Gordon, S., "Fortran IV Program for Calculation of Thermodynamic Data," NASA TN D-4097, July, 1965.
14. Boyd, I.D., "Vectorization of a Monte Carlo Simulation Scheme for Nonequilibrium Gas Dynamics," J. Comp. Phys. 96, 411 (1991).
15. Boyd, I.D., Penko, P.F., Meissner, D., and DeWitt, K.J., "Experimental and Numerical Investigations of Low-Density Nozzle and Plume Flows of Nitrogen," AIAA J. 30, 2453 (1992).
16. Boyd, I.D., Jafry, Y., and Vanden Beukel, J., "Particle Simulation of Helium Microthruster Flows," J. Spacecraft 31, 271 (1994).
17. Boyd, I.D., "Analysis of Vibrational-Translational Energy Transfer Using the Direct Simulation Monte Carlo Method," Physics of Fluids A 3, 1991, pp. 1785-1791.
18. Boyd, I.D., "Analysis of Vibration-Dissociation-Recombination Processes Behind Strong Shock Waves of Nitrogen," Physics of Fluids A 4, 1992, pp. 178-185.
19. D.E. Kelleher, W.L. Wiese, V. Helbig, R.L. Greene and D.H. Oza; "Advances in Plasma Broadening of Atomic Hydrogen"; *Phys. Scripta*, T47, 75 (1993).
20. C.R. Vidal, J. Cooper and E.W. Smith; "Hydrogen Stark Broadening Tables"; *The Astrophysical Journal Supplement Series* 25 no. 214, 37 (1973).
21. P.V. Storm and M.A. Cappelli, "Laser-Induced Fluorescence Measurements Within an Arcjet Thruster Nozzle", AIAA -95-2381, 31st Joint Propulsion Conference, San Diego, July, 1995..

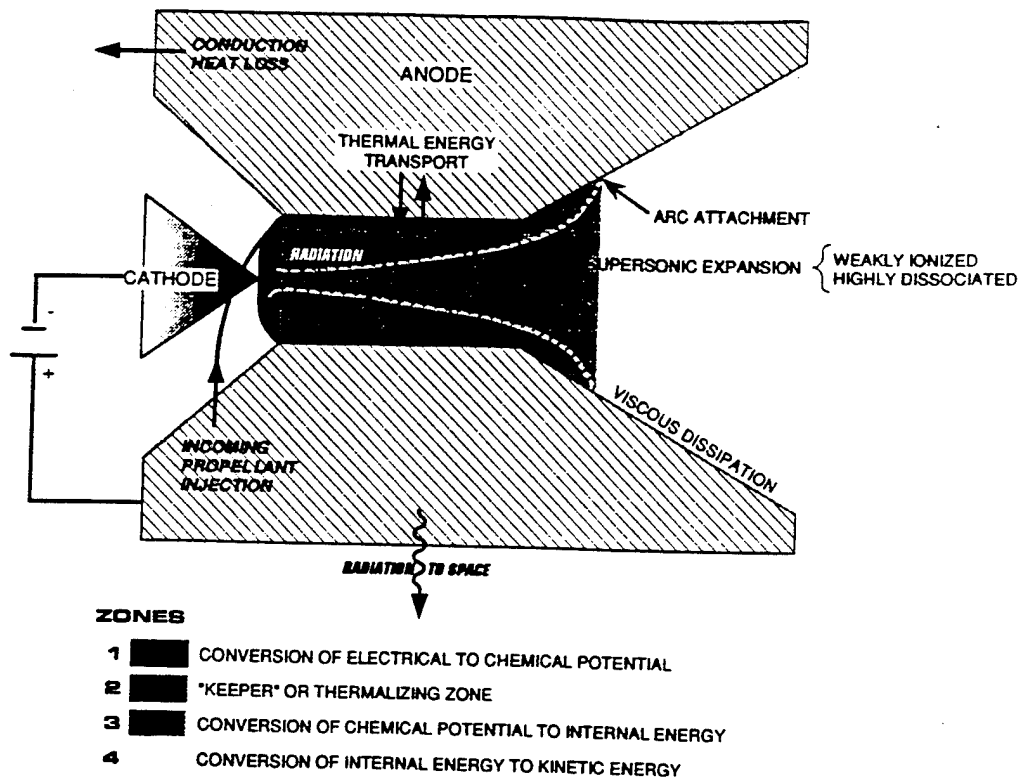


Fig. 1. Key features of the arcjet physics.

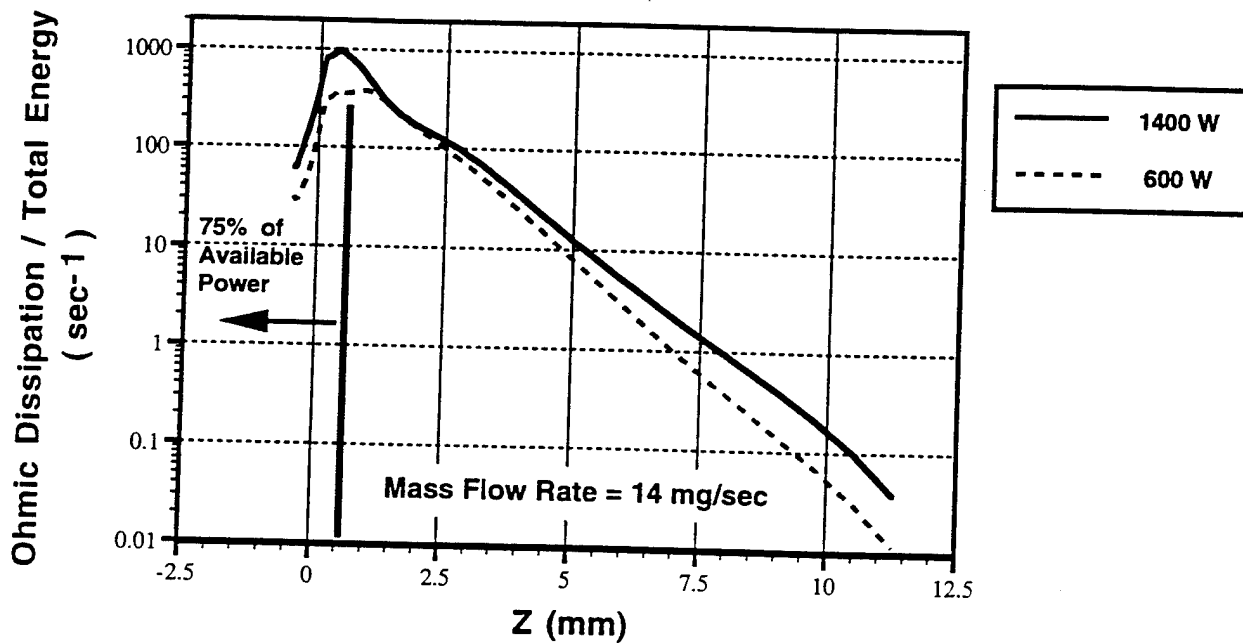


Fig. 2. Single fluid prediction of the ratio of ohmic dissipation to internal energy along the axis of an H<sub>2</sub> arcjet.

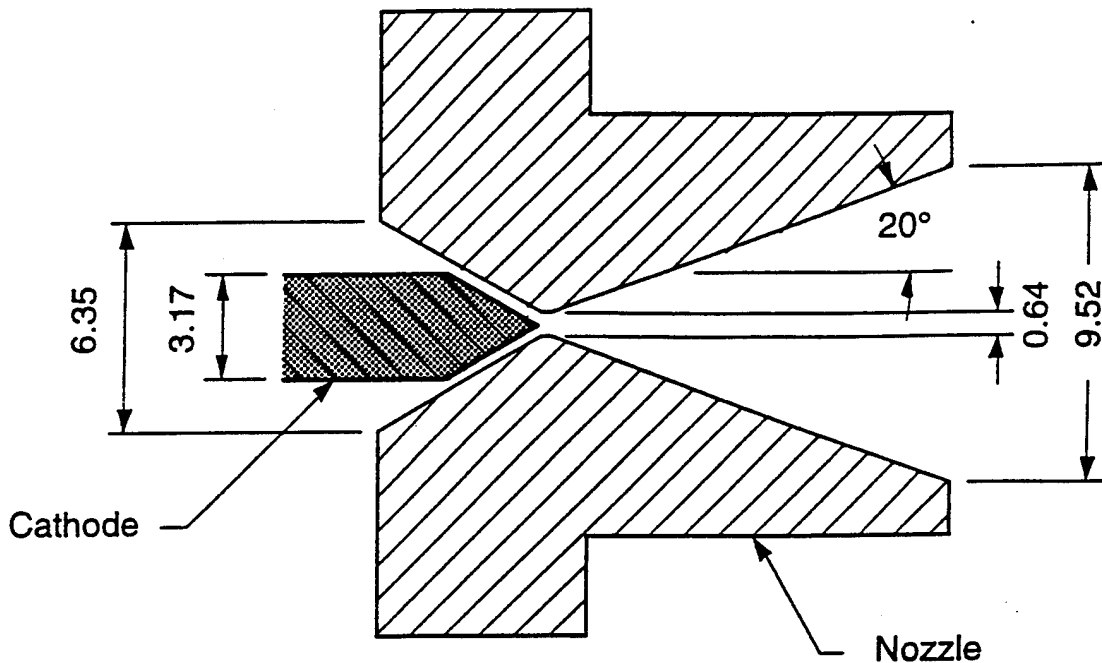


Fig. 3. Drawing of the 1 kW-class arcjet nozzle and cathode, key dimensions in mm.

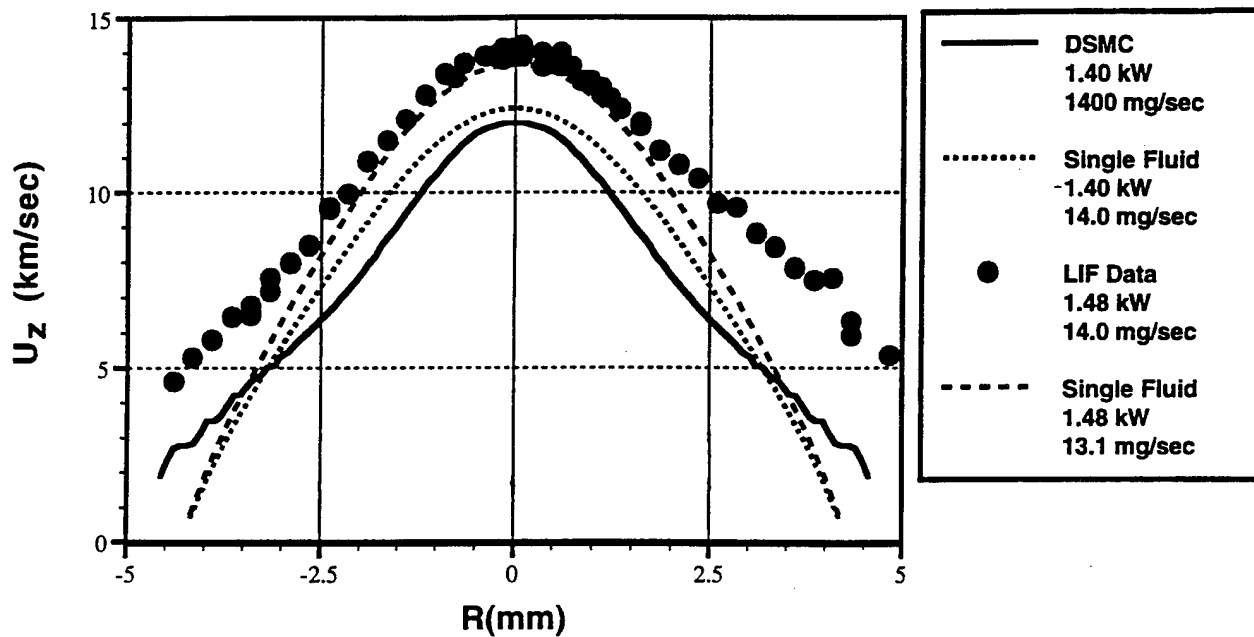


Fig. 4. LIF data with DSMC and single fluid model predictions of H<sub>2</sub> arcjet exit plane velocity.

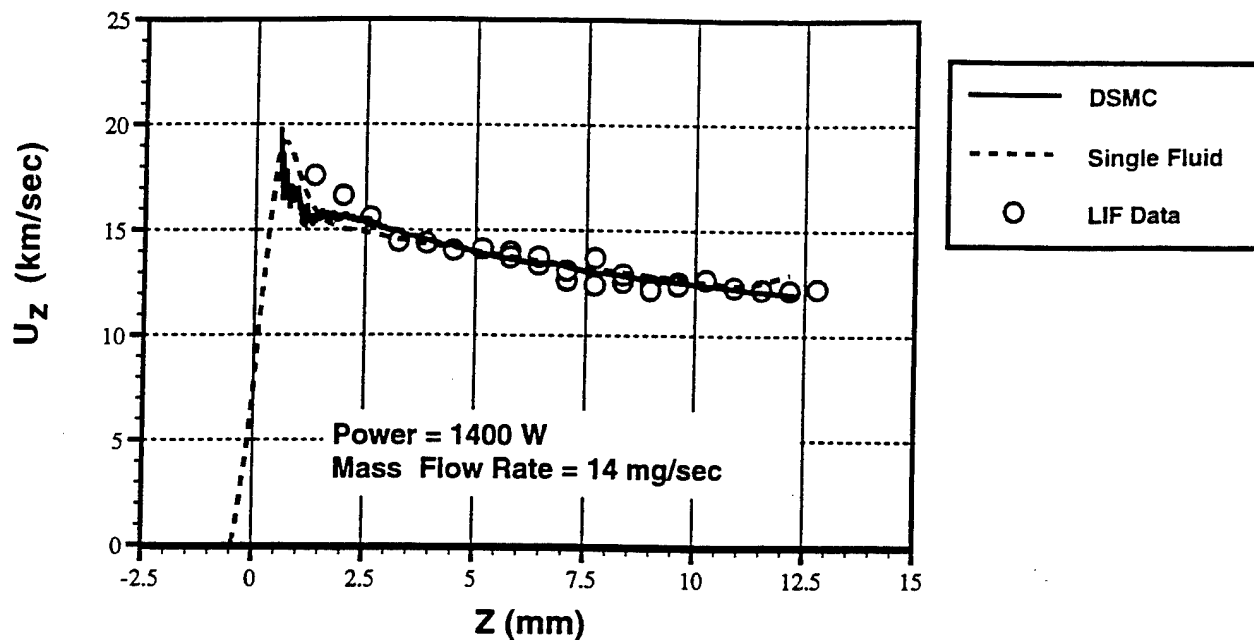


Fig. 5. Comparison of LIF data with DSMC and single fluid model predictions of axial velocity.

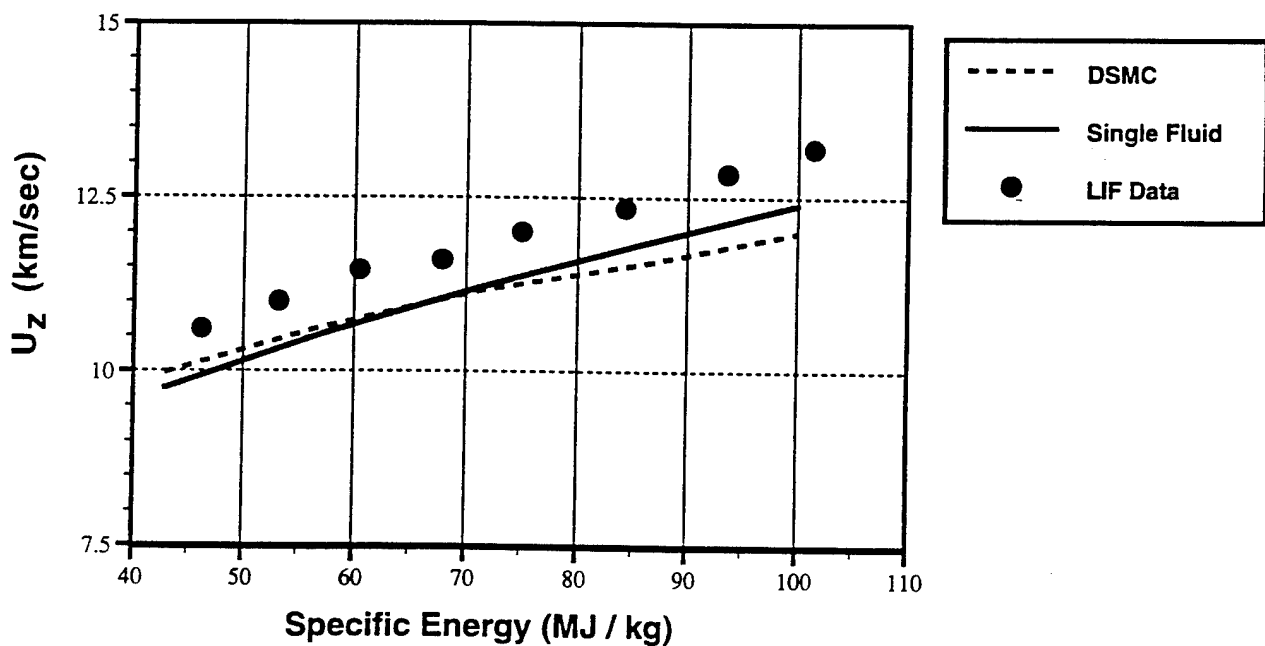


Fig. 6. Comparison of LIF data with DSMC and single fluid model predictions of H<sub>2</sub> arcjet centerline velocity.

- Specific energies from 40 to 100 MJ/kg
- Mass flow rate = 14 mg/sec

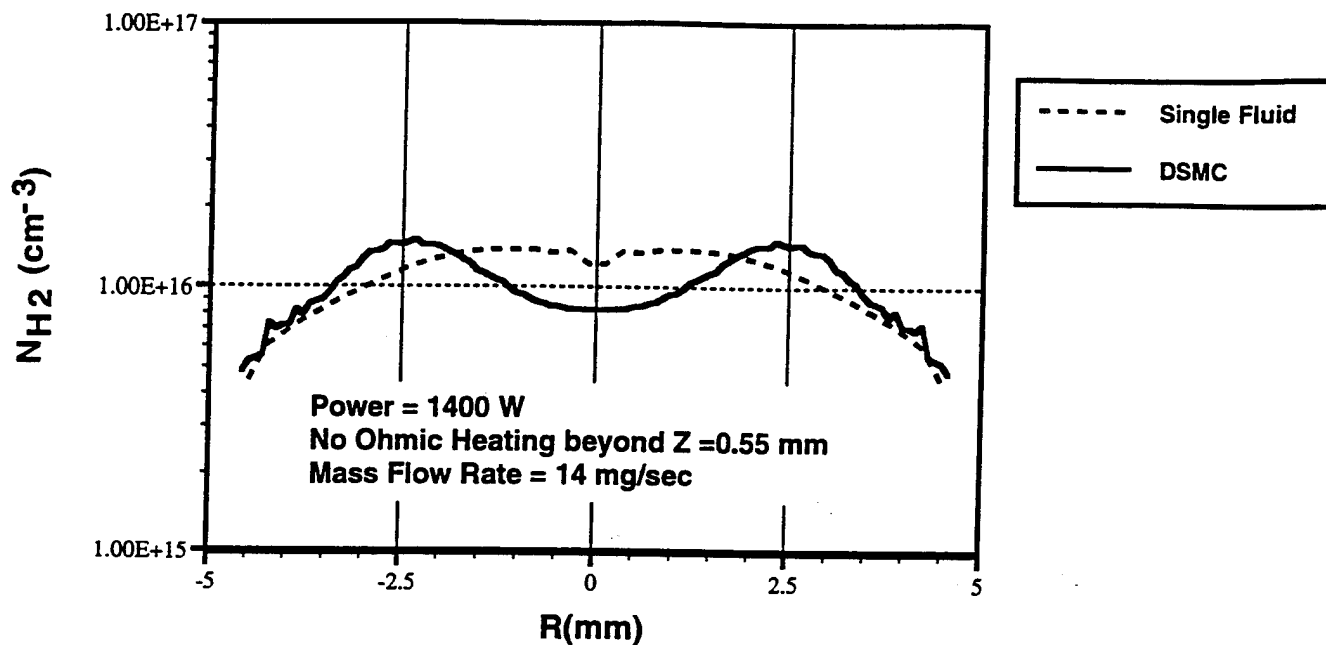


Fig. 7. Comparison of DSMC and single fluid model predictions of H<sub>2</sub> exit plane density.

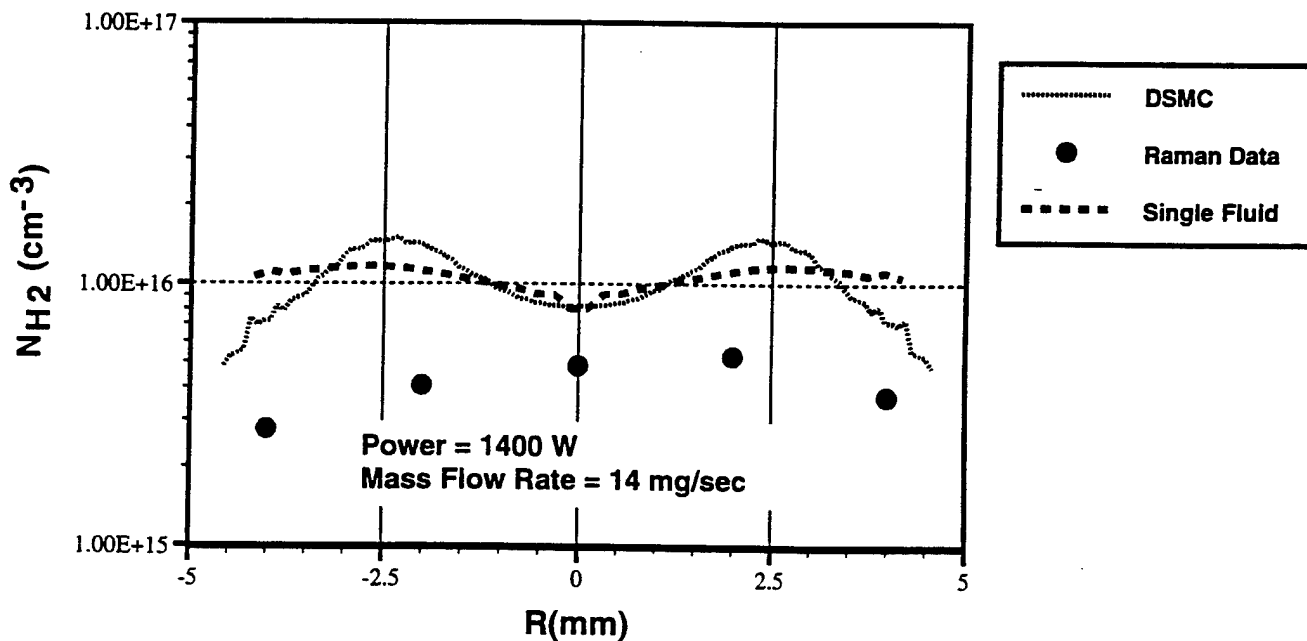


Fig. 8. Comparison of Raman data with DSMC and single fluid model predictions of H<sub>2</sub> exit plane number density.

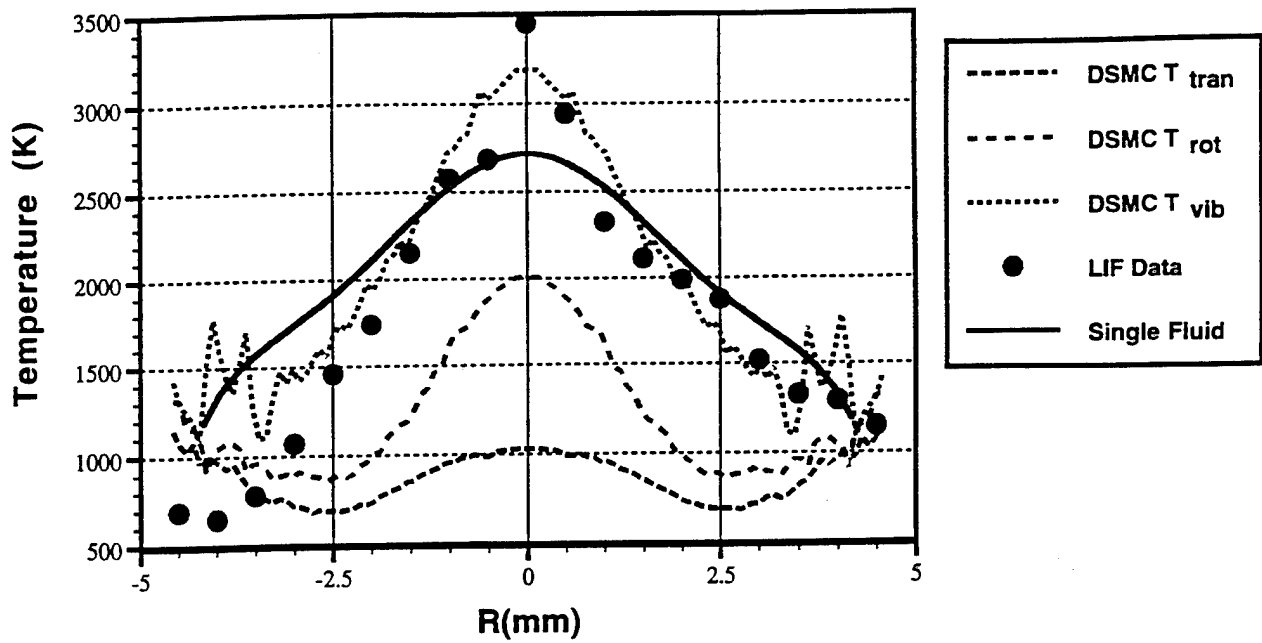


Fig. 9. Comparison of LIF data with DSMC and single fluid model predictions of H<sub>2</sub> arcjet exit plane temperatures.

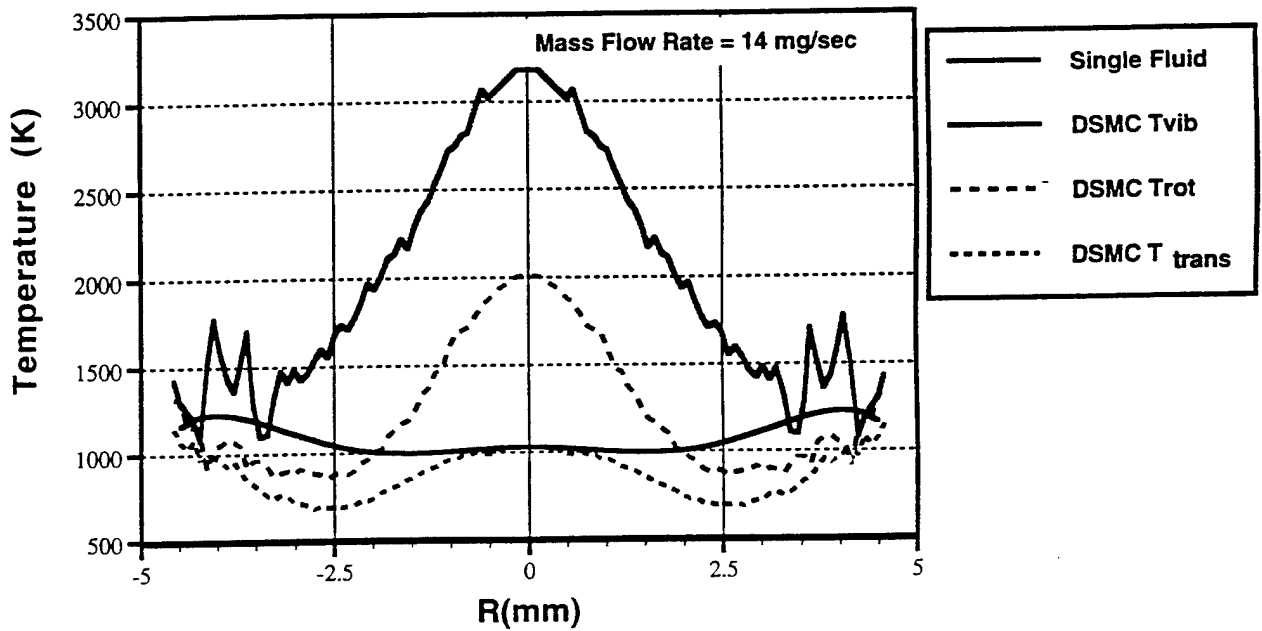


Fig. 10. Comparison of DSMC and single fluid model predictions of H<sub>2</sub> arcjet exit plane temperatures.

● No ohmic heating beyond Z = 0.55 mm

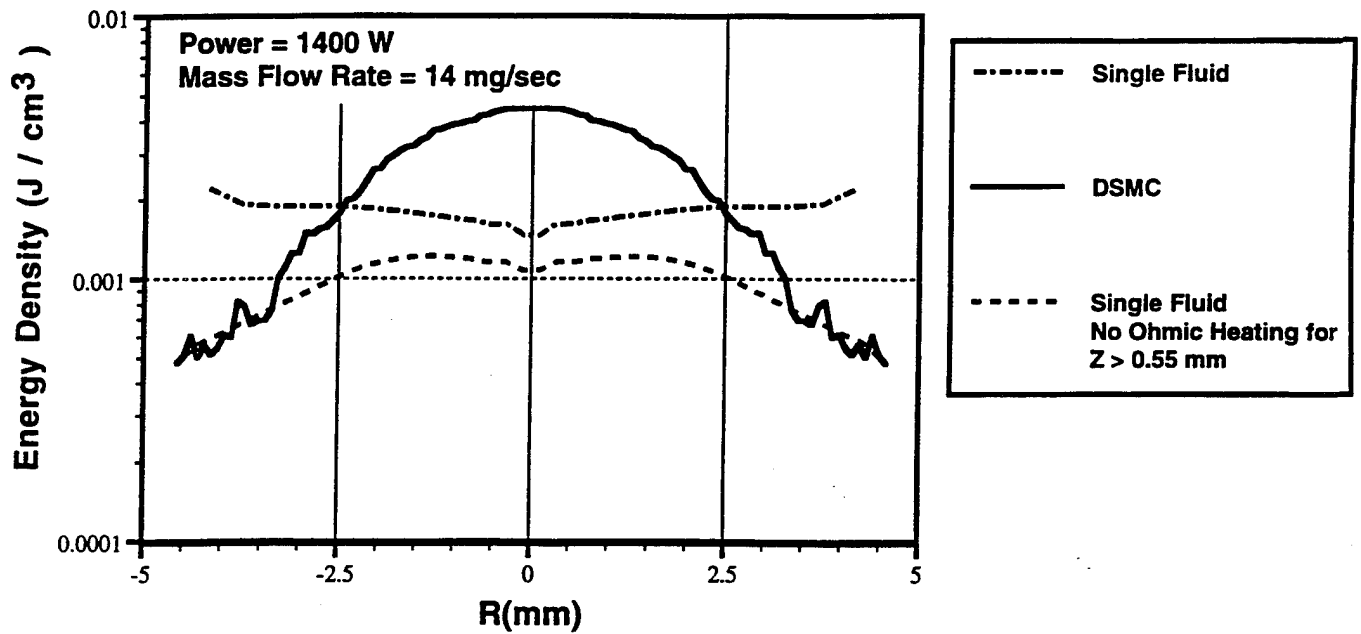


Fig. 11. A comparison of DSMC and single fluid model predictions of H<sub>2</sub> exit plane number density.

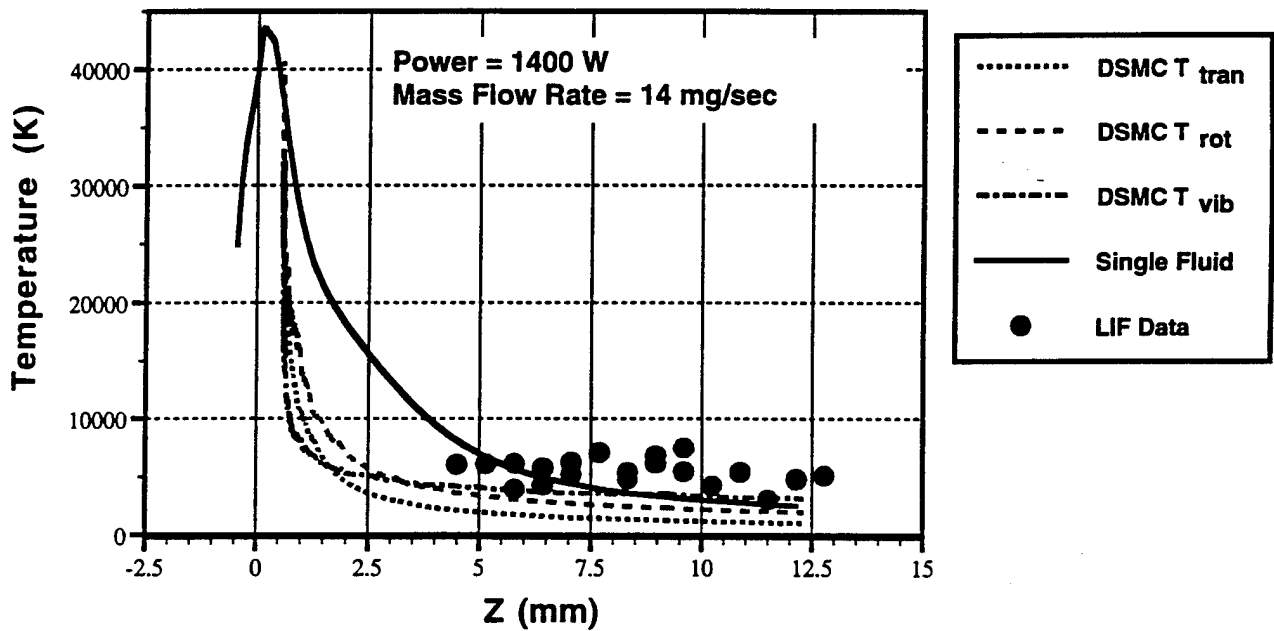


Fig. 12. Comparison of LIF data with DSMC and single fluid model predictions of H<sub>2</sub> arcjet centerline temperatures.

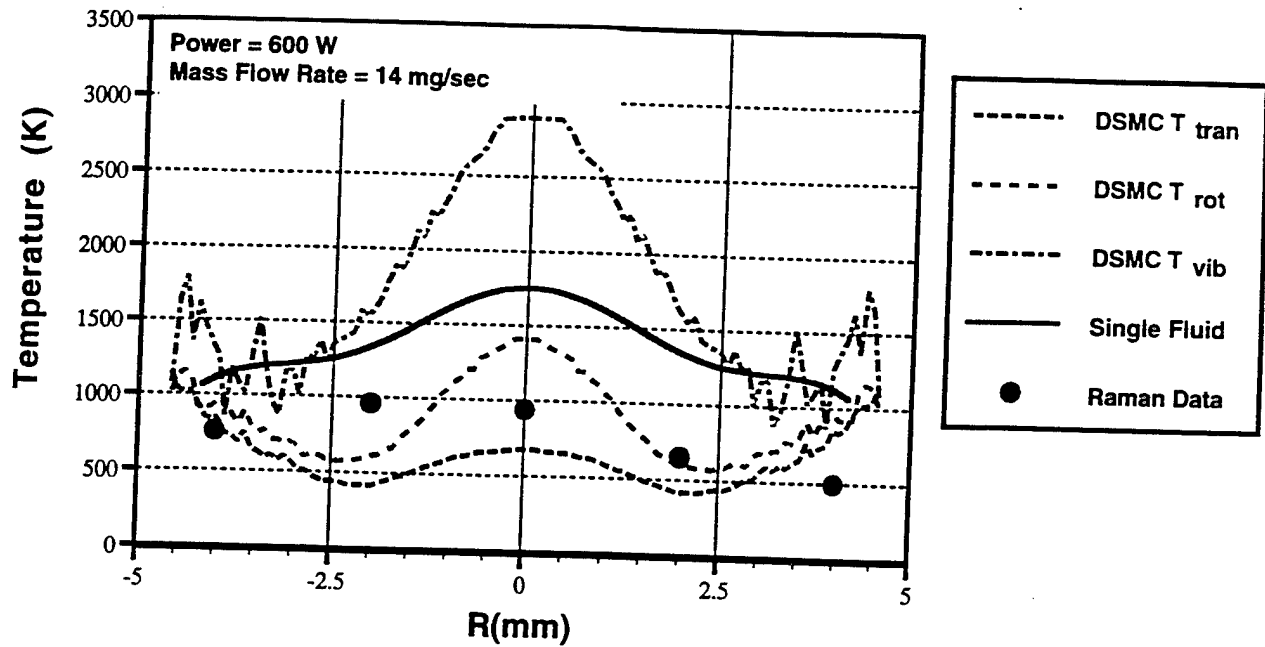


Fig. 13a. Comparison of Raman data with DSMC and single fluid model predictions of H<sub>2</sub> arcjet exit plane temperatures.

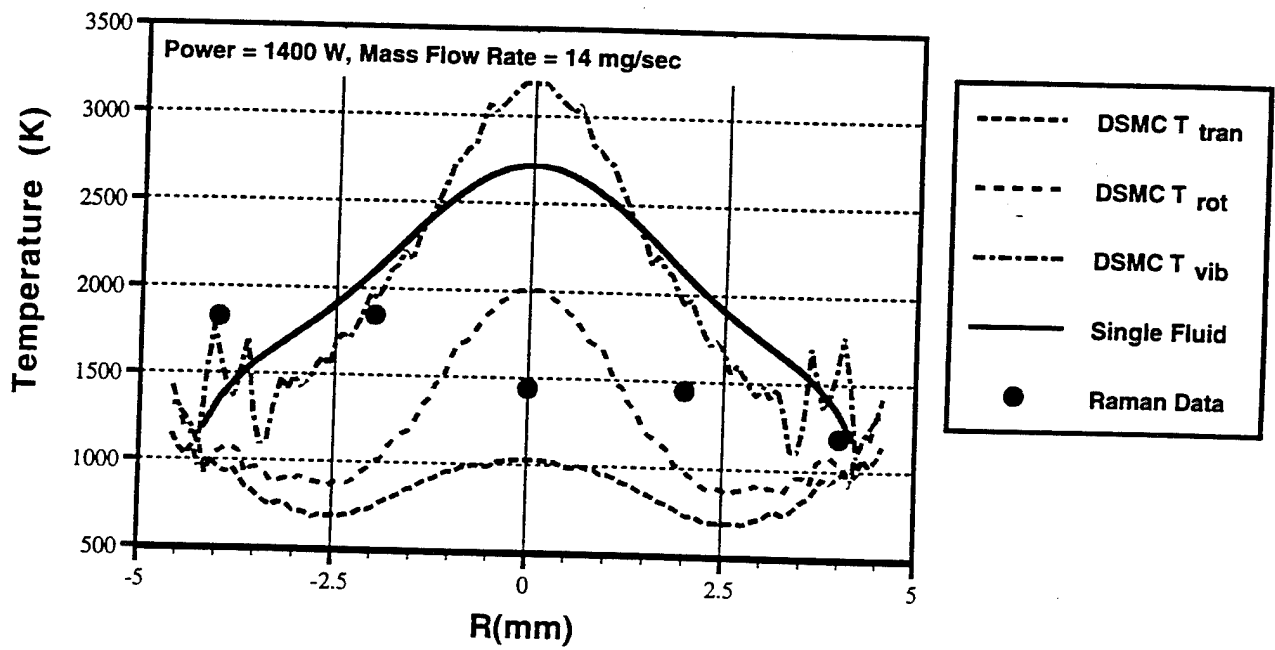


Fig. 13b. Comparison of Raman data with DSMC and single fluid model predictions of H<sub>2</sub> arcjet exit plane temperatures.

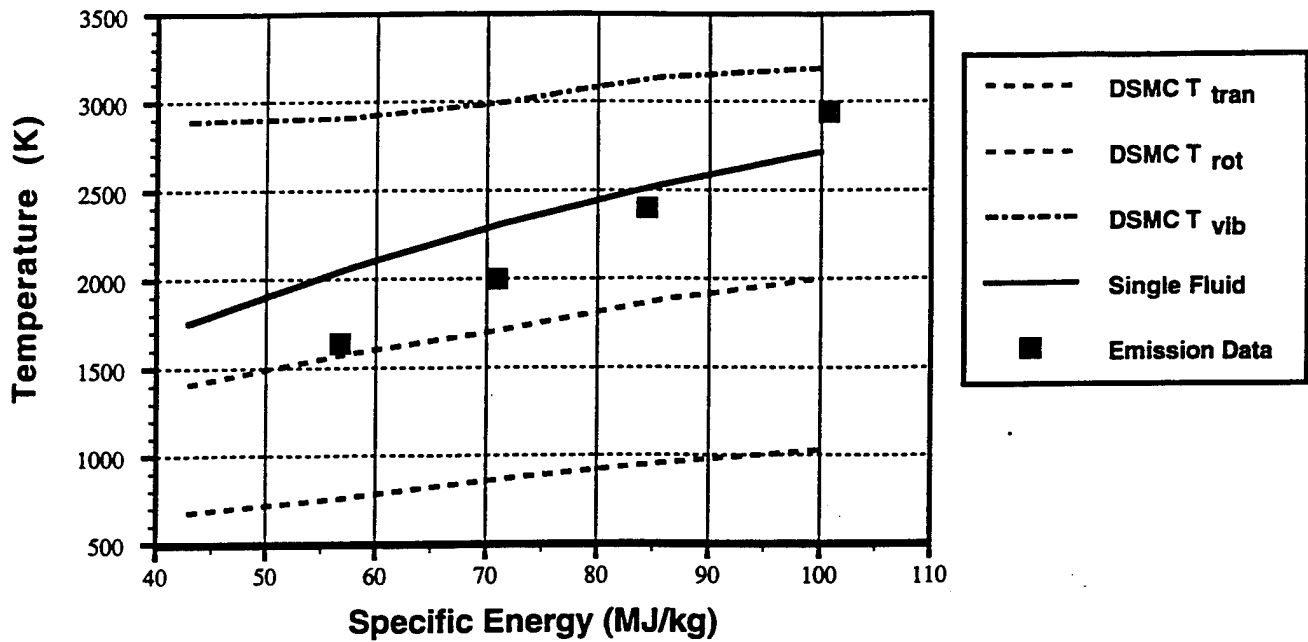


Fig. 14. Comparison of LIF data with DSMC and single fluid model predictions of  $H_2$  arcjet centerline temperatures.

- Specific energies from 40 to 100 MJ/kg
- Mass flow rate = 14 mg/sec

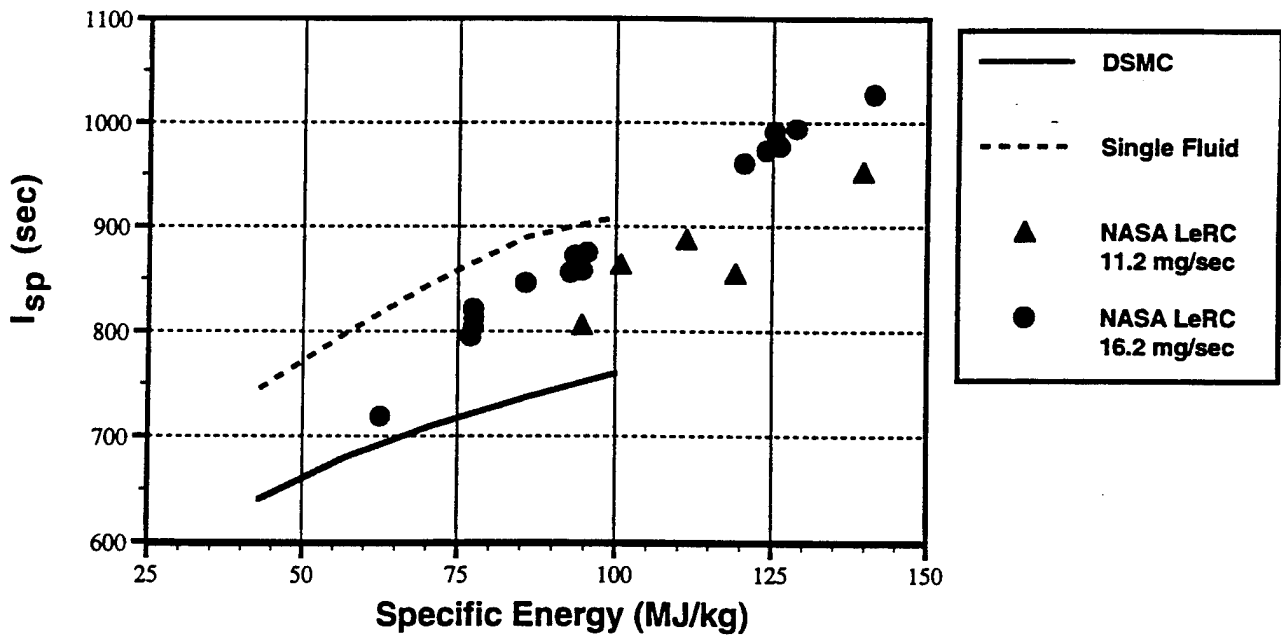


Fig. 15. Comparison of model predictions and measured  $H_2$  arcjet performance.